Doctoral Thesis

Studies on Conversion of Metal-Organic Frameworks Toward Synthesis of Functional Nanomaterials

Kyung Joo Lee

Department of Chemistry

Graduate School of UNIST

2017

Studies on Conversion of Metal-Organic Frameworks Toward Synthesis of Functional Nanomaterials

Kyung Joo Lee

Department of Chemistry

Graduate School of UNIST

Studies on Conversion of Metal-Organic Frameworks Toward Synthesis of Functional Nanomaterials

A dissertation
submitted to the Graduate School of UNIST
in partial fulfillment of the
requirements for the degree of
Doctor of Philosophy

Kyung Joo Lee

07. 17. 2017

Approved by

Advisor
Hoi Ri Moon

Studies on Conversion of Metal-Organic Frameworks Toward Synthesis of Functional Nanomaterials

Kyung Joo Lee

This certifies that the dissertation of Kyung Joo Lee is approved.

07. 17. 2017

Advisor: Hoi Ri Moon

Myoung Soo Lah

Wonyoung Choe

Soojin Park

Sang Hoon Joo

Abstract

Recently, the utilization of metal-organic frameworks (MOFs) has attracted great interest as precursors for synthesizing functional nanostructured materials, which are difficult to obtain by conventional methods. Since MOFs comprise the alternating array of organic and inorganic components, nanostructured materials such as porous metal oxides, assembled metal/metal oxide nanoparticles, porous carbon and their composites can synthesize through transformation of well-tailored MOFs. Those converted materials have been studied due to diverse applications including energy conversion and storage, gas sorption, and catalysis.

We synthesized the Mg-based MOF constructed from aliphatic carboxylate ligands which are thermally less stable and much labile than aromatic ligands. The thermal conversion of the aliphatic-ligand based MOF (Mg-*aph*-MOF) leads to the formation of nanoporous metal oxides. During the thermal decompositions of MOF, aliphatic ligands transformed into organic vesicles which acted as self-templates, and finally were converted to porous structure. Furthermore, MOFs also appear as promising templates for the fabrication of well-defined microstructures that are difficult to obtain from conventional approaches. In this regard, we prepared two different Co-based MOFs composed of the same building blocks. Through proper heat treatment of MOFs, the two kinds of Co_3O_4 were obtained with the retention of parent MOF morphology such as plate-like and rod-like shapes.

Along with metal oxide nanomaterials, three-dimensional mesoporous graphitic carbon (3D *meso*G) was synthesized via the thermal conversion of Ni^{II} coordination compounds. During the thermolysis of $[Ni_2(EDTA)]$ ($EDTA^{4-}$ = ethylenediaminetetraacetate), Ni^{II} ions are transformed into metallic Ni nanoparticles (Ni NPs) which act as a catalyst for graphitization of decomposed ligands and a template for generating mesopores. By varying the type of ligands and metal centers of the starting compounds, we can examine the role of *in-situ* generated species from those components during thermolysis and manipulate the structure of resultant 3D *meso*G.

Lastly, understanding the conversion phenomena of a Zn-based MOF could be exploited for synthesizing metal-carbon composites. Zn-based MOFs have been adopted for the preparation of nanoporous carbon, evaporating an intermediate Zn metal via carbothermic reduction during thermolysis. Therefore, we utilized the Zn metal *in situ* evolved in Zn-based MOF conversion, which play an important role as a reducing agent for foreign metal oxides, or zincothermic reduction. In the reaction system of a Zn-MOF with GeO_2, *in situ* evolved Zn reduce GeO_2, producing Ge and ZnO. Interestingly, ZnO is automatically reduced to Zn via a carbothermic reduction during the conversion process, which returns reducing agent to the reaction. Thus, the repeated occurrence of the zincothermic and carbothermic reduction reaction promotes a *recyclable redox-metallothermic reaction*.

Contents

List of Figures

Chapter III

Chapter IV

List of Tables

Chapter I. Introduction

1.1 Metal-organic frameworks

Metal-organic frameworks (MOFs) are a class of porous crystalline materials which possess a high surface area and large pore volume.[1,2] MOFs are composed of metal clusters and organic ligands via coordination bonds between inorganic parts and organic parts. They have attracted attention in extensive applications such as gas separation and storage,[3,4] molecular sensing,[5] and catalysis[6] because, an appropriate choice of metal and organic building blocks enables the rational design with structural control over pore size, surface area and functionality.[7,8]

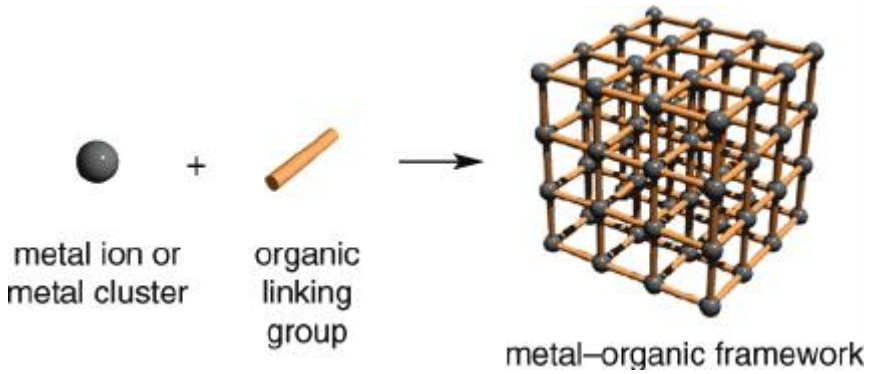

Figure 1.1 Schematic illustration of metal-organic frameworks.[9]

However, their poor chemical and thermal stability is the main obstacle for practical applications of pristine MOFs. MOFs which are coordination network consisting of metal ions and organic ligands can easily degrade via displacement of organic ligands by water molecules, leading to losing the crystallinity.[10,11] Thus, researchers have devoting their effort and attention to improving their stability.[12-14] The Cohen group demonstrated that integration of alkyl groups within MOF can improve the moisture resistance.[12] Amine-containing MOF, IRMOF-3 could be easily introduced hydrophobic alkyl chains via postsynthetic modification approach and IRMOFs modified with longer alkyl chains showed large contact angles ≥ 116° which were considered as hydrophobic materials. The Zhou group has reported the synthesis of porphyrinic zirconium MOF, PCN-223 constructed from 12-connected Zr_6 cluster.[13] With its high connectivity, PCN-223 exhibited outstanding stability in aqueous solutions with board pH values from 0 to 10. In other way, MOFs combine water-tolerant polymers leading to improved stability as well as fabricating with ease.[14]

Another approach is to utilize the instability of MOFs. In the view of materials chemistry, MOFs composed of metal clusters and organic linkers are promising precursors for synthesizing metal/metal oxides, carbon and its hybrid materials. In recent decade, conversion reactions that transform MOF precursors into new materials have emerged as new synthetic approaches.[15-18] Furthermore, well-tailored nanomaterials derived from transformation of metal-organic frameworks have attracted attention due to widespread applications including energy conversion and storage,[19] catalysis,[20] gas sorption,[21] and sensors.[22]

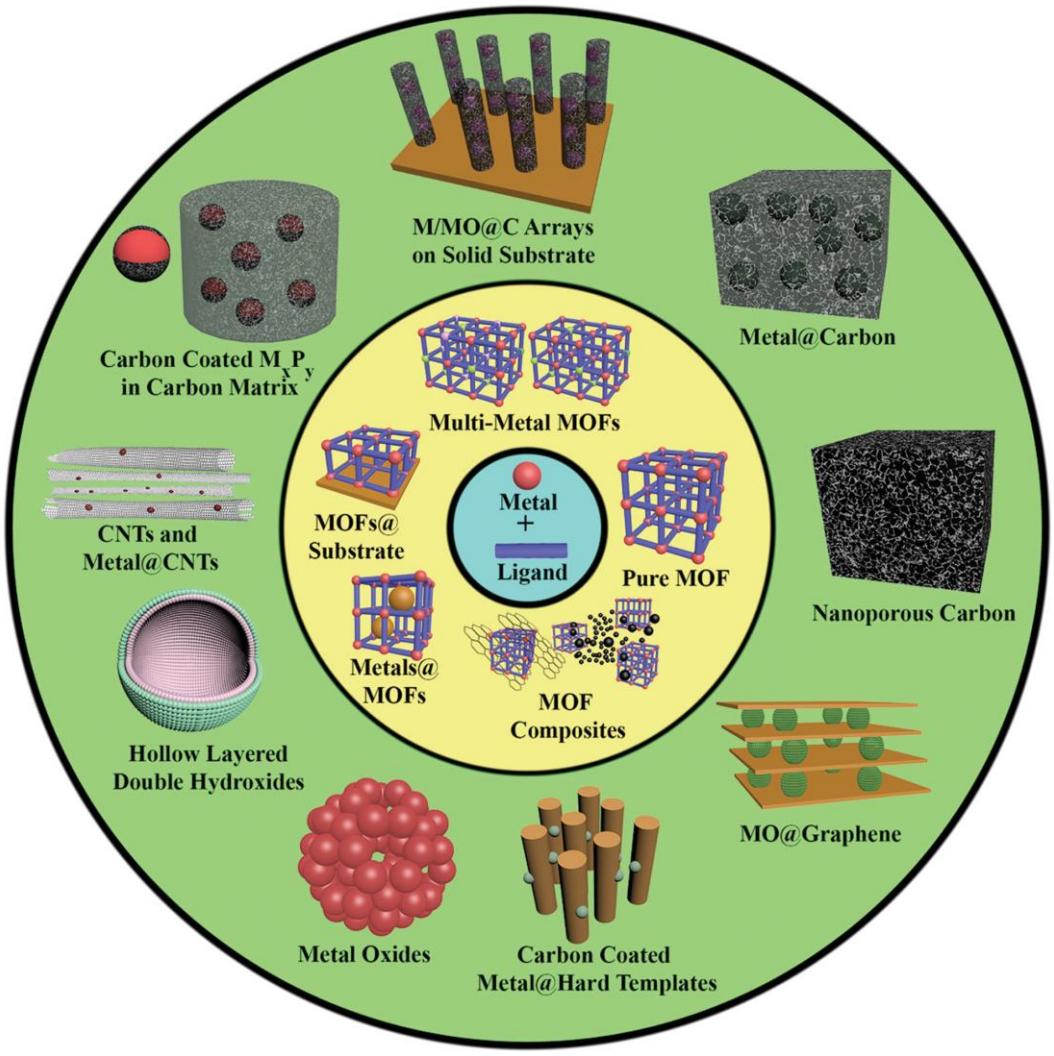

Figure 1.2 Schematic illustration regarding the utilization of metal-organic frameworks as precursors.

1.2 Conversion of metal-organic frameworks

In early stages of transformation of metal-organic frameworks, researchers discovered the materials after measurement of thermogravimetric analysis. Subsequently, they traced solid-state transformation along with temperatures. In 2004, the Loye group published a report regarding solid-state transformation study of a metal-organic precursor, [ZnF(3-amino-1,2,4-triazole)].[23] During the thermolysis, even though the framework decomposed and chemical composition changed, the intrinsic shape of MOFs was retained. They suggested the solid-state transformation of a metal-organic precursor was an easy and straightforward method to fabricate the nanomaterials. Since then papers regarding the synthesis of not only metal oxide also metal and/or carbon via solid-state transformation of MOF have been reported.

The early attempts in the decomposition of MOFs rely on calcination which was defined as heating to high temperatures in air or O_2 by IUPAC and consequentially metal oxide materials without carbogenic species are almost obtained.[15] The CuO microplates were synthesized after calcination at 500 ^oC for 6 h of Cu-based complex, [Cu(*N*,*N*-bis(2-hydroxyethyl)glycinate$)_2$].[24] The average size and shape of plates remained unchanged with a Cu-based complex. The Chen and co-workers reported that the macroporous monolithic foams of lanthanide oxides were synthesized after direct calcination of lanthanide-organic coordination polymers comprised of asparagine as ligands without the need of additional templates or surfactants.[25] During the heat treatment under inert atmosphere, lanthanum-organic precursors were aggregated as solid spheres which became hollow and combined with each other. The inside-out Ostwald ripening process could be driven by release of ligands during calcination resulting in the macroporous foams of lanthanide oxide.

The thermal decompositions under oxidative atmosphere usually result in the formation of carbon-free metal oxides that are prone to be aggregated. It is very difficult to fabricate the nanosized metal/metal oxide as well as nanostructured carbon after calcination of MOFs. Thus, to prepare the carbon or metal/metal oxide nanoparticles, researchers have used a thermolysis of MOFs in inert environments such as N_2, Ar and so forth.

In 2008, the Xu group reported the use of MOFs as a sacrificial template for synthesis of nanoporous carbons for the first time.[26] They introduced furfuryl alcohol as carbon precursors into cavities of porous MOF-5, [Zn_4O(1,4-benzenedicarboxylate$)_3$] used as a template. After thermal conversion at 1000 ^oC under inert atmosphere, highly porous carbon without Zn-related species, which exhibits a high specific surface area and hydrogen uptake was obtained. The authors explained that Zn ions within metal-organic frameworks formed ZnO owing to decomposition between 425 and 525 ^oC and ZnO was reduced at temperature higher than 800 ^oC. Subsequently metallic Zn easily vaporized away along with the Ar flow, leading to formation of pure carbon species.

Upon this paper, the use of a MOF as a template as well as a precursor followed by the thermolysis under inert atmospheres have been researched for synthesizing well-tailored nanomaterials. MOFs possessing a high surface area and pore volumes afford access to diverse molecules including not only carbon precursors but metal-complex,[27] metal oxide species,[28] and polyoxometalate.[29] The introduction of foreign precursors into MOFs followed by thermal decompositions enables us to control the contents of carbon and metal-related species.

Actually, the MOF itself comprising inorganic parts and coordinating organic ligands is fully qualified for precursors to synthesize metal/metal oxide and or nanoporous carbon materials. Furthermore, a proper condition of conversion such as target temperature, holding time, atmosphere, and flow rates leads to controlled morphology and properties of nanomaterials.

1.3 Nanostructured materials via conversion of metal-organic frameworks

As mentioned above, metal-organic frameworks are comprised of metal clusters and organic linkers by coordination bonds. In the view of materials, MOFs positioning metal atoms and organic parts periodically are close to an ideal precursor for synthesizing diverse kinds of nanomaterials. These are mainly three types of resultant materials, metal/metal oxides, carbon and its hybrid materials. In this section, I will introduce several papers regarding the synthesis of nanomaterials via conversion of metal-organic frameworks with control over structures, dimensionality, morphology, and porosity.

1.3.1 Metal oxides

To prepare the metal oxides derived from metal-organic frameworks, the calcination of MOFs is generally used. However, the harsh heat treatment such as oxidative atmosphere and high temperature commonly leads to the collapse of desired structures. To overcome this obstacle, the choice of suitable precursors considering thermal stability, structures, compositions and porosity with controlled heating conditions including ramping rate, atmosphere, target temperature and holding time is important to realize the desired structures of converted materials.

In 2011, the Oh group synthesized the nanorods of hematite (α-Fe_2O_3) and magnetite (Fe_3O_4) prepared by controlling the calcination conditions of coordination polymers, Fe-MIL-88B consisting of FeO_6 octahedral trimers coordinated with 1,4-benzenedicarboxylate ligands (BDC).[30] The calcination of nanorods of Fe-MIL-88B in air at 380 ^oC produced the hematite nanorods so that the morphology of parent MOF was well-retained. For reduction of hematite to magnetite by heat treatment, a reducing agent is necessary such as hydrogen or organic species. Thus, second thermal treatment of organic residue-containing hematite was performed under inert atmosphere. These results suggested the synthetic strategy for synthesis of iron oxides with defined morphology and phase via MOF conversion.

That is called as pseudomorphic conversion; the morphologies of resultant materials after thermolysis are similar to/same as the morphologies of parent MOFs. Actually, the architecture of higher level structures is not well-established. Fortunately, MOFs have diverse structures with well-defined morphologies and proper thermolysis conditions of MOFs enable the pseudomorphic conversion. Thus, as shown in Figure 1.4, rod-like α-Fe_2O_3 and Fe_3O_4 were synthesized by thermolysis of rod-shaped iron-based metal organic frameworks.[30]

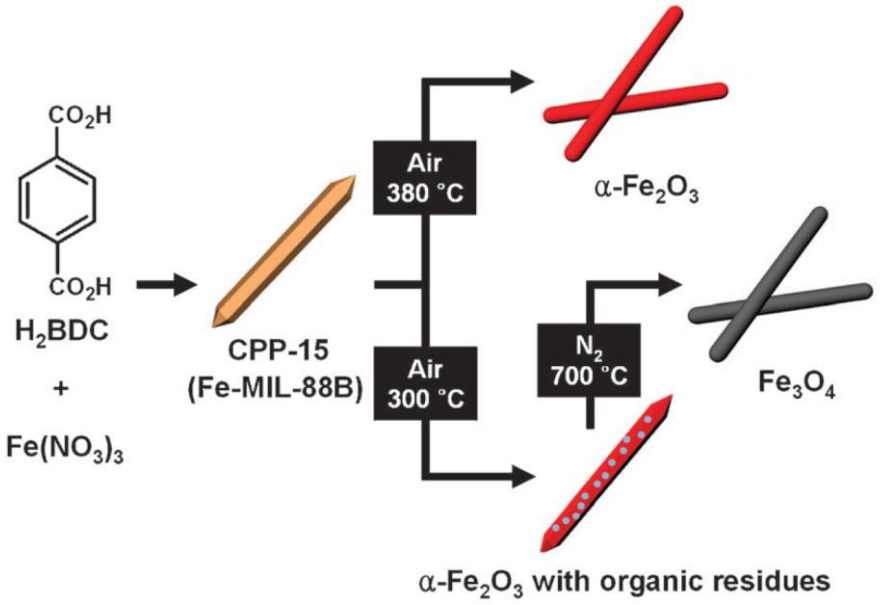

Figure 1.3 The selective preparation of hematite (α-Fe_2O_3) and magnetite (Fe_3O_4) nanorods from coordination polymer nanorods (CPP-15, Fe-MIL-88B).

In addition, spindle-like iron oxide derived from another iron-based MOF was reported by the Cho group.[31] They prepared MIL-88-Fe, which showed bipyramidal hexagonal prism with uniform size as a precursor for iron oxide. Two steps of heat treatment were utilized to synthesize mesoporous spindle-like α-Fe_2O_3 as shown in Figure 1.5. As synthesized α-Fe_2O_3 exhibited improved capability of Li storage and outstanding rate capability as an anode material.

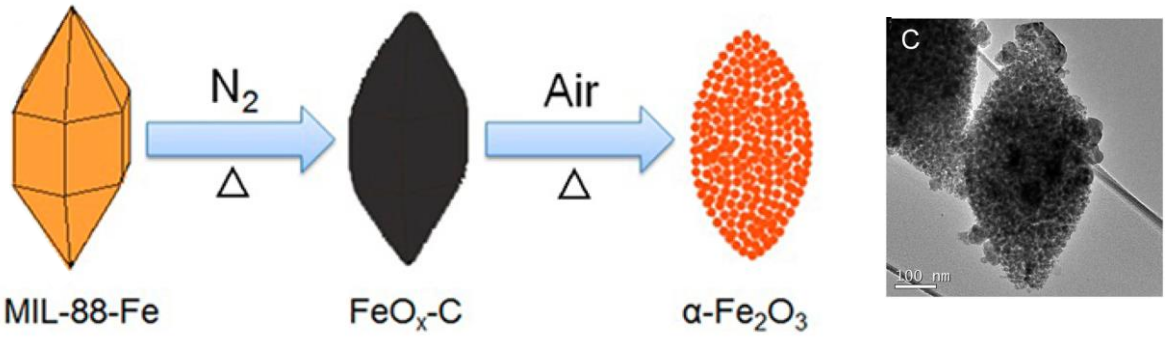

Figure 1.4 Illustration of the fabrication of spindle-like porous α-Fe_2O_3 and TEM image of the as-synthesized spindle-like α-Fe_2O_3.

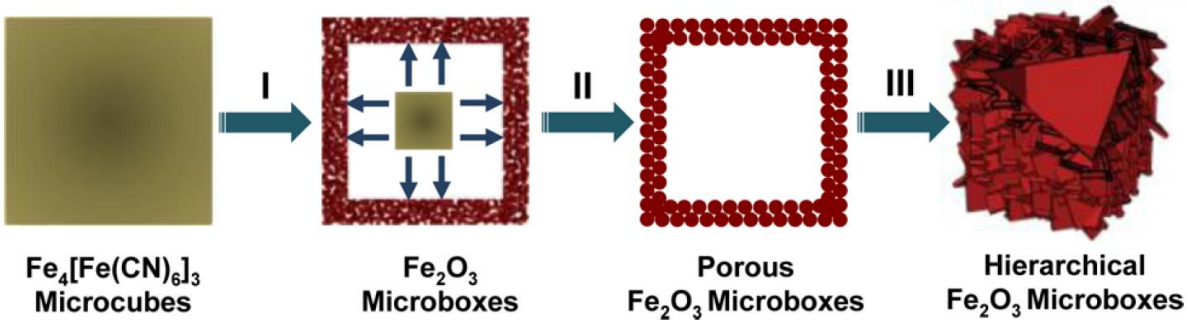

Figure 1.5 Schematic illustration of the formation of hollow Fe_2O_3 microboxes and the evolution of the shell structure with the increasing calcination temperature.

By choosing suitable MOF and modified thermal conditions, the other groups have fabricated the hollow and/or porous structures of metal oxides using MOFs as precursors. Especially, Prussian Blue (PB) and its analogue (PBA) usually transformed into hollow/porous structures of metal oxides.[32-37] The PBA of chemical formula is $M_3^{II}[M^{III}(CN)_6]_2 \cdot nH_2O$ comprised of octahedral $M^{III}(CN)_6^{3-}$ complexes. During the thermal transformation, the CO_2 and N_xO_y gases were internally generated and released, leading to hollow/porous nanostructured oxides. The Lou group synthesized the porous Fe_2O_3 microboxes by annealing the microcube-shaped iron-based PB, $Fe_4[Fe(CN)_6]_3$.[35] During the thermal decompositions, gas was generated and flowed out from interior of microcubes, resulting in the formation of microboxes of iron oxide. With the increase of annealing temperature from 350 ^oC to 550 ^oC, highly porous shells of microboxes were obtained.

Carboxylate-based metal-organic frameworks could also convert hollow and porous structured metal oxides. The Zheng and co-workers presented the Co_3O_4 hollow dodecahedrons were synthesized from transformation of a Co-based zeolitic imidazolate frameworks, ZIF-67.[38] They were used the uniform-sized ZIF-67 dodecahedrons as precursors to prepare Co_3O_4 materials. After the single-step calcination at 350 ^oC under air flow, ball-in-dodecahedron Co_3O_4 was obtained as shown in Figure 1.7. The formation mechanism of a ball-in-dodecahedron Co_3O_4 through simple calcination of ZIF-67 is similar to formation of yolk-shell microspheres derived from the solid precursor via thermal decompositions. At the initial stage of decompositions, the Co_3O_4 shells are first formed on the surface of ZIF-67 dodecahedrons. As the calcination progressed, there will be two forces with opposite directions; outward direction to formation of Co_3O_4 shells and inward direction for Co_3O_4 core, consequently forming the unique ball-in-dodecahedron structure. The effect of calcination atmosphere may strongly affect the morphology of the resultant Co_3O_4 materials. Concave-dodecahedron Co_3O_4 was prepared by

two-step of thermolysis at 500 °C under N_2 and at 350 °C in air flow. During the first pyrolysis in N_2, the surface of dodecahedrons became concave owing to shrinkage of ZIF-67 precursors. The sequent heat treatment in air led to the removal of carbogenic species and oxidizing Co or CoO_x to Co_3O_4.

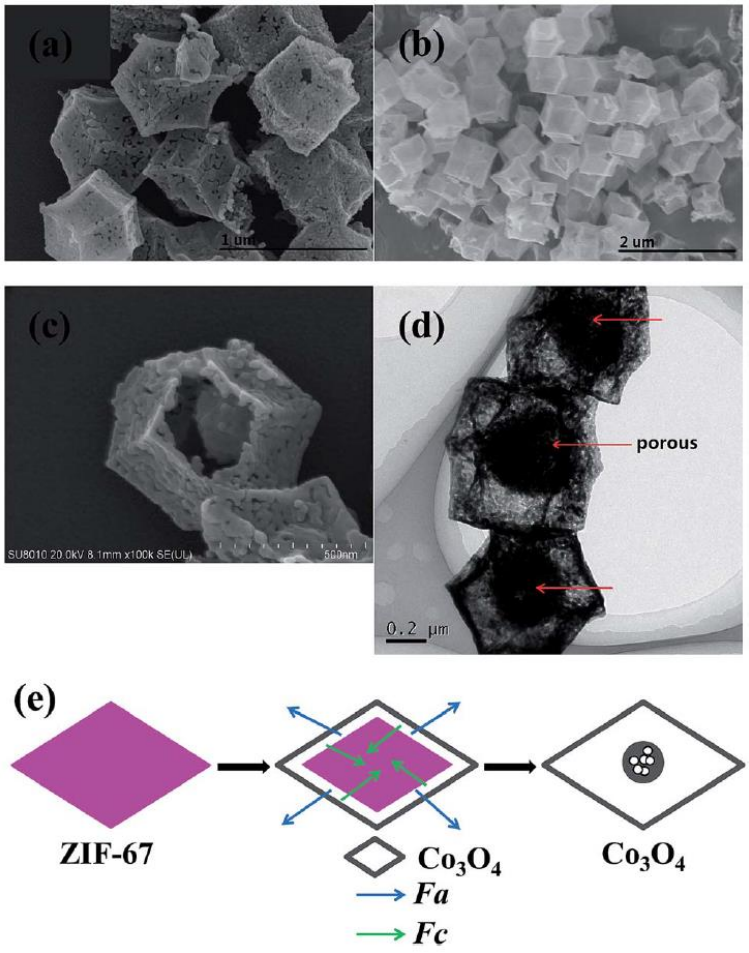

Figure 1.6 Structural investigation of Co_3O_4 obtained through the one-step calcination of ZIF-67 under air flow. (a)-(c) SEM images and (d) TEM image of as-synthesized Co_3O_4 after calcination of ZIF-67. (e) Schematic view of the formation of ball-in-dodecahedron Co_3O_4.

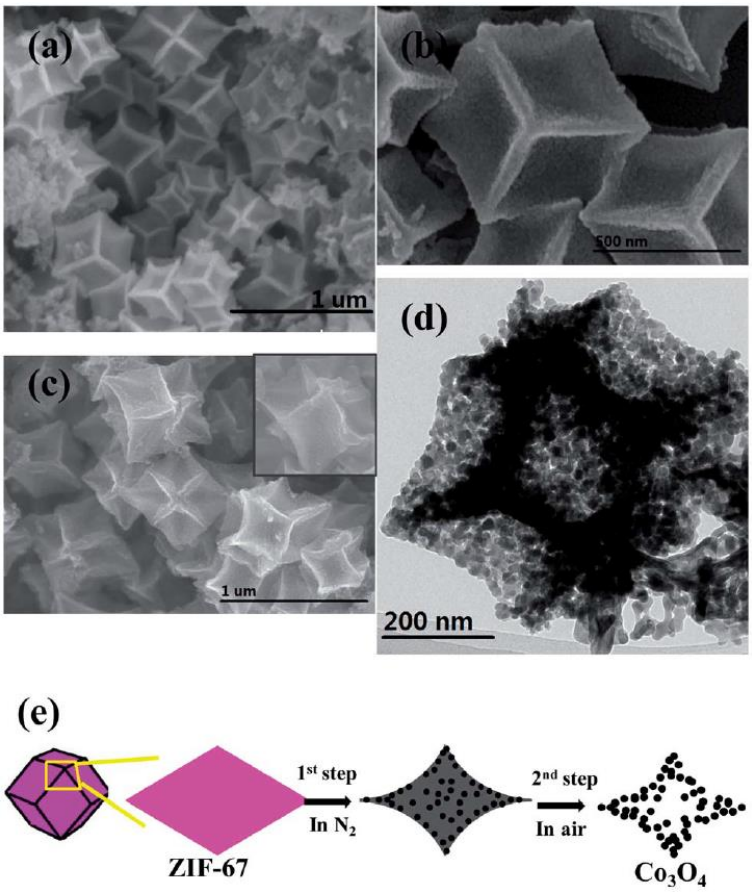

Figure 1.7 Structural investigation of Co_3O_4 obtained via two-step pyrolysis of ZIF-67. (a)-(b) SEM images of as-synthesized Co_3O_4 products after two-step thermolysis. (c) SEM image of the intermediate materials after first step under N_2. (d) TEM image of as-synthesized Co_3O_4. (e) Schematic view of the formation of Co_3O_4 dodecahedrons with concave surfaces.

1.3.2 Carbon

Nanoporous carbons with high surface area have attracted because of their numerous applications including catalysis,[39] energy storage and conversion,[40] and gas sorption.[41] Many papers have been reported for preparing porous carbon with novel structures and properties derived from metal-organic frameworks.[42,43] As mentioned earlier, MOFs are consisted of metal clusters as well as organic ligands. Thus, it is necessary to remove metal-related species in resultant materials after decomposition of MOFs in order to obtain pure carbon. Interestingly, metal-related species easily evaporated under heat treatment at high temperature under inert atmosphere in the case of thermolysis of Zn-based MOFs due to low boiling point of zinc (907 ^{o}C). Thus, Zn-MOFs have been usually used for synthesizing pure carbon via thermolysis without any need of removal of metal-related species.[44-48] In the following contents, several literatures that were demonstrated the synthesis of carbon with different dimensionality and morphology will be briefly summarized.

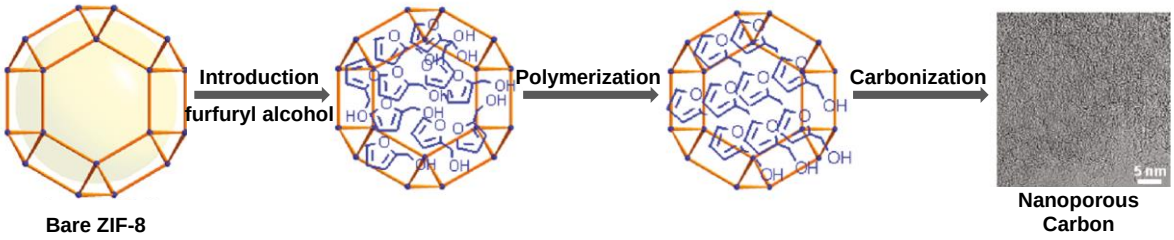

Figure 1.8 Schematic illustration of synthesis of nanoporous carbon.

In 2011, Xu and his co-workers reported the nanoporous carbon synthesized from a zeolite-type metal-organic framework as a template as well as a precursor with furfuryl alcohol as a second carbon precursor.[44] A highly porous zeolite-type MOF (ZIF-8, [Zn(2-methylimidazole)$_2$]) is suitable as a template and a precursor to produce N-doped carbon resulting from N-containing ligand, 2-methylimidazole. After introduced furfuryl alcohol into pores of ZIF-8 and polymerized furfuryl alcohol inside the MOF pores, ZIF-8 frameworks decompose upon further heating to 1000 ^{o}C under inert atmosphere. The resultant carbon material with highly surface area and porosity which was mainly comprised of micropores was successfully synthesized. Interestingly, there is no metal-related species in resultant materials after thermolysis. The authors mentioned that Zn ions transformed into zinc oxide (ZnO), and then ZnO reduced by carbon which is an active reducing agent at high temperature. Fortunately, since the thermolysis temperature was closed to the boiling point of Zn metal, pure carbon could be obtained without any acid treatment.

Interestingly, an appropriate choice of thermolysis condition leads to the formation of zero-dimensional (0D) carbon dots derived from MOFs having infinite coordination bonds between metal ions and ligands.[43] The same group demonstrated the synthesis of fluorescent carbon nanodots by using the same framework with a size of 20-100 nm. Whereas the porous carbon was carbonized at high temperature, carbon nanodots were synthesized at relatively low temperature, 500 °C. After thermolysis at 500 °C under argon flow, carbon nanodots with ZnO phase were formed and subsequent acid treatment which could remove ZnO remained pure carbon.

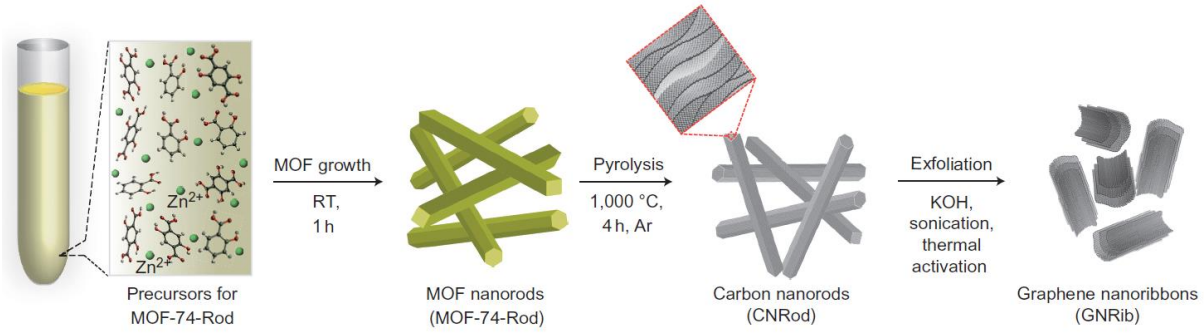

Figure 1.9 Schematic illustration of synthesis of one-dimensional carbon nanorods and two-dimensional graphene nanoribbons

Besides, one-dimensional carbon nanorods and two-dimensional graphene nanoribbons were successfully fabricated by using metal-organic frameworks.[45] The carbon nanorods was prepared by thermal treatment of a one-dimensional rod-shaped metal-organic framework. One- and two-dimensional carbon nanomaterials have attracted much attention owing to their useful properties. Several methods for preparing the carbon nanomaterials are as follows: arc discharge, laser ablation, nanocasting and chemical vapor depositions (CVD). However, these traditional methods are commonly unsuitable for large-scale synthesis and often require catalyst. MOF-derived strategy for preparing the one- and two dimensional carbon nanomaterials is catalyst-free, self-templated and facile. By the preserved-morphology during thermal transformation of rod-shaped MOF followed by unveiling with KOH-assisted sonochemical treatment, two-dimensional graphene nanoribbons with 2-6 layers thickness were synthesized. As synthesized graphene nanoribbons exhibited excellent supercapacitor performance.

Not only dimensionality, but also controlling porosity in carbon nanomaterials are important. Many researchers have reported for synthesizing nanoporous carbon derived from MOFs. There are several factors researchers suggested, which will affect to porosity of resultant carbon. The Yildirim group proposed that initial porosity of parent MOF is a critical role in developing porosity in carbon nanomaterials.[46] Kim *et al.* claimed that the surface area of resultant carbon is linearly proportional to Zn/C ratio in Zn-based MOF precursors.[47] Recently, our group presented interesting results regarding to the synthesis of nanoporous carbon derived from nonporous MOF. In the report, based on the understanding mechanism of conversion of Zn-MOF, porosity of carbon can be controlled by simple experimental factors such as target temperature and holding time.[48]

The integration of heteroatoms into carbon frameworks is also important to fabricate the defect sites and catalytically active sites and improve the performances directly. The heteroatom-containing ligands comprised of metal-organic frameworks act as carbon precursors, transforming into the heteroatom-doped carbon. The Cao group synthesized the phosphorous-nitrogen-codoped carbon materials derived from a MOF after postsynthetic modification.[49] Through the postsynthetic modification of MOFs, the P-N-rich precursors (glyphosin) were decorated with UiO-66-NH_2 MOF resulting in the P-N-codoped carbon materials. The effect of heteroatom doping on the carbon materials exhibited improved electrocatalytic performance.

1.3.3 Metal/Metal oxides decorated with carbon

MOFs, which are composed of metal clusters and organic linkers, have possessing interesting properties such as structural tunability and diverse functionality. The versatility of MOFs provides an opportunity to synthesize a wide variety of nanomaterials including metal and or metal oxides-carbon composites. The metal/metal oxide nanoparticles and carbon materials are complementary to each other and the combination of them may allow synergistic tunability and significant enhancement of the resultant material's potential functions.[50,51] There are several reports with respect to the synthesis of nanocomposites.

The Park group reported that through a single-step pyrolysis of the metal-organic framework IRMOF-1, hierarchically porous carbon-coated ZnO quantum dots (QDs) were synthesized.[52] During the thermolysis of IRMOF-1, zinc ions in MOFs were transformed into ZnO nanoparticles and the ligands were converted into organic substances which prevented aggregation of the metal oxide nanocrystals. They explained that the control over precise pyrolysis conditions of IRMOF-1 enabled us to synthesize the carbon-coated ZnO QDs without additional agglomeration. These composites exhibited outstanding performances as an anode material for lithium ion batteries, because amorphous carbon acts as a buffer against the volume expansion of ZnO during an electrochemical reaction.

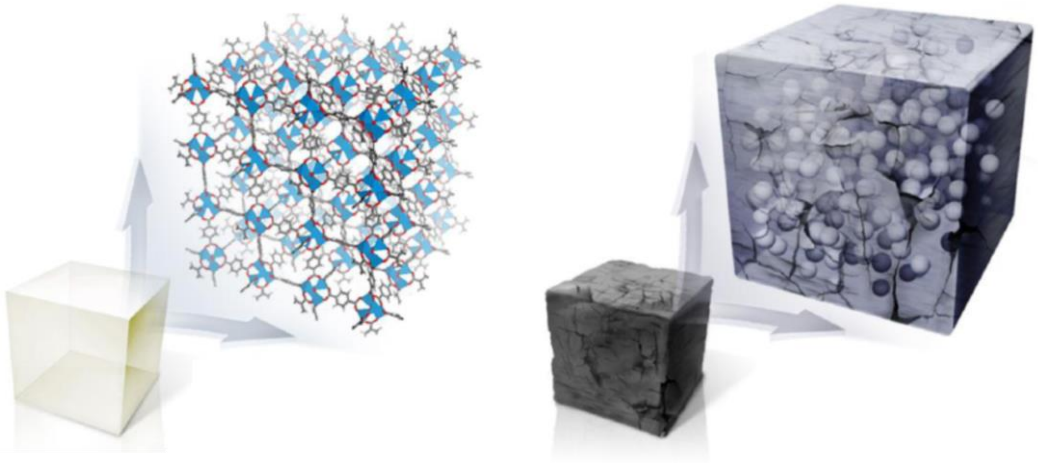

Figure 1.10 Schematic diagrams of IRMOF-1 (left) and IRMOF-1 after controlled pyrolysis to produce carbon-coated ZnO quantum dots without agglomeration (right).

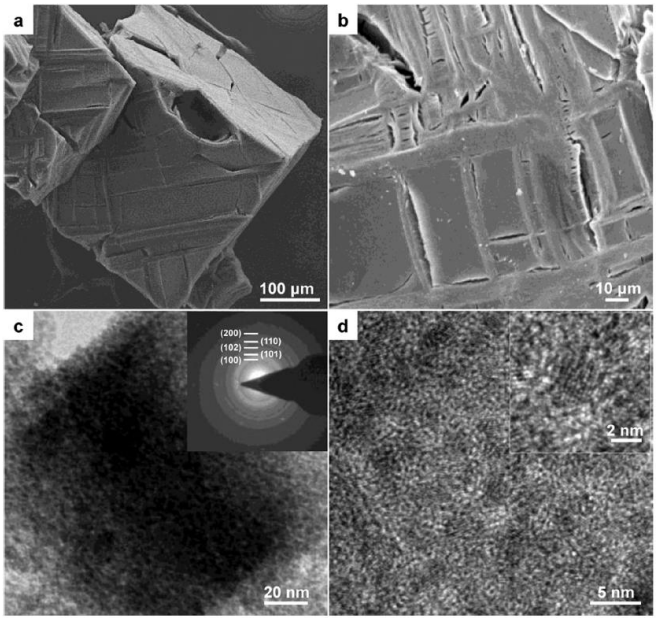

Figure 1.11 ZnO QDs@porous carbon obtained from IRMOF-1. (a)-(b) SEM images. (c) TEM image (inset: SAED pattern). (d) high-resolution TEM image.

The nanocomposites dispersed copper nanoparticles within a carbon matrix (Cu NPs@C) is synthesized via a one-pot thermolysis of HKUST-1, a Cu-based MOF precursor by Tan *et al*.[53] The confinement effect of MOF precursors enables the Cu NPs to be dispersed in porous carbon matrix. Thermolysis under inert atmospheres leads to the formation of pure Cu phase without the presence of CuO. As synthesized Cu NPs@C exhibited catalytic ability for oxidation of 3,3',5,5'-tetramethylbenzidine (TMB) by H_2O_2 with high efficiency and stability.

MOF-derived strategy can easily overcome an obstacle in different field of applications. In energy conversion and storage systems such as batteries, fuel cells, and water splitting devices, the active materials should be loaded on the substrates, requiring time-consuming fabrication procedure with the aid of polymeric binders. Additionally, the easy peeling of active materials from the electrodes leads to a decline in performances. Therefore, the direct attachment of active materials on the substrate is of great importance for enhancing the electron transport and structural stability. To realize this, researchers have utilized the conversion of MOFs directly grown on the substrate. The Qiao group reported the hybrid Co_3O_4-carbon porous nanowire prepared by carbonization of metal-organic framework directly grown on Cu foil.[54] The metal-organic frameworks is easy to grow directly on the electrode. Thus, after pyrolysis of them under inert atmosphere, the catalytically active Co_3O_4 nanoparticles were directly contacted with Cu foil as shown in Figure 1.13. This materials exhibited outstanding OER performance, which could be attributed to the porous structures of nanowires. This strategy has been combined with

the use of mixed-metal organic frameworks, and/or an additional phosphidation/selenylation process to tailor the chemical compositions and improve their performances.

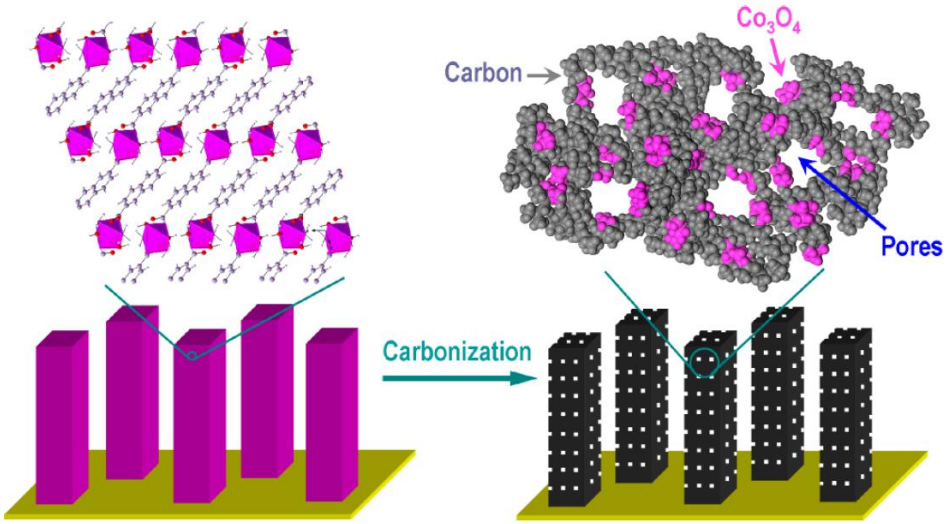

Figure 1.12 Fabrication of hybrid Co_3O_4-carbon porous nanowire arrays.

1.4 Mechanisms of conversion of metal organic frameworks

The formation of nanomaterials derived from MOFs is governed by the type of metal species and organic ligands that comprise the MOF precursors, because the metal species generated during thermal conversion strongly affect the phase of metal-related species and structures of the carbon. Thus, it is imperative to understand the transformation mechanism of the resultant materials so as to enable the preparation of well-designed nanomaterials. There are several reports with respect to conversion mechanism of MOFs.[55,56]

In 2010, Hu and co-workers reported a systematic investigation of decomposition of MOF-5, consisting of Zn-oxo clusters and coordinated terephthalate ligands.[55] During thermal decompositions of MOF-5, there were three types of bond breaking carboxylate bridges: (a) Zn-O bond breaking between Zn4O cluster and carboxylate ligand, (b) O-C bond breaking within terephthalate ligands and (c) C-C bond breaking between benzene and carboxylate group within ligands. Depending on the positions of bond breaking, different kinds of intermediates, organic substances in-situ generated during thermal decompositions and resultant materials were predicted. They proposed the mechanism based on bond breaking for the thermal decomposition of MOF-5.

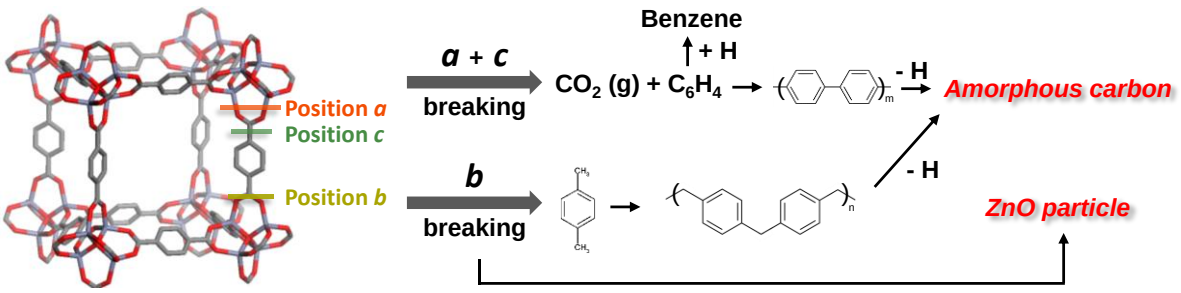

Figure 1.13 Three types of bond cleavage within MOF-5 during the thermal decompositions

Banerjee group investigated the effect of reduction potential of metal ions consisted of MOFs on the preparation of metal/metal oxide nanoparticles.[56] After the thermolysis of diverse MOFs containing Zn^{2+}, Mn^{2+}, Mg^{2+} and Cd^{2+} ions in N_2 atmosphere, the reduction potential of metal ions is a critical factor to decide the metallic phase or metal oxide. The metal ion having a reduction potential of -0.27 V or larger formed metallic nanoparticles, whereas metal ion with a reduction potential lower than -0.27 V transformed metal oxide phase after thermolysis under N_2.

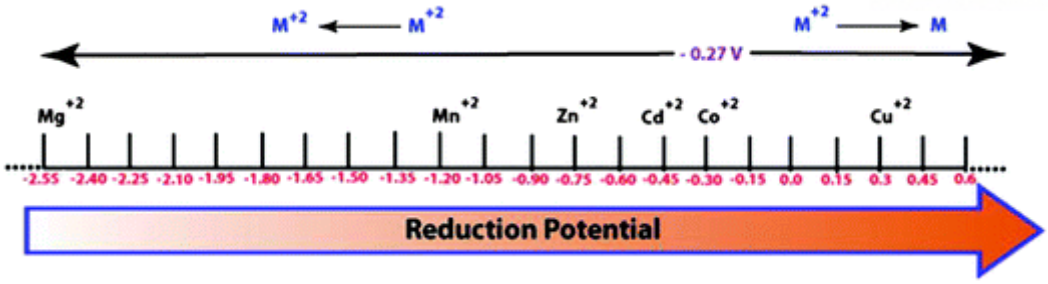

Figure 1.14 The effect of reduction potential of metal ions comprised of metal-organic frameworks on the formation of metal or metal oxide phase after thermolysis in a N_2 atmosphere.

Along with the effect of reduction potential of metal ions with MOFs, metallic phase can be obtained by reduction of carbon during thermal treatment because, carbon is an active reducing agent at high temperature. Thus, the competition of the Gibbs free energy (ΔG) of reactions between reduction of metal oxide and oxidation of carbon will be a critical factor to determine the carbothermic reduction will occur. In metallurgy, the Ellingham diagram is used to expect the equilibrium between a metal, its oxide and oxygen at certain temperature.[57] Thus, in the field of MOF conversion, the utilization of Ellingham diagram is helpful to predict whether carbothermic reduction will proceed during heat treatment. For example, zinc oxide can be reduced by carbon at high temperature (~900 ^{o}C) based on the Ellingham diagram. In the conversion of MOF, these redox reactions can be expected. During the thermal decomposition of Zn-based metal organic framework, IRMOF-1, the Park and his co-workers reported the metallic Zn species were released by the reduction of ZnO in the presence of carbogenic substances.[58] Likewise, the understanding the mechanism and reactions occurred at high temperature enables us to define the intermediate, which consequently gives the opportunity to design and tailor the nanomaterials after thermal conversion.

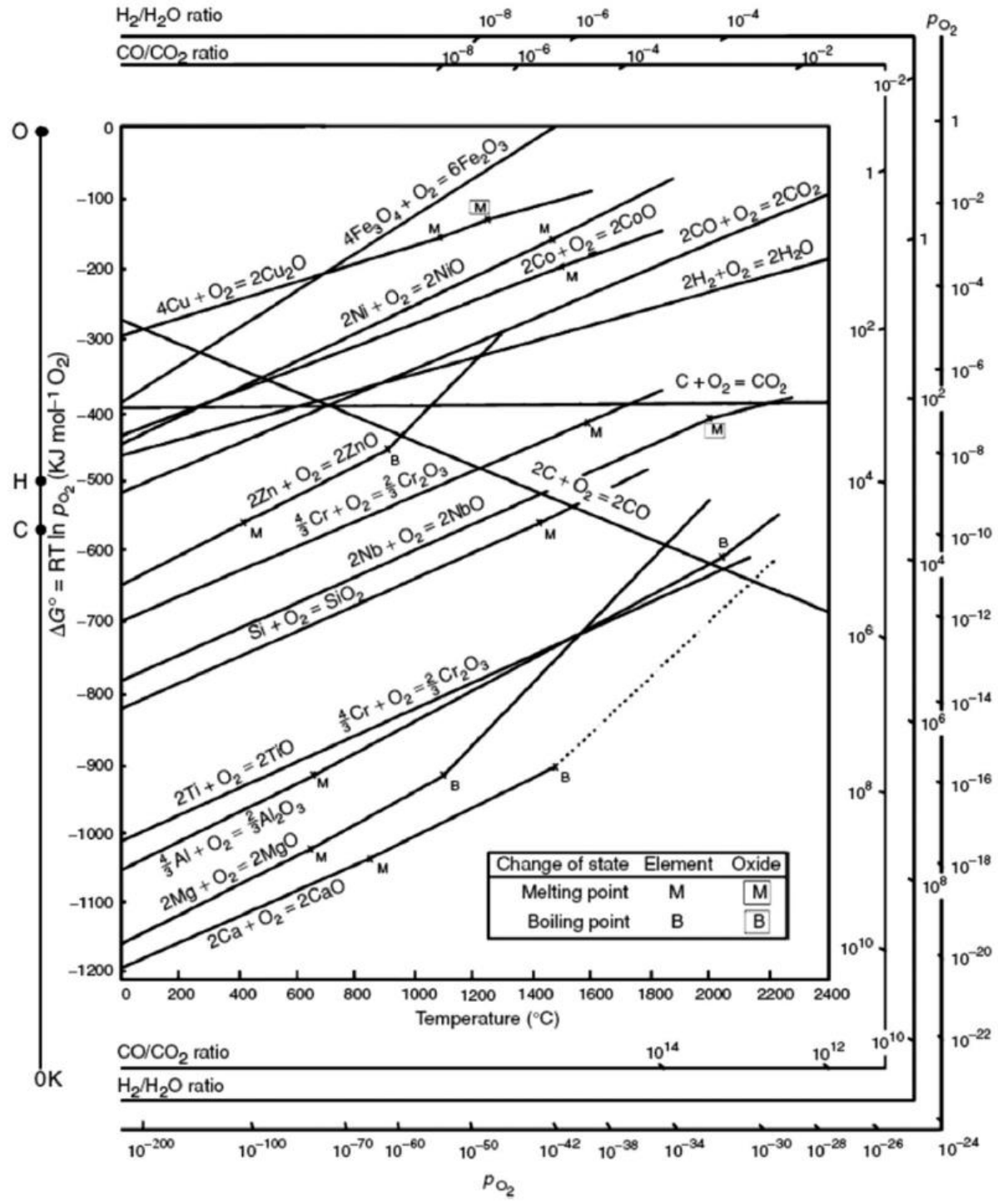

Figure 1.15 Ellingham diagram for the formation of metal or metal oxides based on their standard Gibbs free energy over temperature.[59]

The last parameter to govern the morphologies and particle sizes of metal or metal oxide nanoparticles as converted materials is the Tammann temperature of the metal species comprised of metal-organic frameworks, which is generally half the melting point of metal itself. The Tammann temperature is considered to be sufficient to make atoms of the bulk of a solid sufficiently mobile for bulk-to surface migrations, whereas the Hüttig temperature which is approximately one-third of the melting point is enough to make the species already located on the surface sufficiently mobile to undergo agglomeration or sintering.[60] In MOF conversion, the Tammann temperature of metal species is usually above the decomposition temperature of metal-organic framework precursors and important to control the nanoparticle size in resultant materials.

Table 1.1 Melting and boiling points of different metals.[61]

Metal	Melting point (°C)	Boiling point (°C)
Al	660	2519
Cr	1907	2671
Co	1495	2927
Cu	1085	2560
Fe	1538	2861
Mg	650	1090
Mn	1246	2061
Ni	1455	2913
Ru	2334	4150
Ti	1668	3287
Zn	420	907
Zr	1855	4409

1.5 Dissertation organization

There are four chapters in this thesis. Chapter I is the introduction part of metal-organic frameworks, explanation of transformation of metal-organic frameworks, and previous literatures regarding conversion of metal-organic frameworks. Chapter II deals with synthesis of nanostructured metal oxides derived from metal-organic precursors focusing on their morphologies. Chapter III focuses on the graphitization of carbon during thermal conversion. In Chapter IV, metal-carbon composites were synthesized by utilizing conversion mechanism of Zn-based MOF. Besides, the loading of nanoparticles into MOF and followed by transformation is another way to prepare the metal-carbon hybrid materials.

1.6 References

1. Cook, T. R.; Zheong, Y.-R.; Stang, P. J. Metal-Organic Frameworks and Self-Assembled Supramolecular Coordination Complexes: Comparing and Contrasting the Design, Synthesis and Functionality of Metal-Organic Materials. *Chemical Reviews* **2013**, *113*(1), 734-777.
2. Furukawa, H.; Cordova, K. E.; O'Keeffe, M.; Yaghi, O. M. The Chemistry and Applications of Metal-Organic Frameworks. *Science* **2013**, *341*, 1230444.
3. Lee, Y.-G.; Moon, H. R.; Cheon, Y. E.; Suh, M. P. H_2 Sorption Capacities of Isostructural MOFs without and with Accessible Metal Sites: $[Zn_2(ABTA)(DMF)_2]_3$ and $[Cu_2(ABTC)(DMF)_2]_3$ vs. $[Cu_2(ABTC)]_3$. *Angewandte Chemie International Edition* **2009**, *47*, 7741.
4. Henke, S.; Fischer, R. A. Gated Channels in a Honeycomb-like Zinc-Dicarboxylate-Bipyridine Framework with Flexible Alkyl Ether Side Chains. *Journal of the American Chemical Society* **2011**, *133*, 2064.
5. Lan, A. J.; Li, K. H.; We, H. H.; Olson, D. H.; Emge, T. J.; Ki, W.; Hong, M.; Li, J. A Luminescent Microporous Metal-Organic Framework for the Fast and Reversible Detection of High Explosives. *Angewandte Chemie International Edition* **2009**, *48*, 2334.
6. Corma, A.; Garcia, H.; Xamena, F. K. L. Engineering Metal-Organic Frameworks for Heterogeneous Catalysis. *Chemical Reviews* **2010**, *110*, 4606.
7. Yaghi, O. M.; O'Keeffe, M.; Ockwig, N. W.; Chan, H. K.; Eddaoudi, M.; Kim, J. Reticular Synthesis and the Design of New Materials. *Nature* **2003**, *423*, 705.
8. Tranchemontagne, D. J.; Mendoza-Cortés, J. L.; O'Keeffe, M.; Yaghi, O. M. Secondary Building Units, Nets and Bonding in the Chemistry of Metal-Organic Frameworks. *Chemical Society Reviews* **2009**, *38*, 1257-1283.
9. Sumida, K.; Arnold, J. Preparation, Characterization, and Postsynthetic Modification of Metal-Organic Frameworks: Synthetic Experiments for an Undergraduate Laboratory Course in Inorganic Chemistry. *Journal of Chemical Education* **2011**, *88*, 92-94.
10. Guo, P.; Dutta, D.; Wong-Foy, A. G.; Gidley, D. W.; Matzger, A. J. Water Sensitivity in Zn_4O-Based MOFs is Structure and History Dependent. *Journal of the American Chemical Society* **2015**, *137*, 2651-2657.
11. Greathouse, J. A.; Allendorf, M. D. The Interaction of Water with MOF-5 Simulated by Molecular Dynamics. *Journal of the American Chemical Society* **2016**, *128*, 10678-10679.
12. Nguyen, J. G.; Cohen, S. M. Moisture-Resistant and Superhydrophobic Metal−Organic Frameworks Obtained via Postsynthetic Modification. *Journal of the American Chemical Society* **2010**, *132*, 4560-4561.
13. Feng, D.; Gu, Z.-Y.; Chen, Y.-P.; Park, J.; Wei, Z.; Sun, Y.; Bosch, M.; Yuan, S.; Zhou, H.-C. A Highly Stable Porphyrinic Zirconium Metal–Organic Framework with shp-a Topology. *Journal of*

the American Chemical Society **2014**, *136*, 17714-17717.

14. Campbell, J.; Davies, R. P.; Braddock, D. C.; Livingston, A. G. Improving the Permeance of Hybrid Polymer/Metal-Organic Framework (MOF) Membranes for Organic Solvent Nanofiltration (OSN) – Development of MOF Thin Films via Interfacial Synthesis. *Journal of Materials Chemistry A* **2015**, *3*, 9668-9674.
15. Masoomi, M. Y. Morsali, A. Applications of Metal-Organic Coordination Polymers as Precursors for Preparation of Nano-materials. *Coordination Chemistry Reviews* **2012**, *256*, 2921-2943.
16. Sun, J.-K.; Xu, Q. Functional Materials Derived from Open Framework Templates/Precursors: Synthesis and Applications. *Energy and Environmental Science* **2014**, *7*, 2071-2100.
17. Lux, L.; Williams, K.; Ma, S. Heat-treatment of Metal-Organic Frameworks for Green Energy Applications. *CrystEngComm* **2015**, *17*, 10-22.
18. Mai, H. D.; Rafiq, K.; Yoo, H. Nano Metal-Organic Framework-Derived Inorganic Hybrid Nanomaterials: Synthetic Strategies and Applications. *Chemistry - A European Journal* **2017**, *23*, DOI: 10.1002/chem.201604703.
19. Xia, W.; Mahmood, A.; Zou, R.; Xu, Q. Metal-Organic Frameworks and Their Derived Nanostructures for Electrochemical Energy Storage and Conversion. *Energy and Environmental Science* **2015**, *8*, 1837-1866.
20. Mahmood, A.; Guo, W.; Tabassum, H.; Zou, R. Metal-Organic Framework-Based Nanomaterials for Electrocatalysis. *Advanced Energy Materials* **2016**, *6*, 1600423.
21. Kreno, L.E.; Leong, K.; Farha, O.K.; Allendorf, M.; Van Duyne, R.P.; Hupp, J. T. Metal organic framework materials as chemical sensors. *Chemical Review* **2011**, *112*, 1105–1125.
22. Srinivas, G.; Krungleviciute, V.; Guo, Z.-X.; Yildirim, T. Exceptional CO_2 Capture in a Hierarchically Porous Carbon with Simultaneous High Surface Area and Pore Volume. *Energy and Environmental Science* **2014**, *7*, 335-342.
23. Su, C.-Y.; Goforth, A. M.; Smith, M. D.; Pellechia, P. J.; Loye, H.-C. Exceptionally Stable, Hollow Tubular Metal−Organic Architectures: Synthesis, Characterization, and Solid-State Transformation Study. *Journal of the American Chemical Society* **2004**, *126*(11), 3576-3586.
24. Thakuria, H.; Das, G. CuO Micro Plates from a 3D Metallo-Organic Framework (MOF) of a Binary Copper(II) Complex of *N*,*N*-Bis(2-hydroxyethyl)glycine. *Polyhedron* **2007**, *26*(1), 149-153.
25. Shen, Z.; Zhang, G.; Zhou, H.; Sun, P.; Li, B.; Ding, D.; Chen, T. Macroporous Lanthanide-Organic Coordination Polymer Foams and Their Corresponding Lanthanide Oxides. *Advanced Materials* **2008**, *20*(5), 984-988.
26. Liu, B.; Shioyama, H.; Akita, T.; Xu, Q. Metal-Organic Framework as a Template for Porous Carbon Synthesis. *Journal of the America Chemical Society* **2008**, *130*(16), 5390-5391.
27. Palaniselvam, T.; Biswal, B. P.; Banerjee, R.; Kurungot, S. Zeolitic Imidazolate Framework (ZIF)-Derived, Hollow-Core, Nitrogen-Doped Carbon Nanostructures for Oxygen-Reduction Reactions

in PEFCs. *Chemistry - A European Journal* **2013**, *19*(28), 9335-9342.

28. Yang, J.; Zhang, F.; Wang, X.; He, D.; Wu, G.; Yang, Q.; Hong, X.; Wu, Y.; Li, Y. Porous Molybdenum Phosphide Nano-Octahedrons Derived From Confined Phosphorization in UIO-66 for Efficient Hydrogen Evolution. *Angewandte Chemie International Edition* **2016**, *55*(41), 12854-12858.
29. Lan, Q.; Zhang, Z.-M.; Qin, C.; Wang X.-L.; Li, Y.-G.; Tan, H.-Q.; Wang, E.-B. Highly Dispersed Polyoxometalate-Doped Porous Co_3O_4 Water Oxidation Photocatalysts Derived from POM@MOF Crystalline Materials. *Chemistry - A European Journal* **2016**, *22*(43), 15513-15520.
30. Cho, W.; Park, S.; Oh, M. Coordination Polymer Nanorods of Fe-MIL-88B and Their Utilization for Selective Preparation of Hematite and Magnetite Nanorods. *Chemical Communications* **2011**, *47*(14), 4138-4140.
31. Xu, X.; Cao, R.; Jeong, S.; Cho, J. Spindle-like Mesoporous α-Fe_2O_3 Anode Material Prepared from MOF Template for High-Rate Lithium Batteries. *Nano Letters* **2012**, *12*(9), 4988-4991.
32. Hu, L.; Yan, N.; Chen, Q.; Zhang, P.; Zhong, H.; Zheng, X.; Li, Y.; Hu, X. Fabrication Based on the Kirkendall Effect of Co_3O_4 Porous Nanocages with Extraordinarily High Capacity for Lithium Storage. *Chemistry - A European Journal* **2012**, *18*(29), 8971-8977.
33. Hu, L.; Zhang, P.; Zhong, H.; Zheng, X.; Yan, N.; Chen, Q. Foamlike Porous Spinel $Mn_xCo_{3-x}O_4$ Material Derived from $Mn_3[Co(CN)_6]_2{\cdot}nH_2O$ Nanocubes: A Highly Efficient Anode Material for Lithium Batteries. *Chemistry - A European Journal* **2012**, *18*(29), 15049-15056.
34. Hu, L.; Huang, Y.; Chen, Q. $Fe_xCo_{3-x}O_4$ Nanoporous Particles Stemmed from Metal–Organic Frameworks $Fe_3[Co(CN)_6]_2$: A Highly Efficient Material for Removal of Organic Dyes from Water. *Journal of Alloys and Compounds* **2013**, *559*, 57-63.
35. Zhang, L.; Wu, H. B.; Madhavi, S.; Hng, H. H.; Lou, X. W. Formation of Fe_2O_3 Microboxes with Hierarchical Shell Structures from Metal–Organic Frameworks and Their Lithium Storage Properties. *Journal of the America Chemical Society* **2012**, *134*(42), 17388-17391.
36. Zhang, L.; Wu, H. B.; Xu, R.; Lou, X. W. Porous Fe_2O_3 Nanocubes Derived from MOFs for Highly Reversible Lithium Storage. *CrystEngComm* **2013**, *15*(45), 9332-9335.
37. Xu, M.; Belik, A. A.; Imura, M.; Mibu, K.; Tsujimoto, Y.; Yamauchi, Y. Synthesis of Superparamagnetic Nanoporous Iron Oxide Particles with Hollow Interiors by Using Prussian Blue Coordination Polymers. *Chemistry of Materials* **2012**, *24*(14), 2698-2707.
38. Shao, J.; Wan, Z.; Liu, H.; Zheng, H.; Gao, T.; Shen, M.; Qu, Q.; Zheng, H. Metal Organic Frameworks-Derived Co_3O_4 Hollow Dodecahedrons with Controllable Interiors as Outstanding Anodes for Li Storage. *Journal of Materials Chemistry A* **2014**, *2*(31), 1219-12200.
39. Yang, H. Y.; Han, Z. J.; Yu, S. F.; Pey, K. L.; Ostrikov, K.; Karnik, R. Carbon Nanotube Membranes with Ultrahigh Specific Adsorption Capacity for Water Desalination and Purification. *Nature Communications* **2013**, *4*, 2220.

40. Merlet, C.; Rotenberg, B.; Madden, P. A.; Taberna, P.-L.; Simon, P.; Gogotsi Y.; Salanner, M. On the Molecular Origin of Supercapacitance in Nanoporous Carbon Electrodes. *Nature Materials* **2012**, *11*, 306-310.
41. Su, D. S.; Perathoner, S.; Centi, G. Nanocarbons for the Development of Advanced Catalysts. *Chemical Reviews* **2013**, *113*(8), 5782-5816.
42. Zhang, W.; Xu, Z.-Y.; Jiang, H.-L.; Yu, S.-H. Nanowire-Directed Templating Synthesis of Metal-Organic Framework Nanofibers and Their Derived Porous Doped Carbon Nanofibers for Enhanced Electrocatalysis. *Journal of the American Chemical Society* **2014**, *136*, 14395-14388.
43. Amali, A. J.; Hoshino, H.; Wu, C.; Ando, M.; Xu, Q. From Metal–Organic Framework to Intrinsically Fluorescent Carbon Nanodots. *Chemistry - A European Journal* **2014**, *20*(27), 8279-8282.
44. Jiang, H.-L.; Liu, B.; Lan, Y.-Q.; Kuratani, K.; Akita, Y.; Shioyama, H.; Zong, F.; Xu, Q. From Metal–Organic Framework to Nanoporous Carbon: Toward a Very High Surface Area and Hydrogen Uptake. *Journal of the American Chemical Society* **2011**, *133*(31), 11854-11857.
45. Pachfule, P.; Shinde, D.; Majumder, M.; Xu, Q. Fabrication of Carbon Nanorods and Graphene Nanoribbons from a Metal–Organic Framework. *Nature Chemistry* **2016**, *8*, 718-724.
46. Srinivas, G.; Krungleviciute, V.; Guo, Z.-X.; Yildirim, T. Exceptional CO_2 Capture in a Hierarchically Porous Carbon with Simultaneous High Surface Area and Pore Volume. *Energy and Environmental Science* **2014**, *7*(1), 335-342.
47. Lim, S.; Suh, K.; Kim, Y.; Yoon, M.; Park, H.; Dybtsev, D. N.; Kim, K. Porous Carbon Materials with a Controllable Surface Area Synthesized from Metal–Organic Frameworks. *Chemical Communications* **2012**, *48*(60), 7447-7449.
48. Jeoung, S.; Sahgong, S. H.; Kim, J. H.; Hwang, S. M.; Kim, Y.; Moon, H. R. Upcycling of Nonporous Coordination Polymers: Controllable-Conversion Toward Porosity-Tuned N-Doped Carbons and Their Electrocatalytic Activity in Seawater Batteries. *Journal of Materials Chemistry A* **2016**, *4*(35), 13468-13475.
49. Fu, Y.; Huang, Y.; Xiang, Z.; Liu, G.; Cao, D. Phosphorous–Nitrogen-Codoped Carbon Materials Derived from Metal–Organic Frameworks as Efficient Electrocatalysts for Oxygen Reduction Reactions. *European Journal of Inorganic Chemistry* **2016**, (13-14), 2100-2105.
50. Wu, Z.-S.; Zhou, G.; Yin, L.-C.; Ren, W.; Li, F.; Cheng, H.-M. Graphene/Metal Oxide Composite Electrode Materials for Energy Storage. *Nano Energy* **2012**, *1*, 107-131.
51. Liu, Y.; Wang, R.; Yan, X. Synergistic Effect between Ultra-Small Nickel Hydroxide Nanoparticles and Reduced Graphene Oxide sheets for the Application in High-Performance Asymmetric Supercapacitor. *Scientific Reports* **2015**, *5*, 11095.
52. Yang, S. J.; Nam, S.; Kim, T.; Im, J. H.; Jung, H.; Kang, J. H.; Wi, S.; Park, B.; Park, C. R. Preparation and Exceptional Lithium Anodic Performance of Porous Carbon-Coated ZnO

Quantum Dots Derived from a Metal–Organic Framework. *Journal of the American Chemical Society* **2013**, *135*, 7394-7397.

53. Tan, H.; Ma, C.; Gao, L.; Li, Q.; Song, Y.; Xu, F.; Wang, T.; Wang, L. Metal–Organic Framework-Derived Copper Nanoparticle@Carbon Nanocomposites as Peroxidase Mimics for Colorimetric Sensing of Ascorbic Acid. *Chemistry A European Journal* **2014**, *20*, 16377-16383.
54. Ma, T. Y.; Dai, S.; Jaroniec, M.; Qiao, S. Z. Metal–Organic Framework Derived Hybrid Co_3O_4-Carbon Porous Nanowire Arrays as Reversible Oxygen Evolution Electrodes. *Journal of the American Chemical Society* **2014**, *136*, 13925-13931.
55. Zhang, L.; Hu, Y. H. A Systematic Investigation of Decomposition of Nano $Zn_4O(C_8H_4O_4)_3$ Metal−Organic Framework. *The Journal of Physical Chemistry C* **2010**, *114*, 2566-2572.
56. Das, R.; Pachfule, P.; Banerjee, R.; Poddar, P. Metal and metal oxide nanoparticle synthesis from metal organic frameworks (MOFs): finding the border of metal and metal oxides. *Nanoscale* **2012**, *4*, 591-599.
57. Acton, C. R. *Processing of Metal and Oxygen From Lunar Deposits.*
58. Yang, S. J.; Kim, T.; Im, J. H.; Kim, T. S.; Lee, K.; Jung, H.; Park, C. R. MOF-Derived Hierarchically Porous Carbon with Exceptional Porosity and Hydrogen Storage Capacity. *Chemistry of Materials* **2012**, *24* (3), 464-470.
59. Birks, N.; Meier, G. H.; Pettit F. S. *Introduction to the High Temperature Oxidation of Metals,* Cambridge University, Press, Cambridge, 2nd ed, 2006.
60. Etrl, G.; Weitkamp, J.; Knözinger, H. *Preparation of solid catalysts* John Wiley & Sons, 1999. 11. 12, 4.8 Spreading and Wetting (page 507)
61. Elements MaBPoC.http://www.chemistry.patent-invent.com/chemistry/melting_boiling_point.html, updated April 2011.

Chapter II. Nanostructured metal oxides

2.1 Introduction

MOF-derived metal oxide nanomaterials have attracted tremendous interest, caused by their numerous potential applications in energy storage and conversion,[1] catalysis[2] and gas sorption.[3] As mentioned in Chapter I, nanostructured metal oxides whose morphologies of parent MOFs are well-maintained are synthesized by controlling over the thermal conditions; this transformation is known as a pseudomorphic conversion. Through pseudomorphic conversion of metal-organic frameworks, the macroscopic morphologies with higher level of architectures can be controlled, which can hardly be achieved by the bottom-up approaches. MOFs with different microstructures and morphologies even composed of the same building blocks can be synthesized by tuning the synthetic conditions such as solvent system, temperature, and the use of structure-directing agents. Because of their versatility in structures and pseudomorphic conversion, we can suggest the synthetic strategy for controlled macroscopic structures composed of metal oxide nanoparticles. Furthermore, this strategy gave us the opportunity to understand the effect of microstructures with higher level of architecture on the electrochemical performance as anodes in lithium ion battery, which is a representative of practical applications.[35]

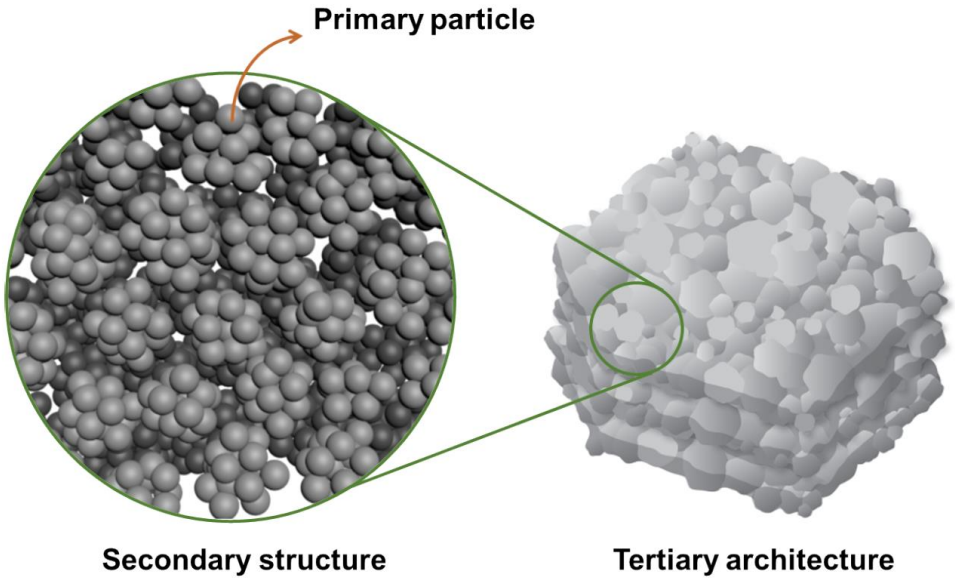

Figure 2.1 Illustration of a hierarchical structure in nanostructured metal oxides.

Well-designed structures of metal-organic frameworks as precursors broaden the scope of nanostructures of resultant materials beyond the pseudomorphic conversion. Nanoporous metal oxide materials have been demonstrated in various applications. There are several synthetic strategies for the preparation of nanoporous metal oxides such as surfactant-assisted methods,[4] hard/soft templating routes,[5] and self-assembly of nanoparticles.[6] The conversion reactions of metal-organic frameworks also provide the nanoporous metal oxides. The key to synthetic approach toward nanoporous metal oxides lies in the use of a MOF comprised of aliphatic carboxylate ligands, which are thermally less stable and more labile, even under inert atmosphere, than aromatic ligands. During the thermolysis of aliphatic ligand-based MOF, aliphatic ligands act as the self-generated porogen in the solids, leading to the nanoporous metal oxide. They also prevent the aggregation of metal oxide nanocrystals. Based on the understanding the formation mechanism, the pore size of resultant materials could be easily tuned by controlling the simple experimental factors.[36]

Furthermore, as-synthesized nanoporous metal oxides can be exploited as metal precursors for synthesis of MOFs. MOFs are also extensively studied for various applications per se as mentioned earlier.[7] Most of pores of MOFs belong to the micropores (less than 2 nm) which restrict the diffusion of large molecules from the MOF channels. The small pore size in microporous MOFs results in the limitations their applications in bulky molecules transportation.[8] Recently, considerable efforts have been devoted to the creation of mesoporous MOFs. In this study, we synthesized a hierarchically nanoporous MOF via replication of nanoporous MgO which acts as a metal precursor as well as architecture-directing agents. By adopting nanoporous MgO prepared from aliphatic-based Mg-MOF, we could obtain the hierarchically nanoporous Mg-based MOF with replicated structure. Eventually, the replicated Mg-MOF will have inherited porosity and morphology from its parent nanoporous MgO.

2.2 Experimental section

Materials and characterizations. All chemicals and solvents were of reagent grade and used without further purification. Infrared spectra were recorded with a ThermoFisher Scientific iS10 FT-IR spectrometer. Elemental analyses (for C, H, N, S, and O) were performed using a Thermo Scientific Flash 2000 series CHNS/O analyzer. Thermogravimetric analysis (TGA) was performed under N_2 (g) at a scan rate of 5 $^oC\ min^{-1}$, using a TGA Q50 from TA Instruments. Transmission electron microscope (TEM) images were obtained with a JEOL JEM-2100F microscope. X-ray powder diffraction (XRPD) data of as-synthesized cobalt-based MOFs were recorded at the Pohang Accelerator Laboratory, Korea. To obtain the XRPD patterns, the well-ground powders of as-synthesized cobalt-based MOFs were loaded into the capillaries, respectively (diameter, 0.3 mm; wall thickness, 0.01 mm). Diffraction data were collected at room temperature with detector distance of 180 mm and 60 s exposures using synchrotron radiation (λ = 1.20024 Å) on an ADSC Quantum-210 detector at 2D SMC with a silicon (111) double-crystal monochromator (DCM). The *ADS* program[9] was used for data collection, and the *Fit2D*[10] program was used to convert a two-dimensional diffraction image to a one-dimensional diffraction pattern. X-ray powder diffraction (XRPD) data of other materials including Mg-*aph*-MOF and converted materials were recorded on a Bruker D8 advance diffractometer at 40 kV and 40 mA for Cu Kα (λ = 1.541 Å), with a step size of 0.02° in 2θ.

Gas sorption study. N_2 sorption isotherms of converted materials including *p*-Co_3O_4, *r*-Co_3O_4, and *np*-MgO-500 were obtained by BELSORP-max at 77 K. Prior to the adsorption measurements, *p*-Co_3O_4 and *r*-Co_3O_4 were evacuated ($p < 10^{-5}$ mbar) at 200 ^{o}C for 6 h and *np*-MgO-500 sample was evacuated ($p < 10^{-5}$ mbar) at 200 ^{o}C for 12 h. The specific surface area was determined in the relative pressure range from 0.05 to 0.3 of the Brunauer-Emmett-Teller (BET) plot, and the total pore volume was calculated from the amount adsorbed at a relative pressure of about 0.98-0.99.

Single-crystal X-ray crystallography. Single crystals of *p*-MOF, *r*-MOF and Mg-*aph*-MOF coated with paratone-*N* oil were mounted on a loop. Diffraction data of *p*-MOF were collected at 100 K with synchrotron radiation (λ = 0.70002 Å) on an ADSC Quantum-210 detector at 2D SMC with a silicon(111) DCM at the Pohang Accelerator Laboratory, Korea. The ADSC Q210 *ADX* program[9] was used for data collection, and HKL3000sm (Ver. 703r)[11] was used for cell refinement, reduction, and absorption correction. Diffraction data of *r*-MOF and Mg-*aph*-MOF were collected at 173 K using a Rigaku R-aix Rapid II diffractometer (Mo Kα λ= 0.71073 Å), equipped with a diffraction camera system and an imaging plate. Full sphere data were collected for all crystals, and the raw data were processed and scaled using the RapidAuto software suite.[12] The crystal structures of *p*-MOF, *r*-MOF and Mg-*aph*-MOF were solved by direct methods[13] and refined by full-matrix least-squares refinement using the SHELXL-97 computer program[14] for *p*-MOF and Mg-*aph*-MOF and SHELX-TL (Ver. 2008) program

package[15] for *r*-MOF. The positions of all non−hydrogen atoms were refined with anisotropic displacement factors. The hydrogen atoms were positioned geometrically using a riding model. For Mg-*aph*-MOF, the electron density of the disordered guest molecules was flattened using the 'SQUEEZE' option of the program PLATON.[16] Relevant crystallographic data and bond lengths (Å) and angles (°) for *p*-MOF, *r*-MOF and Mg-*aph*-MOF are summarized in Supporting Information in Table S1-S6.

Synthesis of plate-shaped Co-MOF ($[Co_3(BDC)_3(DMF)_4]_n$, *p*-MOF). H_2BDC (29 mg, 0.17 mmol) and adipic acid (37 mg, 0.25 mmol) were dissolved in DMF (3 mL), and mixed with a DMF solution (2 mL) of $Co(NO_3)_2 \cdot 6H_2O$ (99 mg, 0.34 mmol). The solution was sealed in a glass jar, heated to 100 °C for 24 h, and then cooled to room temperature. Purple plate-shaped crystals formed, which were filtered and washed briefly with fresh DMF. Yield: 51 mg (94% based on H_2BDC). Anal. Calcd for $Co_3C_{36}H_{40}N_4O_{16}$: C, 44.97; H, 4.19; N, 5.83. Found: C, 44.51; H, 4.55; N, 6.44. FT-IR (KBr, cm^{-1}): ν_{O-H}, 3417(br); $\nu_{C-H(aromatic)}$, 3072(w); $\nu_{C=O(DMF)}$, 1650(s); $\nu_{O-C=O(carboxylate)}$, 1609, 1385(s); $\nu_{C=C(aromatic\ ring)}$, 1502(w).

Synthesis of rod-shaped Co-MOF ($[Co(BDC)(DMSO)]_n$, *r*-MOF). $Co(NO_3)_2 \cdot 6H_2O$ (99 mg, 0.34 mmol) was dissolved in DMF (2 mL), and mixed with a DMSO (3 mL) solution of H_2BDC (40 mg, 0.24 mmol). The solution was kept in a glass-jar at 120 °C for 24 h, and then cooled to room temperature. Pink rod-shaped crystals formed, which were filtered, and washed briefly with fresh DMSO. Yield: 44 mg (60% based on H_2BDC). Anal. Calcd for $Co_1C_{10}H_{10}S_1O_5$: C, 39.88; H, 3.35; N, 0.00; S, 10.65. Found: C, 39.88; H, 3.33; N, 0.06; S, 11.84. FT-IR (KBr, cm^{-1}): ν_{O-H}, 3431(br); $\nu_{C-H(aromatic)}$, 3073, 3016(w); $\nu_{O-C=O(carboxylate)}$, 1579, 1392(s); $\nu_{C=C(aromatic\ ring)}$, 1498(w); $\nu_{S=O(coordinating\ DMSO)}$, 943(s).

Synthesis of plate-shaped Co_3O_4 (*p*-Co_3O_4). As-synthesized *p*-MOF (1.02 g) was heated at a rate of 5 °C min^{-1} under N_2 (g) flow of 50 mL min^{-1}. The material was maintained at the target temperature of 440 °C for 12 h. After cooling to room temperature, the second heat treatment to completely transform into Co_3O_4 was performed under O_2 (g) flow of 0.1 L min^{-1} and heated at a rate of 5 °C min^{-1}. The material was maintained at the target temperature of 350 °C for 1 h. After cooling to room temperature, black solid (0.245 g) was obtained.

Synthesis of rod-shaped Co_3O_4 (*r*-Co_3O_4). As-synthesized *r*-MOF (0.83 g) was heated at a rate of 5 °C min^{-1} under N_2 (g) flow of 50 mL min^{-1}. The material was maintained at the target temperature of 500 °C of 1 h. After cooling to room temperature, the second heat treatment completely transform into Co_3O_4 was performed under O_2 (g) flow of 0.1 L min^{-1} and heated at a rate of 5 °C min^{-1}. After reaching the target temperature of 500 °C, the material was maintained at that temperature for 1 h. After cooling to room temperature, black solid (0.20 g) was obtained.

Preparation of Mg-*aph*-MOF ({[Mg_4(adipate)$_4$(DMA)(H_2O)]·5DMA·2MeOH·4H_2O}). Adipic acid (0.053 g, 0.36 mmol) was dissolved in DMA (4 mL), and mixed with an MeOH (2 mL) solution of $Mg(NO_3)_2 \cdot 6H_2O$ (0.084 g, 0.33 mmol). The solution was heated in a Teflon vessel in an autoclave at 120 ℃ for 24 h, and then cooled to room temperature. Colorless rod-shaped crystals formed, which were filtered, and washed briefly with the mother liquor. Yield: 44 mg (38%). Anal. Calcd. for $Mg_4C_{50}H_{104}N_6O_{29}$: C, 44.46; H, 7.76; N, 6.22. Found: C, 44.45; H, 7.03; N, 6.17. FT-IR (Nujol mull, cm^{-1}): ν_{O-H}, 3374(m, br); $\nu_{C=O(DMF)}$, 1651(br); $\nu_{O-C=O(carboxylate)}$, 1605, 1560(s).

Preparation of *np*-MgO-500. Solid Mg-*aph*-MOF was ground into a powder and then heated at 5 ^oC min^{-1} under a nitrogen flow of 60 mL min^{-1}. After reaching the target temperature at 500 ^oC, the material was maintained at the temperature for 12 h and then cooled to room temperature. The resultant solid *np*-MgO-500 was obtained as a white powder.

Electrochemical measurements. The electrochemical properties of *p*-Co_3O_4 and *r*-Co_3O_4 were characterized using coin-type cells (CR2032) assembled in an Ar-filled glove box. The electrodes were fabricated by mixing the cobalt oxide powders (*p*-Co_3O_4 or *r*-Co_3O_4) with polyvinylidene fluoride (PVDF) as a binder and with Super P as a conducting agent at a weight ratio of 8:1:1 in *N*-methyl-2-pyrrolidinone solvent. The slurry was cast onto Cu foil and then dried in a vacuum oven at 120 ^oC for 2 h. A piece of polyolefin membrane, used as a separator was placed between a piece of electrode and Li metal, used as a counter electrode. A 1 M solution of $LiPF_6$ in a mixture of ethylene carbonate (EC) and diethyl carbonate (DEC) at 1:1 v/v was used as an electrolyte. All of the assembled coin cells were initially lithiated to 0.001 V at 0.1C and then delithiated up to 3 V at the same rate. The conditions for the following galvanostatic lithiation and delithiation were indicated in figure captions in electrochemical tests for measuring cyclability and rate capability. 1C was defined as 890 mA g^{-1}, considering the theoretical capacity calculated based on the conversion reaction of Co_3O_4 into Co and LiO_2 (890 mAh g^{-1}).

2.3 Results and discussion

Metal oxide nanostructures composed of the same primary particles, but with different secondary or tertiary architecture, can be generated via pyrolysis of MOFs. By implementing this approach, the synthesis of two different MOFs comprising the same building blocks can provide an opportunity to study how macroscopic structure affects practical application. To synthesize two different MOFs composed of the same building blocks for the comparative studies, Co^{2+} and BDC ligands were reacted under different conditions. Previous studies exhibited that the solvothermal reaction of Co^{2+} ions and BDC ligands in organic amide solvents led to the synthesis of mainly anionic MOF structures requiring protonated dimethylamines as counterions in the pores of a MOF scaffold.[17] The group of Yaghi reported a MOF structure comprised of Co^{2+} and BDC^{2-},[18] unfortunately the reported synthetic condition produced a mixture of products, which is necessary to separate by hand in order to obtain a pure phase. In the present work, we controlled and optimized the synthetic conditions for obtaining each pure phase of MOFs composed of Co^{2+} and BDC ligands possessing either plate-like and rod-like crystal shapes.

The purple plate-shaped MOF (*p*-MOF) crystals of $[Co_3(BDC)_3(DMF)_4]_n$, were obtained from a DMF solution of $Co(NO_3)_2{\cdot}6H_2O$ and two kinds of ligands, H_2BDC and adipic acid via a solvothermal reaction. In the crystal structure of *p*-MOF as shown in Figure 2.2, adipic acid or adipate as deprotonated forms was not contained at all, and may instead act as a structure-directing agent for synthesizing *p*-MOF as a pure phase. The same reaction conditions without adipic acid yielded a mixture of purple microcrystals and powdery products, which were not suitable for X-ray structural analysis. The *p*-MOF comprises of two crystallographically independent cobalt atoms in distorted trigonal bipyramidal and distorted octahedral coordination geometries, respectively. Two 5-coordinating Co^{2+} ions and one 6-coordinating Co^{2+} ion form a $Co_3(COO)_6$ cluster as a secondary building unit (SBU) by coordination with BDC ligands. Since two ends of the Co_3 cluster are terminated by coordinated DMF molecules, the SBUs are interconnected by BDC ligands forming as 2D layers extended in the (10-1) plane (Figure 2.3b), which are infinitely stacked in the [101] direction (Figure 2.3c). The X-ray powder diffraction (XRPD) pattern of *p*-MOF was consistent with the simulated pattern (Figure 2.4). As shown in TGA trace of the as-synthesized *p*-MOF under N_2 atmosphere (Figure 2.5), the four coordinating DMF molecules per formula ($[Co_3(BDC)_3(DMF)_4]_n$) were removed over the range 80-350 ^oC, and decomposition of *p*-MOF ensued above ~440 ^oC.

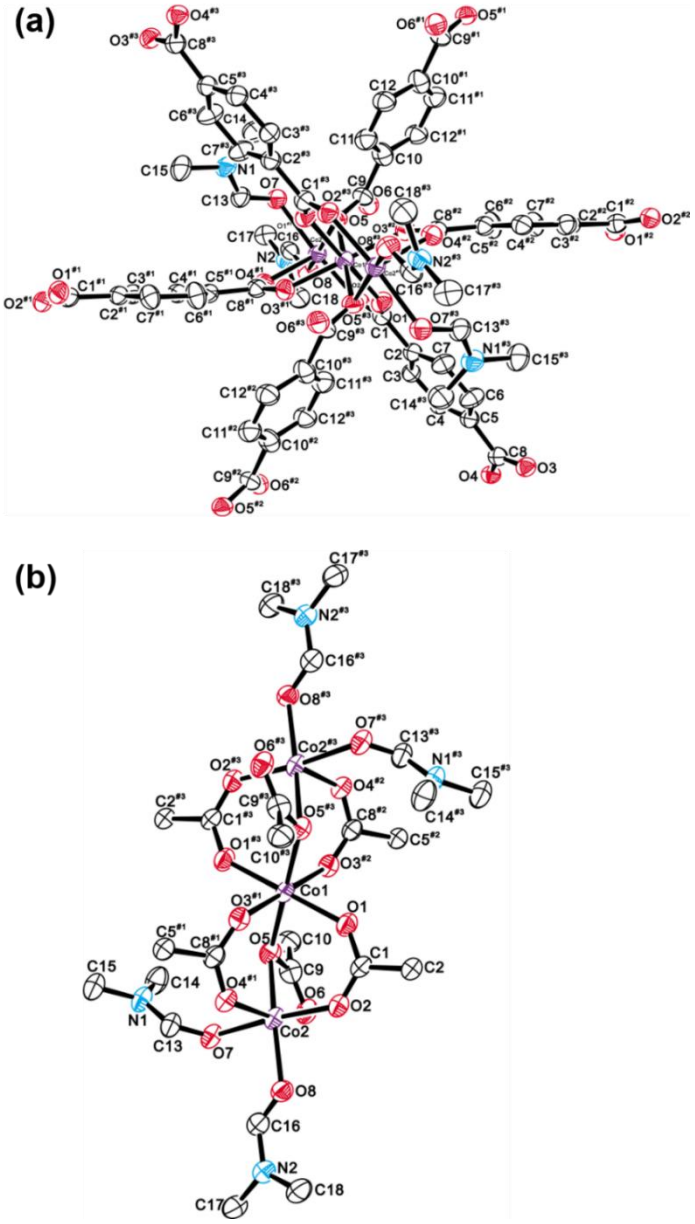

Figure 2.2 An ORTEP drawing of *p*-MOF with an atomic numbering scheme (thermal ellipsoids at 30% probability). (a) A shot for arrangement of ligands around the central cobalt atoms, and (b) a shot showing the coordination modes of the cobalt atoms. Hydrogen atoms are omitted for clarity. Symmetry operations: $^{\#1}$, x, y+1, z; $^{\#2}$, x-1/2, -y+5/2, z-1/2; $^{\#3}$, -x+1, -y+2, -z. Co, purple; C, gray; N, blue; O, red.

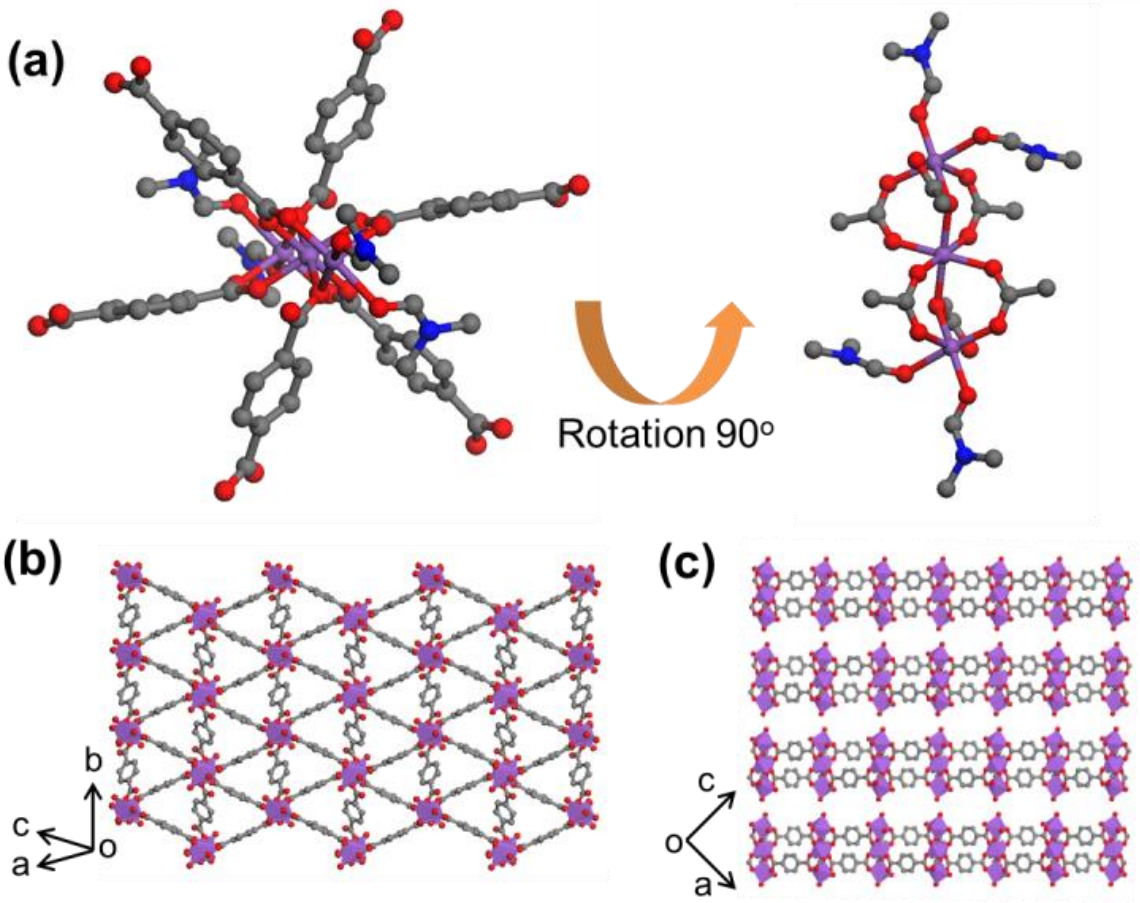

Figure 2.3 Single-crystal X-ray structure of *p*-MOF. (a) The SBU of the $Co_3(COO)_6$ cluster. (b) 2D layered structure of *p*-MOF. (c) 3D structure formed by staking of the 2D layers. Colour scheme: Co, purple; C, grey; O, red; N, blue.

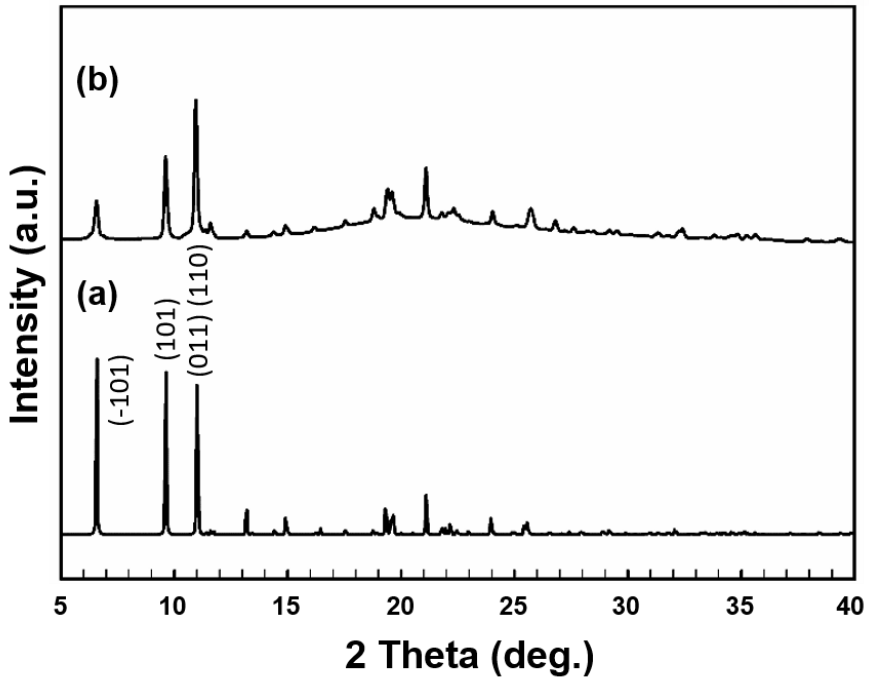

Figure 2.4 XRPD patterns of *p*-MOF. (a) Simulated pattern from single-crystal XRD data, and (b) experimental pattern of as-synthesized *p*-MOF.

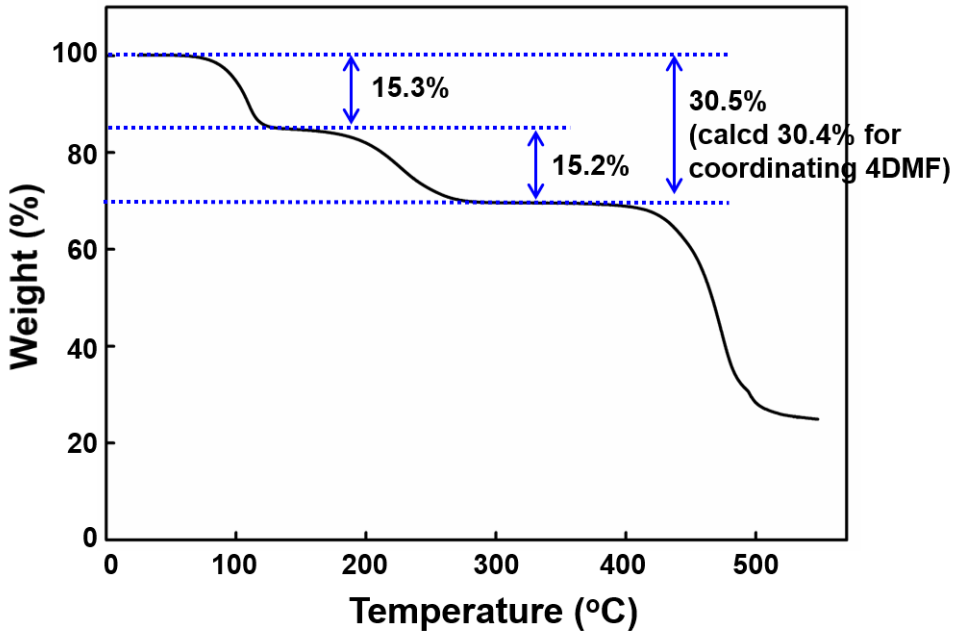

Figure 2.5 TGA trace of $[Co_3(BDC)_3(DMF)_4]_n$ (*p*-MOF). The result indicates that 30.5% weight loss at 80 – 350 ℃, corresponding to the loss of 4 DMF molecules (calc. 30.4%), followed by additional weight loss at ~440 ℃, corresponding to decomposition of *p*-MOF.

Rod-shaped MOF (*r*-MOF) crystals of $[Co(BDC)(DMSO)]_n$ were obtained by a solvothermal reaction of a solution of $Co(NO_3)_2 \cdot 6H_2O$ and H_2BDC in a mixture of DMF and DMSO at 120 °C. Figure 2.6 exhibits the crystallographic structure of *r*-MOF, which possessed same coordination mode as $[Co(BDC)(DMF)]_n$ reported by Yaghi group, except for the presence of coordinating solvent molecules.[18] *r*-MOF consists of two crystallographically independent cobalt atoms in distorted octahedral coordination geometries. Each of the Co^{2+} ions are coordinated by six oxygen atoms, of which four are offered by the BDC ligands while two are attributed to DMSO molecules (Figure 2.6). The infinite metal-ligand coordination leads to the formation of one-dimensional Co-O chains along the *a* axis, which are connected with four neighboring chains by BDC ligands in four different directions to form a 3D framework (Figure 2.7b). The XRPD pattern of *r*-MOF shown good agreement with the simulated pattern (Figure 2.8). Based on the TGA trace of as-synthesized *r*-MOF (Figure 2.9), one coordinating DMSO molecule per formula unit ($[Co(BDC)(DMSO)]_n$) is released between 250 °C and 330 °C, and decomposition of *r*-MOF occurs above ~500 °C.

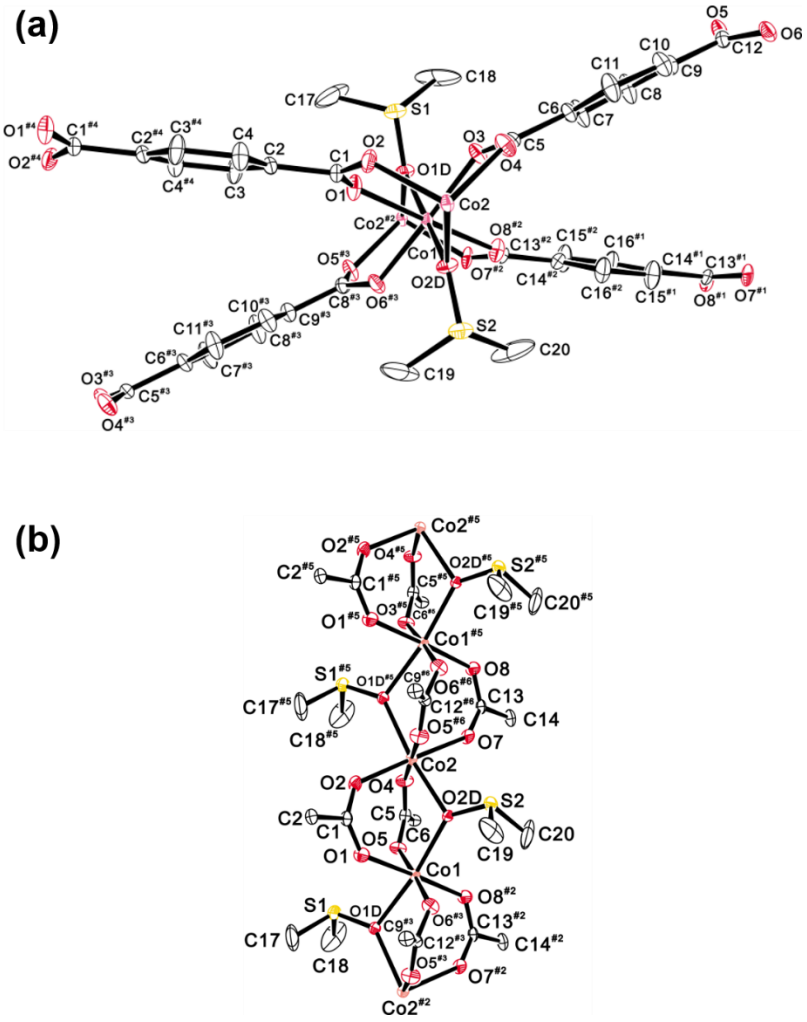

Figure 2.6 ORTEP drawings of *r*-MOF with an atomic numbering scheme (thermal ellipsoids at 30% probability). (a) A shot for arrangement of ligands around the central cobalt atoms, and (b) a shot showing the coordination modes of the cobalt atoms. Hydrogen atoms are omitted for clarity. Symmetry operations: $^{\#1}$, -x+1, -y, -z; $^{\#2}$, x+1, y, z; $^{\#3}$, x, y+1, z; $^{\#4}$, x, y+1, z+1; $^{\#5}$, x-1, y, z; $^{\#6}$, x-1, y+1, z. Co, pink; C, gray; S, yellow; O, red.

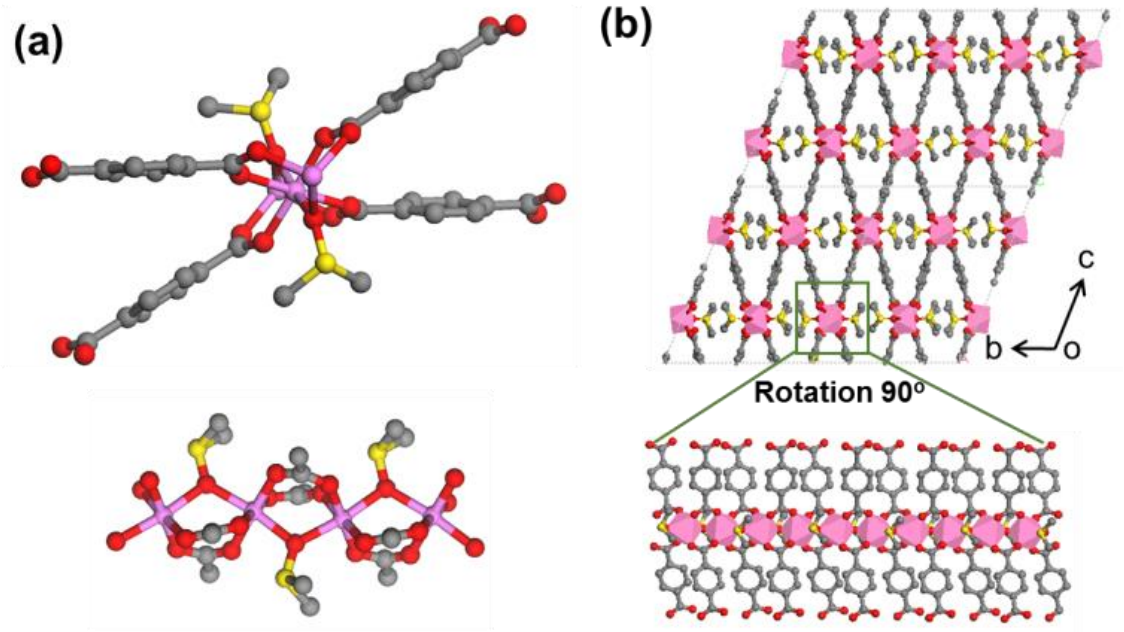

Figure 2.7 Single-crystal X-ray structure of *r*-MOF. (a) The SBU of the Co-O chain. (b) The *bc* plane of the 3D network, which is constructed by association of the SBUs and BDC ligands. Colour scheme: Co, pink; C, grey; O, red; S, yellow.

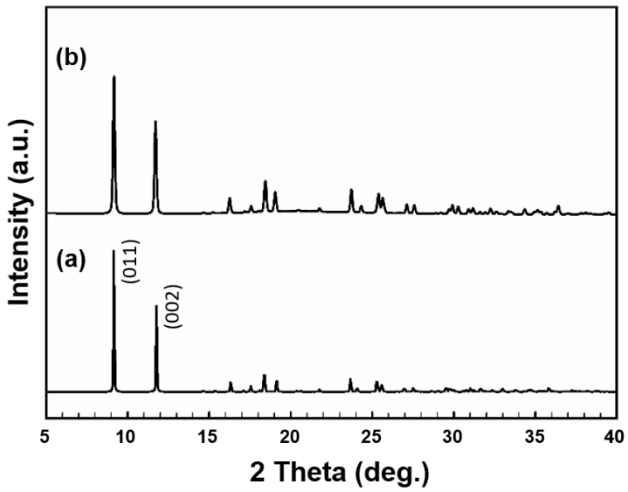

Figure 2.8 XRPD patterns of *r*-MOF. (a) Simulated pattern from single-crystal XRD data, and (b) experimental pattern of as-synthesized *r*-MOF.

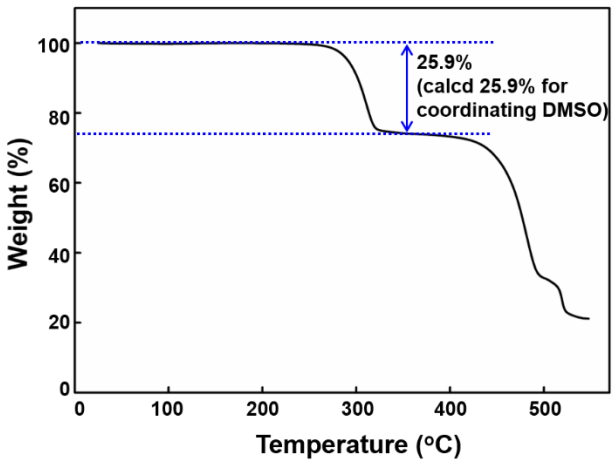

Figure 2.9 TGA trace of $[Co(BDC)(DMSO)]_n$ (*r*-MOF). The result indicates that 25.9% weight loss at 250 – 330 ℃, corresponding to the loss of a DMSO molecule (calc. 25.9%), followed by additional weight loss above ~500 ℃, corresponding to decomposition of *r*-MOF.

To comprehend the different crystal shapes of *p*- and *r*-MOF, their crystal morphologies were simulated using the Bravais-Friedel-Donnay-Harker (BFDH) model based on the single crystal X-ray diffraction data.[19-21] As shown in Figure 2.10a, the (10-1) plane of *p*-MOF corresponding to a 2D layer is placed on the board side of the crystal, and the layers are packed along with the [101] direction, parallel to the thinnest edge of the crystal. As revealed by scanning electron microscope (SEM) images, the actual morphology of *p*-MOF is consistent with the simulation results (Figure 2.10b). Because of the weak interaction between layers, the plates readily flake off (Figure 2.10b, inset). In this sense, the simulated crystal morphology of *r*-MOF exhibits the same rod-type structure as observed experimentally (Figures 2.10c and d). The SBU of Co-O chains oriented with the *a* axis run parallel to the longest edge of the crystal, resulting in their rod-shape.

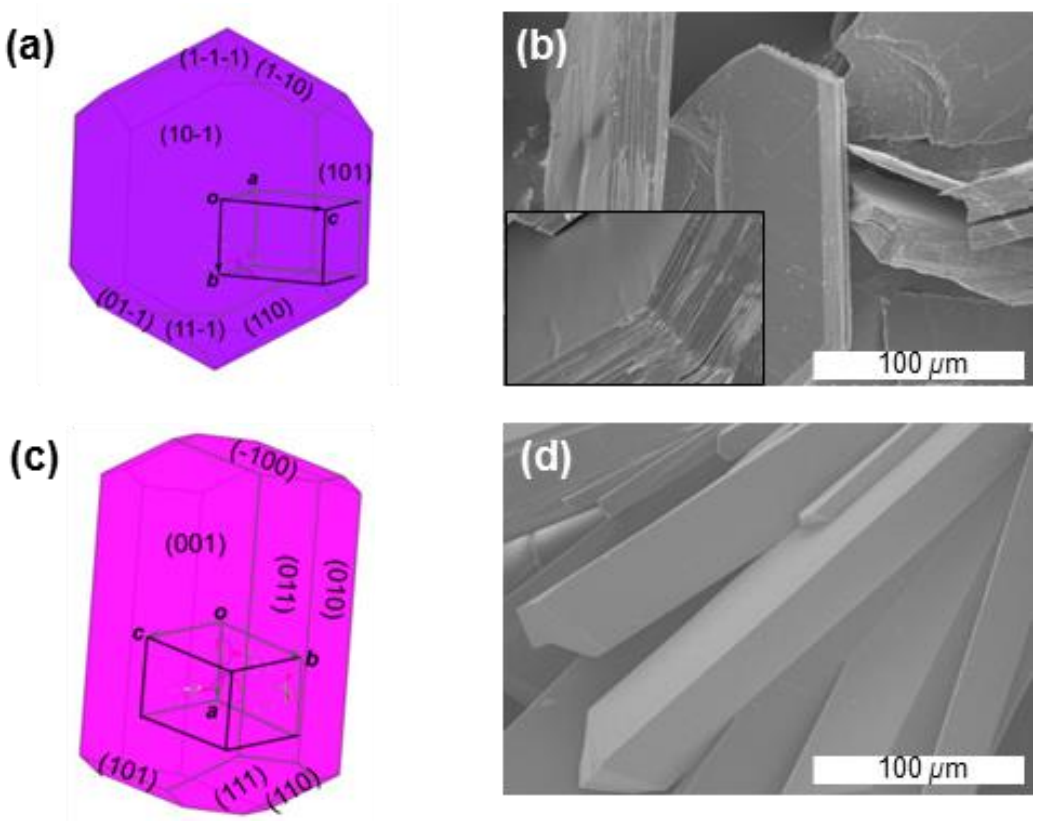

Figure 2.10 Investigation of crystal morphologies for *p*-MOF and *r*-MOF. (a) Simulated crystal morphology and crystallographic facets of *p*-MOF, and (b) a SEM image of the actual crystals. (c) Simulated crystal morphology and crystallographic facets of *r*-MOF, and (d) a SEM image of the actual crystals.

We then examined and optimized the pseudomorphic conversion conditions of Co-MOFs into cobalt oxides. Based on the TGA results, *p*-MOF was heated under N_2 (g) flow of 50 mL min^{-1} at 440 ^oC and maintained at this temperature for 24 h. The XRPD pattern of the resultant material shown a mixture of cubic metallic Co and cubic CoO, which shows good agreement with JCPDS file 71-4651 and 65-2902, respectively (Figure 2.11). To synthesize cobalt oxide with higher oxidation state, Co_3O_4, having a higher theoretical battery capacity of 890 mAh g^{-1}, we conducted sequential thermal treatments under an oxidizing environment. The second pyrolysis step under O_2 (g) flow of 0.1 L min^{-1} at 350 ^oC for 1 h successfully obtained pure Co_3O_4 (Figure 2.11). Similarly, *r*-MOF was transformed into pure phase of Co_3O_4 with an initial heat treatment under N_2 (g) flow at 500 ^oC, followed by a sequent pyrolysis under O_2 (g) flow at 500 ^oC for 1 h (Figure 2.12). The XRPD patterns of the Co_3O_4 shown that the MOF-driven resulting solids corresponded to the single-phase cubic Co_3O_4 with JCPDS file 71-4921. The elemental analysis (EA) exhibited that no organic residue remained within both plate-shaped and rod-shaped Co_3O_4 samples.

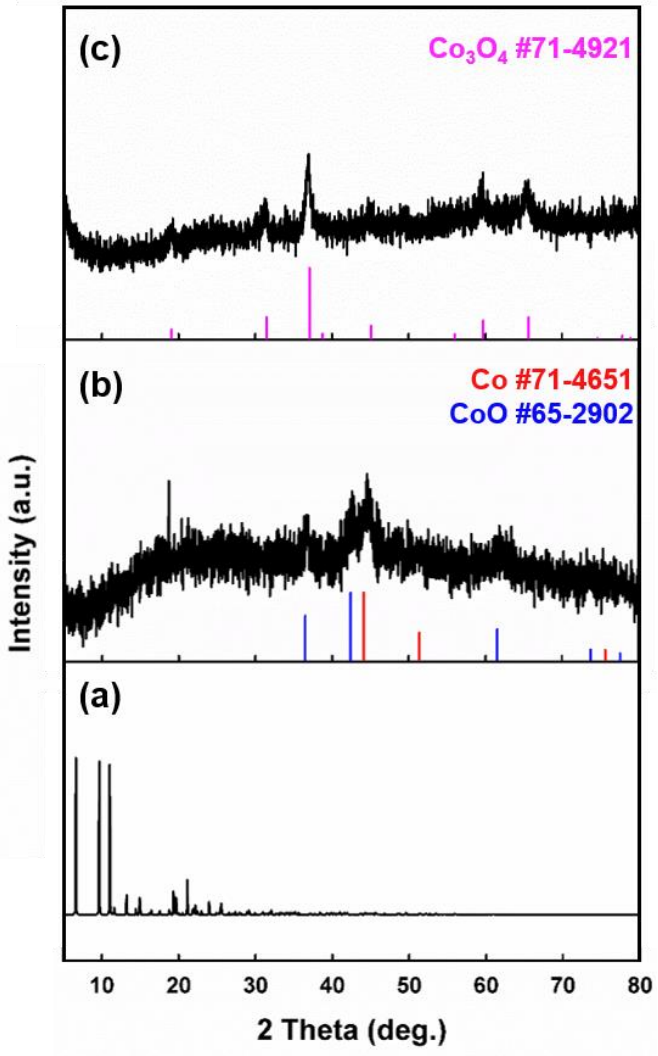

Figure 2.11 XRPD patterns of *p*-MOF and products obtained after heat treatments. (a) Simulated pattern from single-crystal XRD data, (b) sample after the first thermal treatment under a nitrogen flow with red lines and blue lines indicating the reported values of Co (JCPDS file No. 71-4651) and CoO (JCPDS file No. 65-2902), respectively, and (c) sample after the second thermal treatment under an oxygen flow with pink lines indicating the reported values of CO_3O_4 (JCPDS file No. 71-4921).

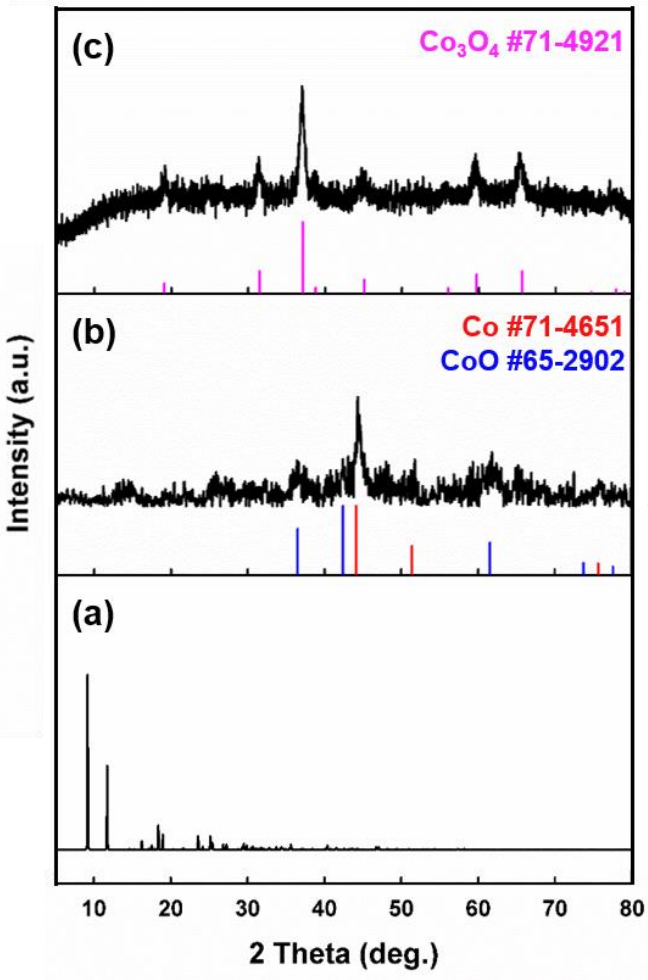

Figure 2.12 XRPD patterns of *r*-MOF and products obtained after heat treatments. (a) Simulated pattern from single-crystal XRD data, (b) sample after the first thermal treatment under a nitrogen flow with red lines and blue lines indicating the reported values of Co (JCPDS file No. 71-4651) and CoO (JCPDS file No. 65-2902), respectively, and (c) sample after the second thermal treatment under an oxygen flow with pink lines indicating the reported values of Co_3O_4 (JCPDS file No. 71-4921).

The structural properties of *p*- and *r*-Co_3O_4, such as primary nanoparticles, assembled structure as a second structure, and tertiary architectures were carefully examined by SEM and TEM (Figure 2.13). A comparison of SEM images showing tertiary architectures as macroscopic structures of *p*- and *r*-Co_3O_4 exhibit the same morphologies as those of the parent MOFs, implying that this conversion process is a pseudomorphic conversion (Figure 2.10b and d, and 2.13a and d). Since organic components in MOFs are decomposed and removed from the solid crystals during conversion, defects on the crystal surfaces were observed, but the external plate-like and rod-like shapes were remained. High magnification SEM and TEM images provide detailed structural information for *p*-Co_3O_4 and *r*-Co_3O_4. As shown in TEM images (Figures 2.13b and e), nanoparticles of Co_3O_4 in both materials are observed as ca. 10 nm-sized nanocrystals, which are consistent with the results calculated by applying the Debye-Scherrer equation to the (311) reflection (diameters of 11 nm for both). Within *p*-Co_3O_4 and *r*-Co_3O_4 almost identical primary particles are assembled to form the secondary structures (100 to 300 nm), which finally construct the macroscopic tertiary architectures. As shown in Figures 2.13c and f, while *p*-Co_3O_4 was consisted of the secondary particles without the integrity between primary particles, the secondary particles of *r*-Co_3O_4 were well-integrated or connected to each other. In order to measure the porosity of the *p*-Co_3O_4 and *r*-Co_3O_4 structures, which is attributed to secondary and tertiary structures, N_2 adsorption-desorption measurements were carried out. As shown in Figure 2.14, *p*-Co_3O_4 and *r*-Co_3O_4 exhibited typical type IV isotherms with *H3* hysteresis, which is indicated the presence of mesopores. The Brunauer-Emmett-Teller (BET) surface areas for *p*-Co_3O_4 and *r*-Co_3O_4 were 57 $m^2 g^{-1}$ and 12 $m^2 g^{-1}$, and the total pore volumes were 0.28 cc g^{-1} and 0.08 cc g^{-1}, respectively. The porosity difference between *p*- and *r*-Co_3O_4 is ascribed to differing assemblage densities of primary Co_3O_4 nanoparticles as mentioned earlier. Meanwhile, compared with *r*-Co_3O_4, the higher surface area and porosity of *p*-Co_3O_4 indicate a looser packing of primary nanoparticles in each plate in addition to spacing between the stacked plates. The pore size distribution curves analyzed by the nonlocal density functional theory (NLDFT) algorithm also demonstrated these explanations. Whereas mesopores in *p*-Co_3O_4 are distributed from 2 to 26 nm broadly, *r*-Co_3O_4 has narrow pores ranging from 2 to 8 nm.

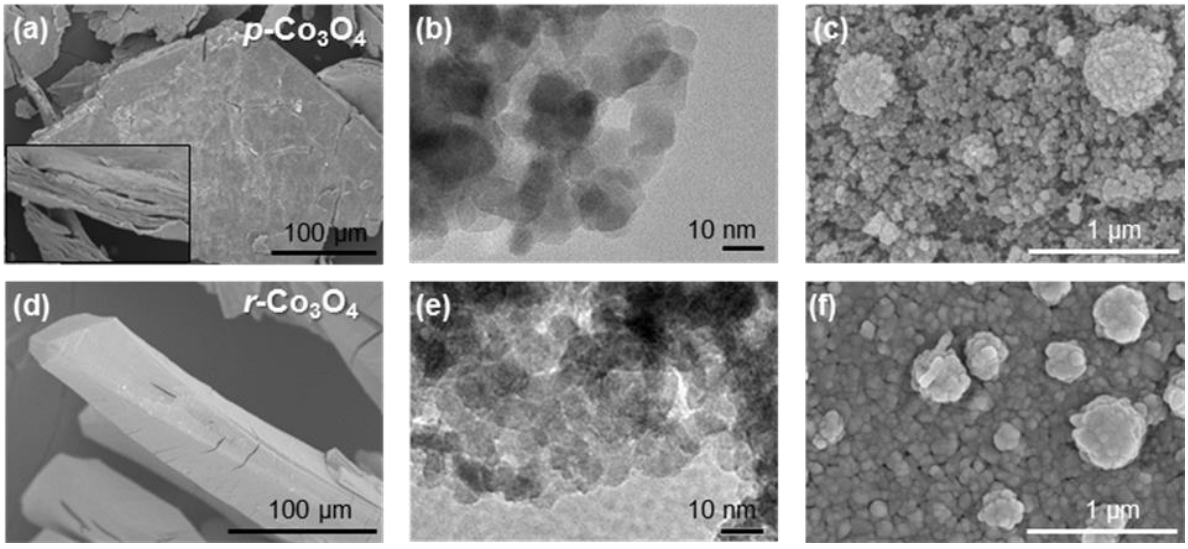

Figure 2.13 Structural properties for *p*-Co_3O_4 and *r*-Co_3O_4. SEM and TEM images (a) – (c) for *p*-Co_3O_4, and (d) – (f) for *r*-Co_3O_4.

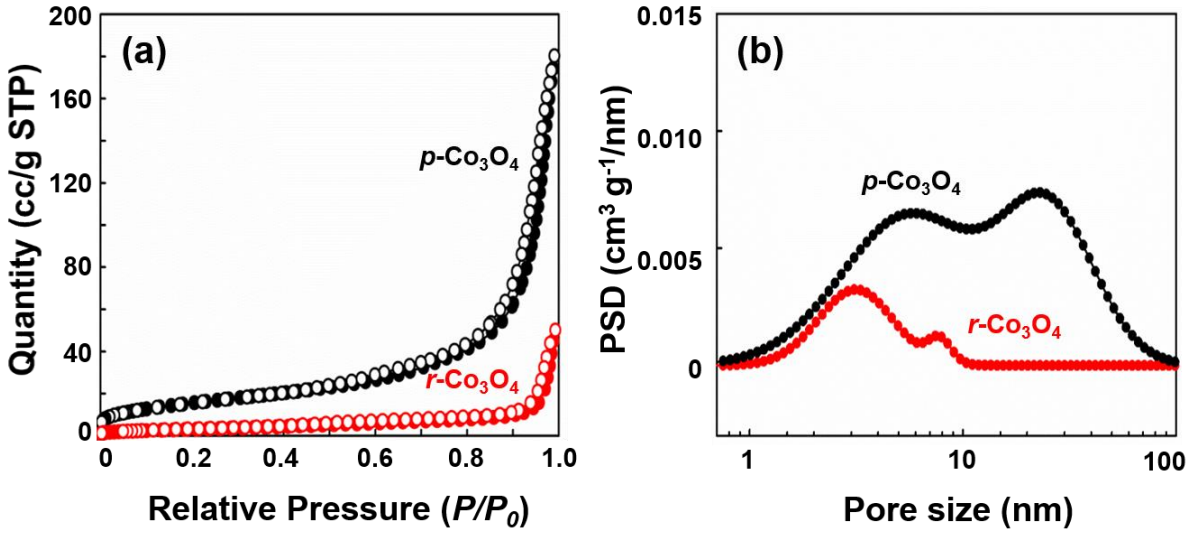

Figure 2.14 Structural properties for *p*-Co_3O_4 and *r*-Co_3O_4. (a) N_2 sorption isotherms and (b) NLDFT pore size distribution curve of *p*-Co_3O_4 as black one and *r*-Co_3O_4 as red one.

The electrochemical characteristics on as-synthesize Co_3O_4 nanostructures were investigated (Fig. 2.15). As mentioned, the structures of *p*- or *r*-Co_3O_4 can be interpreted as multi-leveled. Firstly, nanoparticles of ca. 10 nm are similar for both *p*-Co_3O_4 and *r*-Co_3O_4, but regarding their higher level structures such as secondary and tertiary architectures, the cobalt oxides showed different types of assembly as well as macroscopic morphologies such as *stacked* plates or *independent* rods. Therefore, the morphological determinants of electrochemical performance can be described by depending on secondary structures and macroscopic, tertiary architectures.

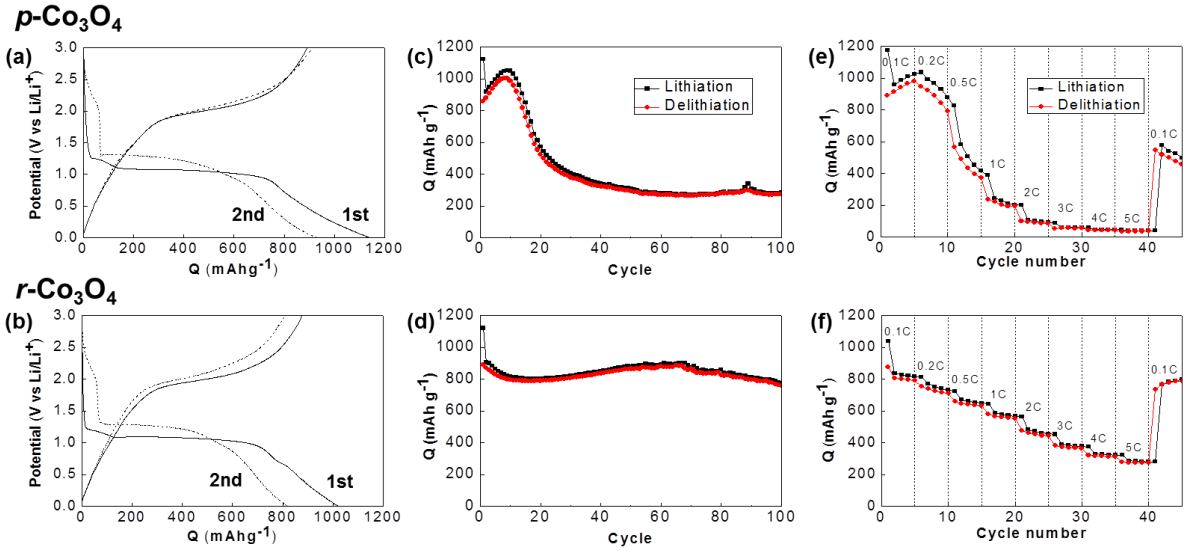

Figure 2.15 Electrochemical characteristics of *p*-Co_3O_4 and *r*-Co_3O_4 in the left and right columns, respectively. (a and b) Potential profiles during lithiation and delithiation at the first and second cycles. (c and d) Capacity retention during repeated cycles of charge and discharge at 0.1C for 100 cycles. (e and f) Capacity dependency on discharge rates. Charge rates were fixed at 0.1C.

Both cobalt oxides were lithiated by the same electrochemistry of the *conversion reaction*. During the initial lithiation caused by the negative potential shift, solvent molecules of electrolyte decompose to generate a solid electrolyte interface (SEI) layer at 1.2 V for both Co_3O_4 (Figures 2.15a and b). The conversion reaction of Co_3O_4 to Co metal embedded in the Li_2O matrix then proceeded at a well-defined reduction potential (1 V), which is responsible for the electrochemically reversible capacities. Additional capacities were delivered due to the pseudocapacitance of the gel-like polymer films formed at the potential-decreasing region after the conversion reactions.[22] Therefore, capacities of Co_3O_4 have often been overestimated at values larger than the theoretical capacity of Co_3O_4, calculated only on the basis of its conversion reaction (890 mAh g^{-1}). During the subsequent delithiation, reverse reactions

proceed, including pseudocapacitance discharging and backward conversion reactions. Size-confined Co metal particles catalytically decompose Li_2O during the backward conversion reaction, forming Co_3O_4.[23] Therefore, a capacity loss is involved between lithiation and delithiation at the first cycle due to the irreversible SEI formation reaction. However, the reversibility of the conversion reaction is guaranteed after the second cycle, showing coulombic efficiency higher than 95 %.

Although during the initial cycles, similar electrochemical behaviors were observed, the measured stability and kinetics of *p*- and *r*-Co_3O_4 were significantly different. The *p*-Co_3O_4 exhibited unstable capacity retention with a capacity increase up to the 10th cycle followed by a dramatic decrease up to 20th cycle (Figure 2.15c). Reversely, its rod-shaped electrodes (*r*-Co_3O_4) was observed to be much more stable, providing an enhanced cyclability (Figure 2.15d): ~800 mAh g^{-1} with *r*-Co_3O_4 versus less than 300 mAh g^{-1} with *p*-Co_3O_4 at the 100th cycle. Besides to the cycle stability, the kinetics of the conversion reaction of *r*-Co_3O_4 was superior to that of *p*-Co_3O_4 (Figures 2.15e and f). The plate-shaped cobalt oxide did not deliver a meaningful capacity at discharge rates faster than 2C: less than 100 mAh g^{-1} with *p*-Co_3O_4 versus ~400 mAh g^{-1} with *r*-Co_3O_4 at 2C. Regarding the capacity recovery after rate-variable tests, the rod-shaped oxides were also favored, observing the same capacity at 0.1C.

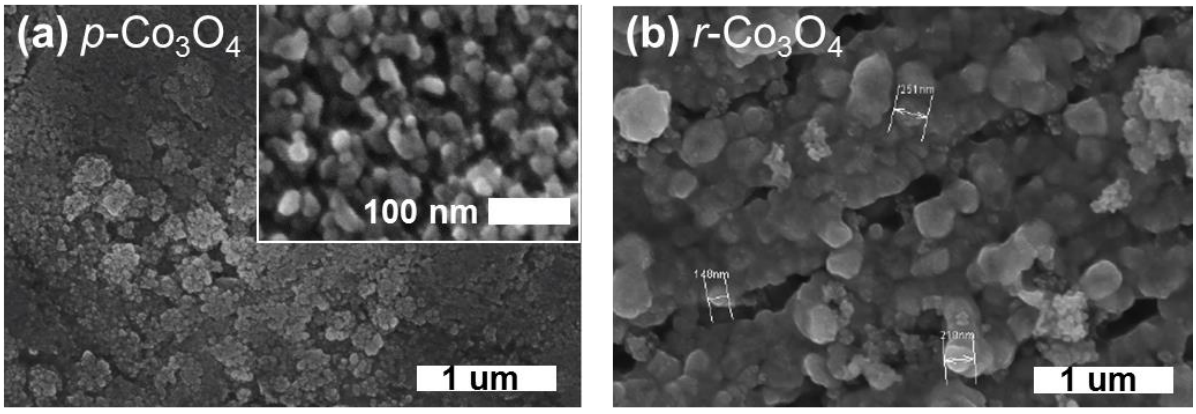

Figure 2.16 SEM images of composite electrodes containing (a) *p*-Co_3O_4 and (b) *r*-Co_3O_4. The interconnected secondary particles is clearly shown in (b) while the primary particles agglomerates without connectivity between them recognized in (a).

Difference of cyclability and rate capability is ascribed to the different architectures at higher levels in *p*- and *r*-Co_3O_4 as evidenced by microscopies and N_2 sorption studies (Figure 2.16). During the conversion reaction, gel-like polymers are formed around metal/Li_2O nanoparticles. The insulating polymer layers could isolate the active mass from electric pathways if the oxide particles were not

interconnected.[24] *p*-Co_3O_4 is considered to be the case. However, the interconnected network of active mass like *r*-Co_3O_4 (pseudo-monolithic structure) prevents the isolation from electric pathways. The importance of the pseudo-monolithic integrity for stable and kinetically fast performances is supported by other works. Cyclability of nanoparticular metal oxides was inferior to that of microsized counterparts.[24] Lu *et al*. showed that the electrochemical performances, especially cyclability, were improved as Co_3O_4 particles were monolithically integrated from a physical agglomerate to nano-clusters and further macro-porous platelets.[25] In addition to the reason mentioned above in terms of the primary and secondary levels of morphology, there is every possibility that the spacing between stacked plates in *p*-Co_3O_4 (as the tertiary-level structure) provide reaction surface on which the gel-like polymer layers are formed during lithiation. A macroscopic portion of plates located within the body of stacks could be isolated from electric pathways due to development of the insulating polymer films because the inner plates are not the pseudo-monolithic extension of exterior plates.

Not only the pseudomorphic conversion, but also the fabrication of porous structures were realized by choosing suitable MOFs and optimizing conversion conditions. The strategy toward hierarchically nanoporous metal oxide materials with nanocrystalline frameworks lies in the use of MOFs based on *aliphatic* carboxylate ligands. The aliphatic ligand-based MOFs (*aph*-MOF) are thermally less stable and much more labile, even under inert atmosphere, than those of aromatic ligands (*ar*-MOF). During the thermolysis of an *aph*-MOF, the ligands were transformed into organic moieties *via* chemical decomposition, and were confined as vesicles in the solids. The organic vesicles acted as self-generated porogens, which were transformed into nanopores. Meanwhile, organic substances also prevented aggregation of the metal oxide nanocrystals during thermolysis. Thus, upon thermolysis at higher temperature, the confined organic moieties evaporated, generating highly porous nanostructures possessing nanocrystalline metal oxides (Figure 2.17). Additionally, we note that the control of the retention time and the evaporation rate of the organic moieties in the host solid were important to synthesizing nanoporous metal oxides with nanocrystalline frameworks. We explain our MOF-driven approach to nanoporous metal oxides with the preparation of nanoporous MgO with nanocrystalline frameworks. The pore sizes of these converted nanoporous materials could be easily tuned by simple control of experimental factors such as a target temperature, and a ramping rate. Furthermore, we demonstrate that nanoporous MgO materials show exceptionally high CO_2 absorption storage with recyclability. Our MOF-driven strategy was simple yet powerful to generate nanoporous metal oxide structures.

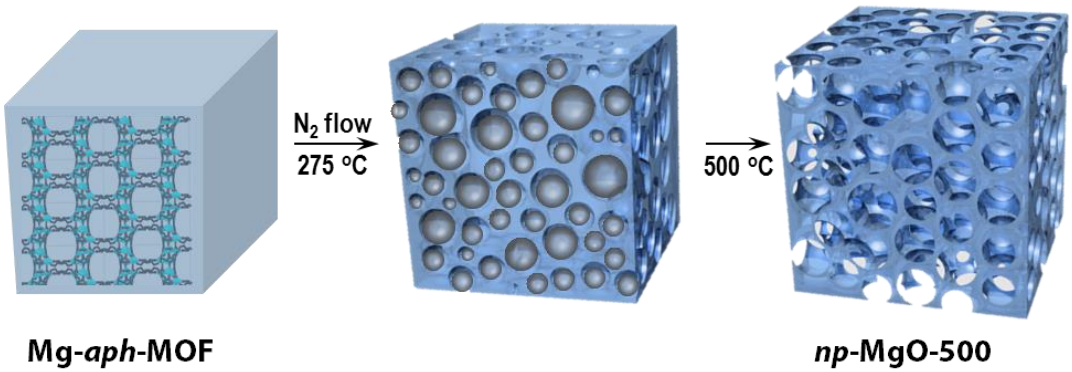

Figure 2.17 Schematic view of the direct conversion mechanism from Mg-*aph*-MOF to *np*-MgO-500 by heating under nitrogen atmosphere.

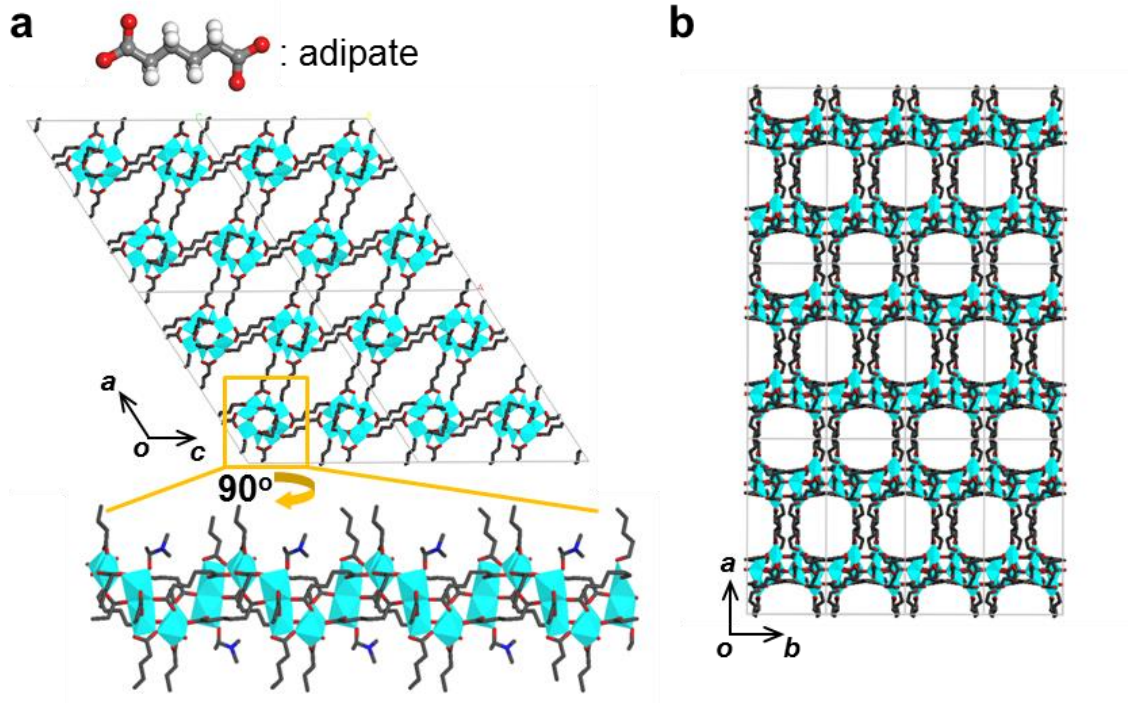

Figure 2.18 Single-crystal X-ray structure of Mg-*aph*-MOF. a, 3D framework formed by association of secondary building units (SBUs) of Mg-O chain and organic ligands, adipate. The yellow rectangle indicates the (SBU) of the Mg-O chain. b, Structure projected along the c-axis, showing 11 x 11 Å channels. Hydrogen atoms and guest molecules are omitted for clarity. (Color scheme: C, grey; O, red; and Mg, light blue)

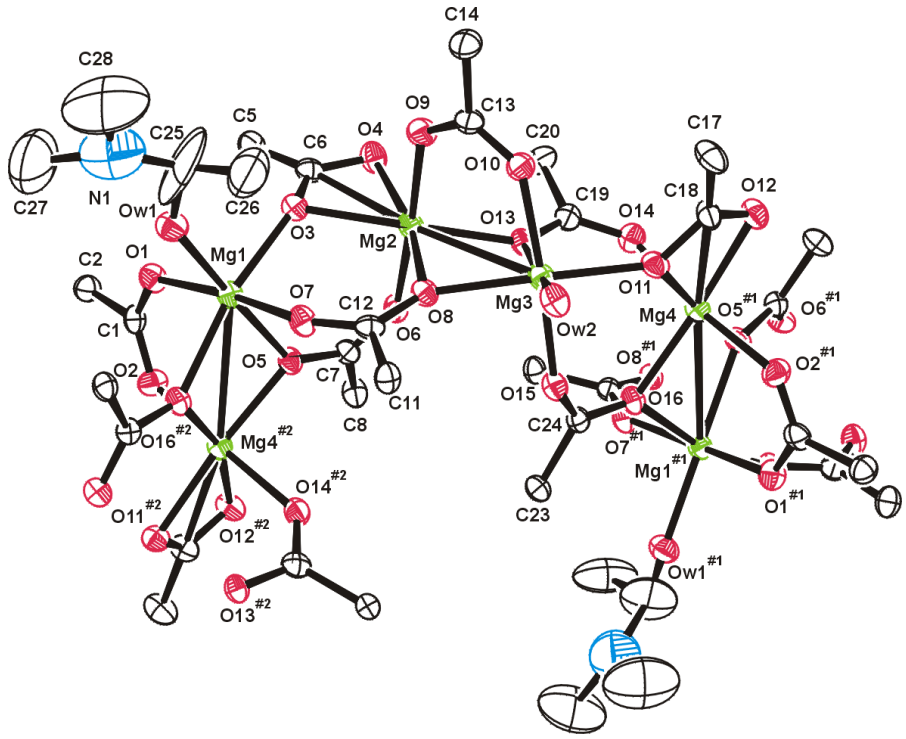

Figure 2.19 An ORTEP drawing of Mg-*aph*-MOF with an atomic numbering scheme (thermal ellipsoids at 30% probability). Hydrogen atoms are omitted for clarity. The hydrogen atoms of coordinated water molecules were not located. Symmetry operations: #1, -x+3/2, y-1/2, -z+3/2; #2: -x+3/2, y+1/2, -z+3/2.

For the synthesis of an *aph*-MOF, commercially available, inexpensive adipic acid ($HCOO(CH_2)_4COOH$) was chosen as the aliphatic ligand. The solvothermal reaction of $Mg(NO_3)_2 \cdot 6H_2O$ and adipic acid in a mixture of *N,N'*-dimethylacetamide (DMA) and methanol (MeOH) obtained block-shaped crystals of $[Mg_4(adipate)_4(DMA)(H_2O)] \cdot 5DMA \cdot 2MeOH \cdot 4H_2O$ (Mg-*aph*-MOF). Single crystal X-ray crystallographic data exhibited that the structure of Mg-*aph*-MOF was constructed of Mg-O chains as the SBUs, and adipates as the bridging ligands (Figure 2.18). Mg-*aph*-MOF had four crystallographically independent Mg atoms in distorted octahedral coordination geometries. Among the four Mg atoms, two Mg^{2+} ions were coordinating to five oxygen atoms, among which four came from the adipate ligands and one was provided by a solvent molecule such as DMA or H_2O. The other two Mg^{2+} ions were coordinated with six oxygen atoms of the adipate ligands (Figure 2.19). The infinite metal-ligand coordinations formed 1D Mg-O chains as SBUs, which were connected with four neighboring chains by adipate ligands in four different directions to construct 11 × 11 Å 3-D

pores containing guest solvent molecules, DMA, MeOH, and water. Based on TGA trace of the as-synthesized Mg-*aph*-MOF (Figure 2.20), the guest solvent molecules were occupied the void spaces in the Mg-*aph*-MOF scaffold and were removed over a range from room temperature to ca. 220 °C. To release the coordinated guest molecules such as DMA and H_2O, the temperature required was 320 °C, and decomposition of Mg-*aph*-MOF ensued above ca. 330 °C.

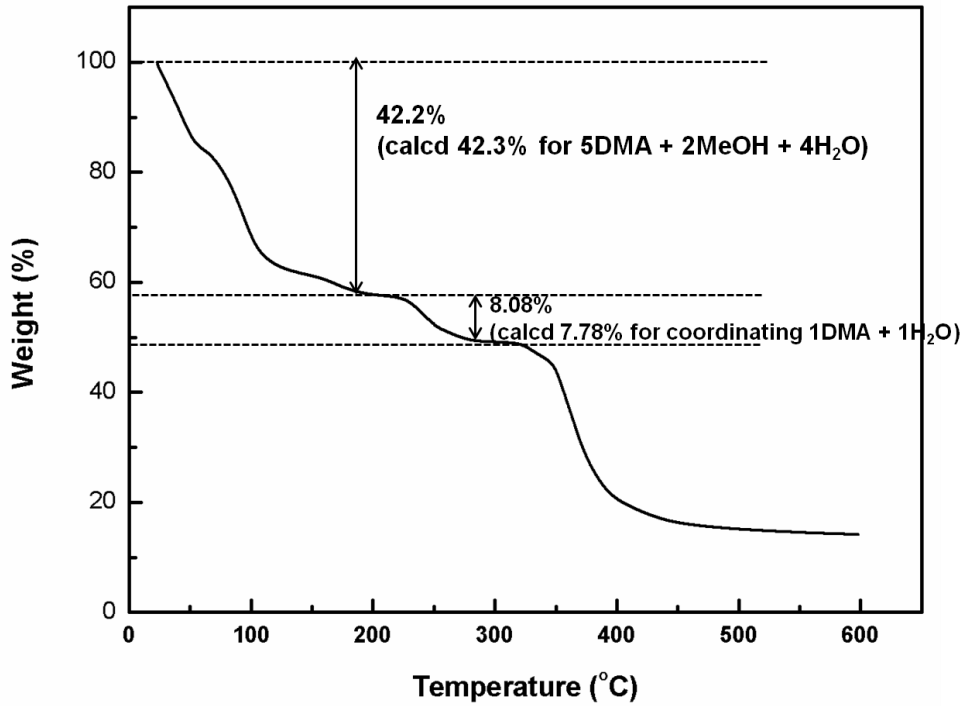

Figure 2.20 TGA trace of {[$Mg_4(C_4DC)_4(DMA)(H_2O)$]·5DMA·2MeOH·$4H_2O$} (Mg-*aph*-MOF). TGA trace indicates that 42.2% weight loss at 25 – 220 °C, corresponding to the loss of 5 DMA, 2 MeOH, and 4 H_2O guest molecules of **1** (calcd 42.3%), followed by additional weight loss of 8.08% at 220 – 320 °C, corresponding to coordinating DMA and H_2O molecules. (calcd 7.9%).

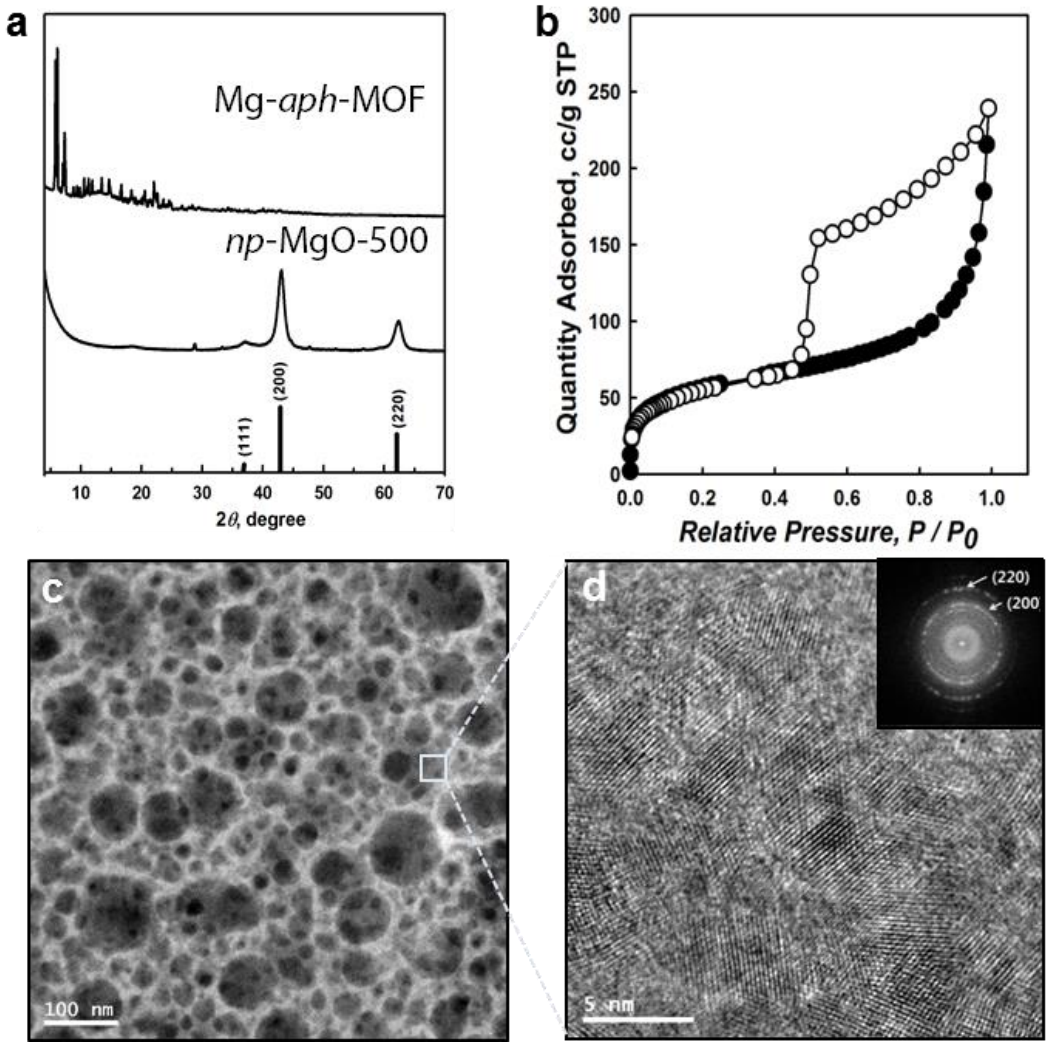

Figure 2.21 Characterization of *np*-MgO-500. a, Comparison of XRPD patterns of Mg-*aph*-MOF (top) and *np*-MgO-500 (bottom). b, BET measurement of *np*-MgO-500. c, Dark-field TEM image of *np*-MgO-500, and **d**, HR-TEM image of framework walls in *np*-MgO-500.

Based on the TGA traces, the decomposition of Mg-*aph*-MOF was performed at 500 °C by heating with a ramping rate of 5 °C/min under a nitrogen flow of 60 cc/min (Figure 2.21). After thermal treatment at 500 °C for 12 h, we could obtained an off-white solid. As evidenced by XRPD pattern, it was identified as cubic MgO, showing good agreement with JCPDS file 89-7746 (Figure 2.21a). The crystalline size of MgO, calculated by applying the Debye–Scherrer equation to the (200) reflection, implies the formation of MgO nanocrystals with diameters of 6.3 nm. Interestingly, the TEM images of the resultant solid (Figures 2.21c and d) exhibited that these MgO nanocrystals comprised highly nanoporous structures (*np*-MgO-500). The *np*-MgO-500 had hierarchical porous structures, possessing both mesopores (a few tens of nanometers) and macropores (~ 100 nm). The lattice fringes in the high-resolution TEM (HR-TEM) image (Figure 2.21d) of *np*-MgO-500 along with the corresponding selected area electron diffraction image (Figure 2.21d, inset) also indicated that the nanoporous solids were constructed from MgO nanocrstalline particles. The MgO NCs, which were interconnected in the nanoporous solid (*np*-MgO-500) wall, coexisted with a small amount of carbon (1.79 wt%) based on EA analysis. In order to evaluate the porosity of the *np*-MgO-500, a N_2 adsorption-desorption measurement was carried out. As shown in Figure 2.21b, the *np*-MgO-500 exhibited a typical type IV isotherm with an *H2* type hysteresis loop over a relative pressure range of $0.5 < P/P_0 < 0.95$, characteristic of cage-like pore structures with large mesopores and narrow channel interconnections. The Brunauer-Emmett-Teller (BET) surface area for the *np*-MgO-500 was 200 m^2/g, and the total pore volume was 0.37 cc/g. Interestingly, a significant portion of the total pore volume was attributed by micropores, with their value reaching 0.13 cc/g, which indicated that the *np*-MgO-500 was composed of triply hierarchical porous structures of micro-, meso-, and macropores.

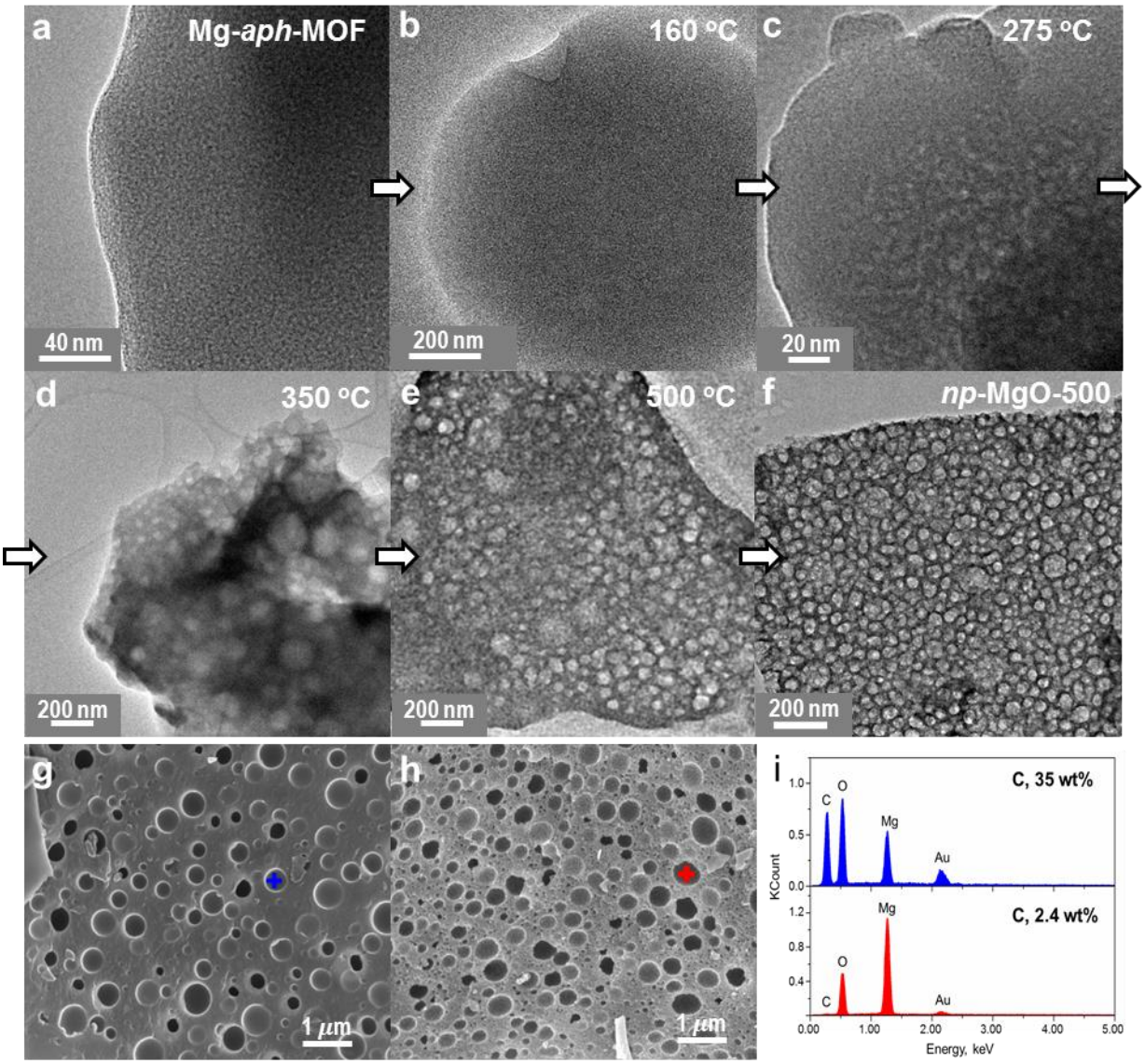

Figure 2.22 Temperature-dependent evolution of conversion of Mg-*aph*-MOF to nanoporous MgO. High-resolution transmission electron microscopy (HR-TEM) images for Mg-*aph*-MOF before (a) and after heat treatment at 160 °C (b), 275 °C (c), 350 °C (d), and 500 °C (e). (f) *np*-MgO-500. SEM images for (g) Mg-*aph*-MOF after heat treatment at 350 °C, and (h) *np*-MgO-500. (i) EDS data for the positions, which are indicated with cross marks (+, +) in (g) and (h).

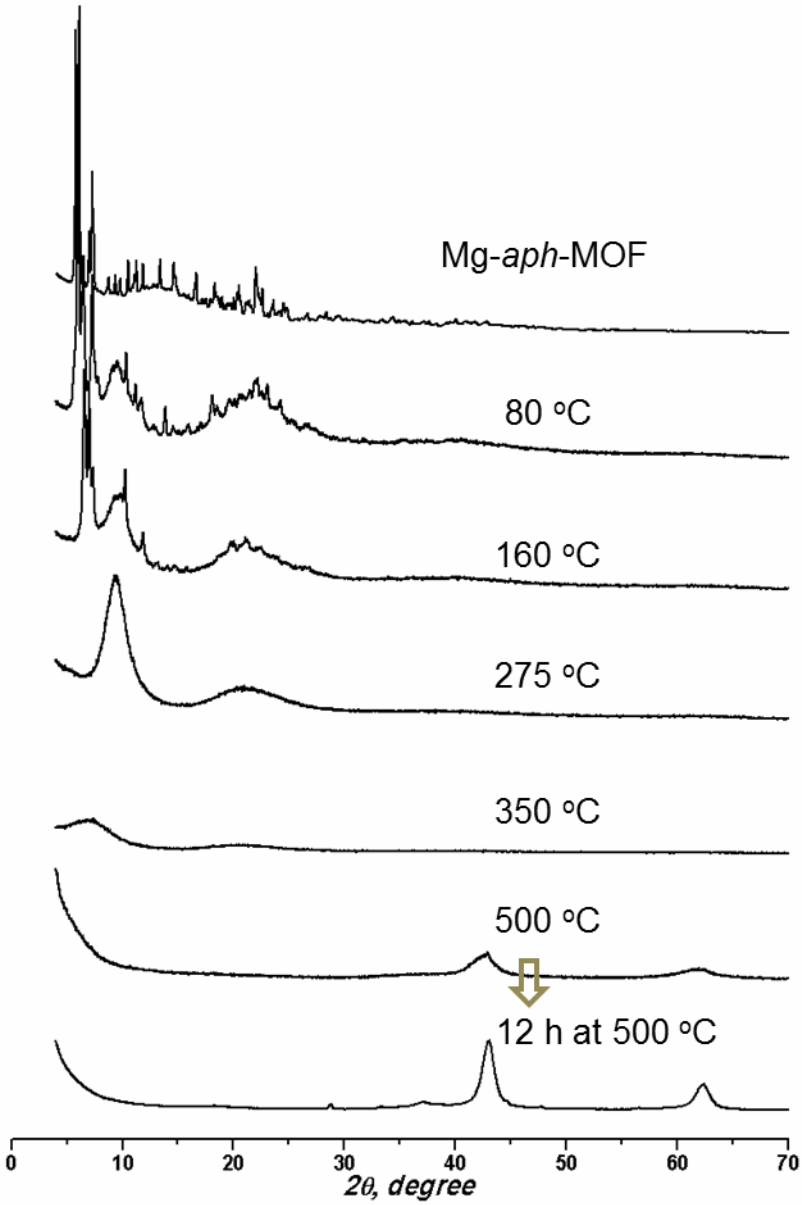

Figure 2.23 Temperature-dependent evolution of conversion of Mg-*aph*-MOF to nanoporous MgO. Temperature-dependent XRD patterns of Mg-*aph*-MOF.

Table 2.1 Py-GC/MS result of Mg-*aph*-MOF.

Temperature range (°C)	Product name	Structure	Boiling point (℃)
60 ~ 100	Dimethylacetamide	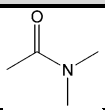	165
120 ~ 200	Dimethylacetamide	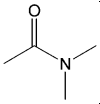	165
250 ~ 300	Dimethylacetamide	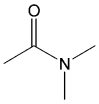	165
	Dimethyl adipate	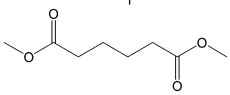	229
	N,N-dimethyldodecanamide	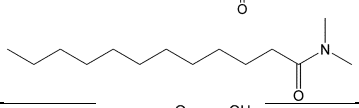	285
330 ~ 400	1-Hydroxyxanthone	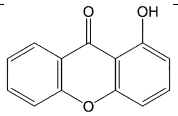	409
	2-Cyclopentylidene-1-cyclopentanone	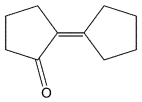	257.8
	2,6-Diaminopurine	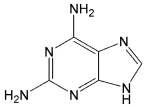	285
	Trimethylquinone	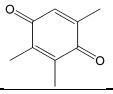	215
450 ~ 550	3-Hydroxyxanthone	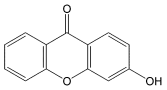	404
	3,3’-dimethyl-4,4’-biphenyldiamine	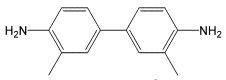	300
	Tricyclotrimethylenebenzene	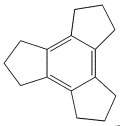	301
	Methylpyridoindolol	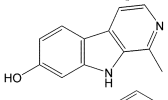	553
	2-Styrylbenzenol	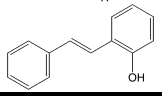	338

It is noteworthy that thermal treatments converted the Mg-*aph*-MOF into 3-dimensionally nanoporous MgO frameworks instead of discrete MgO nanoparticles embedded in a carbon matrix. To understand the structural transformation along with increasing temperature, we monitored *ex-situ* TEM images taken at each increment of temperature (Figures 2.22a – f). As shown in Figures 2.22a and b, the crystals of Mg-*aph*-MOF hadn't changed until 160 ºC, except liberating only non-coordinating guest molecules. Upon heat treatment to 275 ºC, irregular pores began to form (Figures 2.22c), primarily due to the removal of coordinating molecules including DMA and water molecules. The pores might have been formed by the confinement of liberated coordinating guest molecules and decomposed organic ligands. These transformation phenomena were also supported by the temperature-dependent XRPD patterns (Figure 2.23). The XRPD pattern of as-synthesized Mg-*aph*-MOF showed strong reflections in the region 5 ~ 25º, as same as the simulated pattern from single crystal X-ray diffraction data. Up to 160 ºC the typical patterns of Mg-*aph*-MOF were retained, except for a slight broadening and shift of the peaks. However, above 275 ºC all peaks from the crystalline Mg-*aph*-MOF were gone, which are indicated that the MOF solid lost crystallinity. When the temperature reached 350 ºC, the pores were widely distributed over the solid, implying the generation and confinement of large amounts of organic substances at the high temperature (Figure 2.22d). However, the shapes of the pores were still irregular, and the crystalline metal oxide had not yet form. Upon heating to 500 ºC, the size distribution of the spherical pores became narrower (Figure 2.22e), and the resulting solid began to show crystallinity (Figure 2.23). Finally, after thermal treatment of Mg-*aph*-MOF at 500 ºC for 12 h under inert atmosphere, highly crystalline 3D nanoporous MgO, *np*-MgO-500 was obtained (Figure 2.22f). Comparison of the SEM images and EDS results for the cross-sections of Mg-*aph*-MOF which had just reached 350 ºC without a holding time and *np*-MgO-500 also supported this transformation, because the former still possessed the organic porogens in the solid, but *np*-MgO-500 contained a high distribution of pores and hierarchical structures (Figures 2.22g to i). To examine the organic substances which were *in-situ* generated by thermolysis over each temperature range, the Mg-*aph*-MOF was analysed by pyrolysis-gas chromatography/mass spectrometry (py-GC/MS). As shown in Table 2.1, even below 300 ºC the formation of new organic species was detected, and at higher temperature, diverse organic substances with high boiling points were formed. Thus, during the thermal treatment of Mg-*aph*-MOF, decomposed organic compoments reacted to generate new species, which were confined in the solid until the temperatures were high enough to volatilize them.

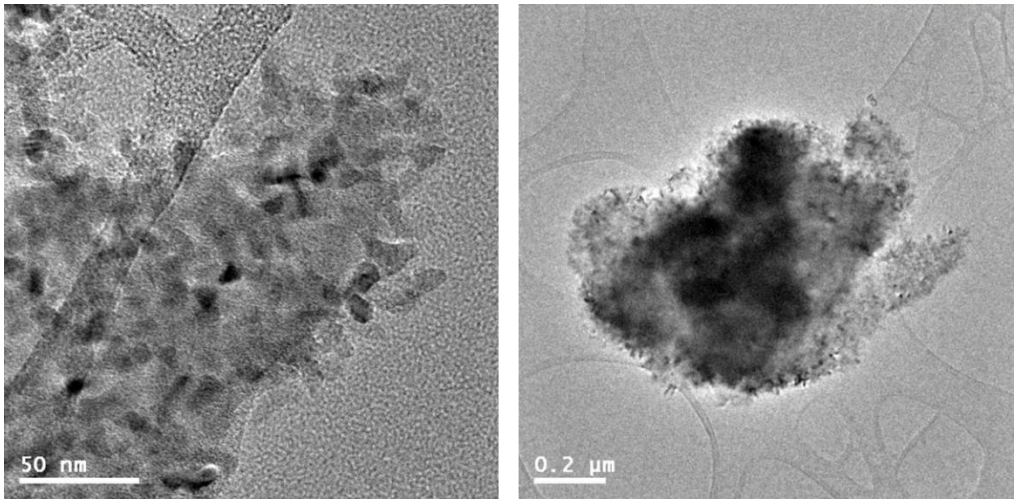

Figure 2.24 TEM images of MgO, which were prepared by thermolysis of Mg-*ar*-MOF, $[Mg_3(bpdc)_3(DMA)_4]$.

Table 2.2 Py-GC/MS result of Mg-*ar*-MOF.

Temperature range (ºC)	Product name	Structure	Boiling point (℃)
160 ~ 200	Dimethylacetamide	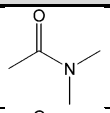	165
220 ~ 260	Dimethylacetamide	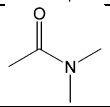	165
280 ~ 340	Dimethylacetamide	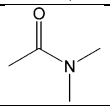	165
450 ~ 520	1,1'-Biphenyl	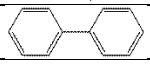	255
580 ~ 620	Acenaphthene	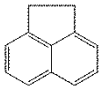	279
	1,4-Methanobiphenylene-9-one	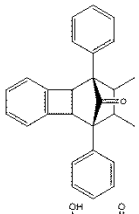	476
	8-Acetyl-6,11-dihydroxy-9,10-dihydro-5,12-naphthacenedione	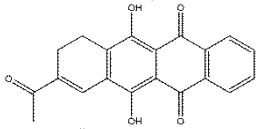	611
	1-Azabicyclo[2.2.2]oct-2-ene-3-carboyxlic acid, ethyl ester	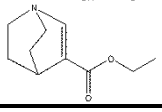	268

Based on the above results, we suggest that organic substances *in-situ* generated during the thermal decomposition of the MOF formed vesicles which acted as self-templates, and after, were transformed to nanopores. Meanwhile, inorganic SBUs nucleated and grew to nanocrystals at high temperature, but their growth were limited to growth as sizes below 10 nm due to the presence of the organic templates. Under subsequent high temperature treatment, the organic vesicles were liberated, generating numerous spherical nanopores and a nanocrystalline metal oxide framework. There has, hitherto, been no report of the successful prepration of 3D porous structures composed of metal oxides by the thermal decomposition of MOFs. We suggest that the high thermal and chemical stabilities of conventional aromatic organic ligands, which have been used in the majority of the previous work,[26-28] induce their preferential conversion into carbogenic structures, with the simultaneous agglomeration of the metal oxides. Therefore, MOFs composed of aromatic carboxylate ligands (*ar*-MOF) appear to be unsuitable precursors for the preparation of porous metal oxides. To test this hypothesis, we synthesized an aromatic ligand-based MOF (Mg-*ar*-MOF), $Mg_3(bpdc)_3(DMA)_4$ (bpdc = biphenyl-4,4′-dicarboxylate; DMA = dimethylacetamide) according to a previous report.[29] The thermolysis of the Mg-*ar*-MOF provided only aggregated MgO nanoparticles (Figure 2.24). Py-GC/MS results for Mg-*ar*-MOF revealed that new organic species were not formed, even at 450 ^{o}C, which means that there were no porogens to direct nanoporous structure formation during the decompostion and oxidiation of the MOF (Table 2.2).

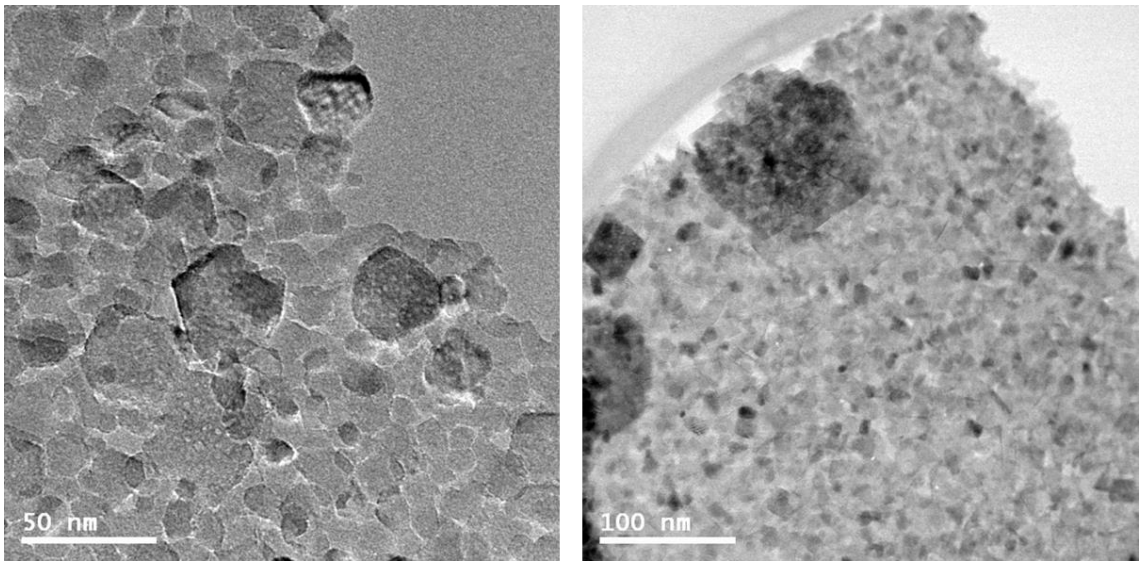

Figure 2.25 TEM image of MgO, which were prepared by thermolysis of Mg-*aph*-MOF under oxygen atmosphere.

The contrasting results from the thermolysis of Mg-*aph*-MOF and Mg-*ar*-MOF highlight the competition between the duration of the organic vesicles and the growth rate of the MgO nanoporous structure. Organic vesicle removal that is faster than the structuring of the 3D porous structure may result in the agglomeration of MgO particles. The rapid oxidation of Mg^{2+} in the MOF to MgO will generate large MgO particles before forming the organic vesicles. This expectation was proven by the thermal treatment of Mg-*aph*-MOF under oxygen atmosphere instead of nitrogen gas flow. As shown in Figure 2.25, the product was composed of highly crystalline cubic-shaped MgO nanocrystals of ca. 50 nm in size.

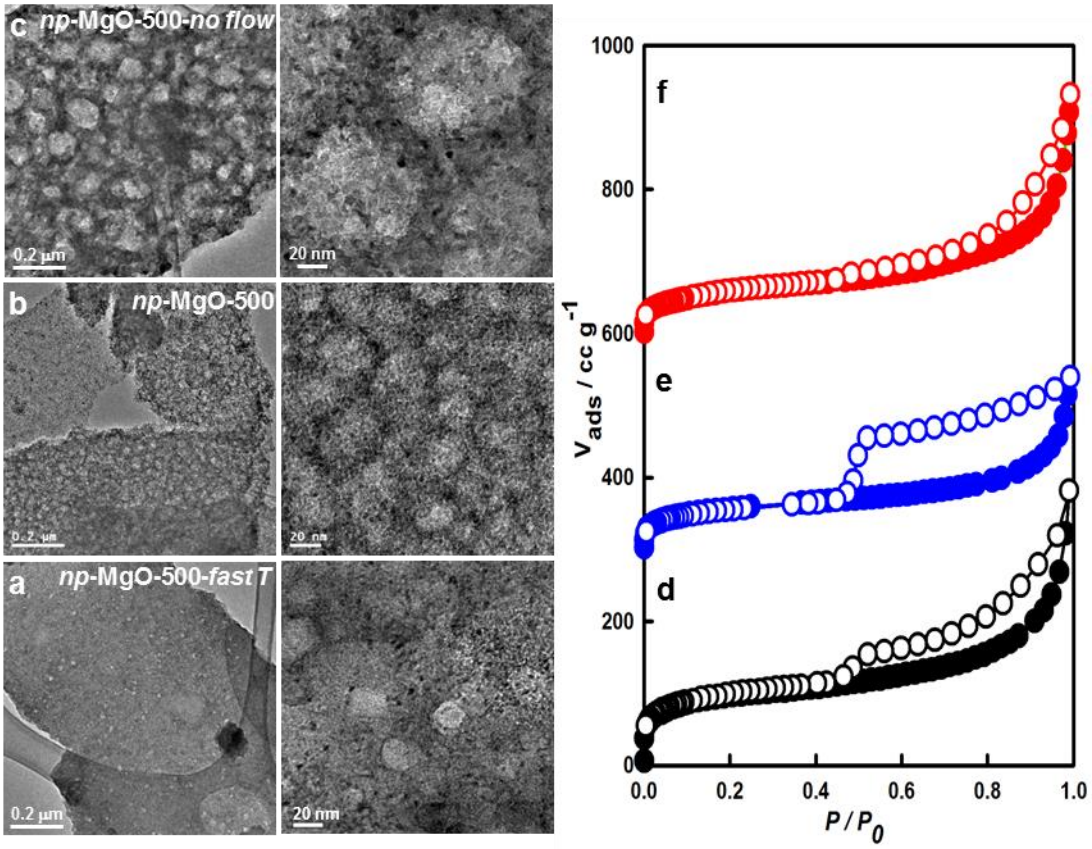

Figure 2.26 Pore size control of *np*-MgO under different reaction conditions. TEM and BET isotherms for *np*-MgO-500-*fast T* (a, d), *np*-MgO-500 (b, e), and *np*-MgO-500-*no flow* (c, f), respectively.

Table 2.3 Textural properties of the *np*-MgOs.

Sample	S_{BET}[a] ($m^2\ g^{-1}$)	V_t[b] ($cm^3\ g^{-1}$)	V_{meso}[c] ($cm^3\ g^{-1}$)	V_{micro}[d] ($cm^3\ g^{-1}$)	D_{BJH}[e] (nm)	D_{HK}[f] (nm)	Pore size[g] (nm)
np-MgO-500	200	0.37	0.24	0.13	3.77	0.67	~50
np-MgO-500-*no flow*	207	0.51	0.37	0.14	3.77	0.66	~100
np-MgO-500-*fast T*	318	0.59	0.39	0.20	3.77	0.69	~20

[a] The specific surface area (S_{BET}) was calculated by Brunauer-Emmet-Teller (BET) method.

[b] V_t represented the total pore volume at $P/P_0 = 0.99$.

[c] The mesopore volume (V_{meso}) was obtained by subtracting the microporous volume from total volume.

[d] The micropore volume (V_{micro}) was determined by applying Dubinin-Astakhov (DA) analysis.

[e] The mesopore size distribution (D_{BJH}) calculated from the desorption isotherm by the Barrett-Joyner-Halenda (BJH) method.

[f] D_{HK} represents the micropore size by the Horvath-Kawazoe (HK) method.

[g] Pore size was estimated by TEM images.

Based on our understanding of the formation mechanism of the Mg-*aph*-MOF, we speculate that the thermal conversion conditions such as gas flow rate and temperature ramping rate can be critical factors for determining the size of the organic vesicles, which consequently control the nanopore size. For instance, when Mg-*aph*-MOF was thermally treated with a ten-fold faster ramping rate (50 ^{o}C/min), nanoporous MgO with a much smaller pore size (~ 20 nm) (*np*-MgO-500-*fast T*, Figure 2.26a) than that of *np*-MgO-500 (~ 50 nm) (Figure 2.26b) was obtained, which was due to the fast transport and removal of organic vesicles before they could congregate. In contrast, thermal treatment of Mg-*aph*-MOF under static nitrogen atmosphere without flow promoted the growth of the organic vesicles, thus resulting in larger pores, around 100 nm (*np*-MgO-500-*no flow*, Figure 2.26c). Nitrogen isotherm results also supported the synthesis of pore size-controlled MgO nanostructures (Figures 2.26d to f). Since the rapid escape of small organic vesicles in MgO synthesized with rapidly increasing temperature rates (Figure 2.26a) generated high proportion of the micropores as well as mesopores, the BET isotherm showed a large uptake at pressures below 0.01 atm, and the pore volume for the micropores reached 0.20 cc/g out of a total pore volume of 0.589 cc/g.

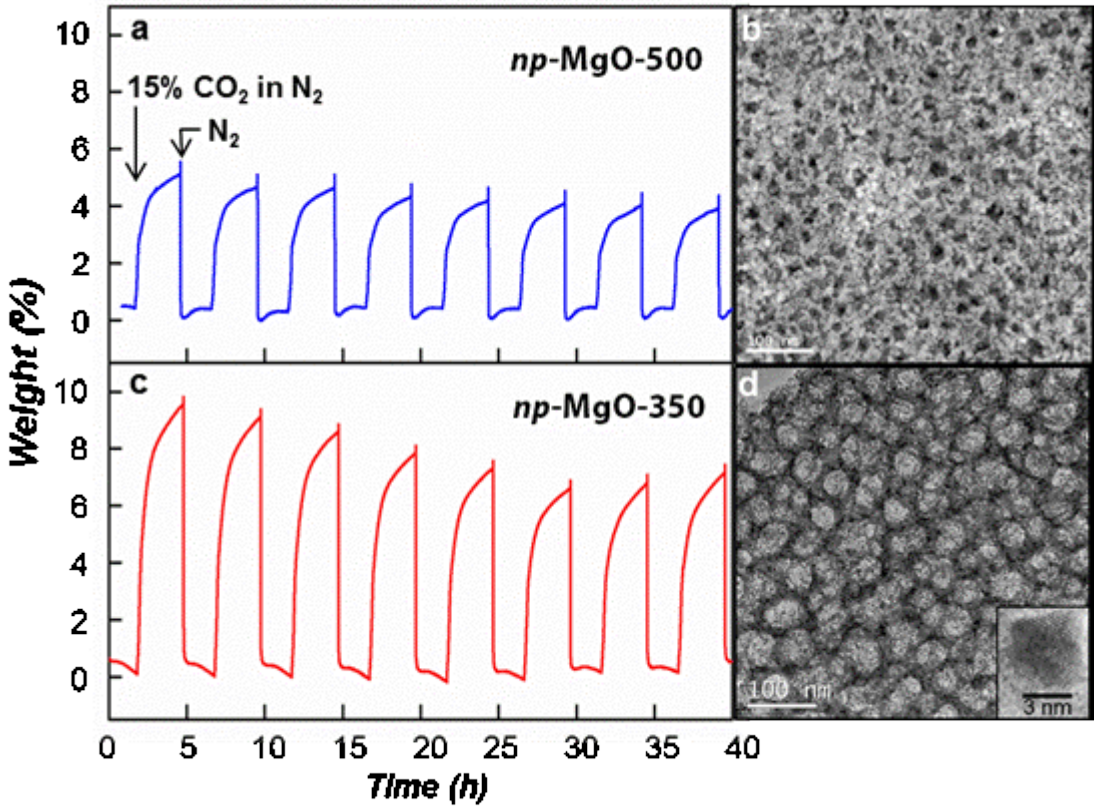

Figure 2.27 Studies of *np*-MgO upon carbon dioxide gas cycling experiment. (a) and (c) Gas cycling result, and (b) and (d) TEM image after the cycles for *np*-MgO-500 and *np*-MgO-350, respectively.

To explore the advantages of the hierarchically nanoporous MgO with a nanocrystalline framework, we studied the behaviour of *np*-MgO in a carbon dioxide gas cycling experiment using a TGA apparatus with a flow of 15% (v/v) CO_2 in N_2, which mimicked flue gas. As-prepared *np*-MgO-500 absorbed 5.2 wt% CO_2 at 27 ^oC (Figure 2.27a). After eight cycles of CO_2 adsorption/desorption over *np*-MgO-500, TEM images showed that the nanocrystalline framework became aggregated, generating secondary nanoparticles. Also, the nanopores (ca. 100 nm) in the as-prepared *np*-MgO-500 were reduced to around 20 nm in size (Figure 2.27b). The small carbon content (1.76 wt%) in *np*-MgO-500 was inadequate to sustain the hierarchically nanoporous MgO structure during the several cycles of adsorption/desorption, because *np*-MgO-500 suffers from significant changes in the crystal systems between MgO (cubic) and $MgCO_3$ (trigonal). To increase the carbon content as an adhesive and protectant, but to still provide the hierarchical structure, the thermal treatment of Mg-*aph*-MOF was conducted at a lower temperature, 350 ^oC, for 12 h under inert atmosphere. The resultant solid, designated as *np*-MgO-350, was a nanoporous, dark brown solid with a carbon content of 10 wt%. The BET surface area was 160 m^2/g

(Figure 2.28). As shown in Figure 2.27c, the CO_2 uptake capacity of *np*-MgO-350 at 27 ^oC was much higher than *np*-MgO-500 at 9.2 wt%, which was the highest recorded value for MgO nanomaterials under similar conditions,[30-32] and was 12 times better than commercially available 50 nm-sized-MgO powder (0.76 wt%) (Table 2.4 and Figure 2.29). More importantly, even after eight cycles of CO_2 adsorption/desorption, the hierarchically nanoporous structures of *np*-MgO-350 remained intact, as evidenced by TEM (Figure 2.27d). Since acidic CO_2 molecules are adsorbed at low-coordinated and basic O^{2-}–Mg^{2+} sites on MgO, a high surface area which provides many edge- and corner-located oxygen atoms is critical to the CO_2 capacity of MgO adsorbents.[33,34] Therefore, in the present work, hierarchically porous MgO prepared by our MOF-driven method assured superior performance associated with facile mass transport and recyclability. In addition, the large population of surface states on the MgO nanocrystals comprising the framework wall allowed a low regeneration temperature of 300 ^oC, which affords a definite advantage for practical application.

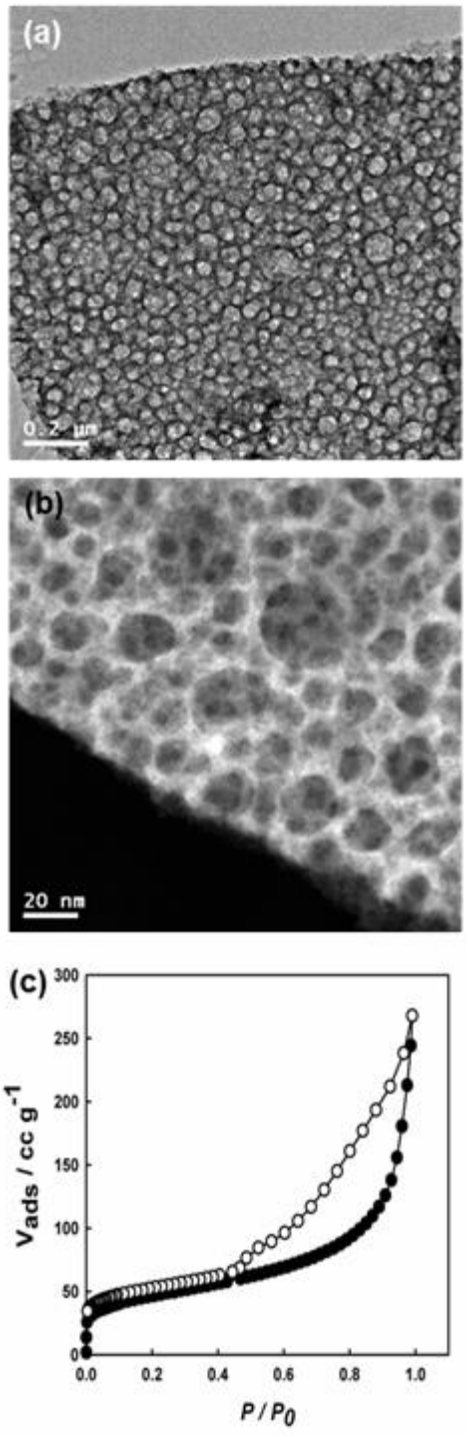

Figure 2.28 Characterizations of *np*-MgO-350. (a) HR-TEM image, (b) dark-field TEM image, and (c) BET data.

Table 2.4 CO_2 sorption capacities over MgO sorbents from the literature.

sorbent	CO_2 adsorption temperature (°C)	desorption temperature (°C)	adsorption capacity (%)	CO_2 gas concentration (%)	Ref.
np-MgO-350	27	500	9.2	14.95	*Pre-sent work*
	27	300	6.4	14.95	
	50	500	6.4	14.95	
	75	500	4.7	14.95	
	100	500	4.2	14.95	
	150	500	3.0	14.95	
np-MgO-500	27	500	5.2	14.95	
	50	500	3.6	14.95	
	75	500	2.9	14.95	
	100	500	2.6	14.95	
	150	500	2.1	14.95	
Commercially available MgO powder (< 50 nm)	27	500	0.76	14.95	
MgO-NP1	60	60	0.7	99.99	*30*
	600	600	0.54	99.99	
MgO-NP2	60	60	0.22	99.99	
	600	600	0.04	99.99	
Mesoporous MgO	25	800	8.0	99.99	*31*
	100	800	10.0	99.99	
MgO	0	-	2.8	20.0	*32*
	100	-	1.9	20.0	

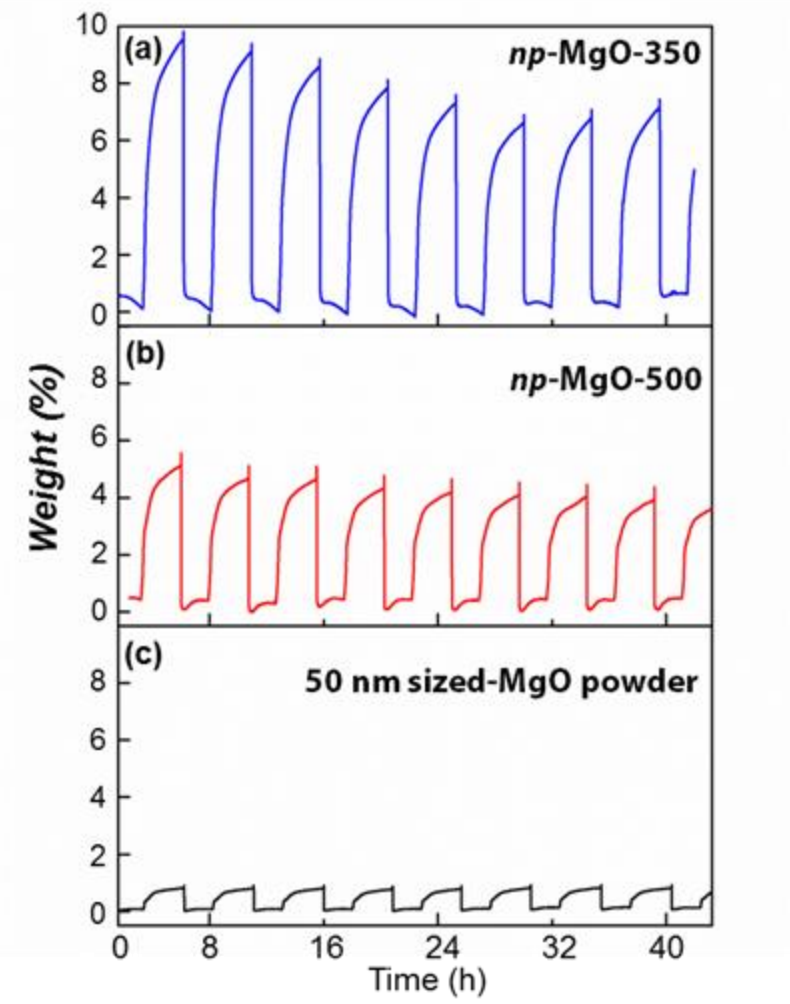

Figure 2.29 Comparison of CO_2 gas sorption cycling results of (a) *np*-MgO-350, (b) *np*-MgO-500, and (c) commercially available 50 nm sized-MgO powder.

2.4 Conclusion

In conclusion, we synthesized nanostructured metal oxide via thermal transformation of MOFs. By using the pseudomorphic conversion, we prepared plate-like and rod-like aggregates comprised of Co_3O_4 nanoparticles. The precursor MOFs were built from Co^{2+} and BDC^{2-} ions, however due to the different reaction conditions, the resulting structures were different from each other even if the framework scaffolds were same. After two-step thermal treatments of their Co-MOFs, the resulting Co_3O_4 nanoparticles had almost same sizes and shapes. However, the macrostructure as well as the defects or void spaces in the aggregates were quite different. The different packing of nanoparticles affects their electrochemical properties as anodes in the lithium ion batteries. Furthermore, by employing labile aliphatic ligand into Mg-based MOF, we synthesized highly nanoporous MgO with nanocrystalline framework. As evidenced as HRTEM images and pyrolysis GC/MS analysis, we found that the aliphatic adipate linker in the MOF acted as a pore-directing agent via forming vesicles during thermal conversion. With these understanding of Mg-*aph*-MOF conversion, the porosity of resultant MgO could be adjusted by controlling thermolysis conditions such as ramping rates and temperatures.

2.5 References

1. Hu, L.; Chen, Q. Hollow/Porous Nanostructured Derived Fromm Nanoscale Metal-Organic Frameworks towards High Performance Anodes for Lithium-Ion Batteries. *Nanoscale* **2014**, *6*, 1236-1257.
2. Mahmood, A.; Guo, W.; Tabassum, H.; Zou, R. Metal-Organic Framework-Based Nanomaterials for Electrocatalysis. *Advanced Energy Materials* **2016**, *6*, 1600423.
3. Kim, T. K.; Lee, K. J.; Cheon, J. Y.; Lee, J. H.; Joo, S. H.; Moon, H. R. Nanoporous Metal Oxides with Tunable and Nanocrystalline Frameworks via Conversion of Metal-Organic Frameworks *Journal of the American Chemical Society* **2013**, *135*, 8940-8946.
4. Lyu, Y.-Y.; Yi, S. H.; Chon, J. K.; Chang, S.; Pu, L. S.; Lee, S.-Y.; Yie, J. E.; Char, K.; Stucky, G. D.; Kim, J. M. Highly Stable Mesoporous Metal Oxides Using Nano-Propping Hybrid Gemini Surfactants. *Journal of the American Chemical Society* **2004**, *126*, 2310-2311.
5. Schüth, F. Non-siliceous Mesostructured and Mesoporous Materials. *Chemistry of Materials* **2001**, *13*, 3184-3195.
6. Buonsanti, R.; Pick, T. E.; Krins, N.; Richardson, T. J.; Helms, B. A.; Milliron, D. J. Assembly of Ligand-Stripped Nanocrystals into Precisely Controlled Mesoporous Architectures. *Nano Letters* **2012**, *12*, 3872-3877.
7. Murry, L. J.; Dincă, M.; Long, J. R. Hydrogen Storage in Metal–Organic Frameworks. *Chemical Society Reviews* **2009**, *38*, 1294-1314.
8. Ma, L.; Falkowski, J. M.; Abney, C.; Lin, W. A Series of Isoreticular Chiral Metal-Organic Frameworks as a Tunable Platform for Asymmetric Catalysis. *Nature Chemistry* **2010**, *2*, 838-846.
9. Arvai, A. J.; Nielsen, C. *ADSC Quantum-210 ADX program*; Area Detector System Corp.; Poway, CA, 1983.
10. *Fit2D* program: Andy Hammersley (e-mail: hammersley@esrf.fr), ESRF, 6 rue Jules Horowitz, BP 220, 38043 Grenoble Cedex 9, France.
11. Otwinowski, Z.; Minor, W. In *Methods in Enzymology*; Carter C. W.; Jr., Sweet, R. M., Eds.; Academic Press: New York, 1997; Vol. *276*, Part A, p 307.
12. Rapid Auto software, R-Axis series, Ca. No. 9220B101, Rigaku Corporation
13. Sheldrick, G. M. Phase annealing in SHELX-90: direct methods for larger structures. *Acta Crystallographica Section A* **1990**, *A46*, 467-473.
14. Sheldrick, G. M. *SHELXL97, Program for the crystal structure refinement*; University of Göettingen: Göettingen, Germany, 1997.
15. Sheldrick, G. M. *SHELXTL-PLUS, Crystal Structure Analysis Package*; Bruker Analytical X-ray: Madison, WI, 1997.
16. Sluis, P.v.d.; Speck, A. L. BYPASS: an effective method for the refinement of crystal structures

containing disordered solvent regions. *Acta Crystallographica Section A* **1990**, *A46*, 194-201.

17. Luo, F.; Che, Y.; Zheng, J. Trinuclear Cobalt Based Porous Coordination Polymers Showing Unique Topological and Magnetic Variety upon Different Dicarboxylate-like Ligands. *Crystal Growth and Design* **2009**, *9*, 1066-1071.
18. Rosi, N. L.; Kim, J.; Eddaoudi, M.; Chen, B.; O'Keeffe, M.; Yaghi, O. M. Rod Packings and Metal−Organic Frameworks Constructed from Rod-Shaped Secondary Building Units *Journal of the American Chemical Society* **2005**, *127*, 1504-1518.
19. Bravais, A. *Etudes Cristallographiques*; Gauthier Villars: Paris, 1866.
20. Friedel, G. *Bull. Soc. Franc. Mineral.,* **1907**, *30*, 326-455.
21. Donnay, J. D. H.; Harker, D. A new law of crystal morphology extending the Law of Bravais. *American Mineralogist* **1937**, *22*, 446-467.
22. Laruelle, S.; Grugeon, S.; Poizot, P.; Dolle, M.; Dupont L.; Tarascon, J.-M. On the Origin of the Extra Electrochemical Capacity Displayed by MO/Li Cells at Low Potential. *Journal of The Electrochemical Society* **2002**, *149*, A627-A634.
23. Poizot, P.; Laruelle, S.; Grugeon, S.; Dupont, L.; Tarascon, J.-M. Nano-sized Transition-Metal Oxides as Negative-Electrode Materials for Lithium-Ion Batteries. *Nature*, **2000**, *407*, 496-499.
24. Jiao, F.; Bao, J.; Bruce, P. G. Factors Influencing the Rate of Fe_2O_3 Conversion Reaction. *Electrochemical and Solid-State Letters* **2007**, *10*, A264-A266.
25. Lu, Y.; Wang, Y.; Zou, Y.; Jiao, Z.; Zhao, B.; He, Y.; Wu, M. Macroporous Co_3O_4 Platelets with Excellent Rate Capability as Anodes for Lithium Ion Batteries. *Electrochemistry Communications* 2010, **12**, 101-105.
26. Yang, S. J.; Park, C. R. Preparation of Highly Moisture-Resistant Black-Colored Metal Organic Framework. *Advanced Materials* **2012**, *24*, 4010-4013.
27. Parast, M. S. Y.; Morsali, A. Synthesis and Characterization of Porous Al(III) Metal-Organic Framework Nanoparticles as a New Precursor for Preparation of Al_2O_3 Nanoparticles. *Inorganic Chemistry Communication* **2011**, *14*, 645-648.
28. Cho, W.; Park, S.; Oh, M. Coordination Polymer Nanorods of Fe-MIL-88B and Their Utilization for Selective Preparation of Hematite and Magnetite Nanorods. *Chemical Communications* **2011**, *47*, 4138-4140.
29. Davies, R. P.; Less, R. J.; Lickiss, P. D.; White, J. P. Framework Materials Assembled from Magnesium Carboxylate Building Units. *Dalton Transactions* **2007**, 2528-2535.
30. Ruminski, A. M.; Jeon, K.-J.; Urban, J. J. Size-Dependent CO_2 Capture in Chemically Synthesized Magnesium Oxide Nanocrystals. *Journal of Materials Chemistry* **2011**, *21*, 11486-11491.
31. Bhagiyalakshmi, M.; Lee, J. Y.; Jang, H. T. *Synthesis of Mesoporous Magnesium Oxide: Its Application to CO_2 Chemisorption. International Journal of the Greenhouse Gas Control* **2010**, *4*, 51-56.

32. Gregg, S. J.; Ramsay, J. D. Adsorption of Carbon Dioxide by Magnesia Studied by Use of Infrared and Isotherm Measurements. *Journal of the Chemical Society A* **1970**, 2784-2787.
33. Meis, N.; Bitter, J. H.; de Jong, K. P. Support and Size Effects of Activated Hydrotalcites for Precombustion CO_2 Capture. *Industrial and Engineering Chemistry Research* **2010**, *49*, 1229-1235.
34. Daub, C. D.; Patey, G. N.; Jack, D. B.; Sallabi, A. K. Monte Carlo Simulations of the Adsorption of CO_2 on the MgO(100) Surface. *The Journal of Chemical Physics* **2006**, *124*, 114706.
35. Lee, K. J.; Kim, T.-H.; Kim, T. K.; Lee, J. H.; Song, H.-K.; Moon, H. R. Preparation of Co3O4 electrode materials with different microstructures via pseudomorphic conversion of Co-based metal-organic frameworks. *Journal of Materials Chemistry A* **2014**, *2*, 14393.
36. Kim, T. K.; Lee, K. J.; Cheon, J. Y.; Lee, J. H.; Joo, S. H.; Moon, H. R. Nanoporous Metal Oxides with Tunable and Nanocrystalline Frameworks via Conversion of Metal-Organic Frameworks. *Journal of the American Chemical Society* **2013**, *135*, 8940.

Chapter III. Three-dimensional mesoporous graphene

3.1 Introduction

Porous carbon materials have attracted tremendous interest, due to their numerous potential applications in gas adsorption[1], energy storage[2-4], and catalysis[5-7]. In particular, given the high porosity of carbon combined with graphitic frameworks, the resulting materials are expected to have excellent electrochemical and mechanical properties[8,9], and high thermal conductivity[10]. Of several forms of graphitic porous carbons, 3D porous graphene represents the most desirable structure to possess prominent properties such as high conductivity and large surface area. While ideal graphene is composed of a single layer of sp^2 hybridized carbon atoms with a high theoretical surface area (2630 $m^2 g^{-1}$), its strong stacking affinity via infinite π-π interactions hampers the full utilization of its intrinsic properties in practical applications.[8,11] With the purpose of integrating the functionality of 2D graphene sheet with structural complexity, multidirectional efforts have been carried out to synthesize 3D porous graphene networks. For instance, Chen *et al.* reported the synthesis of graphene foams in template-directed chemical vapor deposition (CVD) using nickel foam as both a template and catalyst.[12] Similarly, 3D porous graphene networks have been prepared by CVD in the presence of templates such as 3D assembled colloidal silica[13] and porous MgO,[14] with additional catalysts for graphitization. However, such template-assisted CVD methods are commonly unsuitable for large-scale syntheses and require cumbersome template preparation steps. The alternative approach is the assembly of chemically derived graphene such as graphene oxide (GO) and reduced graphene oxide (rGO), followed by activation steps.[15-17] Despite the potential advantage of mass production, this method might yield the lower electrochemical performances unavoidably caused by significant damages of GO and rGO surfaces. Another method is the hybridization of graphene with organic or inorganic materials as spacers between the graphene layers.[18-21] However, this approach is susceptible to the restacking of 2D graphene layers due to low pillar densities as compared to 2D graphene area.[21]

Recently, the conversion of MOFs as precursors to nanostructured carbon materials has attracted tremendous interest, caused by their numerous potential applications in gas sorption, energy storage and catalysis.[22-26] The versatility in the chemical and physical properties of MOFs can realize carbon materials with different structures and properties. A representative example is the use of a series of IR-MOFs constructed using Zn(II) and ditopic aromatic carboxylates as precursors for the synthesis of amorphous carbon materials.[27] These materials exhibit hierarchically porous structures with a large surface area and high pore volume, resulting from the evaporation of evolved species such as Zn metals and organic molecules. In this study, IR-MOFs of different organic ligands were converted to porous carbon with different textural properties.

The formation of nanostructured carbon derived from MOFs is governed by the type of metal species and organic ligands that comprise the MOFs, because the metal species generated during thermal conversion strongly affect the structures of the carbon resulting from the transformation of decomposed ligands. Thus, it is imperative to understand the formation mechanism of the resultant materials so as to enable the preparation of carbon with well-tailored nanostructures. The Yamauchi group has reported the synthesis of a hybrid carbon material, which consists of nitrogen-doped carbon as the core and graphitic carbon as the shell, by the thermal conversion of core–shell-structured ZIF-8.[28] In the parent core–shell MOF of the study, the metal ions are different with Zn^{2+} and Co^{2+} constituting the core and shell, respectively, and each metal species evolved by thermolysis produces carbon with different graphitic degrees, caused by those different chemical reactivity with the organic species. Although interesting results regarding the synthesis of new materials by the conversion of MOFs have been reported,[29-32] the fundamental phenomenon of conversion during thermolysis is still not completely understood. Moreover, some researchers have claimed that the dimensionality and structure of MOFs are important factors in the thermally converted materials.[33,34] However, this claim is applicable only for a specific group of MOFs, which follows the same conversion mechanism. To affirm the relationship between the intrinsic nature of the parent MOFs and the converted materials, more diverse coordination compounds need to be examined. Hence, it is worthwhile to examine the conversion of small molecule metal complexes as well as MOFs to nanostructured materials. Therefore, in this chapter we will deal with coordination compounds as well as metal-organic frameworks.

Herein, we report our discovery that the direct thermal conversion of Ni(II) coordination complexes followed by etching can yield 3D mesoporous graphene (*meso*G) structure. This method is extremely simple, readily scalable up to the gram scale, and can proceed without the use of additional templates and catalysts or CVD as shown in Figure 3.1.[58] A Ni(II) ion and hexadentate hydrocarbon ligand were selected for the synthesis of the precursor coordination compound. During the thermal conversion of the Ni(II) complex under an inert atmosphere, the Ni(II) ionic centers are transformed *in situ* into 4 nm-sized Ni NPs, which act as catalysts for the C-C bond cleavage and graphitization of amorphous carbon from organic ligands and also serve as a template for the creation of mesopores. The resulting 3D *meso*G is composed of a 3D interconnected structure of hollow carbon shells comprised of 3 – 4 graphene layers. The 3D *meso*G features very uniform mesopore (~ 4 nm in diameter), a large surface area, and a very high C/O ratio. Varying the ligands with different physical and chemical stabilities leads 3D *meso*G to different structural properties, including its pore and graphitization degree.

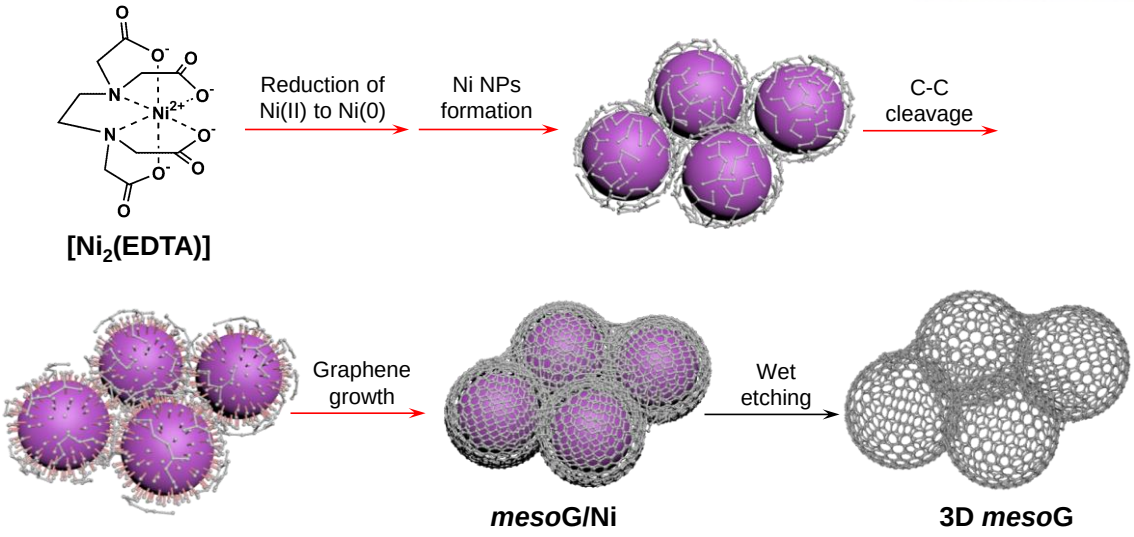

Figure 3.1 Schematic of the thermal conversion of [Ni_2(EDTA)] into three-dimensional mesoporous graphene, 3D *meso*G. [Ni_2(EDTA)] powder was heated at 10 $^oC\ min^{-1}$ to 1000 ^oC under a nitrogen flow of 500 mL min^{-1}. During this time, the Ni(II) centres were reduced to Ni(0) metals, which agglomerated to form Ni NPs. Simultaneously, carbogenic species from the EDTA ligand generated carbon and hydrogen atoms on the surface of hot Ni NPs. Because Ni NPs are suitable catalysts for sp^2 carbon formation as well as sp^3 C-C bond cleavage, the evolved carbon atoms formed high-quality graphene shells on the Ni NPs (*meso*G/Ni). The processes indicated by red arrows occurred during the one-step heat treatment of [Ni_2(EDTA)]. After etching the remaining Ni contents, 4 nm-sized mesoporous graphene with a 3D network (3D *meso*G) was obtained.

3.2 Experimental section

Characterization Methods. All chemicals and solvents were of reagent grade and were used without further purification. Infrared spectra were recorded using a ThermoFisher Scientific iS10 FT-IR spectrometer. Raman spectroscopy measurements were performed using a micro-Raman system (WITec) with an excitation energy of 2.41 eV (532 nm). Elemental analyses were performed at the UNIST Central Research Facilities Center (UCRF) at Ulsan National Institute of Science and Technology (UNIST). UV/Vis spectra were recorded with a Cary 5000 UV/vis spectrophotometer. Fluorescence spectra were measured with a Cary Eclipse fluorescence spectrometer. TGA was performed under N_2(g) at a scan rate of 10 ^oC min^{-1}, using a TGA Q50 from TA instruments. X-ray powder diffraction data were recorded on a Bruker D2 phaser diffractometer at 30 kV and 10 mA for Cu Kα (λ = 1.54050 Å), with a step size of 0.02º in 2θ. N_2 sorption isotherms of *meso*G/Ni and 3D *meso*G were obtained using a BELSORP-max at 77 K. Prior to the adsorption measurements, the samples were evacuated ($p < 10^{-5}$ mbar) at 100 ^oC for 4 h. The specific surface area was determined in the relative pressure range from 0.05 to 0.3 of the Brunauer-Emmett-Teller (BET) plot, and the total pore volume was calculated from the amount adsorbed at a relative pressure of about 0.98-0.99. TEM images were obtained using a JEOL JEM-2100F microscope. AR-TEM images were collected using an image-side spherical aberration corrected TEM (Titan^3 G2 60-300, FEI Company, Netherlands), operated at 80 kV.

Synthesis

Preparation of [Ni_2(EDTA)]. a DMF (20 mL) solution of $Ni(NO_3)_2{\cdot}6H_2O$ (1.16 g, 4.0 mmol) was added to a DMF (30 mL) solution of H_4EDTA (0.59 g, 2.0 mmol) and triethylamine (1.5 mL, 10.8 mmol). A precipitate formed soon after the two solutions were mixed. The resulting solid was filtered and washed with neat DMF. After drying in vacuo at room temperature overnight, blue powder was obtained. Yield: 1.15 g (95%). Elemental analysis (percentage calculated, percentage found for $[Ni_2(EDTA)]{\cdot}1.5DMF{\cdot}5H_2O$, $Ni_2C_{14.5}H_{32.5}N_{3.5}O_{14.5}$): C (28.77, 28.92), H (5.41, 4.26), N (8.10, 8.06). Infrared (KBr): ν = 3373 cm^{-1} (O-H); ν = 2975, 2940 cm^{-1} (aliphatic C-H); ν = 1660 cm^{-1} (C=O, DMF); ν = 1590, 1403 cm^{-1} (carboxylate); ν = 482 cm^{-1} (Ni-N).

Preparation of $[Ni(EN)_3](NO_3)_2$ (EN = *N,N'*-ethylenediamine). $[Ni(EN)_3](NO_3)_2$ was prepared using a modified version of previously reported method1. $Ni(NO_3)_2{\cdot}6H_2O$ (1.16 g, 4 mmol) was dissolved in distilled water (2 mL). To the solution 98% ethylenediamine (0.8 mL, 12 mmol) was added slowly. After evaporating the solvent slowly at room temperature, violet crystals (1.07 g) were obtained. Infrared (KBr): ν = 3332 cm^{-1} (N-H); ν = 2955, 2942 cm^{-1} (aliphatic C-H); ν = 1383, 826 cm^{-1} (free NO_3^-); ν = 437 cm^{-1} (Ni-N).

Preparation of [Ni(adipate)]. A DMF (20 mL) solution of $Ni(NO_3)_2 \cdot 6H_2O$ (1.16 g, 4.0 mmol) was added to a DMF (20 mL) solution of adipic acid (0.59 g, 4.0 mmol) and triethylamine (1.5 mL, 10.8 mmol). The mixture was stirred for 5 minutes, resulting in a green precipitate. The resulting solid was filtered, and washed with neat DMF. After drying in vacuo at room temperature overnight, 1.42 g of a green powder was obtained. Infrared (KBr): ν = 3389 cm^{-1} (O-H); ν = 2937, 2870 cm^{-1} (aliphatic C-H); ν = 1661 cm^{-1} (C=O, DMF); ν = 1583, 1387 cm^{-1} (carboxylate).

Preparation of [Ni(BDC)] (BDC^{2-} = 1,4-benzenedicarboxylate). A DMF (20 mL) solution of $Ni(NO_3)_2 \cdot 6H_2O$ (1.16 g, 4.0 mmol) was added to a DMF solution (20 mL) of H_2BDC (0.66 g, 4.0 mmol) and triethylamine (1.5 mL, 10.8 mmol). The mixture was stirred for 5 min, resulting in a green precipitate. The resulting solid was filtered, and washed with neat DMF. After drying in vacuo at room temperature overnight, 1.44 g of a green powder was obtained. Infrared (KBr): ν = 3386 cm^{-1} (O-H); ν = 3069, 2933 cm^{-1} (aromatic C-H); ν = 1656 cm^{-1} (C=O, DMF); ν = 1586, 1386 cm^{-1} (carboxylate).

Preparation of $[Fe_4(EDTA)_3]$. An aqueous solution (1 mL) of $Fe(NO_3)_3 \cdot 9H_2O$ (0.6 g, 1.5 mmol) was added to a solution of H_4EDTA (0.29 g, 1.0 mmol) and triethylamine (1.0 mL, 7.2 mmol). The mixture was stirred for 5 min, resulting in a brown precipitate. The solid was collected by centrifugation and washed with ethanol several times. After drying in vacuo at room temperature overnight, 0.03 g of a brown powder was obtained. Infrared (KBr): ν = 3409 cm^{-1} (O-H); ν = 2967, 2916 cm^{-1} (aliphatic C-H); ν = 1628, 1383 cm^{-1} (carboxylate).

Preparation of $[Cu_2(EDTA)]$. A DMF (20 mL) solution of $Cu(NO_3)_2 \cdot 2.5H_2O$ (0.93 g, 4.0 mmol) was added to a DMF (30 mL) solution of H4EDTA (0.59 g, 2.0 mmol) and triethylamine (1.5 mL, 10.8 mmol). The mixture was stirred for 5 min, resulting in a blue precipitate. The solid was filtered, and washed with neat DMF. After drying in vacuo at room temperature overnight, 0.95 g of a blue powder was obtained. Infrared (KBr): ν = 3424 cm^{-1} (O-H); ν = 2973, 2938 cm^{-1} (aliphatic C-H); ν = 1606, 1385 cm^{-1} (carboxylate).

Preparation of $[Co_2(EDTA)]$. A DMF (20 mL) solution of $Co(NO_3)_2 \cdot 6H_2O$ (1.16 g, 4.0 mmol) was added to a DMF (30 mL) solution of H_4EDTA (0.59 g, 2.0 mmol) and triethylamine (1.5 mL, 10.8 mmol). The mixture was stirred for 5 min, resulting in a purple precipitate. The solid was filtered and washed with neat DMF. After drying in vacuo at room temperature overnight, 1.16 g of a pink powder was obtained. Infrared (KBr): ν = 3385 cm^{-1} (O-H); ν = 2969, 2922 cm^{-1} (aliphatic C-H); ν = 1591, 1385 cm^{-1} (carboxylate).

Thermolysis. All coordination complexes mentioned above were ground into fine powders and heated at 10 ^oC min^{-1} under a nitrogen flow of 500 mL min^{-1}. After the temperature reached 1000 ^oC, the material were maintained at that temperature for 1 h. After rapidly cooling to room temperature, black

powder were obtained. For the [Ni_2(EDTA)], by using the 1.15 g of powders 0.32 g of black powder (*meso*G/Ni) was obtained after thermolysis. Elemental analysis (percentage found for *meso*G/Ni): C (33.37), H (0.13), N (0.72), O (1.23).

Etching method. *meso*G/Ni composites obtained after the thermolysis of [Ni_2(EDTA)] were etched according to following procedure to obtain pure 3D *meso*G materials[9]: 1 M $FeCl_3 \cdot 6H_2O$ (8 mL) and 1 M HCl (8 mL) were added to a vial containing the *meso*G/Ni (0.32 g). The mixture was heated at 80 °C for 3 h. After cooling to room temperature, the solid product was collected by centrifugation at 7000 rpm and was washed with distilled water several times. The product was dried in vacuo at room temperature overnight to yield a black powder (3D *meso*G, 0.99 g). Elemental analysis (percentage found for 3D *meso*G): C (91.63), H (0.35), N (1.71), O (2.22). For the *meso*G/Ni composites obtained after the thermolysis of [$Ni(EN)_3$](NO_3)$_2$, [Ni(adipate)], and [Ni(BDC)] were etched according to following procedure to obtain pure 3D *meso*G materials: 10 mL of conc. HNO_3 was added very slowly to a vial containing the target material (ca. 0.3 g). After the acid was added, the mixture was stirred at room temperature for 3 - 4 h. The remaining solid was collected by centrifugation at 7000 rpm for 1 h, washed several times with distilled water, and finally dried in vacuo at room temperature overnight.

3.3 Results and discussion

One of the Ni(II) coordination complexes can be readily prepared by a coordination reaction between Ni(II) ions and ethylenediaminetetraacetic acid (H_4EDTA), which contains multiple carboxylic acid and tertiary amine moieties. To completely deprotonate the carboxylic acid, *N*,*N*,*N*-triethylamine (TEA) was used as a base. Ni(II) was chelated by an EDTA ligand to form six coordination bonds with four oxygen

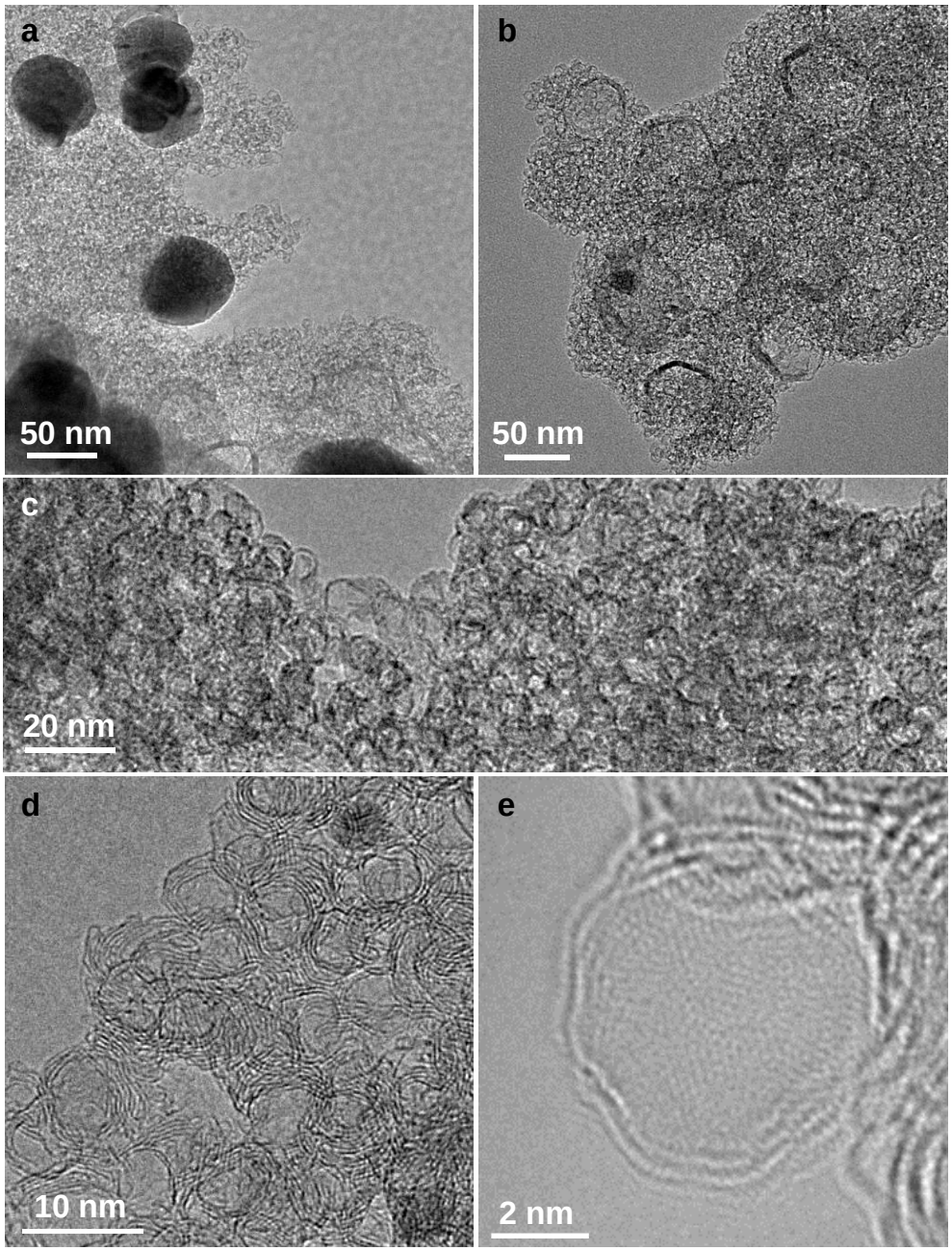

Figure 3.2 Structural characterization of *meso*G/Ni and 3D *meso*G. a, TEM image of *meso*G/Ni. b-e, TEM images of 3D *meso*G at various magnifications.

atoms of the carboxylates and two nitrogen atoms of the tertiary amines.[35] This coordination reaction results in the formation of [Ni_2(EDTA)], blue powder. [Ni_2(EDTA)] (1.15 g) was heated to 1000 ^oC at a ramping rate of 10 ^oC min^{-1} under a nitrogen flow of 500 mL min^{-1}. After maintaining the temperature at 1000 ^oC for 1 h, the solid was cooled to room temperature, resulting in 0.32 g of a black powder. Elemental composition analysis of the resulting powder revealed that during the thermolysis of [Ni_2(EDTA)], most H, N, and O contents were removed, while the all of the Ni and 30% of the C contents remained in the black powder (*meso*G/Ni, Table 3.1). Notably, this synthetic method can be readily scaled up, with few ten grams of the [Ni_2(EDTA)] precursor. Transmission electron microscopy (TEM) (Figure 3.2a) revealed that after the thermal treatment, the black powder was composed of 3D carbon materials and ~50 nm-sized Ni NPs (*meso*G/Ni). The Ni NPs could be removed by a wet etching process to obtain a metal-free carbon material (~0.1 g). Nearly 1 wt% of Ni remained in the 3D *meso*G even after etching, as evidenced by thermogravimetric analysis (TGA) under oxygen (Table 3.1 and Figure 3.5), indicating that several carbon shells completely surrounded the core Ni NPs. The 3D *meso*G also contained 1.7 wt% of nitrogen, originating from the EDTA ligands, and thus can be considered an N-doped carbon. Figures 3.2b - d show that the obtained carbon materials consisted of small hollow carbon shells in addition to large shells. A closer observation (Figure 3.2e) via atomic resolution TEM (AR-TEM) revealed that these small hollow carbon shells were composed of 3-4 layers of graphene with an inner diameter of ~4 nm, and were interconnected to produce the 3D nanostructured *meso*G. We note that even after etching the Ni NPs from hollow carbon, the 3D *meso*G structure did not collapse. Furthermore, elemental composition analysis of the 3D *meso*G (Table 3.1) revealed that etching with a strong acid had a negligible effect on the chemical state of the 3D *meso*G. Scanning electron microscopy (SEM) analysis of the 3D mesoG revealed the external microscopic morphology of the integrated graphene shells, and its macroscopic form of 1.05 g was taken as a photo (Figure 3.6).

Table 3.1 Elemental composition of [Ni_2(EDTA)], *meso*G/Ni, and 3D *meso*G.

Elements \ Materials		[Ni_2(EDTA)][a] (1.15 g)[b]	*meso*G/Ni (0.32 g)[b]	3D *meso*G (0.099 g)[b]
Ni	wt%	19.4	60.8[c]	1.38[c]
	Weight (g)	0.22	0.20	1.4×10^{-3}
C	wt%	28.77	33.37	91.63
	Weight (g)	0.33	0.11	0.091
H	wt%	5.41	0.13	0.35
	Weight (g)	0.062	4.2×10^{-4}	3.5×10^{-4}
N	wt%	8.10	0.72	1.71
	Weight (g)	0.093	2.3×10^{-3}	1.7×10^{-3}
O	wt%	38.33	1.23	2.22
	Weight (g)	0.44	3.9×10^{-3}	2.2×10^{-3}

[a] Calculated values based on the formula determined by elemental combustion analysis.

[b] Weight of the sample obtained by experiments mentioned in methods section.

[c] Calculated values from the amount of NiO, confirmed from TGA results obtained under an oxygen atmosphere (Figures 3.4 and 3.5).

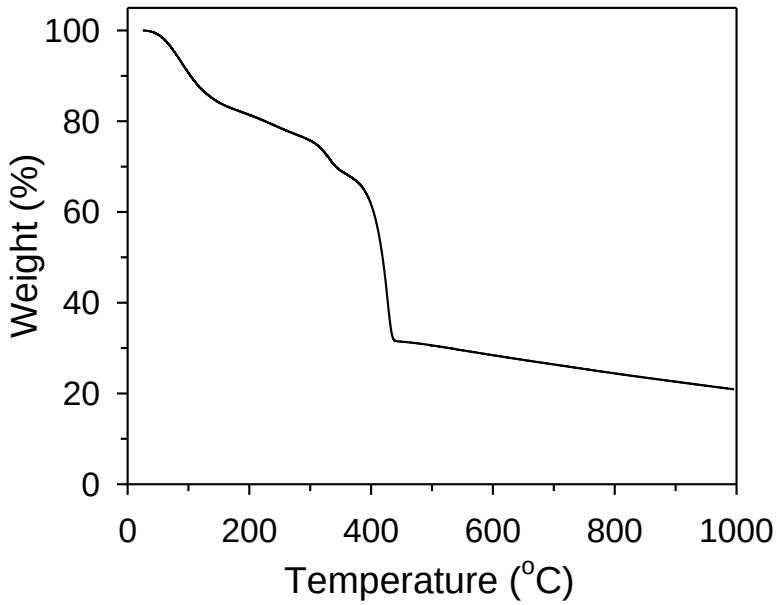

Figure 3.3 TGA trace of [Ni_2(EDTA)] obtained under a nitrogen atmosphere.

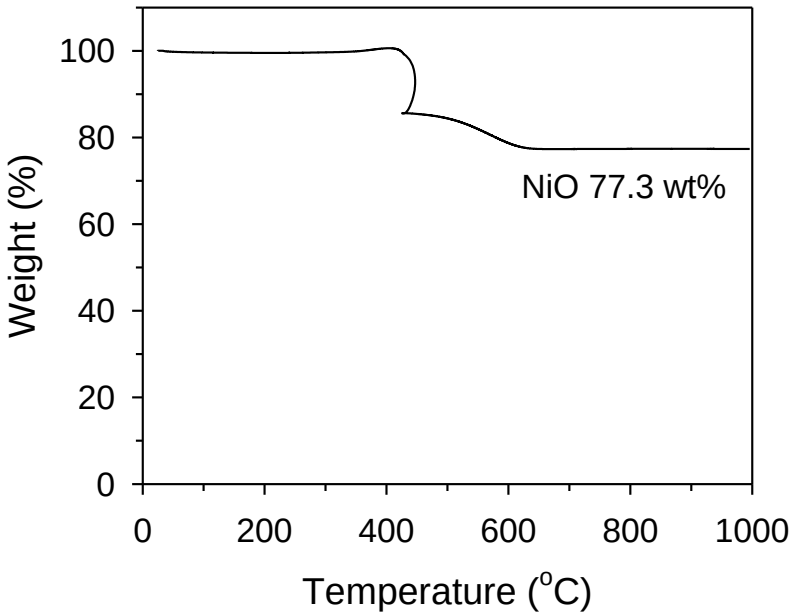

Figure 3.4 TGA trace of *meso*G/Ni obtained under an oxygen atmosphere. From the amount of the resultant solid (NiO), the Ni content in *meso*G/Ni was calculated to be 60.8 wt%.

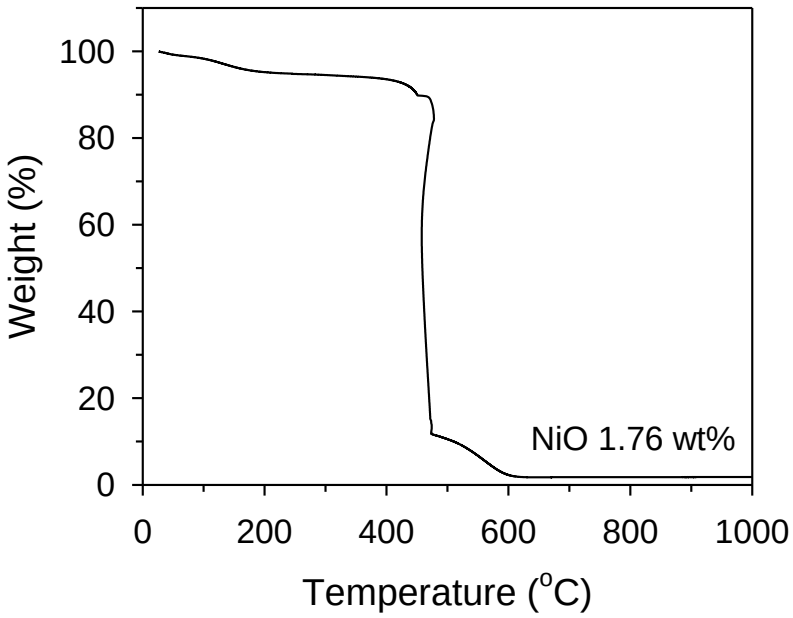

Figure 3.5 TGA trace of 3D *meso*G obtained under an oxygen atmosphere. From the amount of the resultant solid (NiO), the Ni content in 3D mesoG was calculated to be 1.38 wt%.

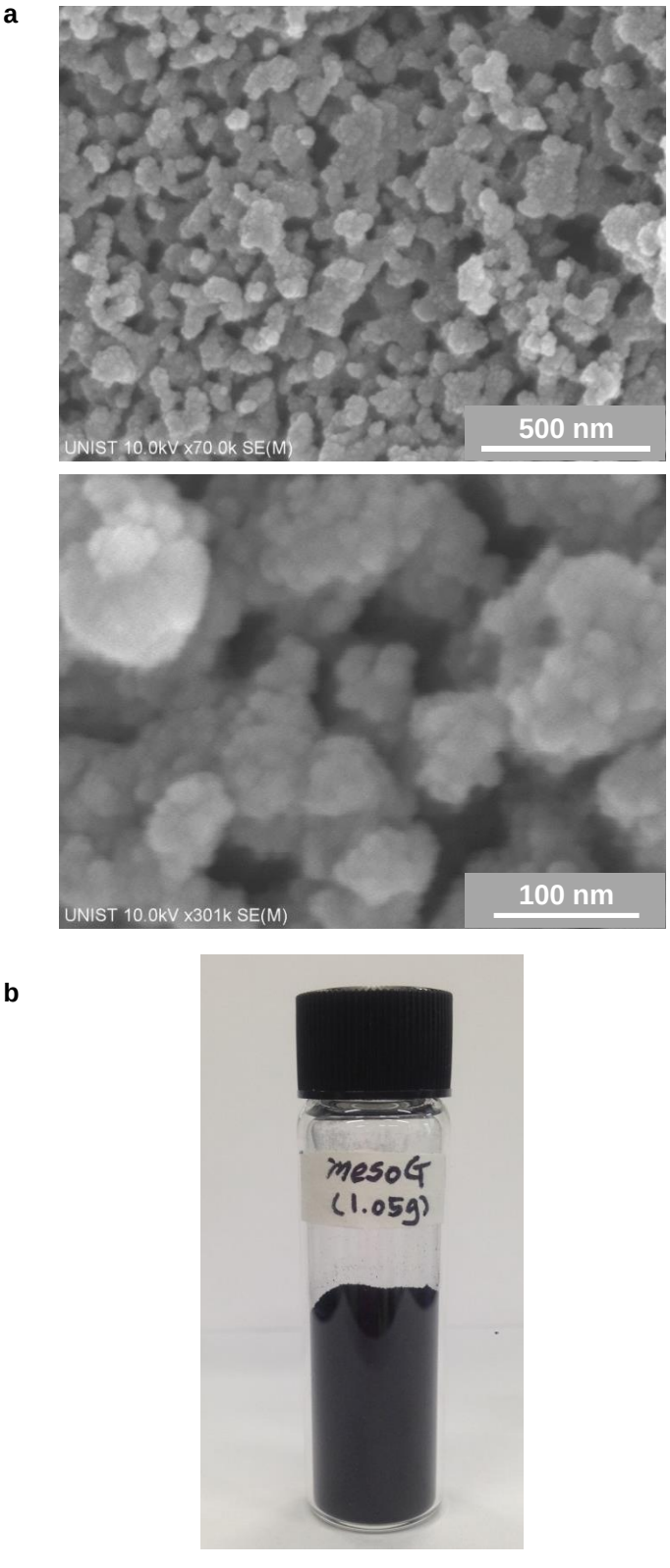

Figure 3.6 Micro- and macro-scopic analyses. a, SEM images of the 3D *meso*G. b, Photographic images of the 3D *meso*G (1.05 g).

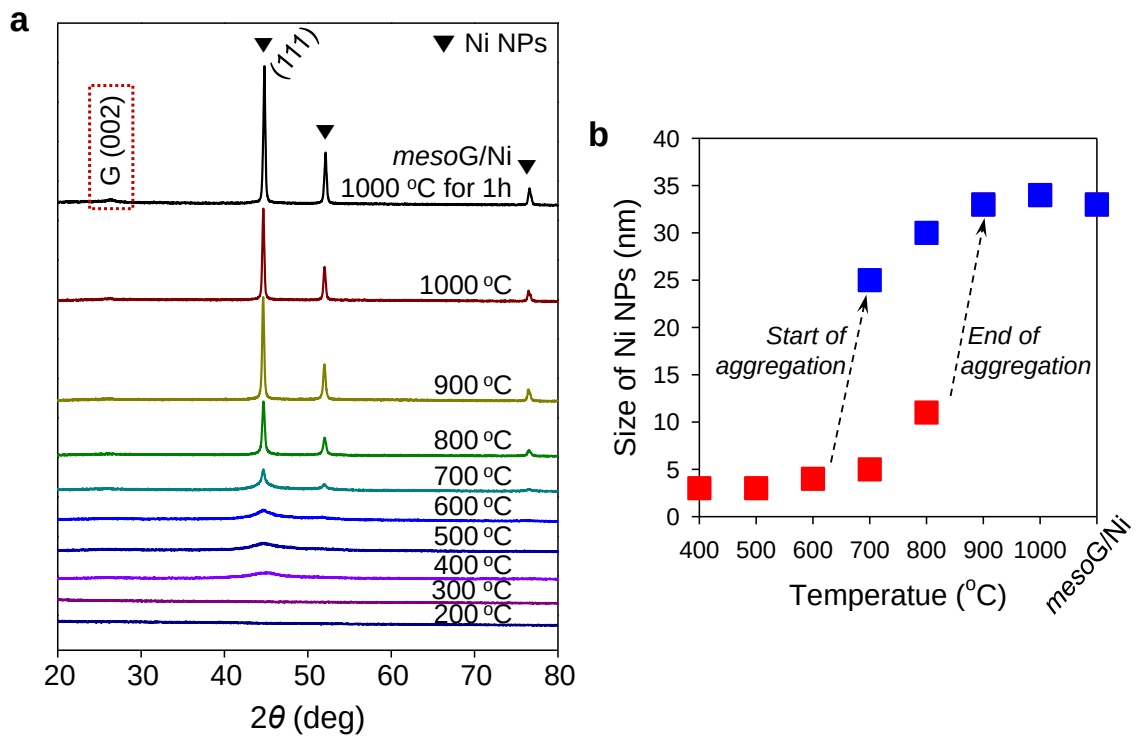

Figure 3.7 Temperature-dependent evolution of mesoporous graphene structures during thermal conversion of [Ni_2(EDTA)] to *meso*G/Ni. a, VT-XRPD data for [Ni_2(EDTA)]. b, Size of Ni nanoparticles calculated with (111) reflection. Red squares represent small NP, and blue squares represent large NPs.

To identify the origin of the formation of the hollow shell and 3D graphene structure, variable temperature X-ray powder diffraction (VT-XRPD) experiments were performed during the treatment of [Ni_2(EDTA)] (Figure 3.7a). When the temperature reached 400 °C, a broad peak around 2θ = 45° was detected. Upon further increase of the temperature, the peak at 45° became sharper with two newly evolved peaks at 52° and 76°, which were characteristic reflections of a cubic Ni(0) structure (JCPDS file no. 04-0850). When the temperature was further increased to 1000 °C, a very small but clear peak at 26° was observed, which was a typical (002) reflection of graphitic carbon. Figure 3.7b shows the size of Ni NPs at each temperature, estimated by applying the Debye-Scherrer equation to the (111) reflection. Below 600 °C, the size of the Ni NPs was less than 5 nm. However, above 700 °C, some of the small nanoparticles began to agglomerate to form larger Ni NPs (plotted as red and blue dots, respectively), as derived from the Debye-Scherrer equation with two deconvolved peaks of the (111) reflection. Subsequently, when the temperature reached 900 °C, the small Ni NPs stopped agglomerating, resulting in a single data point of ~35 nm-sized Ni NPs. The number of expected peaks for deconvolution was determined from TEM images obtained at each temperature (Figure 3.8). Since

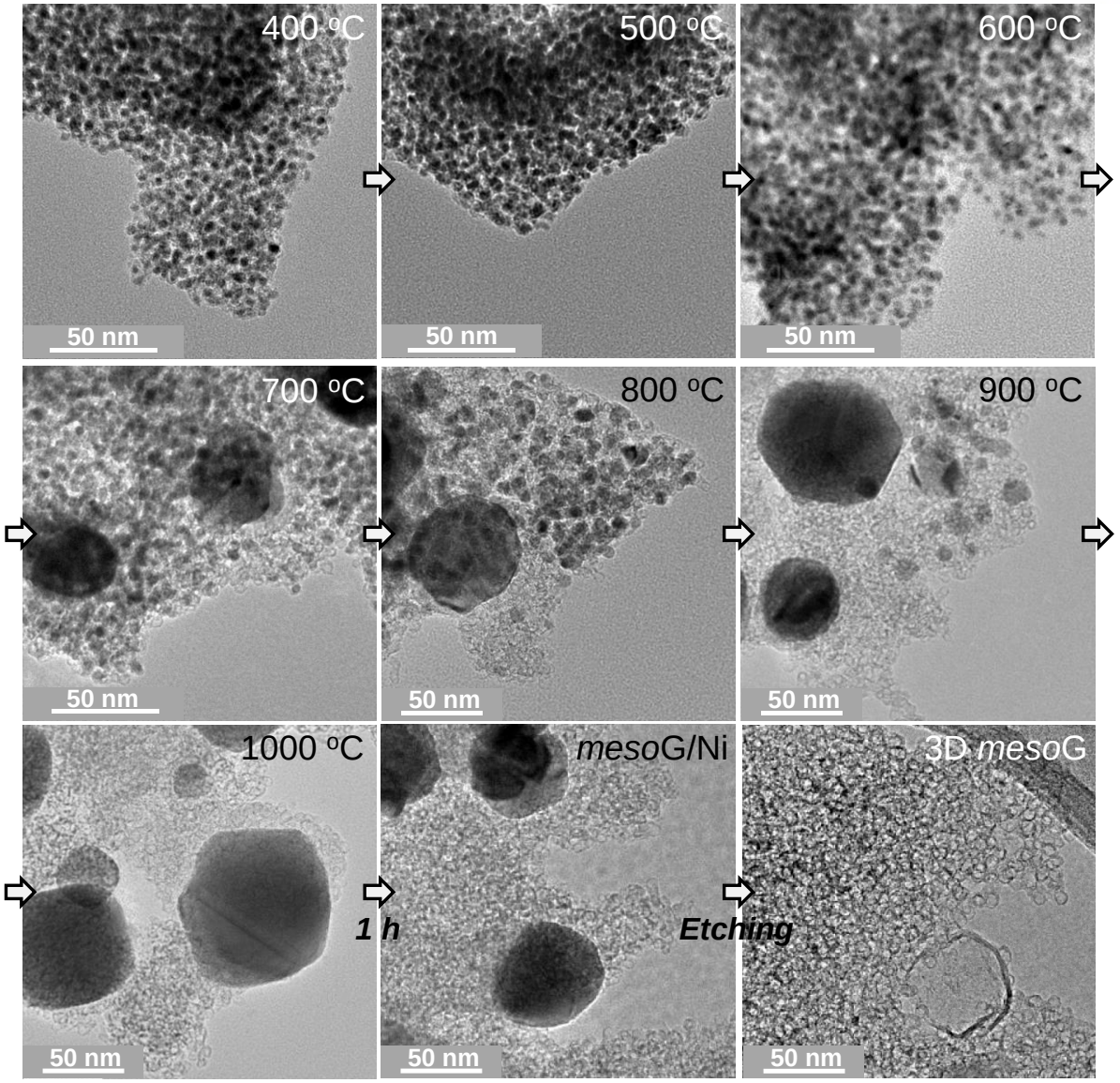

Figure 3.8 Temperature-dependent evolution of mesoporous graphene structures during thermal conversion of [Ni_2(EDTA)] to *meso*G/Ni. TEM images after heat treatment from 400 °C to 1000 °C with 100 °C increments.

the solids heated to less than 300 °C were very unstable under the e-beam during TEM analysis, images were obtained for samples treated at 400, 500, 600, 700, 800, 900, and 1000 °C. Similar to the XRPD results, when the temperature was 400 °C, Ni NPs embedded in the carbon matrix were formed. As the temperature increased, the shapes of the Ni NPs became more regular and crystalline, and had diameters less than 5 nm. Meanwhile, owing to the catalytic function of hot Ni NPs, organic species from EDTA began to decompose to carbon atoms, subsequently forming sp^2 carbons on the Ni NPs. This was a similar phenomenon to that observed in the growth of CNTs assisted by Ni catalysts.[36] In the present

system where Ni NPs are embedded within carbon layers, the total directional contact of carbon with Ni NP surfaces results in spherical shells rather than tubular structures. Therefore, the size of the in situ Ni NPs dictates the inner diameter of the hollow carbon. In the TEM image of the solid treated at 700 oC (Figure 3.8), Ni NPs with diameters larger than 50 nm were observed in the presence of small Ni NPs with diameters of ca. 5 nm. This was due to the secondary agglomeration of the 4 nm Ni NPs that was initiated upon heating at the temperatures above ~600 °C. The mobility of the Ni NPs can be explained by the melting-point depression in nanoscale materials.[37] While the melting temperature of bulk Ni metal is 1453 °C, metal particles smaller than ~100 nm can melt at significantly lower temperatures; the melting point of 4 nm Ni metal particles is calculated to be ~700 °C. This was the temperature at which the Ni NPs began to agglomerate. Therefore, after heating at 1000 °C for 1 h, the 3D *meso*G coexisted with large Ni NPs. Likewise, the surfaces of the large Ni NPs also act as catalysts to generate large carbon shells, as shown in Figure 3.2b.

To explore the structural and electronic properties of the 3D *meso*G, Raman spectroscopy was conducted (Figure 3.9a). A broad D band attributed to the disorder-induced mode and a relatively sharp G band attributed to the E_{2g} mode from the sp^2 carbon domain appeared at 1340 and 1575 cm^{-1}, respectively, along with the 2D band for the second order D band at 2676 cm^{-1}. The G peak indicated the presence of crystalline graphitic carbon in the 3D *meso*G. The ratio between the intensity of the D and G bands (I_D/I_G), which is commonly used as an indicator for the degree of disorder in graphitic materials, was 0.70. This I_D/I_G ratio was comparable to or smaller than those of GO and rGO (I_D/I_G = ~1)[38] and CVD-grown multi-wall CNTs (I_D/I_G = 0.7~1.3),[39-41] thus suggesting high quality 3D *meso*G (Table 3.2). The broad D peak might originate primarily from the distorted nature of the hexagonal sp^2 carbons because of significant lattice stress arising from high curvature of the 4 nm hollow graphene shell in 3D *meso*G. As listed in Table 3.1, elemental analysis of 3D *meso*G revealed a super high C/O ratio of 55, which was much higher than that of chemically or thermally reduced graphene oxide (rGO) (~20).[42] Such a high C/O atomic ratio implies the presence of limited oxygen-containing functionalities, which may lead to excellent physical properties in 3D *meso*G.

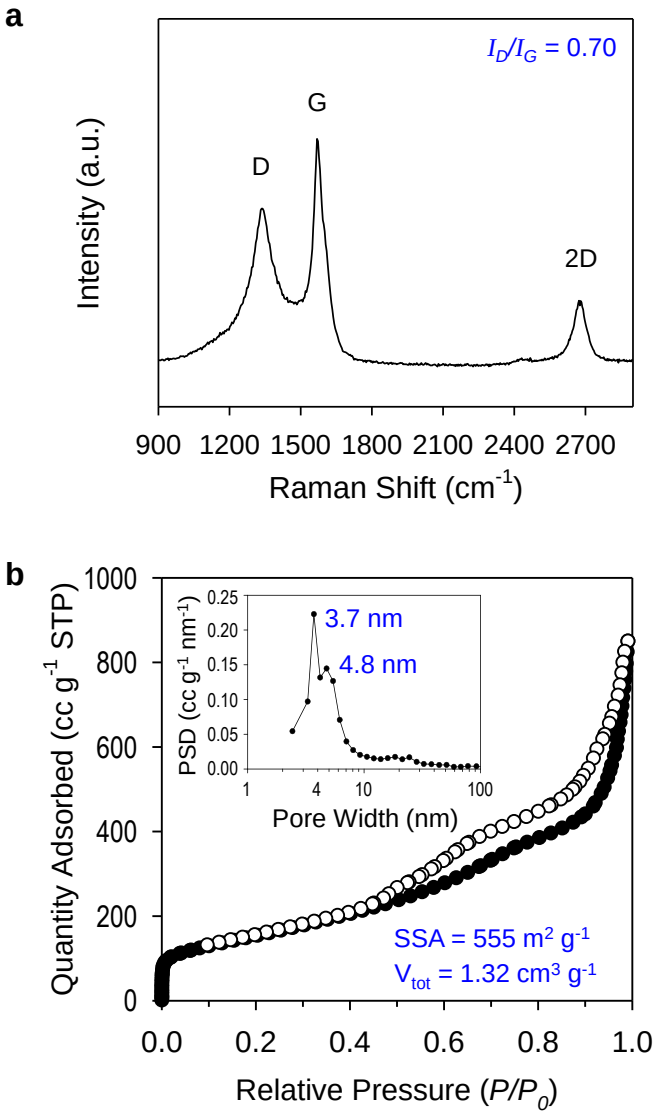

Figure 3.9 Structural and electronic characterization of 3D *meso*G. a, Raman spectrum. b, N_2 adsorption-desorption isotherm and the corresponding BJH pore size distribution curve (inset).

Table 3.2 Comparison of Raman data of graphene- and CNT-related materials.

Materials	Peak position (cm^{-1})			Ratio	References
	D	G	2D	I_D/I_G	
Graphene oxide (GO)	~1325	~1590	~2645	1.88	43
Graphene aerogel (GA)				2.31	
Graphene oxide aerogel (GOA)				2.49	
Reduced graphene oxide (rGO)	1337	1588	-	1.30	44
Hydrazine-reduced GO	1349	1577	-	0.74	45
e^- beam-reduced GO	1328	1594	-	1.51	
GO	1358	1594	2680	0.77	46
$rGO_{HI\text{-}AcOH}$	1350	1581	-	1.10	
rGO/CNT	1353	1582	2697	1.04	47
Repaired GO with multi-layered graphene balls (RGGB)	1355	1575	2700	0.91	18
Multilayer graphene balls	1340	1580	2650	> 1	48
Film of MWCNTs	1349	1579	2701	0.85	39
MWCNTs	1354	1584	2709	0.70	40
Aligned carbon nanotubes	1348	1581	2697	1.3	41
3D *meso*G from $[Ni_2(EDTA)]$	1340	1575	2676	0.70	*Present work*
3D *meso*G from $[Ni(EN)_3]^{2+}$	1342	1578	2677	0.84	
3D *meso*G from [Ni(adipate)]	1354	1590	-	1.14	
3D *meso*G from [Ni(BDC)]	1345	1582	2677	0.96	

In order to assess the porous structure of 3D *meso*G, nitrogen adsorption-desorption measurements were conducted. As shown in Figure 3.9b, 3D *meso*G exhibited typical type IV isotherms with an *H3* type hysteresis loop over a relative pressure range of $0.42 < P/P_0 < 0.99$, which is characteristic of a mesoporous nature. The Barrett–Joyner–Halenda (BJH) pore size distribution curve (Figure 3.9b, inset) indicated mesopores centered around 4 nm, which was in good agreement with the TEM analysis. The highly porous nature of 3D *meso*G gave rise to a large Brunauer-Emmett-Teller (BET) specific surface area (SSA) of 555 $m^2\ g^{-1}$, which was comparable to the specific surface area of five-layered graphene calculated from the theoretical SSA of monolayer graphene (2630 $m^2\ g^{-1}$). In addition, 3D *meso*G exhibited a very high total pore volume (V_{tot}) of 1.32 $cm^3\ g^{-1}$.

Overall, the characterization data suggested a high quality 3D mesoporous graphene material that integrates a very large surface area with highly graphitic frameworks, via the simple thermal conversion of Ni coordination complexes. It is noteworthy that it was previously impossible to prepare 3D graphene with such small, monodisperse mesopores without the need for additional pore generation processes, such as the introduction and removal of template materials such as Ni foams[12] or silica beads.[13] Furthermore, the present method can proceed without the use of reductive gas (H_2), which is typically required to form the conjugated carbons within graphene layers. As such, this method represents a significant advancement in the preparation of 3D graphene materials in terms of simplicity of the synthetic process as well as the quality of the resulting materials.

The aforementioned formation of 3D *meso*G suggests that the organic ligands as well as *in situ* generated metal species play a significant role. With this as a momentum, we explored the impact of organic ligands in the Ni complexes. Organic ligands with different functional groups and struts can modulate the physicochemical properties of Ni(II) coordination complexes, which can in turn control the reduction capabilities of Ni NPs as well as the decomposition of organic ligands to yield carbon and hydrogen atoms. To examine the dependency of 3D *meso*G on ligand in the Ni(II) coordination complexes, three different Ni(II) complexes were thermally treated and characterized (Figures 3.10-13). Specifically, $[Ni(EN)_3](NO_3)_2$ (EN = *N,N'*-ethylenediamine) was treated to examine the effects of complex stability, [Ni(adipate)] was evaluated to explore the effects of infinite coordination, and [Ni(BDC)] (BDC^{2-} = 1,4-benzenedicarboxylate) was utilized to examine the effects of an aromatic carbon source on the graphitic degree of 3D *meso*G.

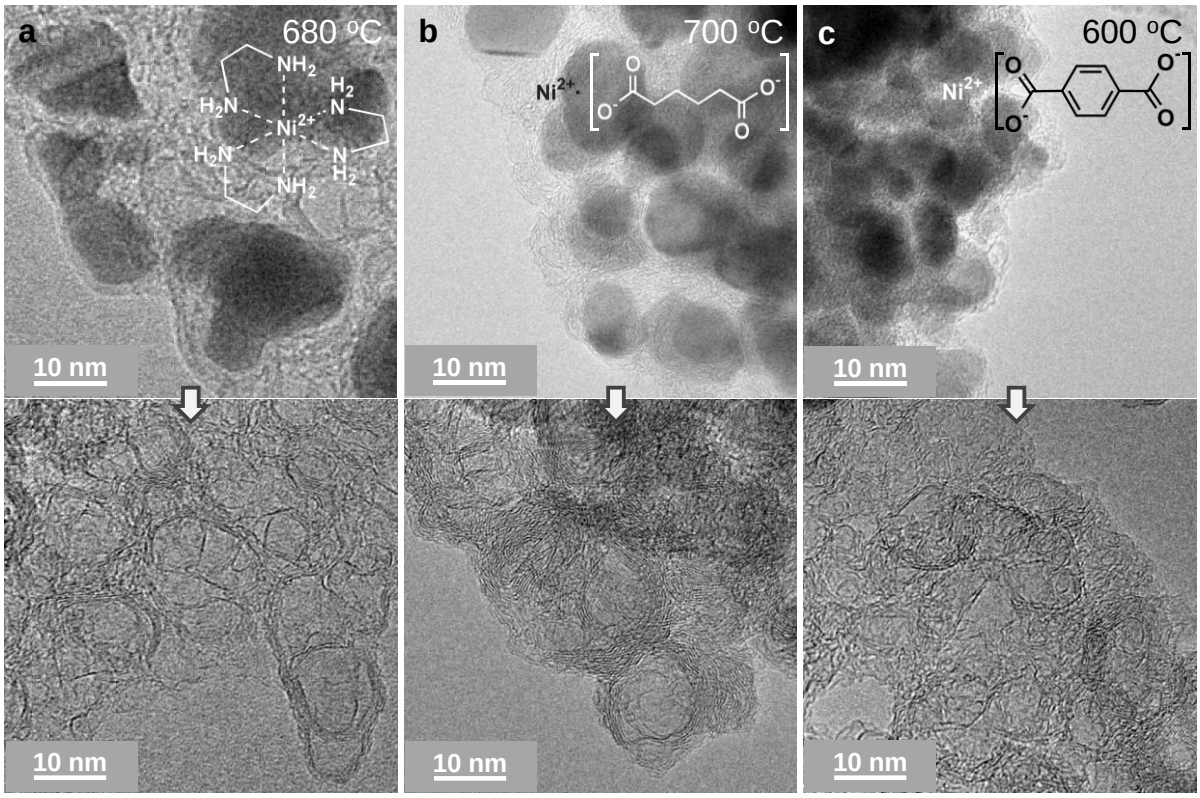

Figure 3.10 Coordination compound-dependent evolution of mesoporous graphene. a-c, TEM images during (upper panels) and after (lower panels) thermal conversion of (a) $[Ni(en)_3](NO_3)_2$, (b) [Ni(adipate)], and (c) [Ni(BDC)]. To see the shape and size of evolved Ni NPs during thermal conversion, each compound was examined at the temperature indicated in TEM images in upper panels. After thermolysis at 1000 °C for 1 h, the small Ni NPs evolved upon heating were aggregated to large Ni NPs, which is the same phenomenon as the case of $[Ni_2(EDTA)]$. TEM images in lower panels were taken in high magnification to show the appearance of carbon shells clearly.

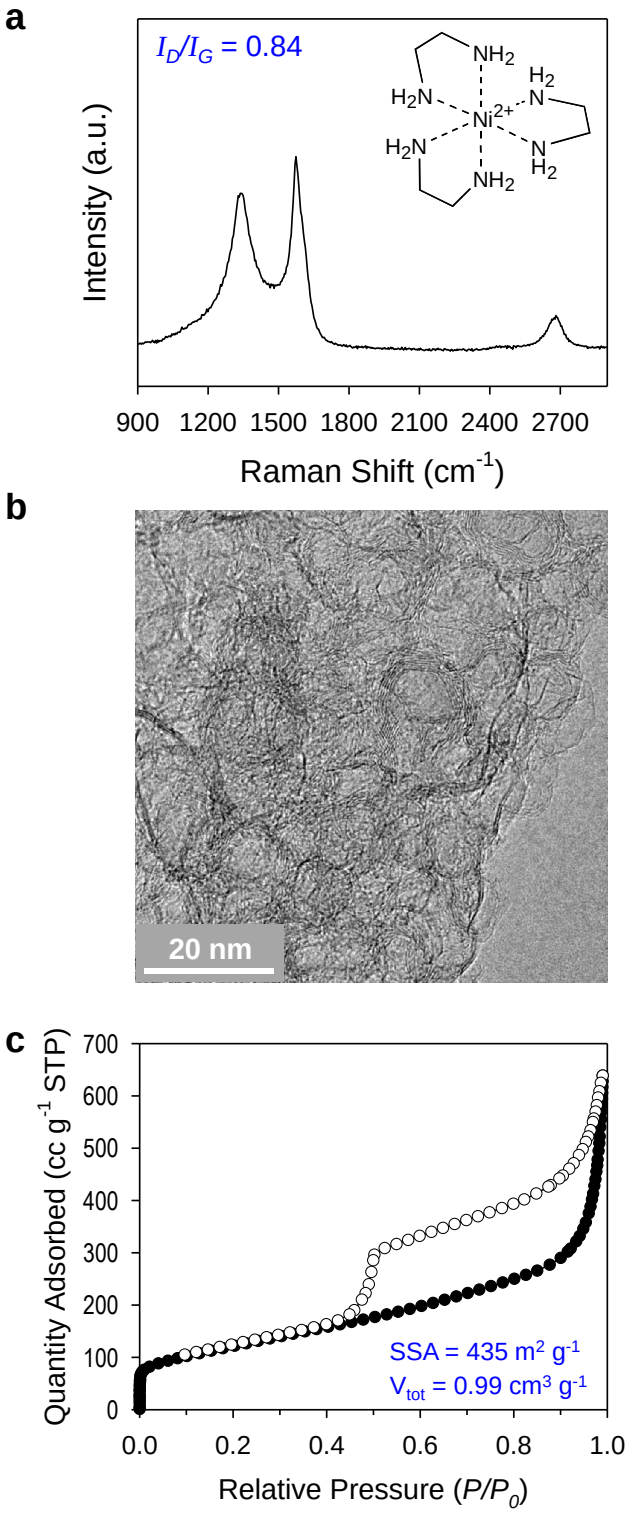

Figure 3.11 Structural and electronic characterization of the resulting material obtained via thermolysis of $[Ni(EN)_3](NO_3)_2$. a, Raman spectrum after thermolysis. TEM image (b) and N_2 adsorption-desorption isotherm (c) of the resulting material followed by etching.

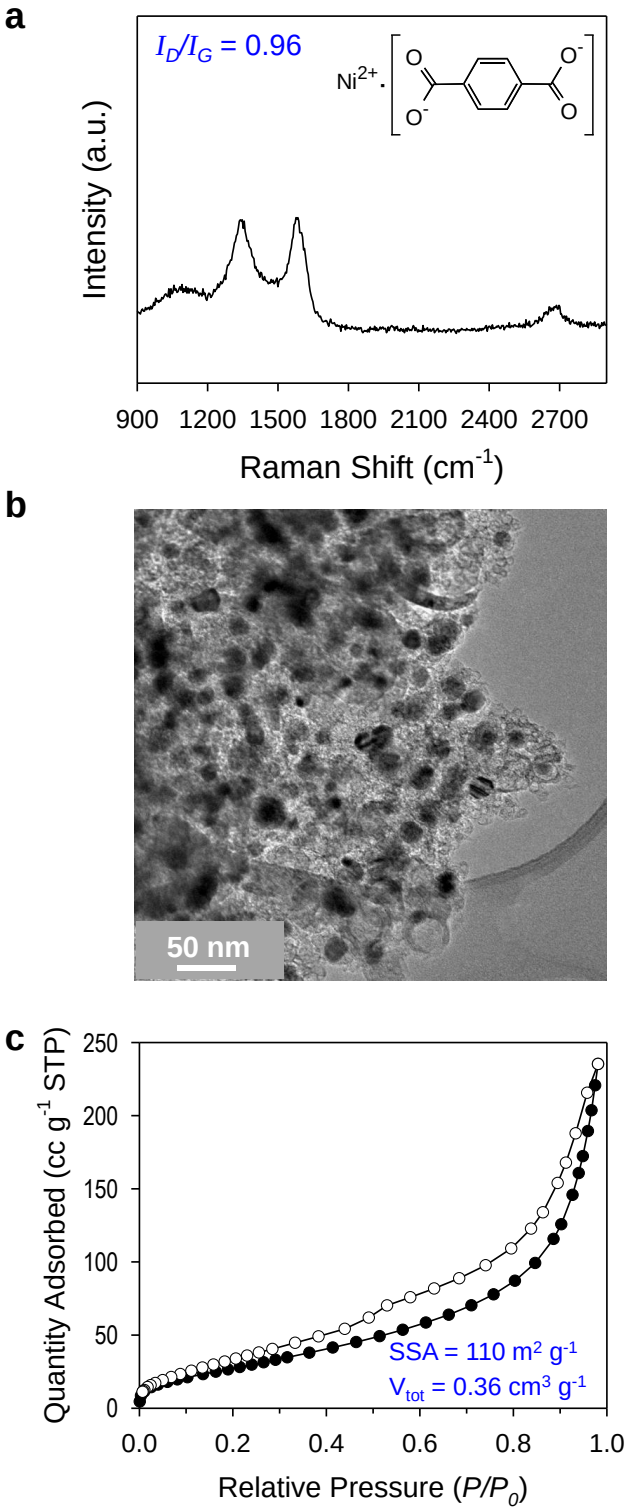

Figure 3.12 Structural and electronic characterization of the resulting material obtained via thermolysis of [Ni(BDC)]. a, Raman spectrum after thermolysis. TEM image (b) and N_2 adsorption-desorption isotherm (c) of the resulting material followed by etching.

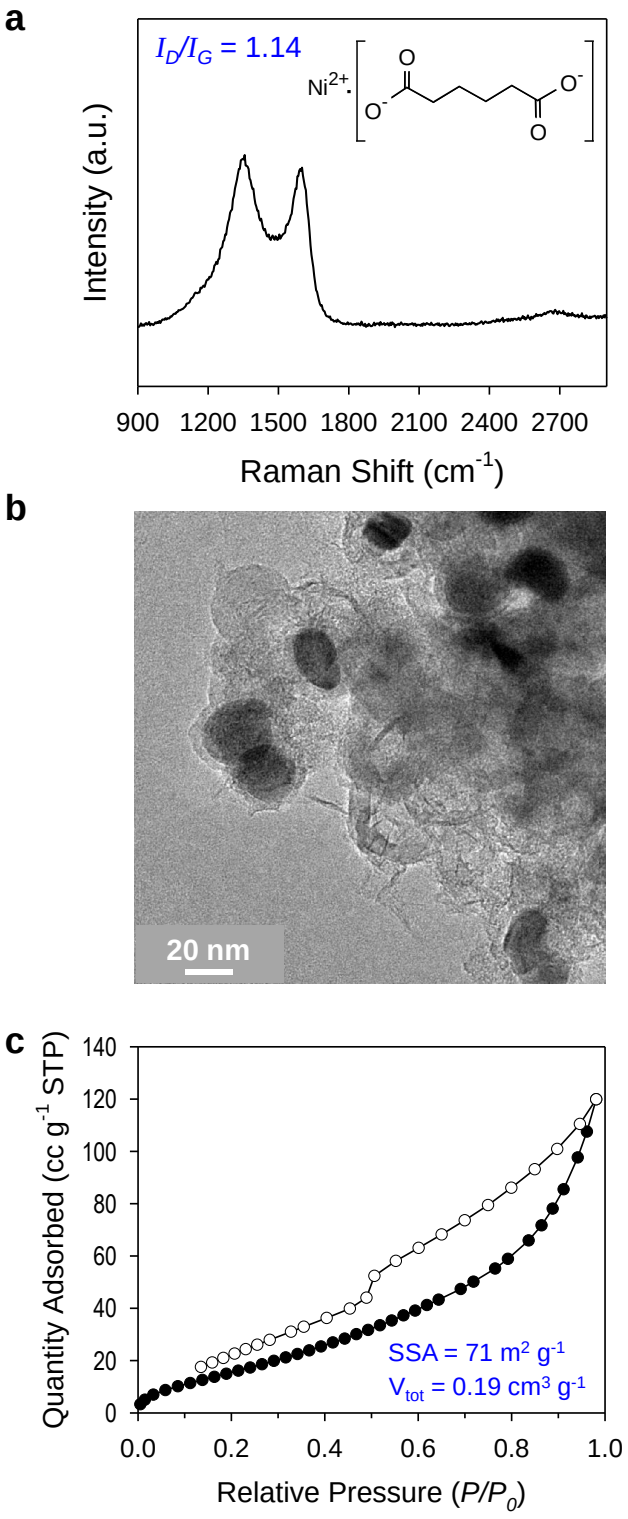

Figure 3.13 Structural and electronic characterization of the resulting material obtained via thermolysis of [Ni(adipate)]. a, Raman spectrum after thermolysis. TEM image (b) and N_2 adsorption-desorption isotherm (c) of the resulting material followed by etching.

Since overly weak coordinating ligands can readily evaporate at low temperatures prior to the reduction of Ni(II) to Ni(0), Ni(II) coordination complexes with significantly lower stability (as compared to that of [Ni_2(EDTA)]) were unsuitable for comparison. Thus, [$Ni(EN)_3$](NO_3)$_2$ with a modestly low stability was selected because the coordinating functional groups of the amine were weak but chelation was still expected. When a $[Ni(EN)_3]^{2+}$ complex was thermally treated, the resulting Ni NPs lacked uniformity in their shape and size, consequently yielding irregular and non-spherical graphitic carbon shells (Figure 3.10a). Despite the inferior appearance of the resulting materials, Raman spectrum and nitrogen adsorption-desorption measurement showed the comparable chemical and physical properties to those of 3D *meso*G resulting from [Ni_2(EDTA)] (I_D/I_G = 0.84, SSA = 435 m^2 g^{-1}, V_{tot} = 0.99 cm^3 g^{-1}) (Table 3.2 and Figure 3.11). In [Ni(adipate)], Ni(II) ions were infinitely coordinated by aliphatic ditopic ligands, but chelation did not occur. The decomposition of this compound led to the production of Ni NPs larger than 10 nm, which might be attributed to non-chelation, and resulted in much thicker carbon shells (Figure 3.10b). During the catalytic C-C bond cleavage reaction over Ni NPs for, evolved carbon atoms diffused onto the surface of the Ni NPs via carburization. At this stage, due to the high carbon solubility of Ni, multi-layered graphene structures were formed. Therefore, under similar synthetic conditions, larger Ni NPs facilitate the dissolution of carbon atoms, which produce thicker carbon shells. Finally, to estimate the effect of the aromaticity of the carbon source on the degree of graphitization in 3D *meso*G, [Ni(BDC)] was subjected to thermal conversion. In the preparation of porous carbon, nanocasting with aromatic carbon sources resulted in a highly graphitic porous carbon wall.[49] However, the resultant solid evolved from [Ni(BDC)] showed inferior quality of carbon to the products resulting from aliphatic $EDTA^{4-}$ and EN ligand-based coordination compounds, as indicated by TEM (Figure 3.10c) and Raman spectroscopy (Figure 10.12 and Table S2). This was because our method necessarily involves C-C bond cleavage of organic ligands by Ni NPs, which is more difficult in conjugated aromatic species.[50,51] During etching of the resulting solids from [Ni(adipate)] and [Ni(BDC)], the carbon species were severely damaged, as evidenced by TEM (Figures 3.12 and 13). Thus, those textural properties confirmed by nitrogen sorption measurement were much worse than those of 3D *meso*G from [Ni_2(EDTA)] (SSA = 71 m^2 g^{-1}, V_{tot} = 0.19 cm^3 g^{-1} for product from [Ni(adipate)]; SSA = 110 m^2 g^{-1}, V_{tot} = 0.36 cm^3 g^{-1} for product from [Ni(BDC)]).

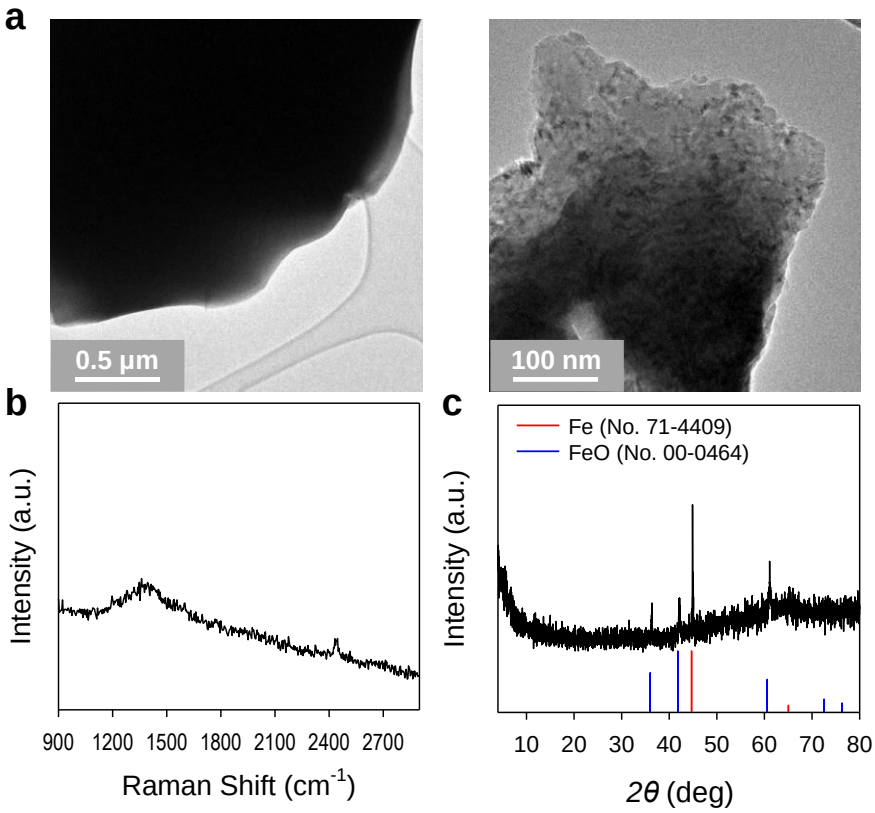

Figure 3.14 Microscopic and structural characterization after thermolysis of $[Fe_4(EDTA)_3]$. a, TEM images after thermal conversion. b, Raman spectrum after thermal conversion. c, X-ray powder diffraction pattern after thermal conversion; red and blue lines indicate the reported values of Fe (JCPDS file no. 71-4409) and FeO (JCPDS file no. 00-0464), respectively.

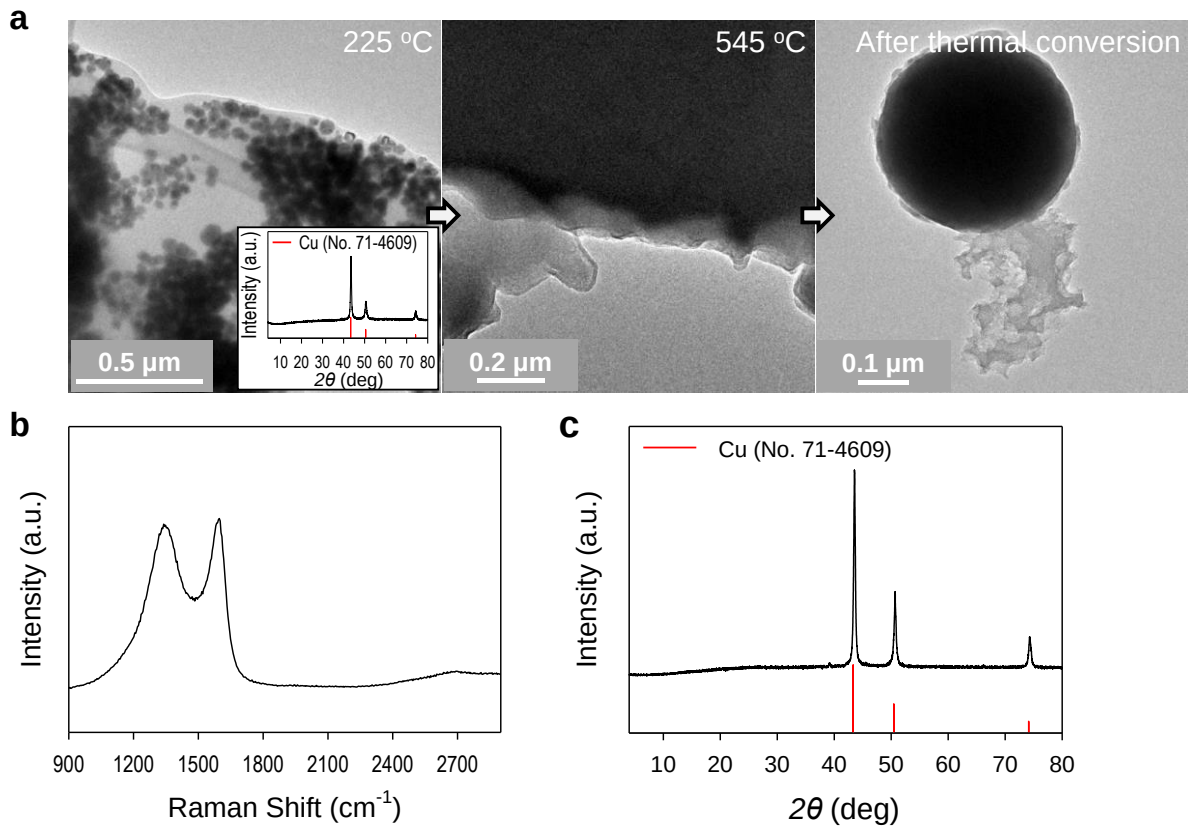

Figure 3.15 Microscopic and structural characterization after thermolysis of [Cu_2(EDTA)]. a, TEM images of temperature-dependent evolution during thermal conversion and X-ray powder diffraction pattern after heat treatment at 225 °C (inset of 1st TEM image on left). b, Raman spectrum after thermal conversion. c, X-ray powder diffraction pattern after thermal conversion. Red lines in (a) and (b) indicate the reported values of Cu (JCPDS file no. 71-4609).

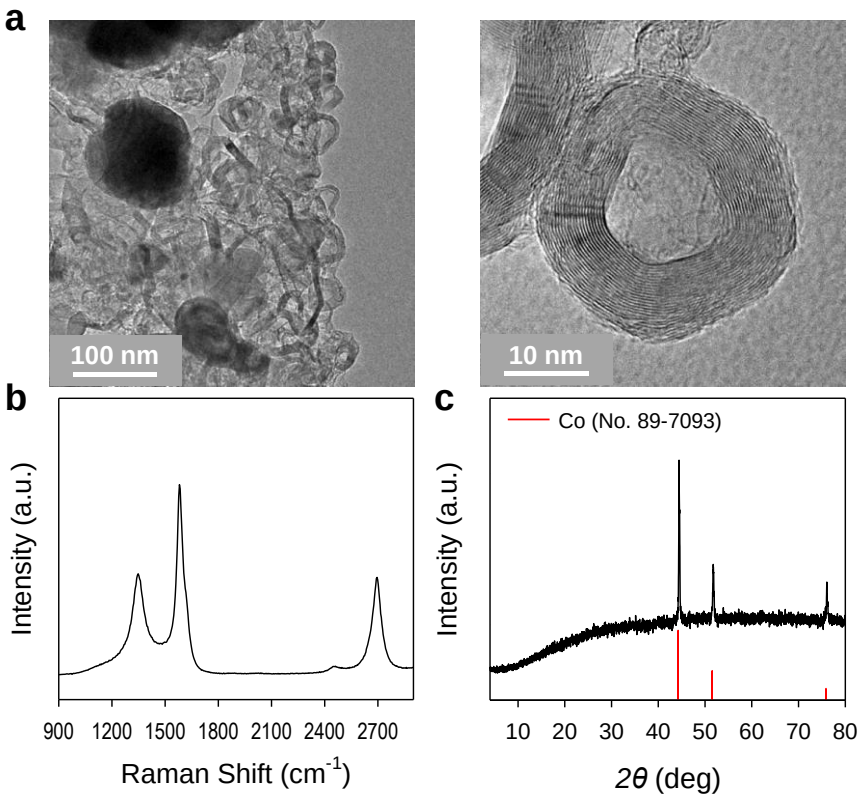

Figure 3.16 Microscopic and structural characterization after thermolysis of [Co_2(EDTA)]. a, TEM images after thermal conversion. b, Raman spectrum after thermal conversion. c, X-ray powder diffraction pattern after thermal conversion; red lines indicate the reported values of Co (JCPDS file no. 89-7093).

We also examined the effect of metal centers during the conversion of the metal complexes. Three coordination compounds were prepared, namely [Fe_4(EDTA)$_3$], [Cu_2(EDTA)], and [Co_2(EDTA)], and were thermally decomposed under the same conditions as [Ni_2(EDTA)]. As shown in Figure 3.14, upon thermolysis, [Fe_4(EDTA)$_3$] resulted in amorphous carbon rather than mesoporous graphene. As judge by the XRPD pattern, the evolved metal species consisted of large agglomerates of FeO and Fe metal, which are known to be inefficient catalysts for C-C bond activation.[52] With [Cu_2(EDTA)], during thermal treatment, even at low temperatures (225 ^{o}C), 50 nm-sized metallic Cu NPs were formed (Figure 3.15). Consequently, even before reaching the temperature required to catalyze carbon species, Cu NPs were severely agglomerated, resulting in microspheres at 1000 ^{o}C. In this process, templating by Cu NPs was hardly expected, and due to the low carbon solubility of Cu metal, only a small amount of graphitic carbon was detected with amorphous carbon via Raman spectroscopy. [Co_2(EDTA)] could be partially converted to graphitic carbon shells with multiple layers, but not 3D mesoporous graphene (Figure 3.16), as previously reported.[53] These results suggested that multiple factors, such as compound stability and the metal and ligand type should be taken into account in the production of 3D *meso*G via the thermolysis of metal coordination compounds.

Inspired by the excellent structural properties of 3D *meso*G, we investigated its bifunctional electrocatalytic activity in ORR and OER, which are relevant for renewable energy technologies[54,55]. The activities of Ir/C (20 wt% Ir, Premetek) and Pt/C (20 wt% Pt, Johnson-Matthey) were also evaluated as benchmarks. The polarization curves for the ORR and OER were measured in 0.1 M KOH at 1600 rpm using the rotating disk electrode (RDE) technique (Figure 3.17a). For the OER, 3D *meso*G showed a very high activity that was comparable to that of noble-metal-based Ir/C and was significantly better than that of Pt/C. Potential to produce 10 mA cm^{-2} for 3D *meso*G was 1.622 V (vs. reversible hydrogen electrode (RHE), overpotential (η) = 393 mV), which was similar to that of Ir/C (1.607 V, η = 378 mV) and far better than that of Pt/C (1.894 V, η = 665 mV). In the ORR, Pt/C exhibited the highest onset and half-wave potentials, indicating the best ORR activity as expected. The 3D *meso*G and Ir/C showed less pronounced ORR activity as compared to Pt/C, as their curves were negatively shifted by ca. 200 mV. To quantitatively compare the bifunctional activity (oxygen electrode activity) of the catalysts for the OER and ORR, the potential difference to drive 10 mA cm^{-2} and −3 mA cm^{-2} (or the sum of overpotentials at those current densities) was calculated (Figure 3.17b and Table 3.3).[56] Remarkably, 3D *meso*G exhibited the best oxygen electrode activity among the compared catalysts; the potential difference of 3D *meso*G (0.923 V) was lower than that of the noble metal-based Ir/C (0.942 V) and Pt/C (1.015 V) catalysts. This indicated that 3D *meso*G could be a promising noble metal-free bifunctional catalyst for use in regenerative fuel cells and rechargeable metal-air batteries. The high bifunctional activity of 3D *meso*G may originate from its very large surface area, with numerous defect sites due to the high curvature of its structure. In addition, the presence of nitrogen and nickel species in the carbon

framework also contributed to the high catalytic activity [57].

Finally, we assessed the excellent structural stability of 3D *meso*G via durability tests in the OER. Specifically, 3D *meso*G as well as Ir/C and Pt/C catalysts were cycled from 1.20 to 1.80 V 100 times (Figure 3.18). A comparison of the current densities at 1.65 V before and after the cycling tests revealed that 3D *meso*G showed only a 3% decay in the current density, whereas the OER activities of Ir/C and Pt/C catalysts declined by 29% and 72%, respectively (Figure 3.17c). Carbon-supported metal nanoparticles are subjected to various deactivation processes, such as carbon oxidation, metal dissolution, and Ostwald ripening, which are more pronounced at high oxidative OER potentials (>1.4 V). The superior stability of 3D *meso*G can be attributed to the highly graphitic carbon framework, which is more resistant to oxidation than amorphous carbon in Ir/C and Pt/C.

Table 3.3 Potentials required to reach 10 mA cm^{-2} for OER and −3 mA cm^{-2} for ORR, and the potential difference to derive 10 mA cm^{-2} and −3 mA cm^{-2}.

Catalysts	E_{OER} **@ 10 mA cm^{-2} (V)[a]**	E_{ORR} **@ -3 mA cm^{-2} (V)[b]**	E_{OER} **-** E_{ORR} **(V)**
3D *meso*G	1.622	0.699	0.923
Ir/C	1.607	0.665	0.943
Pt/C	1.894	0.879	1.015

[a] 10 mA cm^{-2} is the current density required for photochemical fuel production with a 10% solar-to-fuel efficiency at AM1.5G.

[b] −3 mA cm^{-2} corresponds to roughly half of the diffusion-limited current density during the ORR at a rotation speed of 1600 rpm.

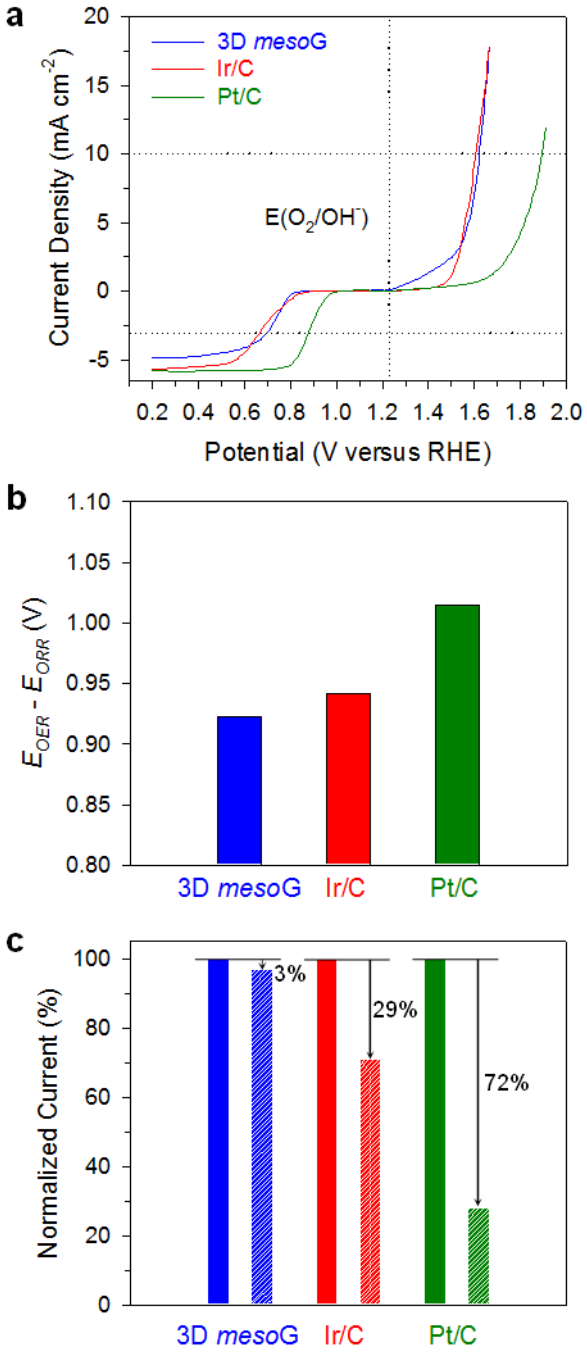

Figure 3.17 Electrocatalytic activity and durability of 3D *meso*G in OER and ORR. a, Polarization curves showing ORR and OER activities of 3D *meso*G, Ir/C, and Pt/C catalysts. Horizontal dotted lines indicate 10 mA cm^{-2} and −3 mA cm^{-2} and the vertical dotted line indicates the equilibrium potential (1.229 V versus RHE) of the ORR and OER. b, Bar graph showing the potential differences to drive 10 mA cm^{-2} for OER and −3 mA cm^{-2} for ORR. c, The changes in relative current densities of 3D *meso*G, Ir/C, and Pt/C catalysts for the OER before and after cycling tests. The catalysts were cycled from 1.20 to 1.80 V (versus RHE) at a scan rate of 20 mV s^{-1} 100 times in 0.1 M KOH electrolyte.

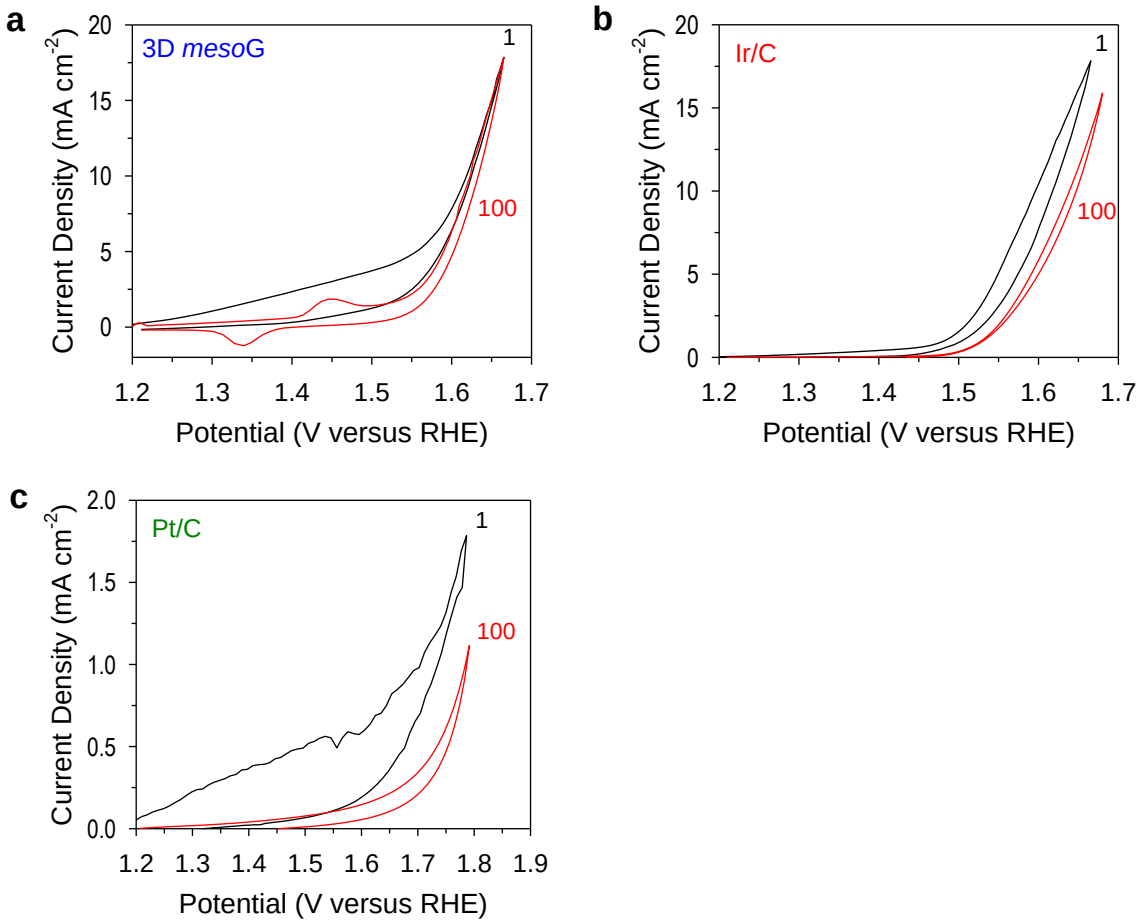

Figure 3.18 Durability of electrocatalytic activity for OER. a, The 1st (black) and 100th (red) CV scans of 3D *meso*G. b, The 1st (black) and 100th (red) CV scans of Ir/C catalyst. c, The 1st (black) and 100th (red) CV scans of Pt/C catalyst.

3.4 Conclusion

In conclusion, we synthesized 3D mesoporous graphene frameworks by the thermal conversion of Ni(II) coordination compounds. The resulting 3D *meso*G was composed of 3D interconnected hollow N-doped graphene shells of 3-4 layers, and featured uniform mesopores, a large surface area and pore volume, and a very high G/O ratio. In the conversion process, *in situ* generated Ni NPs played a critical role as they served as catalysts for the C-C bond cleavage of organic ligands as well as for sp^2 C-C bond formation of the thin graphene layers on their surface, and acted as templates for the formation of mesoporous graphene. As such, the size of the Ni NPs directly influenced the final structure and properties of graphene. Furthermore, the structure of 3D *meso*G could be manipulated by varying the types of ligands and metal centers of the starting metal complexes. We believe that, similar to recent studies regarding the conversion of metal-organic frameworks, this approach can be extended from the conversion of Ni(II) complexes to a variety of porous graphene frameworks. Importantly, Ni(II) complexes with heteroatom-containing ligands as precursors can serve as a route towards highly graphitic, heteroatom-doped carbon that can be utilized as a high-performance material for energy conversion reactions and storage applications. Furthermore, we envisage that the conversion of small metal complexes into nanostructured materials can be exploited for the preparation of unprecedented functional materials.

3.5 References

1. Yang, H. Y.; Han, Z. J.; Yu, S. F.; Pey, K. L.; Ostrikov, K.; Karnik, R. Carbon Nanotube Membranes with Ultrahigh Specific Adsorption Capacity for Water Desalination and Purification. *Nature Communications* **2013**, *4*, 2220.
2. Ji, X.; Lee, K. T.; Nazar, L. F. A Highly Ordered Nanostructured Carbon-Sulphur Cathode for Lithium-Sulphur Batteries. *Nature Materials* **2009**, *8*, 500-506.
3. Merlet, C.; Rotenberg, B.; Madden, P. A.; Taberna, P.-L.; Simon, P.; Gogotsi, Y.; Salanne, M. On the Molecular Origin of Supercapacitance in Nanoporous Carbon Electrodes. *Nature Materials* **2012**, *11*, 306-310.
4. Zhu, Y.; Murali, S.; Stoller, M. D.; Ganesh, K. J.; Cai, W.; Ferreira, P. J.; Pirkle, A.; Wallace, R. M.; Cychosz, K. A.; Thommes, M.; Su, Dong, Stach, E. A.; Ruoff, R. S. Carbon-Based Supercapacitors Produced by Activation of Graphene. *Science* **2011**, *332*, 1537-1541.
5. Su, C.; Loh, K. P. Carbocatalysts: Graphene Oxide and Its Derivatives. *Accounts of Chemical Research* **2013**, *46* (10), 2275-2285.
6. Su, D. S.; Perathoner, S.; Centi, G. Nanocarbons for the Development of Advanced Catalysts. *Chemical Reviews* **2013**, *113* (8), 5782-5816.
7. Navalon, S.; Dhakshinamoorthy, A.; Alvaro, M.; Garcia, H. Carbocatalysis by Graphene-Based Materials. *Chemical Reviews* **2014**, *114* (12), 6179-6212.
8. Zhu, Y.; Murali, S.; Cai, W.; Li, X.; Suk, J. W.; Potts, J. R.; Ruoff, R. S. Graphene and Graphene Oxide: Synthesis, Properties, and Applications. *Advanced Materials* **2010**, *22* (46), 3906-3924.
9. Kim, K. S.; Zhao, Y.; Jang, H.; Lee, S. Y.; Kim, J. M.; Kim, K. S.; Ahn, J.-H.; Kim, P.; Choi, J.-Y.; Hong, B. H. Large-Scale Pattern Growth of Graphene Films for Stretchable Transparent Electrodes. *Nature* **2009**, *457*, 706-710.
10. Balandin, A. A.; Ghosh, S.; Bao, W.; Calizo, I.; Teweldebrhan, D.; Miao, F.; Lau, C. N. Superior Thermal Conductivity of Single-Layer Graphene. *Nano Letters* **2008**, *8* (3), 902-907.
11. Allen, M. J.; Tun, V. C.; Kaner, R. B. Honeycomb Carbon: A Review of Graphene. *Chemical Reviews* **2010**, *110* (1), 132-145.
12. Chen, Z.; Ren, W.; Gao, L.; Liu, B.; Pei, S.; Cheng, H.-M. Three-Dimensional Flexible and Conductive Interconnected Graphene Networks Grown by Chemical Vapour Depositions. *Nature Materials* **2011**, *10*, 424-428.
13. Yoon, J.-C.; Lee, J.-S.; Kim, S.-I.; Kim, K.-H.; Jang, J.-H. Three-Dimensional Graphene Nano-Networks with High Quality and Mass Production Capability via Precursor-Assisted Chemical Vapor Depositions. *Scientific Reports* **2013**, *3*, 1788.
14. Cui, C.; Qian, W.; Yu, Y.; Kong, C.; Yu, B.; Xiang, L.; Wei, F. Highly Electroonductive Mesoporous Graphene Nanofibers and Their Capacitance Performance at 4 V. *Journal of the*

American Chemical Society **2014**, *136* (6), 2256-2259.

15. Wu, Z.-S.; Sun, Y.; Tan, Y.-Z.; Yang, S.; Feng, X.; Müllen, K. Three-Dimensional Graphene-Based Macro- and Mesoporous Frameworks for High-Performance Electrochemical Capacitive Energy Storage. *Journal of the American Chemical Society* **2012**, *134* (48), 19532-19535.
16. Zhang, L.; Zhang, F.; Yang, X.; Long, G.; Wu, Y.; Zhang, T.; Leng, K.; Huang, Y.; Ma, Y.; Yu, A.; Chen, Y. Porous 3D Graphene-Based Bulk Materials with Exceptional High Surface Area and Excellent Conductivity for Supercapacitors. *Scientific Reports* **2013**, *3*, 1408.
17. Wu, C.; Huang, X.; Wang, G.; Ly, L.; Chen, G.; L, G.; Jiang, P. Highly Conductive Nanocomposites with Three-Dimensional, Compactly Interconnected Graphene Networks via a Self-Assembly Process. *Advanced Functional Materials* **2013**, *23* (4), 506-513.
18. Kim, K. H.; Yang, M. H.; Cho, K. M.; Jun, Y.-S.; Lee, S. B.; Jung, H.-T. High Quality Reduced Graphene Oxide through Repairing with Multi-Layered Graphene Ball Nanostructures. *Scientific Reports* **2013**, *3*, 3251.
19. Fan, Z.; Yan, L.; Zhi, L.; Zhang, Q.; Wei, T.; Feng, J.; Zhang, M.; Qian, W.; Wei, F. A Three-Dimensional Carbon Nanotube/Graphene Sandwich and Its Applications as Electrode in Supercapacitors. *Advanced Materials* **2010**, *22* (33), 3723-3728.
20. Burress, J. W.; Gadipelli, S.; Ford, J.; Simmons, J. M.; Zhou, W.; Yildirim, T. Graphene Oxide Framework Materials: Theoretical Predictions and Experimental Results. *Angewandte Chemie International Edition* **2010**, *49* (47), 8902-8904.
21. Kim, T. K.; Cheon, J. Y.; Yoo, K.; Kim, J. W.; Hyun, S.; Shin, H. S.; Joo, S. H. Moon, H. R. Three-Dimensional Pillared Metallomacrocycle-Graphene Frameworks with Tunable Micro- and Mesoporosity. *Journal of Materials Chemistry A* **2013**, *1* (29), 8432-8437.
22. Jiang, H.-L.; Liu, B.; Lan, Y.-Q.; Kuratani, K.; Akita, Y.; Shioyama, H.; Zong, F.; Xu, Q. From Metal-Organic Framework to Nanoporous Carbon: Toward a Very High Surface Area and Hydrogen Uptake. *Journal of the American Chemical Society* **2011**, *133* (31), 11854-11857.
23. Hu, M.; Reboul, J.; Furukawa, S.; Torad, N. L.; Ji, Q.; Srinivasu, P.; Ariga, K.; Kitagawa, S.; Yamauchi, Y. Direct Carbonization of Al-Based Porous Coordination Polymer for Synthesis of Nanoporous Carbon. *Journal of the American Chemical Society* **2012**, *134* (6), 2864-2867.
24. Lim, S.; Suh, K.; Kim, Y.; Yoon, M.; Park, H.; Dybtsev, D. N.; Kim, K. Porous Carbon Materials with a Controllable Surface Area Synthesized from Metal-Organic Frameworks. *Chemical Communications* **2012**, *48* (60), 7447-7449.
25. Zhang, W.; Wu, Z.-Y.; Jiang, H.-L.; Yu, S.-H. Nanowire-Directed Templating Synthesis of Metal–Organic Framework Nanofibers and Their Derived Porous Doped Carbon Nanofibers for Enhanced Electrocatalysis. *Journal of the American Chemical Society* **2014**, *136* (41), 14385-14388.
26. Zheng, F.; Yang, Y.; Chen, Q. High Lithium Anodic Performance of Highly Nitrogen-Doped

Porous Carbon Prepared from a Metal-Organic Framework. *Nature Communications* **2014**, *5*, 5261.

27. Yang, S. J.; Kim, T.; Im, J. H.; Kim, T. S.; Lee, K.; Jung, H.; Park, C. R. MOF-Derived Hierarchically Porous Carbon with Exceptional Porosity and Hydrogen Storage Capacity. *Chemistry of Materials* **2012**, *24* (3), 464-470.
28. Tang, J.; Salunkhe, R. R.; Liu, J.; Torad, N. L.; Imura, M.; Furukawa, S.; Yamauchi, Y. Thermal Conversion of Core–Shell Metal–Organic Frameworks: A New Method for Selectively Functionalized Nanoporous Hybrid Carbon. *Journal of the American Chemical Society* **2015**, *137* (4), 1572-1580.
29. Kim, T. K.; Lee, K. J.; Cheon, J. Y.; Lee, J. H.; Joo, S. H.; Moon, H. R. Nanoporous Metal Oxides with Tunable and Nanocrystalline Frameworks via Conversion of Metal–Organic Frameworks. *Journal of the American Chemical Society* **2013**, *135* (24), 8940-8946.
30. Lee, J. H.; Sa, Y. J.; Kim, T. K.; Moon, H. R.; Joo, S. H. A Transformative Route to Nanoporous Manganese Oxides of Controlled Oxidation States with Identical Textural Properties. *Journal of Materials Chemistry A* **2014**, *2* (27), 10435-10443.
31. Lee, K. J.; Kim, T.-H.; Kim, T. K.; Lee, H. J.; Song, H.-K.; Moon, H. R. Preparation of Co_3O_4 Electrode Materials with Different Microstructures via Pseudomorphic Conversion of Co-Based Metal–Organic Frameworks. *Journal of Materials Chemistry A* **2014**, *2* (35), 14393-14400.
32. Lee, J. H.; Moon, B.; Kim, T. K.; Jeoung, S.; Moon, H. R. Thermal Conversion of a Tailored Metal–Organic Framework into Lithium Silicate with an Unusual Morphology for Efficient CO_2 Capture. *Dalton Transactions* **2015**, *44* (34), 15130-15134.
33. Aiyappa, H. B.; Pachfule, P.; Banerjee, R.; Kurungot, S. Porous Carbons from Nonporous MOFs: Influence of Ligand Characteristics on Intrinsic Properties of End Carbon. *Crystal Growth and Design* **2013**, *13* (10), 4195-4199.
34. Srinivas, G.; Krungleviciute, V.; Guo, Z.-X.; Yildirim, T. Exceptional CO_2 Capture in a Hierarchically Porous Carbon with Simultaneous High Surface Area and Pore Volume. *Energy and Environmental Science* **2014**, *7* (1), 335-342.
35. Coronado, E.; Drillon, M.; Fuertes, A.; Beltrans, D.; Mosset, A.; Galy, J. Structural and Magnetic Study of $Ni_2(EDTA)(H_2O)_4{,}2H_2O$. Alternating Lande Factors in a Two-Sublattice 1D System. *Journal of the American Chemical Society* **1986**, *108* (5), 900-905.
36. Kumar, M. *Carbon nanotubes – synthesis, characterization, applications* Chap. 8 (InTech, 2011).
37. Anna, M.; Albert, G. N.; Esko, I. K. The role of metal nanoparticles in the catalytic production of single-walled carbon nanotubes-a review. *Journal of Physics: Condensed Matter* **2003**, *15*, S3011-S3035.
38. Georgakilas, V.; Otyepka, M.; Bourlinos, A. B.; Chandra, V.; Kim, N.; Kemp, K. C.; Hobza, P.; Zboril, R.; Kim, K. S. Functionalization of Graphene: Covalent and Non-Covalent Approaches, Derivatives and Applications. *Chemical Reviews* **2012**, *112* (11), 6156-6214.

39. Sveningsson, M.; Morjan, R.-E.; Nerushev, O. A.; Sato, Y.; Bäckström, J.; Campbell, E. E. B.; Rohmund, F. Raman Spectroscopy and Field-Emission Properties of CVD-Grown Carbon-Nanotube Films. *Applied Physics A* **2001**, *73*, 409-418.
40. Kwok, K.; Chiu, W. K. S. Growth of Carbon Nanotubes by Open-Air Laser-Induced Chemical Vapor Deposition. *Carbon* **2005**, *43*, 437-446.
41. Li, W.; Zhang, H.; Wang, C.; Zhang, Y.; Xu, L.; Zhu, K.; Xie, S. Raman Characterization of Aligned Carbon Nanotubes Produced by Thermal Decomposition of Hydrocarbon Vapor. *Applied Physics Letters* **1997**, *70*, 2684-2686.
42. Chun, C. K.; Pumera, M. Chemical Reduction of Graphene Oxide: A Synthetic Chemistry Viewpoint. *Chemical Society Reviews* **2014**, *43*, 291-312.
43. Wu, X.; Zhou, J.; Xing W.; Wang, G.; Cui, H.; Zhuo, S.; Xue, Q.; Yan, Z.; Qiao, S. Z. High-Rate Capacitive Performance of Graphene Aerogel with a Superhigh C/O Molar Ratio. *Journal of Materials Chemistry* **2012**, *22*, 23186-23193.
44. Eigler, S.; Dotzer, C.; Hirsch, A. Visualization of Defect Densities in Reduced Graphene Oxide. *Carbon* **2012**, *50*, 3666-3673.
45. Pan, D.; Wang, S.; Zhao, B.; Wu, M.; Zhang, H.; Wang, Y.; Jiao, Z. Li Storage Properties of Disordered Graphene Nanosheets. *Chemistry of Materials* **2009**, *21* (14), 3136-3142.
46. Moon, I. K.; Lee, J.; Ruoff, R. S.; Lee, H. Reduced Graphene Oxide by Chemical Graphitization. *Nature Communications* **2010**, *1*, 73.
47. Sharma, P.; Bhalla, V.; Dravid, V.; Shekhawat, G.; Wu, J.; Prasad, E. S.; Suri, C. R. Enhancing Electrochemical Detection on Graphene Oxide-CNT Nanostructured Electrodes Using Magneto-Nanobioprobes. *Scientific Reports* **2012**, *2*, 877.
48. Yoon, S.-M.; Choi, W. M.; Baik, H.; Shin, H.-J.; Song, I.; Kwon, M.-S.; Bea, J. J.; Kim, H.; Lee, Y. H.; Choi, J.-Y. Synthesis of Multilayer Graphene Balls by Carbon Segregation from Nickel Nanoparticles. *ACS Nano* **2012**, *6* (8), 6803-6811.
49. Kim, T.-W.; Park, I.-S.; Ryoo, R. A Synthetic Route to Ordered Mesoporous Carbon Materials with Graphitic Pore Walls. *Angewandte Chemie International Edition* **2003**, *42*, 4375-4379.
50. Fu, R.; Baumann T. F.; Cronin, S.; Dresselhaus, G.; Dresselhaus, M. S.; Satcher, J. H. Jr. Formation of Graphitic Structures in Cobalt- and Nickel-Doped Carbon Aerogels. *Langmuir* **2005**, *21* (7), 2647-2651.
51. Lu, A.-H.; Li, W.-C.; Salabas, E.-L.; Spliethoff, B.; Schüth, F. Low Temperature Catalytic Pyrolysis for the Synthesis of High Surface Area, Nanostructured Graphitic Carbon. *Chemistry of Materials* **2006**, *18*, 2086-2094.
52. Maldonado-Hódar, F. J.; Moreno-Castilla, C.; Rivera-Utrilla, J.; Hanzawa, Y.; Yamada, Y. Catalytic Graphitization of Carbon Aerogels by Transition Metals. *Langmuir* **2000**, *16*, 4367-4373.
53. Liu, Z.; Zhang, G.; Lu, Z.; Jin, X.; Chang, Z.; Sun, X. One-Step Scalable Preparation of N-Doped

Nanoporous Carbon as a High-Performance Electrocatalyst for the Oxygen Reduction Reaction. *Nano Research* **2013**, *6* (4), 293-301.

54. Park, S.; Shao, Y.; Liu, J.; Wang, Y. Oxygen Electrocatalysts for Water Electrolyzers and Reversible Fuel Cells:Status and Perspective. *Energy Environmental Science* **2012**, *5*, 9331-9344.
55. Cao, R.; Lee, J.-S.; Liu, M.; Cho, J. Recent Progress in Non-Precious Catalysts for Metal-Air Batteries. *Advanced Energy Materials* **2012**, *2*, 816–829.
56. Gorlin, Y.; Jaramillo, T. F. A Bifunctional Nonprecious Metal Catalyst for Oxygen Reduction and Water Oxidation. *Journal of American Chemical Society* **2010**, *132*, 13612-13614
57. Zhao, Y.; Nakamura, R.; Kamiya, K.; Nakanishi, S.; Hashimoto, K. Nitrogen-Doped Carbon Nanomaterials as Non-Metal Electrocatalysts for Water Oxidation. *Nature Communications* **2013**, *4*, 2390.
58. Lee, K. J.; Sa, Y. J.; Jeong, H. Y.; Bielawski, C. W.; Joo, S. H.; Moon, H. R. Simple Coordination Complex-Derived Three-Dimensional Mesoporous Graphene as an Efficient Bifunctional Oxygen Electrocatalyst. *Chemical Communications* **2015**, *51*, 6773.

4.1 Introduction

The metal/metal oxide-carbon composites have attracted attention due to their numerous applications including energy storage and conversion,[1] catalysis,[2] sensors,[3] and so on. Metal oxide or metal nanomaterials usually suffer from coarsening and aggregating, resulting in performance decay. To realize good structural stability, efforts have been devoted toward the combination of metal/metal oxide with carbon as a stabilizer.[4-6] Besides the stabilizing against agglomeration of nanoparticles, carbon materials including graphene, carbo nanotube, porous carbon and carbon fibers have possessing attractive properties such as high electrical and thermal conductivity, tunable porosity and diversity and easy fabrication. These multivariate combinations of carbon nanomaterials and metal/metal oxides may offer a synergistic effect for potential applications.[7,8]

As mentioned previously, the conversion of MOFs is suitable for synthesis of metal/metal oxide-carbon composites. Besides the direct conversion of single MOF precursor, adding foreign precursors into MOFs has advantages over controlling more diverse compositions and morphologies followed by subsequent pyrolysis. Herein, we utilize the conversion mechanism of Zn-based MOF to synthesize composites of porous carbon and metal particles. In the past, carbon materials converted from Zn-based MOFs were mostly composed of micropores, generated by removal of an intermediate Zn metal (Figure 4.1).[9,10] However, chemical utilization of Zn metal has not yet been achieved in MOF conversion systems, even though Zn has been actively used in industry as the reductant to produce high-purity metals via zincothermic reduction. The essence in our approach toward the carbon/metal composites lies in the utilization of Zn metal in situ evolved in the Zn-MOF conversion system, which play an important role as a porogen for porous carbon as well as a reducing agent for metal oxides (Figure 4.2).[31]

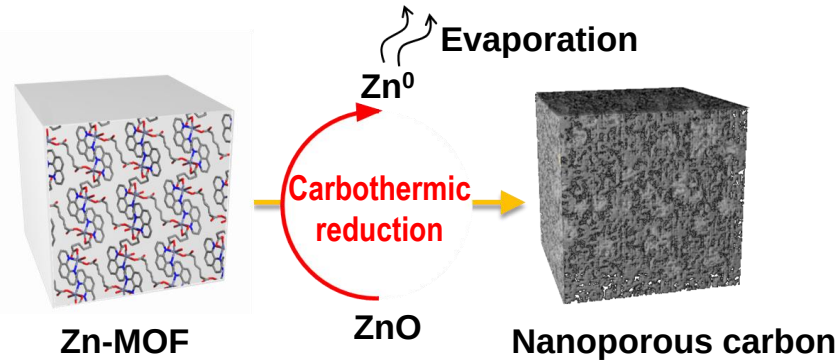

Figure 4.1 Scheme for conversion mechanism of Zn-based MOFs.

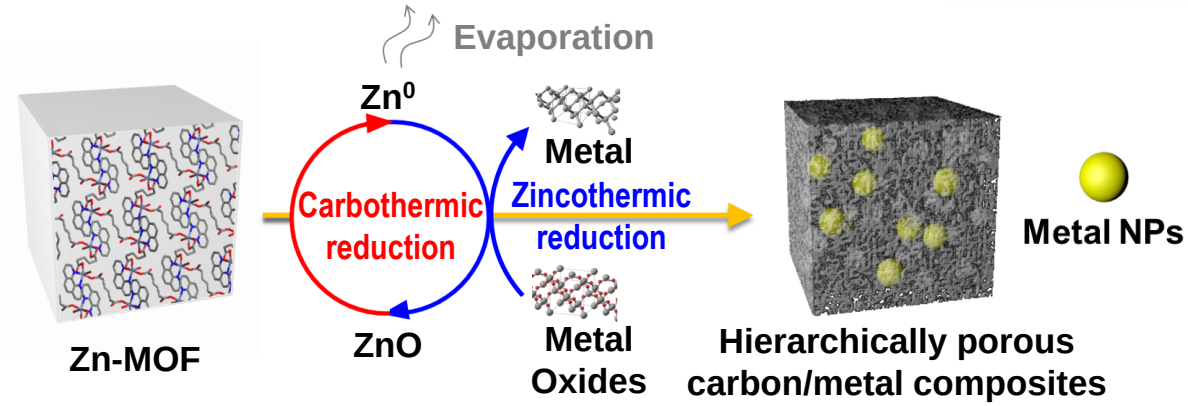

Figure 4.2 Scheme of conversion of a Zn-based MOF and metal oxides to composites of porous carbon and metal particles.

The pre-loading metal nanoparticles into a MOF template followed by conversion is another way to synthesize the composites of metal oxide and carbon supporter. The Pd nanoparticles embedding into redox-active MOF (Pd@*ra*-MOF) has been exploited as a precursor for an active catalyst for CO oxidation. *In-situ* generated PdO_x-NiO_y/C composite under CO oxidation has strong metal-metal oxide interaction as well as carbon-metal oxide interaction, which results in monodispersed metal oxide nanocrystals in carbon matrix (Figure 4.3). The spontaneously formed metal oxide/carbon composite exhibited enhanced catalytic properties and stability, which may be attributed to synergistic stabilization via strong metal oxide-carbon interaction.[32]

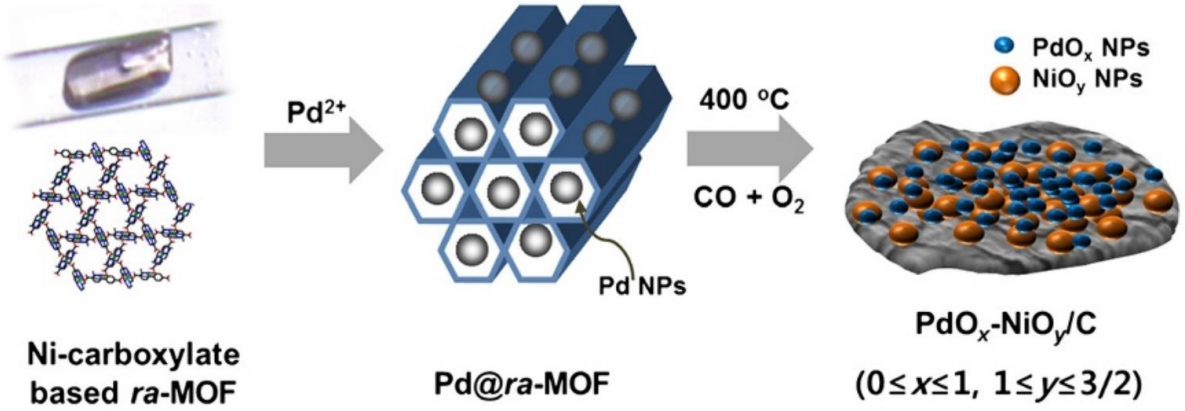

Figure 4.3 Schematic representation for in-situ formation of catalytically active species during CO oxidation reaction.

4.2 Experimental section

Materials and characterizations. All chemicals and solvents were of reagent grade and used without further purification. Infrared spectra were recorded with a ThermoFisher Scientific iS10 FT-IR spectrometer. Raman spectroscopy measurement was performed using a micro-Raman system (WITec) with an excitation energy of 2.41 eV (532 nm). Elemental analyses were performed at the UNIST Central Research Facilities Center (UCRF) in Ulsan National Institute of Science and Technology (UNIST). Thermogravimetric analyses (TGA) were performed under N_2(g) at a scan rate of 10 $^oC\ min^{-1}$, using a TGA Q50 from TA instruments. X-ray photoelectron spectroscopy was performed using a Thermo Scientific K-Alpha XPS spectrometer. X-ray powder diffraction data were recorded on a Bruker D2 phaser diffractometer at 30 kV and 10 mA for Cu Kα (λ = 1.54050 Å), with a step size of 0.02° in 2θ. The chemical composition of Ge/HPC series was analyzed by inductively coupled plasma-mass spectrometry (ICP-MS, Perkin Elmer, ELAN DRC-e). The morphologies of GeO_2 and Ge/HPC-1 were characterized using field-emission scanning electron microscopy (FESEM, Hitachi S-4800), which was performed at 10 kV. Transmission electron microscopy (TEM) image and energy-dispersive X-ray spectroscopy (EDS) mapping were obtained on a JEOL JEM-2100 microscope. N_2 sorption isotherms were obtained by BELSORP-max at 77 K. Prior to the adsorption measurements, Ge/HPC series were evacuated ($p < 10^{-5}$ mbar) at 100 ^oC for 4 h. Resultant materials converted from [Zn(adipate)(phen)(H_2O)] and MOF-5 were evacuated ($p < 10^{-5}$ mbar) at 200 ^oC for 6 h and 120 ^oC for 4 h, respectively. The specific surface area was determined in the relative pressure range from 0.05 to 0.3 of the Brunauer-Emmett-Teller (BET) plot, and the total pore volume was calculated from the amount adsorbed at a relative pressure of about 0.98-0.99. The pore size distribution curve which derived from the adsorption branch of isotherm was analyzed by using a nonlocal density functional theory (NLDFT) algorithm.

Gas sorption studies. N_2 sorption isotherms were obtained by BELSORP-max at 77 K. Prior to the adsorption measurements, Ge/HPC-1 was evacuated ($p < 10^{-5}$ mbar) at 100 ^oC for 4 h. Resultant materials converted from [Zn(adipate)(phen)(H_2O)] and MOF-5 were evacuated ($p < 10^{-5}$ mbar) at 200 ^oC for 6 h and 120 ^oC for 4 h, respectively. The specific surface area was determined in the relative pressure range from 0.05 to 0.3 of the Brunauer-Emmett-Teller (BET) plot, and the total pore volume was calculated from the amount adsorbed at a relative pressure of about 0.98-0.99.

Synthesis of Zn-based MOF ([Zn(adipate)(phen)(H_2O)]). A Zn-based MOF was prepared using a modified version of previously reported method.[11] 1 M Na_2CO_3 solution (10 mL) was added slowly to the 1 M $ZnCl_2$ solution (10 mL). A precipitate formed soon after the two solutions were mixed. The resulting powder was filtered and washed with fresh H_2O. After drying in vacuo at room temperature for overnight, white powder was dispersed in MeOH/H_2O mixture (200 mL, 1:1 v/v) under stirring.

Adipic acid (1.5 g, 10 mmol) and phenanthroline (2.0 g, 10 mmol) were added to the above solution under continuous stirring, resulting in a clear solution. The white solid was formed shortly. After stirring for 1 h, the white solid was filtered and washed with MeOH/H_2O mixture (1:1 v/v). After drying in air, 2.8 g of white solid was obtained. Yield: 69%, FT-IR (KBr pellet, cm^{-1}): ν_{OH}, 3425(br); $\nu_{C\text{-}H(aromatic)}$, 3058(w); $\nu_{C\text{-}H(aliphatic)}$, 2948, 2924, 2857(w); δ_{H2O} = 1623(m); $\nu_{O\text{-}C=O(carboxylate)}$, 1552, 1404(s).

Thermal conversion of a mixture of a Zn-MOF and GeO_2 to Ge/HPC series. The Zn-based MOF, ([Zn(adipate)(phen)(H_2O)]) mentioned above was ground with commercially available GeO_2 powder and heated at 10 °C min^{-1} under a nitrogen flow rate of 100 cc min^{-1}. After the temperature reached target temperature (600, 700, 800, and 900 °C), the material was maintained at that temperature for 6 h. After naturally cooling to room temperature, black powder was obtained. Actual weight and molar ratio of a Zn-MOF and GeO_2 were summarized in Table 4.1-2.

Table 4.1 Summary of experimental conditions with different molar ratio of Zn^{2+} to Ge^{4+} and elemental compositions of resultant materials.

Sample Name[a]	Actual weight Zn-MOF : GeO_2	Molar ratio Zn^{2+}/Ge^{4+}	Thermolysis condition	**Reducing efficiency of Zn[b]**	Elemental composition of the resultant materials (wt%)				
					C[c]	H[c]	N[c]	Ge[d]	Zn[d]
Ge/HPC-2	0.78 g : 0.1 g	2	10 °C/min to 800 °C 800 °C for 6 h	**100%**	60.6	1.1	4.3	33.5	0.5
Ge/HPC-1	0.39 g : 0.1 g	1	10 °C/min to 800 °C 800 °C for 6 h	**200%**	46.7	0.9	3.1	49.1	0.2
Ge/HPC-0.6	0.24 g : 0.1 g	0.6	10 °C/min to 800 °C 800 °C for 6 h	**333%**	29.6	0.4	1.8	68.1	0.08
Ge/HPC-0.3	0.12 g : 0.1 g	0.3	10 °C/min to 800 °C 800 °C for 6 h	**667%**	11.7	0.2	0.9	87.2	0.05

[a] Ge/HPC-X, in which X denotes Zn^{2+}/Ge^{4+} mole ratio in the reactants

[b] Reducing efficiency of Zn was calculated as follows.

Reducing efficiency of Zn = $\frac{mole\ of\ oxygen\ atoms\ in\ GeO_2}{mole\ of\ Zn\ atoms\ in\ the\ Zn-MOF}$ x 100 %

[c] Measured values determined by elemental combustion analysis (EA)

[d] Measured values determined by inductively coupled plasma (ICP)

Table 4.2 Details of experimental conditions about reduction of other metal oxides.

Metal oxide (MO_x)	Actual weight Zn-MOF : MO_x	Molar ratio Zn^{2+}/MO_x	Thermolysis condition	Reducing efficiency of Zn[a]
Bi_2O_3	0.09 g : 0.1 g	1	10 °C/min to 800 °C 800 °C for 6 h	300%
In_2O_3	0.15 g : 0.1 g	1	10 °C/min to 800 °C 800 °C for 6 h	300%
SnO	0.09 g : 0.1 g	0.3	10 °C/min to 800 °C 800 °C for 6 h	300%

[a] Reducing efficiency of Zn was calculated as follows.

Reducing efficiency of Zn = $\frac{mole\ of\ oxygen\ atoms\ in\ MO_x}{mole\ of\ Zn\ atoms\ in\ the\ Zn-MOF}$ x 100 %

Electrochemical Measurements. The electrochemical properties of Ge/HPC electrodes were evaluated using coin-type half cells (2016R) at 25 °C. Ge/HPC electrodes were composed of the Ge active material, super-P carbon black, and poly(acrylic acid)/sodium carboxymethyl cellulose (1:1, w/w) as binder in a weight ratio of 7:1.5:1.5. The electrolyte used was 1.3 M $LiPF_6$ containing ethylene carbonate/diethyl carbonate (PANAX Starlyte, Korea, 3/7 (v/v)) and 10 wt% fluoroethylene carbonate as an additive. The half cells were tested galvanostatically between 0.01 and 3.0 V (versus Li/Li+) for C rates of 0.05–0.5 C. The cell performance was examined using a cycle tester (WBCS 3000 battery systems, Wonatech).

Preparation of *ra*-MOF. $[Ni(C_{10}H_{26}N_6)](ClO_4)_2$ ($C_{10}H_{26}N_6$ = L_{CH3}) was prepared according to a previous report.[12] $[NiL_{CH3}](bpdc)$ (*ra*-MOF; $bpdc^{2-}$ = 4,4′-biphenyldicarboxylate) was synthesized by the modified procedure from the previous reports.[13] Synthetic detail is as follows: $[NiL_{CH3}(ClO_4)_2]$ (0.80 g, 1.64 mmol) was dissolved in water/pyridine (48 mL, 2:1 v/v), and an aqueous solution (16 mL) of Na_2bpdc (0.56 g, 2.10 mmol) was added. The solution was stirred over 20 min at room temperature, and 150 mL of methanol was added to it. The mixture was stirred for 6 h, forming pale purple microcrystals which were obtained by filtration, washed with methanol, and dried in air. The as-prepared metal-organic framework was desolvated at 120℃ under vacuum for 3 h resulting in a purple color. The yield is 57%.

Preparation of the Pd@*ra*-MOF. The desolvated solid (0.43 g, 0.81 mmol) was immersed in 3.12 × 10^{-2} M acetonitrile solution (82 mL) of $Pd(NO_3)_2{\cdot}\times H_2O$ at room temperature and hand-shaken for 10

min, which resulted in a light brown solid. The resulting light brown powder was isolated by filtration, washed with acetonitrile, and dried in air.

Catalytic activity test. The catalytic tests for CO oxidation were performed in a fixed bed reactor at atmospheric pressure, containing 0.06 g of catalyst samples. A feed mixture, prepared using mass flow controllers (MKS Instruments, Inc., Wilmington, MA, USA), contained 3.0% CO and 8.5% O_2 and was balanced with He. The total flow rate of the feed mixture was 52 mL min^{-1} , and the gas hourly space velocity was 1,7316 h^{-1} . The effluent gas stream from the reactor was analyzed online by the thermal conductivity detector of parallel gas chromatography (Younglin Instrument Co., Ltd, Anyang, Korea) with a Carboxen 1000 column. In order to determine the conversion, the products were collected during 40 min of steady-state operation at each temperature. The empty reactor (without catalyst) showed no activity under identical conditions.

4.3 Results and discussion

To construct a suitable MOF precursor for hierarchically porous carbon (HPC), we chose a Zn-MOF with mixed ligands such as aromatic and aliphatic ligands, instead of using reported robust aromatic ligand-based Zn based MOFs. Though a simple self-assembly, adipate and phenanthroline (phen) coordinate a Zn^{II} ion with one water molecule to yield white precipitates, [Zn(adipate)(phen)(H_2O)] (Figure 4.4).[11] A simplified method to prepare the Zn-MOF in gram scale synthesized a coincident phase of a single crystal, as shown in XRPD (Figure 4.5). TGA results showed the evaporation of coordinating a water molecule at 140 °C (calculated 4.4%, experimental 4.6%) and the destruction of Zn-based MOFs above 300 °C, with a loss of the decomposed organic substances from ligands (Figure 4.6). At 650 °C, additional and slight weight loss occurred indicating the release of metallic Zn species. This is an important difference from the MOF-5, as a representative of robust aromatic ligand-based Zn-MOF, where the process of removing Zn metal usually occurs above 750 °C. Due to the temperature shift downward for a mixed ligand system, the conversion reaction can be carried out at lower temperatures to remove metallic Zn species, obtaining pure HPC with high yield. In observing the conversion behavior, the XRPD patterns measured at RT exhibit hexagonal ZnO peaks, implying the formation of metallic Zn/ZnO at 600 °C that was completely evaporated at 800 °C (Figure 4.7a). The Zn metal are formed via reduction by carbon during heat treatment, that is the carbothermic reduction.[10] TEM images of samples obtained after thermal treatment at different temperatures reveal that as the temperature of thermolysis increases, the carbon porosity has developed upon decomposition of organic ligands and release of metallic Zn (Figure 4.7b). Especially, as proved by nitrogen adsorption-desorption measurements, the carbon material derived from [Zn(adipate)(phen)(H_2O)] is HPC with micro- and mesoporosity while MOF-5 comprised of only aromatic ligand converted into micropore-dominated carbon materials (Figure 4.8). Accordingly, the introducing aliphatic ligands into a precursor MOF is critical for changing the thermal stability of MOFs as well as the controlling textural properties of the resultant carbons.

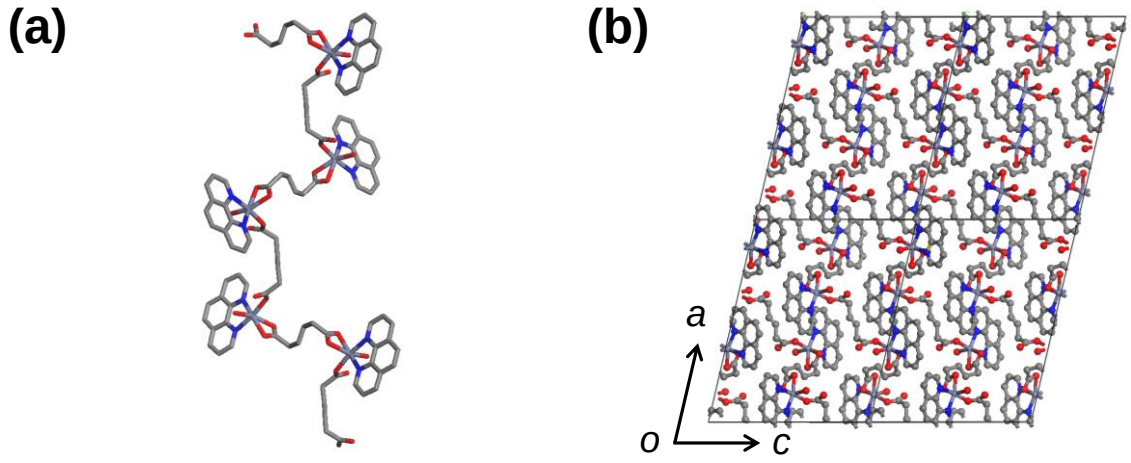

Figure 4.4 X-ray single crystal structures of a Zn-based MOF, [Zn(adipate)(phen)(H_2O)] for (a) its 1-D chain and (b) *ac* plane.

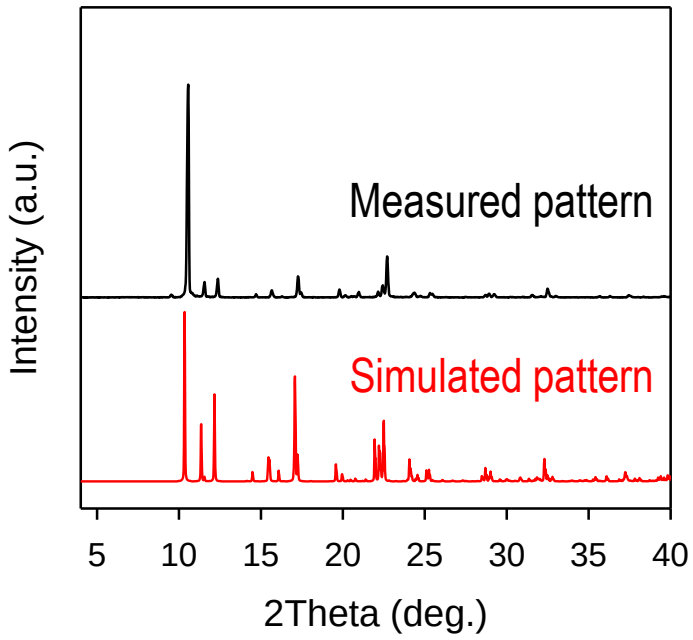

Figure 4.5 XRPD results of simulated pattern (red) and measured pattern (black) of as-synthesized [Zn(adipate)(phen)(H_2O)].

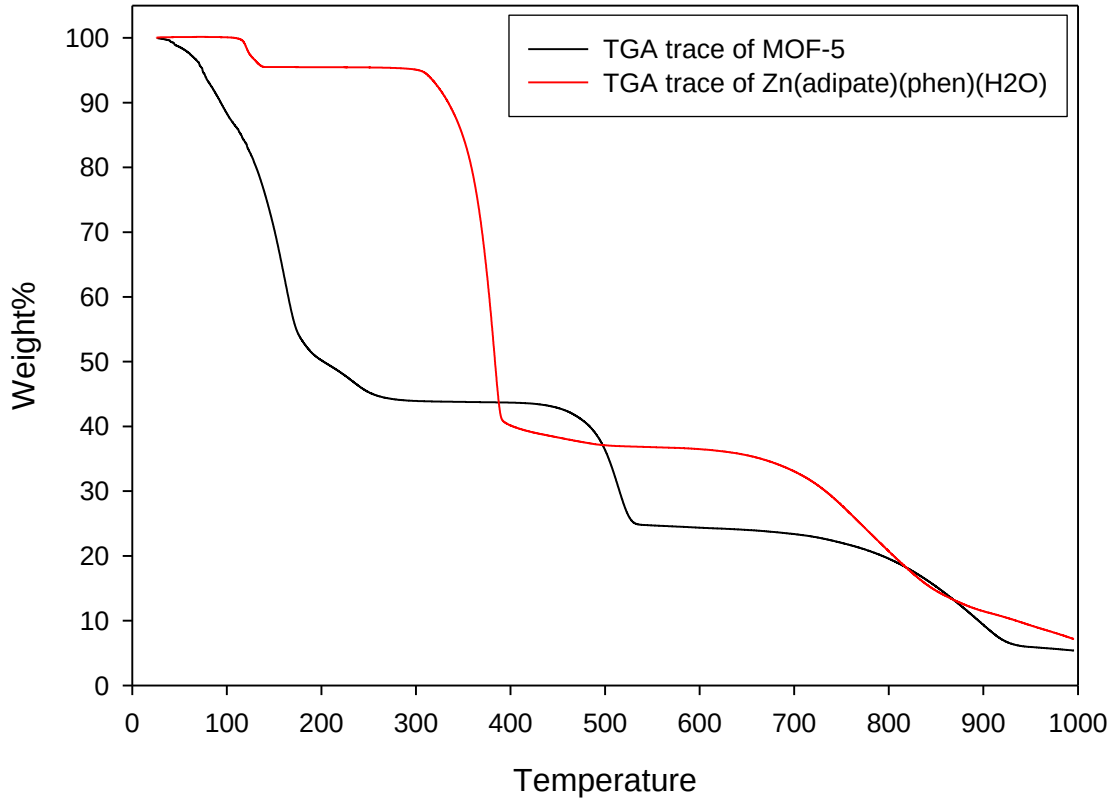

Figure 4.6 Comparison of TGA traces of [Zn(adipate)(phen)(H_2O)] (red) and MOF-5 (black).

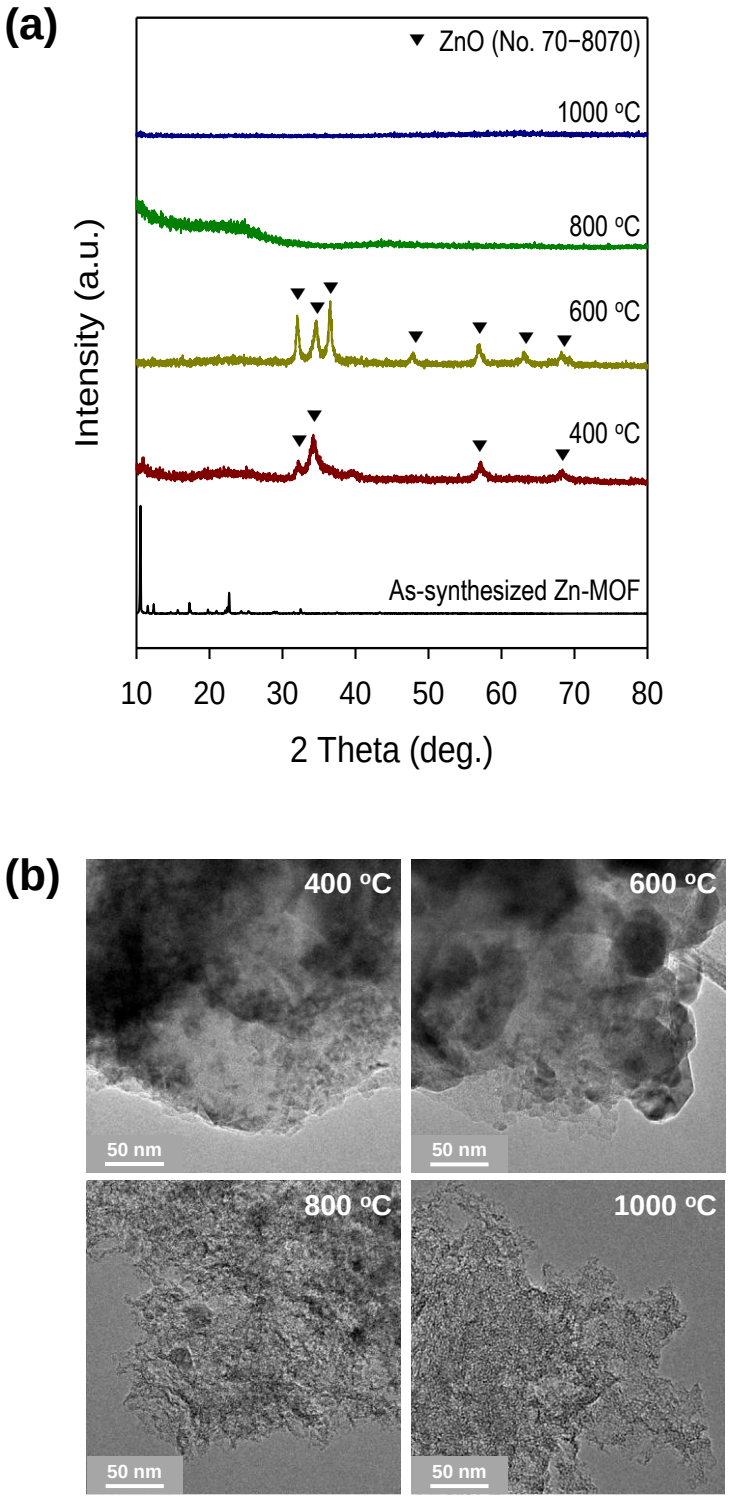

Figure 4.7 Thermal conversion of [Zn(adipate)(phen)(H_2O)]. (a) Variable temperature XRPD patterns of a Zn-MOF. (b) TEM images after heat treatment of a Zn-MOF from 400 °C to 1000 °C with 200 °C increments.

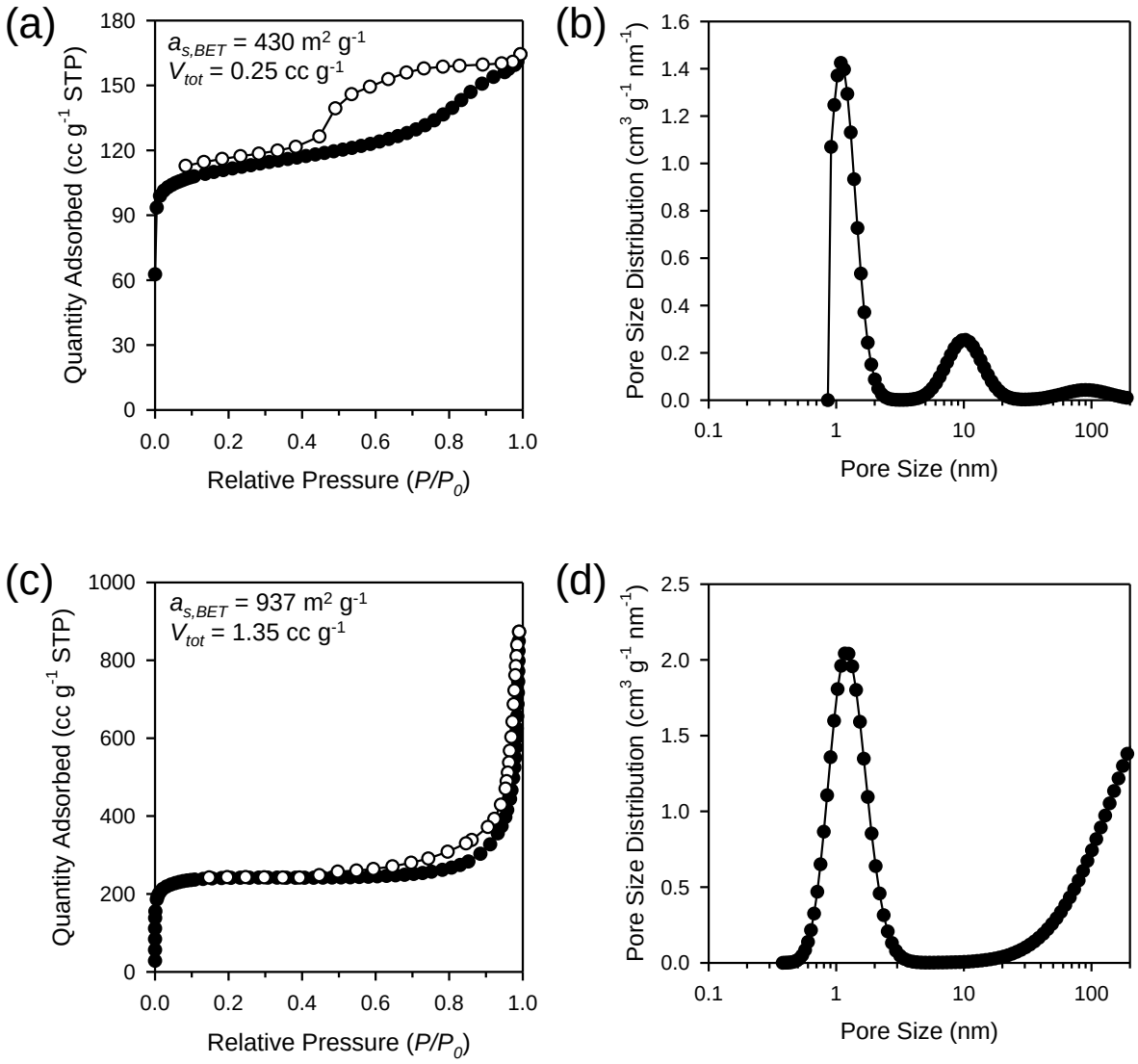

Figure 4.8 N_2 sorption isotherms and NLDFT pore size distribution curves (inset) of the material converted from (a)-(b) [Zn(adipate)(phen)(H_2O)], and (c)-(d) MOF-5.

Upon our understanding of thermally induced transformation of the Zn-MOF, its thermolysis (0.12 g) with GeO_2 (0.1 g) was conducted under an inert atmosphere. As evidenced by XRPD (Figure 4.9), the zincothermic reduction occurred actively at 700 ℃ to produce Ge metal (JCPDS no. 04-0545) along with Zn species. Meanwhile, the XRPD pattern at 800 ℃ only appears diffraction of cubic germanium without any impurities, revealing that the redox-reaction between Zn species and GeO_2 was finished to obtain Ge/HPC composites. The absence of Zn-related peaks implies that ZnO, which is the by-product of zincothermic reaction, was entirely reduced to metallic Zn through a carbothermic reduction, and then vaporized. The quantitative analysis estimated by the XRPD patterns also verifies the conversion of Ge^{4+} to Ge^0 as a reaction temperature increased (Figure 4.10a). When the reaction temperature increases up to 900 ℃, nevertheless the Ge/HPC yield considerably decreased, compared to the yield synthesized at 800 ℃ (from 0.0628 g to 0.004 g), which indicates the vaporization of Ge nanoparticles as well as carbogenic species at the higher temperature. Thus, we determined optimized conditions to produce Ge/HPC with high yield and purity as thermal conversion at 800 ℃ for 6 h under N_2.

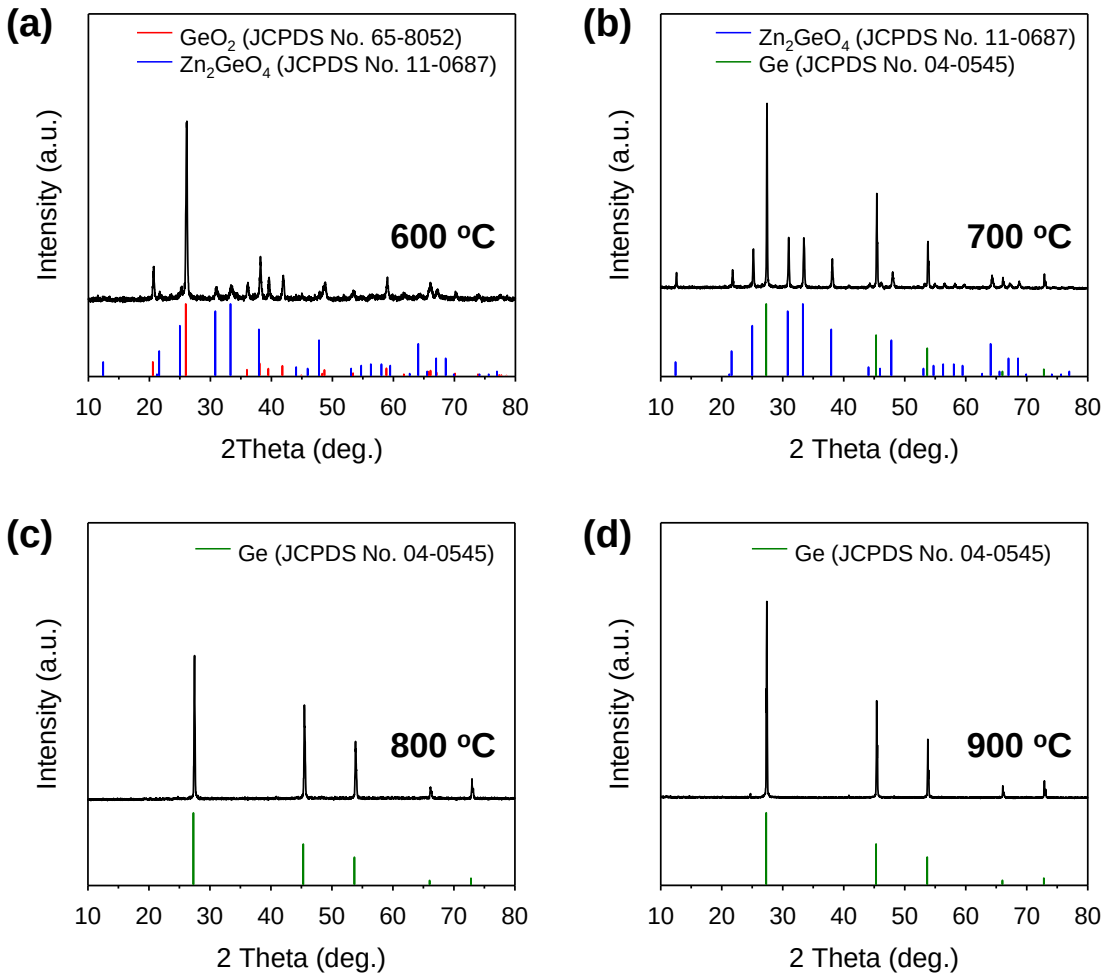

Figure 4.9 XRPD patterns after thermolysis for a mixture of GeO_2 and a Zn-MOF with fixed molar ratio at various temperature for 6 h. (a) 600 °C, (b) 700 °C, (c) 800 °C, and (d) 900 °C.

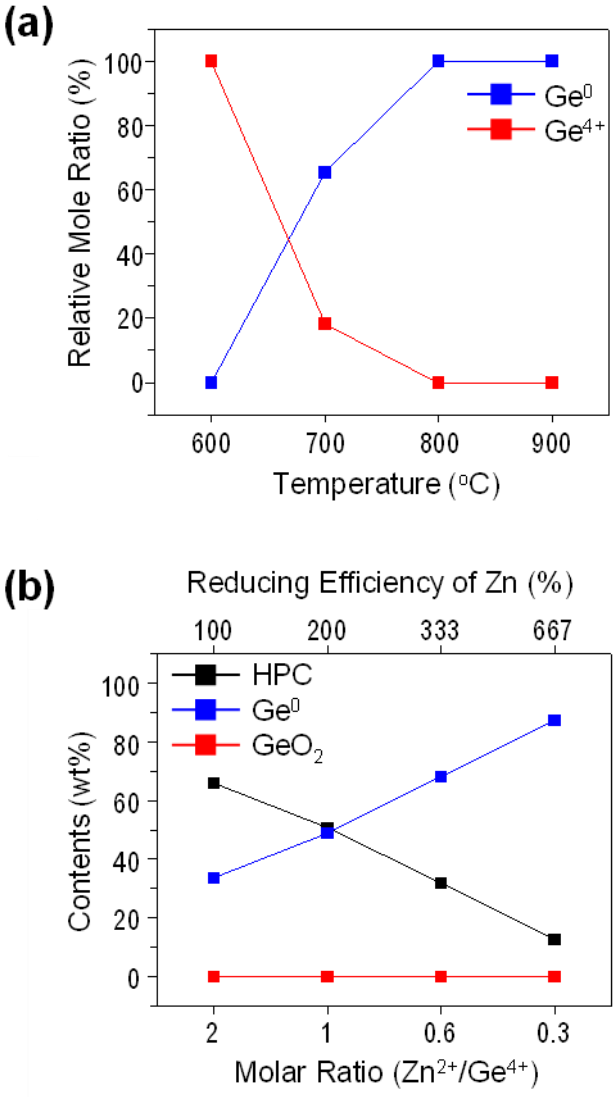

Figure 4.10 (a) Relative mole ratio of Ge^{0} and Ge^{4+} species in the materials after thermal conversion at different temperature. (b) Elemental composition of Ge/HPC series with different molar ratio of Zn^{2+} to Ge^{4+}.

We should recognize that the redox-zincothermal reaction took place due to a stoichiometric relationship, where one mole of GeO_2 reacts with two moles of Zn to produce one mole of Ge and two moles of ZnO. However, as mentioned earlier, ZnO automatically returns to Zn metal via carbothermic reduction during the conversion in the present system. Thus, upon assumption that Zn could be reuse for the reduction of GeO_2 as a reducing agent again, we performed conversion experiments with decreased molar ratios of Zn-MOF to GeO_2, from the stoichiometrically essential amount (Zn^{2+}/Ge^{4+} = 2) to 667% excess of GeO_2 (Zn^{2+}/Ge^{4+} = 0.3) (Table 4.1). As shown in Figure 4.11, in XRPD patterns, all GeO_2 was completely reduced to metallic Ge regardless of the controlling ratio of those precursors exhibiting that the zincothermic and carbothermic reduction reactions repeatedly occur, affording a recyclable redox-metallothermic reaction. Figure 4.10b shows the tendency of contents and reducing efficiency of Zn in Ge/HPC composites as a function of the Zn^{2+}/Ge^{4+} molar ratio used as precursors. Since the carbon and zinc amounts are inseparable in the MOF, using the different ratio of Zn^{2+}/Ge^{4+} leads to different loading amounts of Ge on HPC.

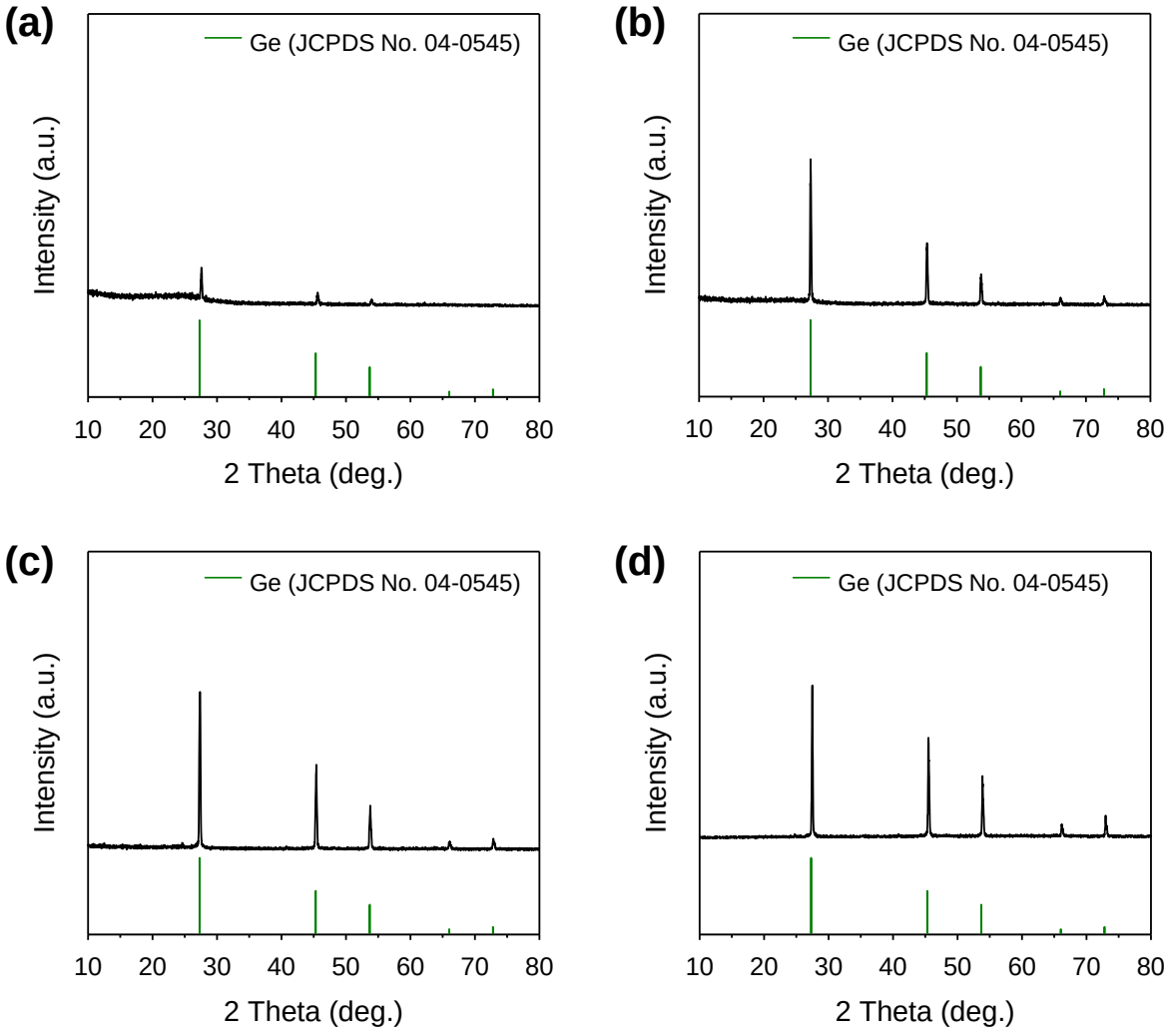

Figure 4.11 XRPD patterns of Ge/HPC series after heat treatment at 800 ºC for 6 h. (a) Ge/HPC-2. (b) Ge/HPC-1. (c) Ge/HPC-0.6. (d) Ge/HPC-0.3.

To verify the repeated redox metallothermic reaction ascribed to the Zn-MOF, we carried out thermal treatment of GeO_2 powder with only organic ligands, phenanthroline and adipic acid, under optimized conditions. Whereas the Ge/HPC is black powder, the product from this comparing experiment is a white solid, which is revealed as GeO_2 by XRPD without metallic phase (Figure 4.12). This resultant GeO_2 is comprised of a hexagonal phase as same as phase of the starting material and a tetragonal phase as a thermodynamically stable product.[14,15] Based on this result, the exclusive use of organic ligands cannot reduce germanium dioxide even at high temperatures. Additionally, a previous report produced a GeO_2/Ge/C composite which was partially reduced GeO_2 by using reductive acetylene gas.[16,17] Therefore, our synthetic strategy of Zn-based MOF thermal conversion is the clever system for synthesizing pure metallic Ge with HPC as metal-carbon composites. This recyclable redox-metallothermic reaction was successfully reduced other metal oxides including In_2O_3, Bi_2O_3, and SnO (Figure 4.13 and Table 4.2). Via thermal conversion with a Zn-based MOF, All metal oxides regardless of the type of metal species were entirely reduced to pure metallic phase.

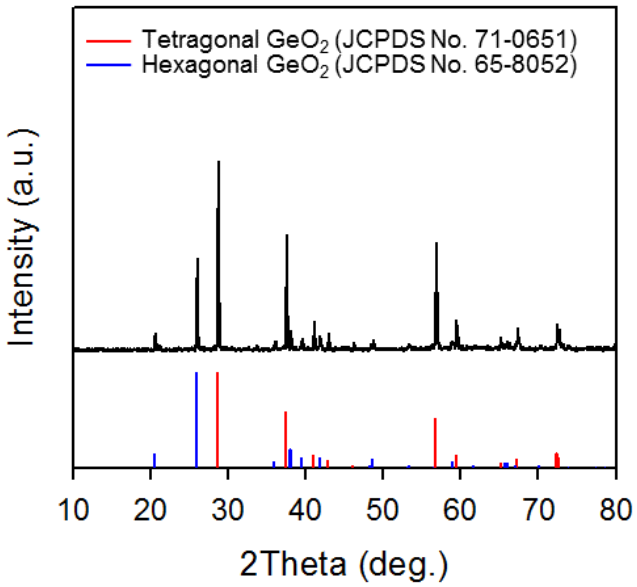

Figure 4.12 XRPD pattern after heat treatment for a mixture of organic ligands and GeO_2 at 800 °C for 6 h.

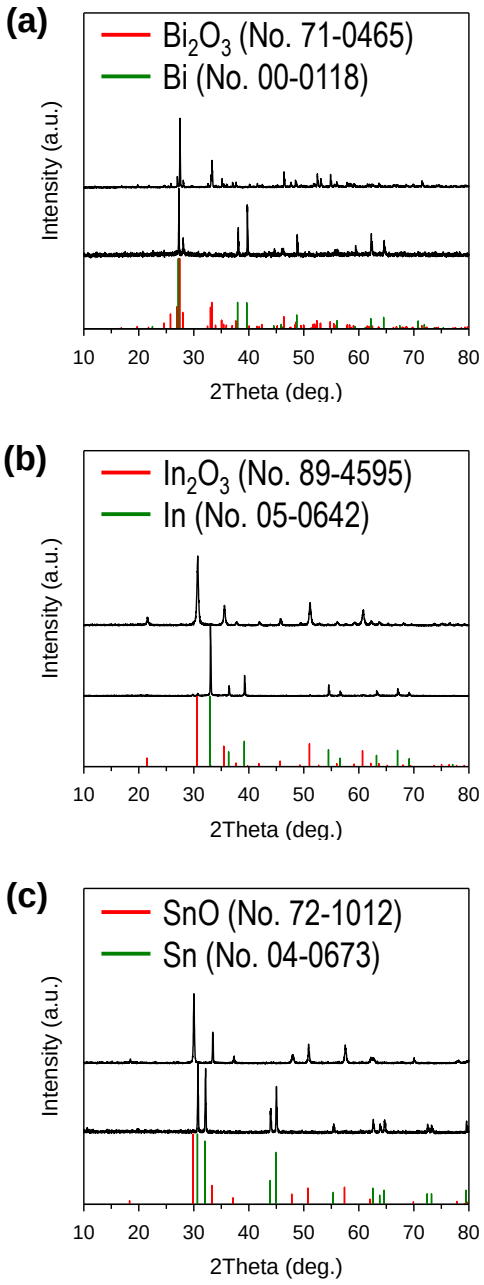

Figure 4.13 XRPD patterns before (top) and after (bottom) thermal conversion of a Zn-MOF mixture with (a) Bi_2O_3, (b) In_2O_3, or (c) SnO.

Based on these results of various reactions, we optimized the synthetic conditions for the Ge/HPC composite such as a reactant ratio (Zn^{2+}/Ge^{4+}) of 1, a target temperature of 800 ℃, obtaining Ge/HPC-1 (Ge/HPC-X, where X denotes the Zn^{2+}/Ge^{4+} molar ratio in the precursors). SEM images of Ge/HPC-1 shown that Ge particles are embedding in the HPC carbon matrix (Figures 4.14a and b). TEM image and EDS also revealed that metallic Ge are well-dispersed all over HPC matrix with a size of ca. 150 nm (Figure 4.15). As shown in Figure 4.14c, D- and G-bands of Raman spectrum (Figure 4.14c) exhibited that Ge/HPC-1 possesses the graphitic carbon as well as amorphous carbon in carbon matrix. The single sharp band at 300 cm^{-1} is corresponding to the metallic phase of Ge. In order to evaluate the porosity of the Ge/HPC-1, N_2 adsorption-desorption measurement was carried out (Figure 4.14d). Ge/HPC-1 shown a typical type IV isotherm with an *H2* type hysteresis loop over a relative pressure range of $0.45 < P/P_0 < 0.99$, characteristic of cage-like pore structure with meso- and micropores. The pore size distribution curve analyzed using a nonlocal density functional theory (NLDFT) algorithm (Figure 4.14d, inset) shown not only micropores centered at 0.9 nm but also mesopores around 2.0 nm. The Brunauer-Emmett-Teller (BET) surface area for the Ge/HPC-1 was 140 $m^2 \cdot g^{-1}$, and the total pore volume was 0.1 $cc \cdot g^{-1}$.

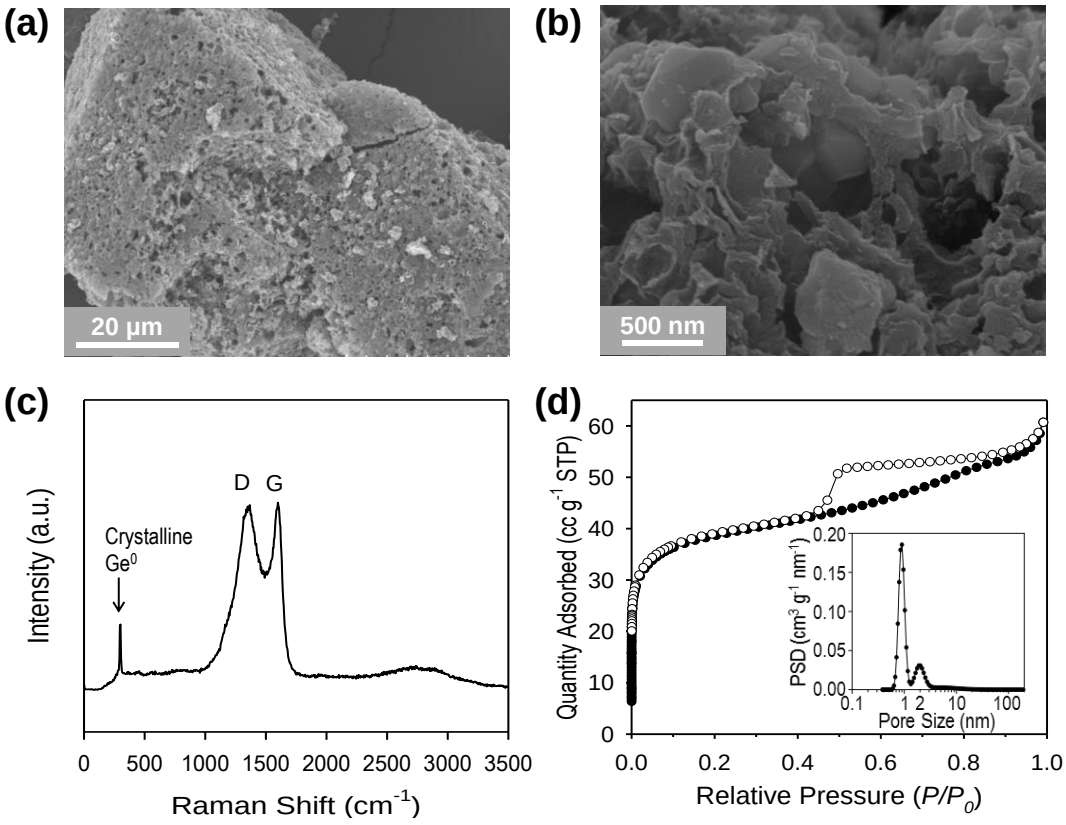

Figure 4.14 Structural investigation of Ge/HPC-1. (a,b) SEM images, (c) Raman spectrum, and (d) N_2 sorption isotherm and NLDFT pore size distribution curve (inset) of Ge/HPC-1.

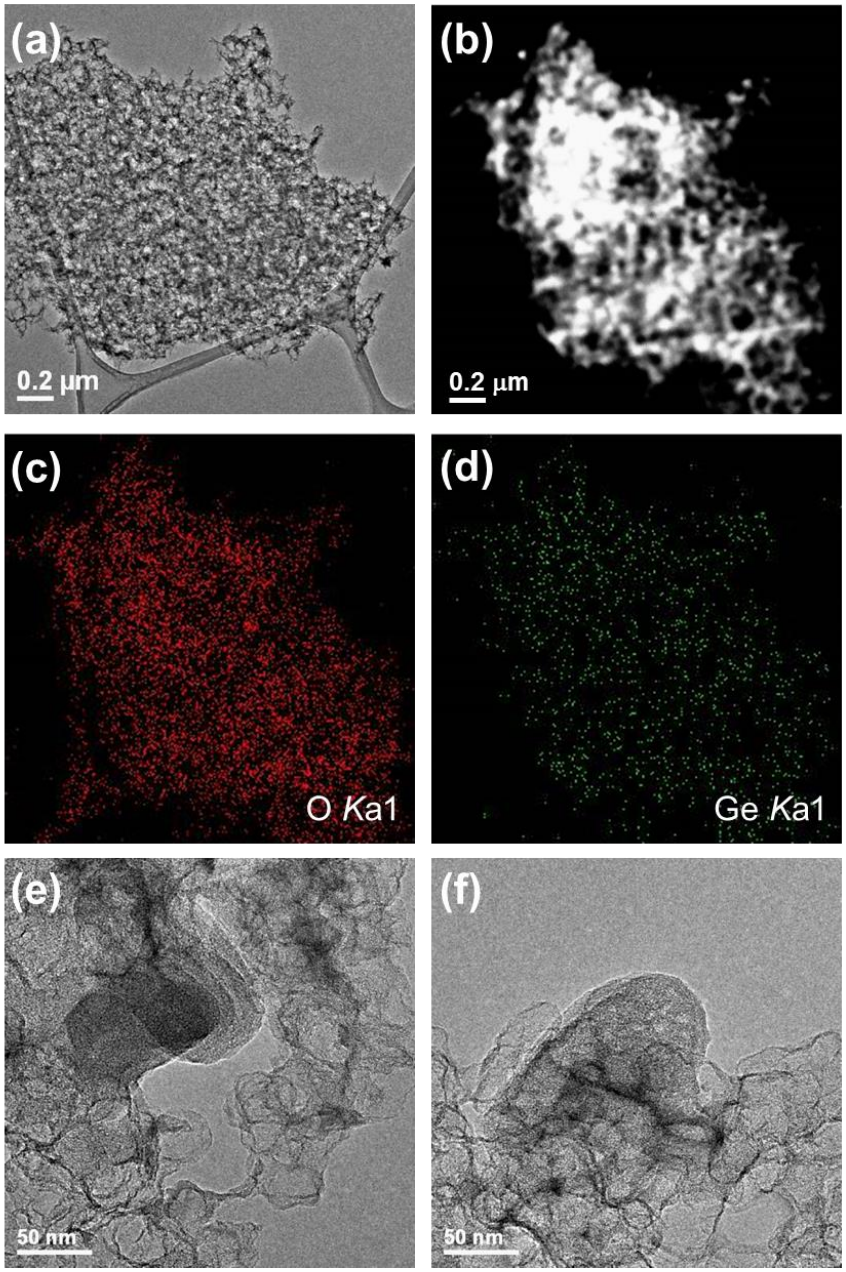

Figure 4.15 TEM images with various magnifications and EDS mapping of Ge/HPC-1.

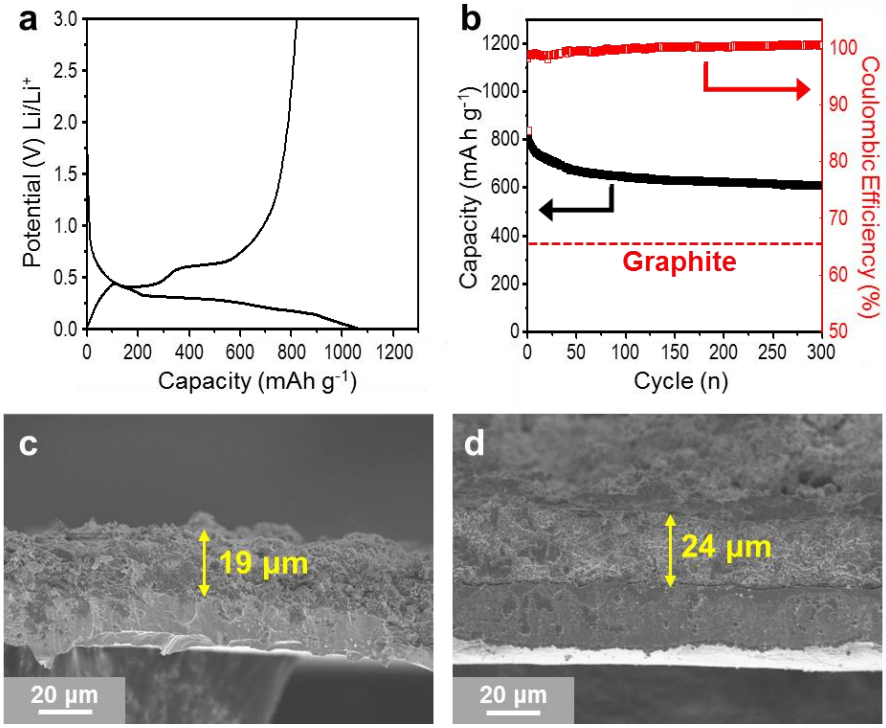

Figure 4.16 (a) First cycle voltage profile of Ge/HPC-1 at rate of C/20, and (b) cycle performance of Ge/HPC-1 at a 0.5 rate in the range of 0.01–3.0 V. Cross-sectional SEM images of Ge/HPC-1 electrode (c) before and (d) after 300 cycles.

Ge/HPC-1 and the compared materials Ge/HPC-2 and Ge/HPC-0.6 having different loading amount of electrochemically active Ge were investigate the performance as anode materials in LIBs. Galvanostatic discharging (= lithiation) and charging (= delithiation) curves of these Ge/HPC electrodes were obtained in a potential window of 0.01–3.0 V at different current densities. In the first cycle voltage profiles of the Ge/HPC-2, -1, and -0.6 electrodes at a rate of C/20, the discharge capacities were 985, 1061, and 1155 mA h g^{-1} with different amounts of Ge, which were corresponded to initial coulombic efficiencies of 60, 77.4, and 79.7%, respectively (Figures 4.16a and 4.17a–c). As the carbon contents with high surface area increased, the initial coulombic efficiency of the composite electrodes decreased due to a side reaction between carbon and the electrolyte. However, the cycling performance of the Ge/HPC anodes shows the opposite tendency (Figures 4.16b and 4.17d–f). Ge/HPC-0.6 with high Ge content shown poor capacity retention (48.2% after 300 cycles), which would be attributed to the large volume change experienced by Ge particles over repeated cycles (Figure 4.17f). In contrast, the Ge/HPC-2 and Ge/HPC-1 materials, where Ge particles are well dispersed in the HPC carbon matrix, exhibited highly stable cycling performances with a capacity retention of 74.2% for Ge/HPC-2 and 76.6% for Ge/HPC-1 (Figures 4.16b and 4.17e). The Ge/HPC-2, Ge/HPC-1, and Ge/HPC-0.6 anodes exhibited usable capacities of 400 mA h g^{-1}, 607 mA h g^{-1}, and 492 mA h g^{-1} after 300 cycles at a 0.5 C rate,

respectively, much higher than conventional graphite anodes (~350 mA·h·g^{-1}). Therefore, proper amounts of electrochemically active Ge and HPC should be combined to provide high reversible capacity and extra void space to accommodate this large volume change during the lithiation/delithiation process.

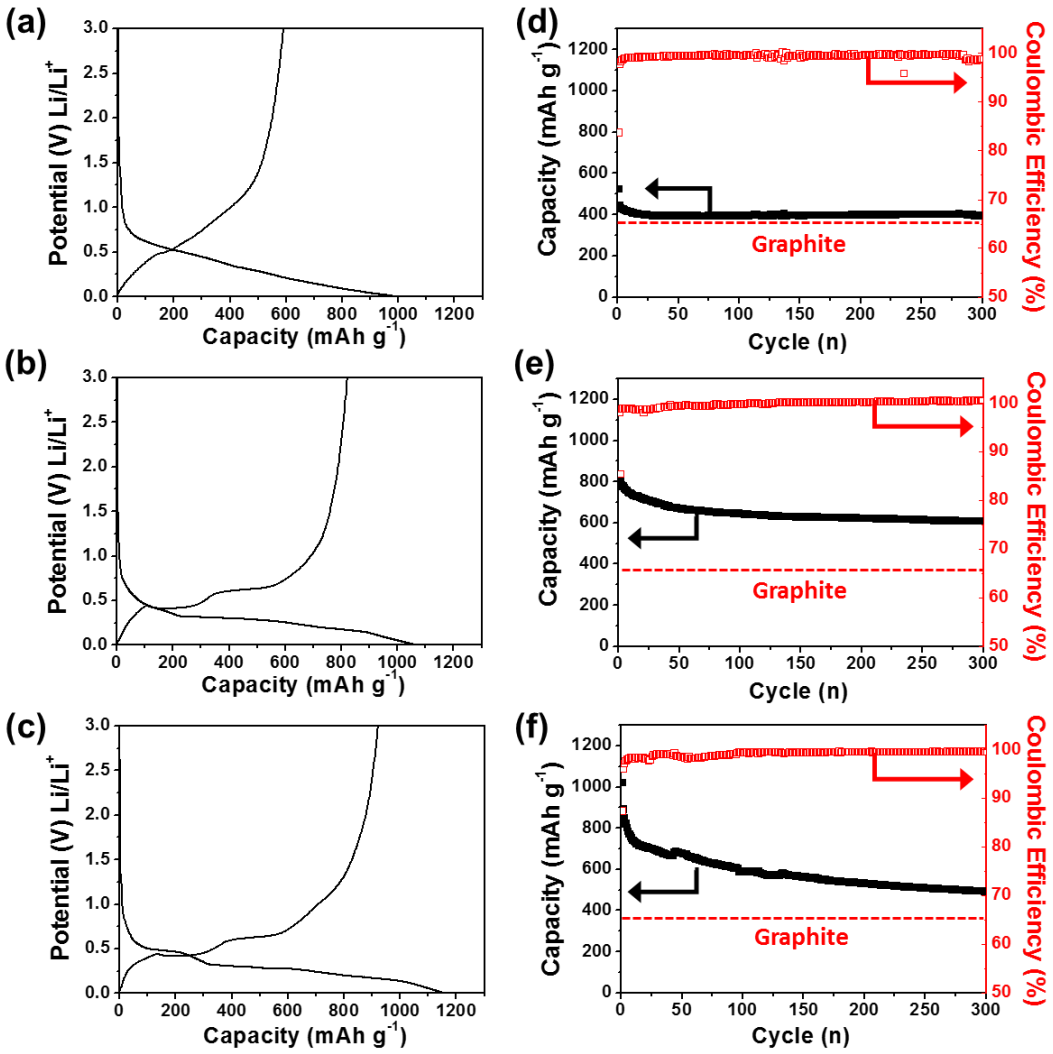

Figure 4.17 Electrochemical performances of Ge/HPC series composite electrodes with three different Ge contents (33% for Ge/HPC-2 (a),(d), 50% for Ge/HPC-1 (b),(e), 68% for Ge/HPC-0.6 (c),(f)). (a-c) The first cycle voltage profiles of each electrode obtained at a rate of C/20 in the range of 0.01-3.0 V. (d-f) Cycle performances of three Ge/HPC series electrodes obtained at 0.5 rate in the range of 0.01-3.0 V.

When we examined the swelling of Ge/HPC electrodes after 300 cycles, the electrode thickness was quite similar to that of an as-fabricated electrode (Figures 4.16c and 4.18a–c). The electrode thickness of Ge/HPC-2 and Ge/HPC-1 was significantly suppressed, corresponding to a swelling of < 30% after long-term cycling (Figures 4.16d and 4.18d). This result demonstrates that Ge nanoparticle-encapsulated HPC mitigates a large volume change during repeated cycles, resulting in highly stable cycling performance. In contrast, the Ge/HPC-0.6 electrode showed a relatively large increase in electrode thickness (swelling of > 70%) due to inefficient wrapping of HPC by its high Ge content (Figure 4.17f).

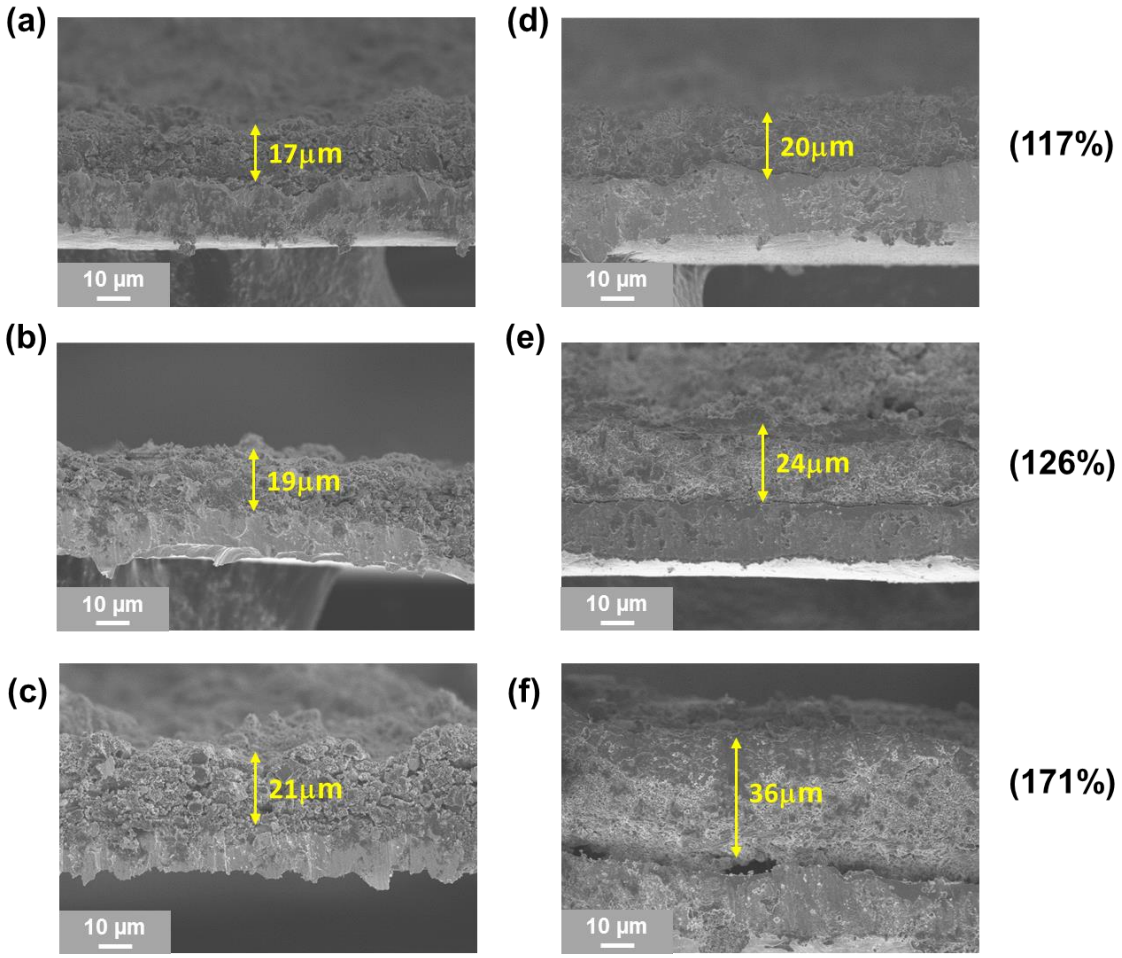

Figure 4.18 Cross-sectional SEM images of Ge/HPC-2 electrodes (a) before and after (d) 300th cycle, Ge/HPC-1 electrodes (b) before and after (e) 300th cycle, and Ge/HPC-0.6 electrodes (c) before and after (f) 300th cycle.

The outstanding electrochemical performances of Ge/HPC composite electrodes can be described as follows. (i) A appropriate molar ratio of Zn-MOF and GeO_2 results in the formation of Ge/HPC composites showing stable cycling performance. (ii) Control over the contents of Ge and HPC enables us to improve the cycling stability by inhibiting particle fracturing and diminishing the volume change underwent during cycling. Finally, (iii) HPC considerably improves the electrical conductivity of Ge and serves as a buffer, which can mitigate a significant volume change of electrochemically active Ge particles during repeated cycling.

As an alternative scheme to the conversion of MOFs into new nanomaterials, MOF-supported nanoparticles could transform into mixed metal oxide embedding into carbon matrix via gas phase CO oxidation. Previous studies reported the formation of metal nanoparticles into pores of MOF scaffold through redox couple-driven method by exploiting redox potential differences between additional metal ions and redox-active MOFs (*ra*-MOFs).[13,18,19] First, we synthesized Pd nanoparticles embedded in Ni-based *ra*-MOF (Pd@*ra*-MOF) via the redox couple-driven method. During gas phase CO oxidation, we found that the Pd@*ra*-MOF transformed into mixed metal oxide-carbon composites (PdO_x-NiO_y/C). The converted metal oxide-carbon composite showed improved and sustainable catalytic activity toward CO oxidation.

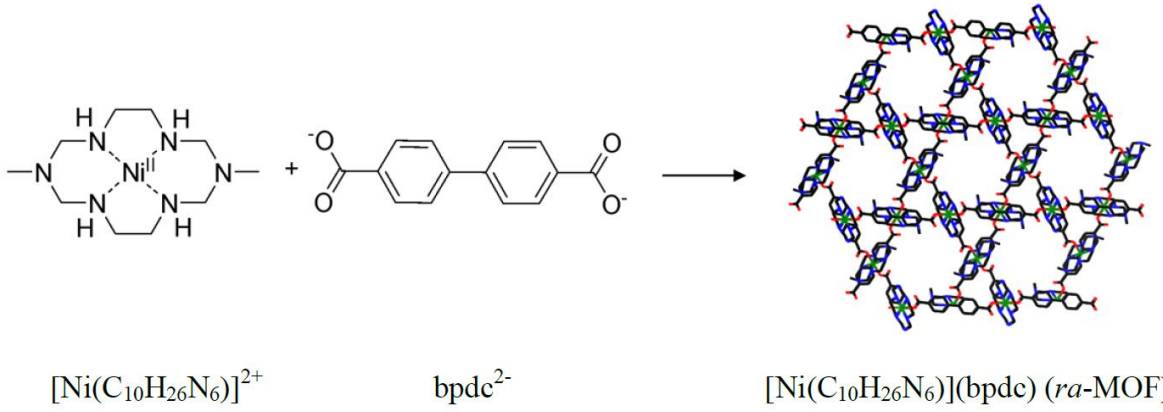

Figure 4.19 Synthetic scheme of *ra*-MOF by self-assembly of $[Ni(C_{10}H_{26}N_6)]^{2+}$ and $bpdc^{2-}$.

$[NiL_{CH3}](bpdc)$, composed of Ni(II) hexaaza macrocycle and linear-shaped carboxylate and had one-dimensional channels with a 7.3-Å pore opening (Figure 4.19), was chosen as the *ra*-MOF.[13] In the previous report,[13,18,19] the MOF constructed by Ni(II) macrocyclic complexes and multidentate carboxylate ligands possesses redox-active properties that derived from the six-coordinated Ni(II) sites. The *ra*-MOF, $[NiL_{CH3}](bpdc)$ (bpdc = 4,4′-biphenyldicarboxylate), was synthesized by the facile self-assembly of $[NiL_{CH3}](ClO_4)_2$ macrocycle and Na_2bpdc ligand in a H_2O/pyridine mixture, producing $[(NiL_{CH3})_3(bpdc)_3]\cdot 2pyridine\cdot 6H_2O$. After activating at 120 ℃ under dynamic vacuum for 3 h and subsequently soaking the *ra*-MOF in a Pd^{2+} solution at RT for 10 min, Pd NPs were spontaneously formed in the *ra*-MOF scaffold (Pd@*ra*-MOF). Based on the oxidation potential of Ni(II) to Ni(III) in the macrocyclic complexes ranges from 0.90 to 0.93 V,[20] the redox reaction of a *ra*-MOF possessing Ni(II) macrocyclic complexes with Pd ions results in the simultaneous oxidation of Ni(II) to Ni(III) and the reduction of Pd(II) ions to the metallic Pd NPs.

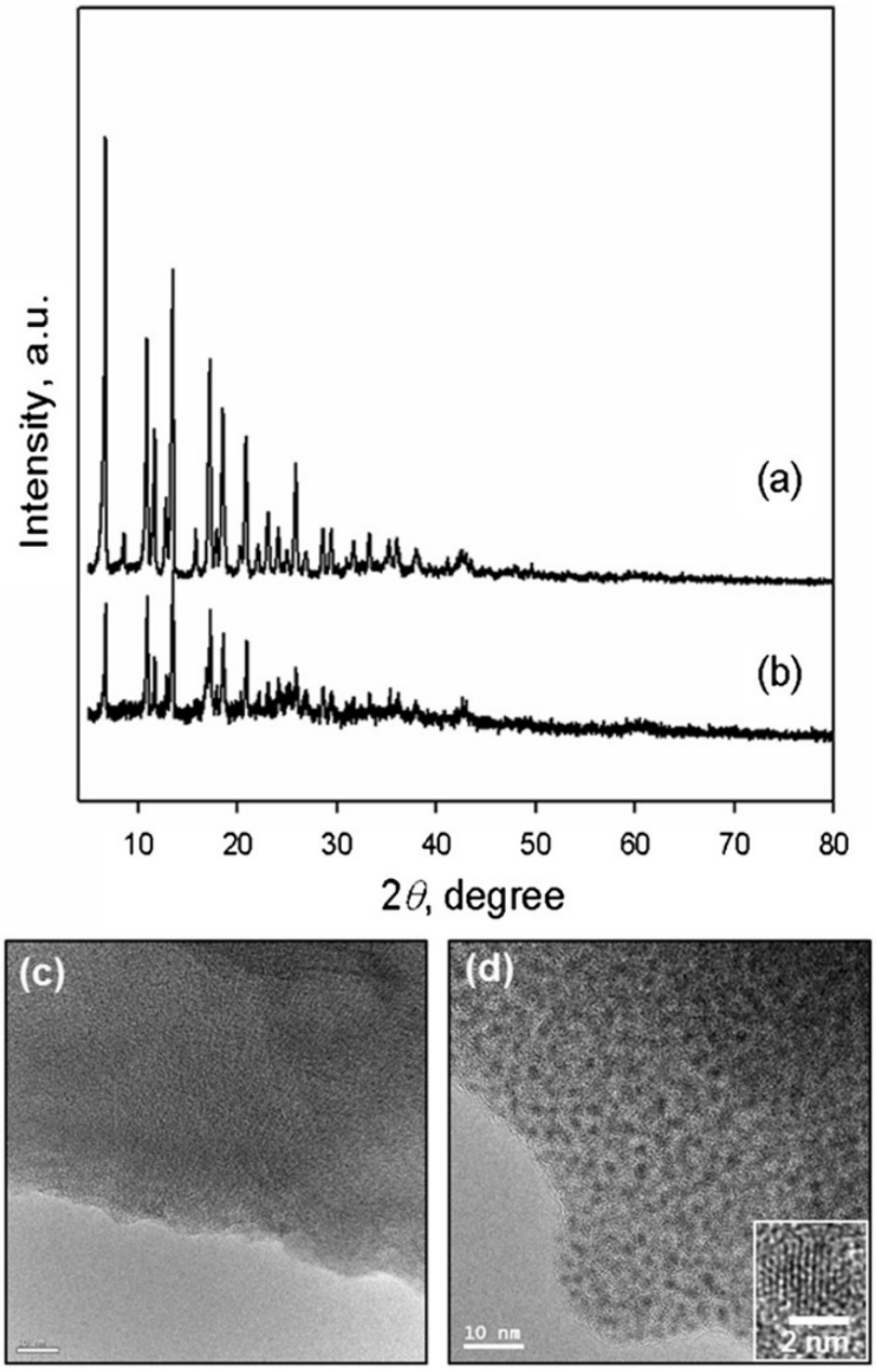

Figure 4.20 XRD patterns and TEM images of (a, c) *ra* -MOF, and (b, d) Pd@*ra*-MOF, respectively.

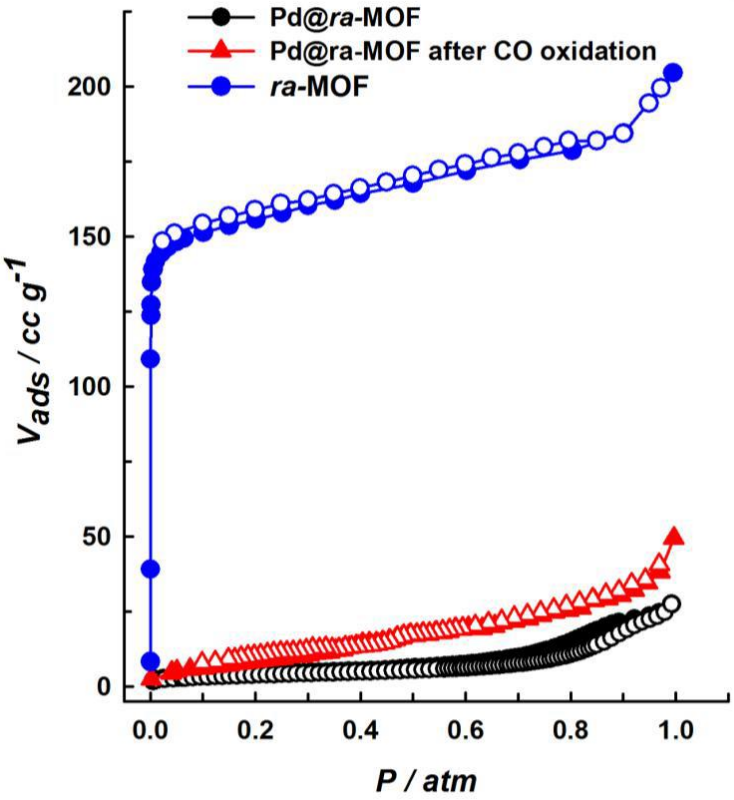

Figure 4.21 Comparison of N_2 sorption data for *ra*-MOF and Pd@*ra*-MOF before and after CO oxidation reaction

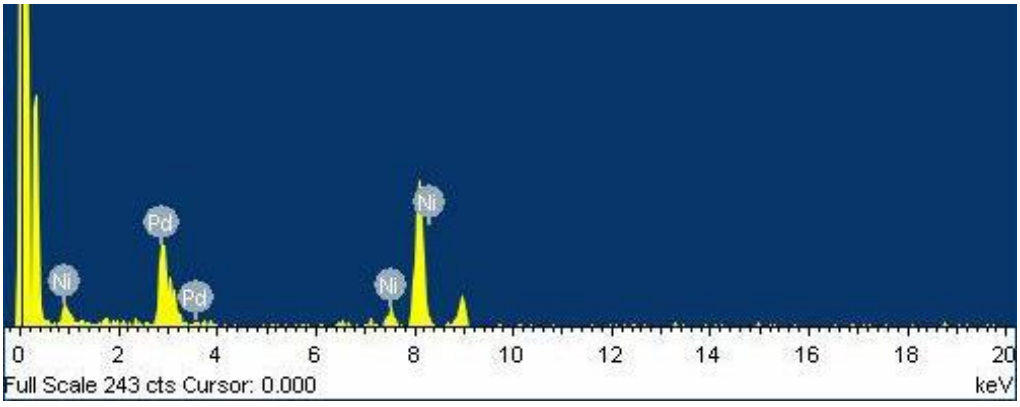

Figure 4.22 EDS result of Pd@*ra*-MOF

Figure 4.20 (a) and (b) exhibit the XRD patterns of the as-synthesized *ra*-MOF and Pd@*ra*-MOF. The intensities of XRD peak measured from Pd@*ra*-MOF quite decreased compared to those of the as-synthesized *ra*-MOF, which would be attributed to not only the partial destruction of a crystalline framework of *ra*-MOF but also the occupation of Pd NPs in the pores of the MOF scaffold. This result was also supported by N_2 adsorption measurements. The specific BET surface areas estimated from N_2 adsorption significantly decreased from 462 to 14 $m^2 g^{-1}$ upon the formation of Pd NPs in the *ra*-MOF (Figure 4.21). There are no specific peaks from metallic Pd in the XRD pattern of Pd@*ra*-MOF, indicating that small-sized Pd NPs were too small to appear in XRD pattern and homogeneous dispersed throughout the *ra*-MOF support. The *ra*-MOF and Pd@ra-MOF materials were analyzed by TEM images (Figure 4.21c and d) and EDS (Figure 4.22). The TEM image clearly exhibited that small Pd NPs that were 1.8 ± 0.3 nm in diameter with narrow distribution were well dispersed throughout the *ra*-MOF matrix. A HR-TEM image (Figure 4.20d, inset) clearly showed the lattice fringes of metallic Pd, indicating the single crystallinity of Pd NPs in Pd@*ra*-MOF. As determined by inductively coupled plasma (ICP) analysis, the loading amount of Pd metal in the *ra*-MOF was calculated to be 3.6 wt.%.

The catalytic properties of Pd@*ra*-MOF were examined by using CO oxidation as a probe reaction, and the bare *ra*-MOF without Pd NPs was also tested as comparison. The catalytic oxidation of CO to CO_2 has long been a benchmark reaction in heterogeneous catalysis; it is a continuous subject of fundamental mechanistic studies as well as of practical importance in many industrial processes, including the reduction of CO in automobile exhaust gases and the selective oxidation of fuel streams for polymer electrolyte fuel cells.[21-23] CO oxidation was performed in a fixed bed flow reactor at elevated temperatures under atmospheric pressure in a mixed gas composed of 3.0% CO, 8.5%O_2, and 88.5% He. As shown in Figure 4.23, the as-synthesized *ra*-MOF shown poor catalytic activity, as evidenced by a very high CO conversion temperature, with T_{50} and T_{100} (temperatures for 50% and 100% conversion, respectively) being 364℃ and 500℃, respectively. Sequent four runs exhibited similar catalytic performances. On the contrary, the loading of Pd NPs into *ra*-MOF gave rise to markedly lower conversion temperatures of T_{50} and T_{100} at 222℃ and 250℃, respectively, that means, the Pd@*ra*-MOF had slightly improved catalytic activity over the *ra*-MOF for CO oxidation. However, the catalytic abilities of Pd@*ra*-MOF in the first run are not superior to those of other Pd-based catalysts, and this may come from the significantly decreasing surface area after synthesizing of larger-sized Pd NPs than the channel size of *ra*-MOF, which is hard to access CO and O_2 molecules to catalytic active Pd NPs embedded in *ra*-MOF. The CO oxidation activities over Pd@*ra*-MOF were repeatedly explored, and the Pd@*ra*-MOF displayed further lowered conversion temperatures in the second run, with decline in T_{50} and T_{100} to 125℃ and 150℃, respectively, thus indicating substantially improved CO oxidation activity as compared to the first run (Figure 4.23). Based on this result, we assumed the formation of new species from the Pd@*ra*-MOF material during the first run for CO oxidation reaction. As shown

in Figure 4.23, three more reaction runs over the Pd@*ra*-MOF produced the same results as the second run, exhibiting its long-term stability.

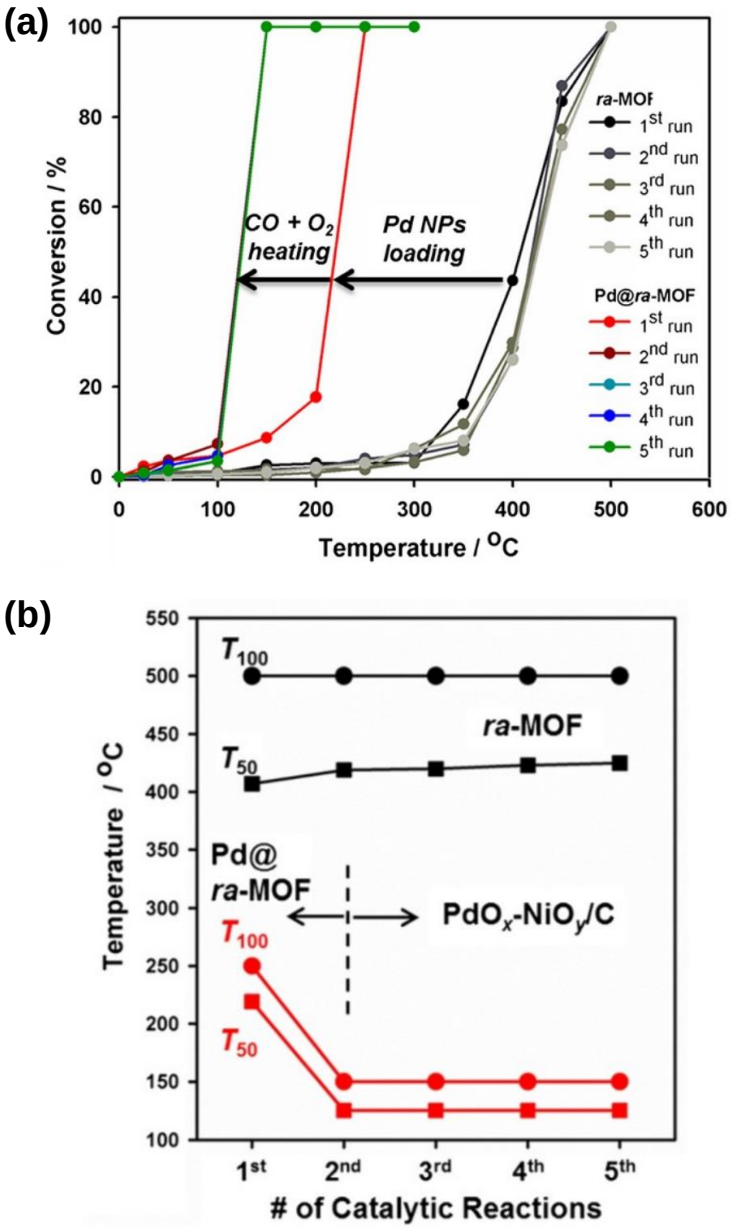

Figure 4.23 Catalytic activities and conversion temperatures. (a) Catalytic performance for CO oxidation of the as-prepared *ra*-MOF and Pd@*ra*-MOF. (b) Comparison of T_{100} and T_{50} for *ra*-MOF and Pd@*ra*-MOF according to the number of cycles.

To investigate the structural and compositional transformation of the Pd@*ra*-MOF during a gas phase CO oxidation reaction, the XRD patterns and TEM images of the as-synthesized *ra*-MOF and Pd@*ra*-MOF after catalytic reactions were compared (Figure 4.24 and 25). The XRD pattern of the *ra*-MOF after the 5th run of the catalytic reactions (Figure 4.24a) was entirely different from that of the as-prepared *ra*-MOF (Figure 4.20a), assigning as a cubic phase of NiO (JCPDS 47–1049). Thus, during CO oxidation, building blocks of *ra*-MOF scaffolds were converted into different species under oxidative reaction conditions. Thermally labile hexaaza macrocyclic ligands, L_{CH3}, coordinating Ni ions in the *ra*-MOF could be easily destructed and underwent chemical reactions during a catalytic reaction at high temperature. This was supported by the XPS of the *ra*-MOF, whose N content determined to almost zero after CO oxidation reaction (Figure 4.26). During the catalytic reaction condition, Ni ions comprised of *ra*-MOF scaffolds were oxidized to form NiO and/or Ni_2O_3 species under an oxidative reaction environment, which was evidenced by Ni $2p_{3/2}$ spectra in XPS that revealed the formation of Ni_2O_3 (855.7 eV) as well as NiO (853.9 eV) (Figure 4.27b) from N-coordinating Ni(II) (854.9 eV) (Figure 4.27a). Meanwhile, the organic ligand ($bpdc^{2-}$) was decomposed and transformed to a carbogenic substances by heating up to 500℃, as shown in a TGA trace (Figure 4.28) and IR spectra before and after catalytic reactions (Figure 4.29). Overall, the resulting material after the catalytic reaction for the *ra*-MOF was a NiO_x/C nanocomposite. The TEM image also exhibited the formation of spherical crystalline NiO_x NPs on a carbogenic matrix (Figure 4.25a). The size of the NiO NPs was calculated by applying the Debye-Scherrer equation to the (200) reflection at $2\theta = 43.2°$ of the XRD pattern (Figure 4.24a), and the derived diameter of crystalline NiO NPs was 9.8 nm, which was consistent with the TEM image.

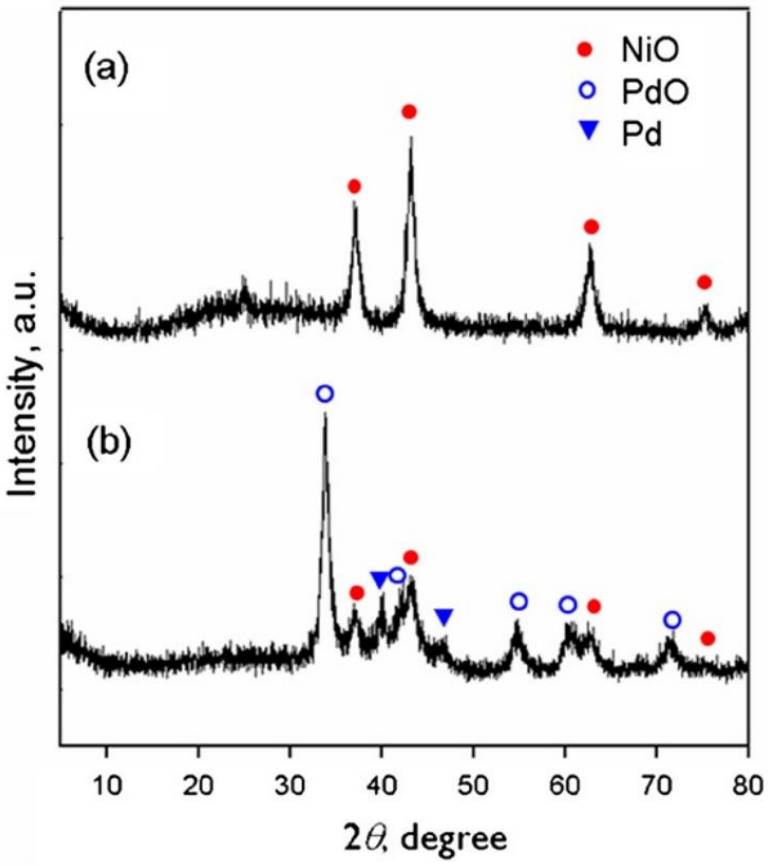

Figure 4.24 XRD patterns of (a) *ra*-MOF and (b) Pd@*ra*-MOF after CO oxidation reactions, respectively.

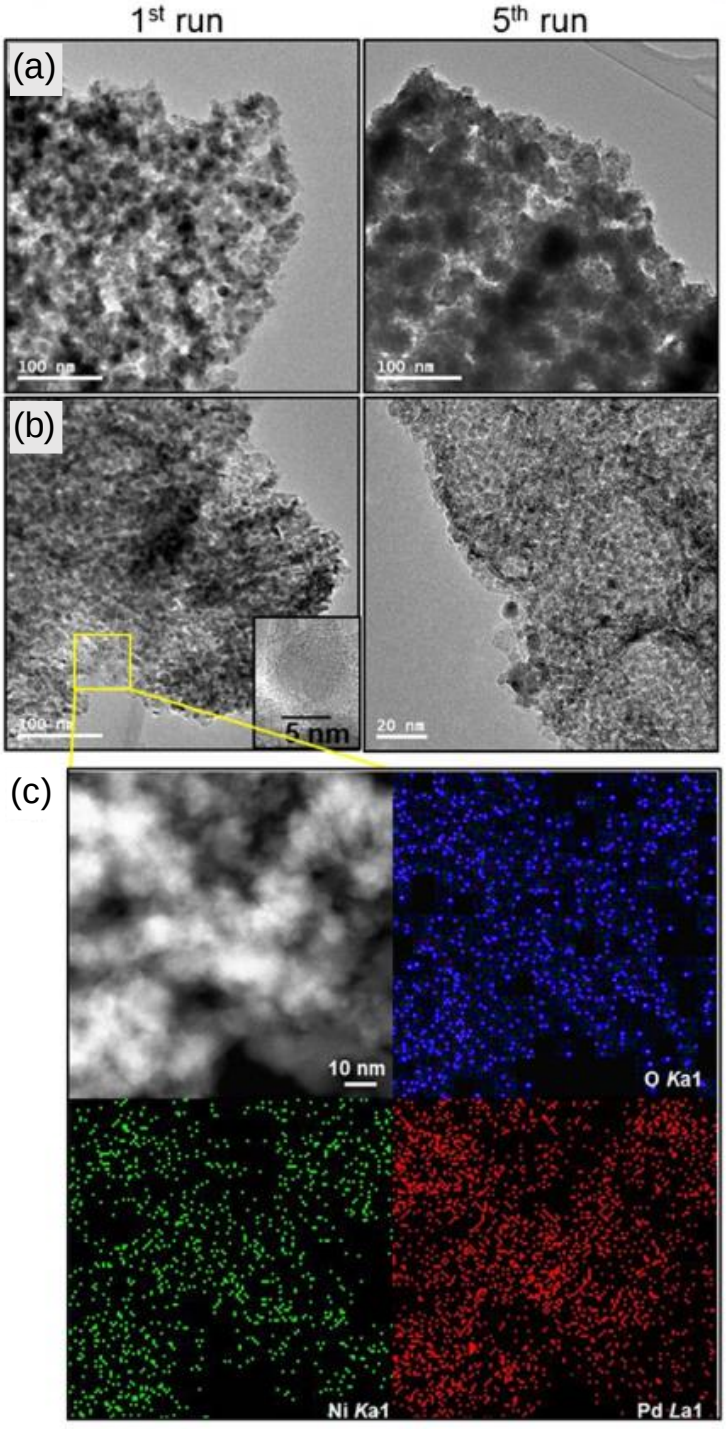

Figure 4.25 TEM images of (a) *ra*-MOF and (b) Pd@*ra*-MOF after CO oxidation reactions, respectively. (c) EDS mapping of Pd@*ra*-MOF after CO oxidation reaction.

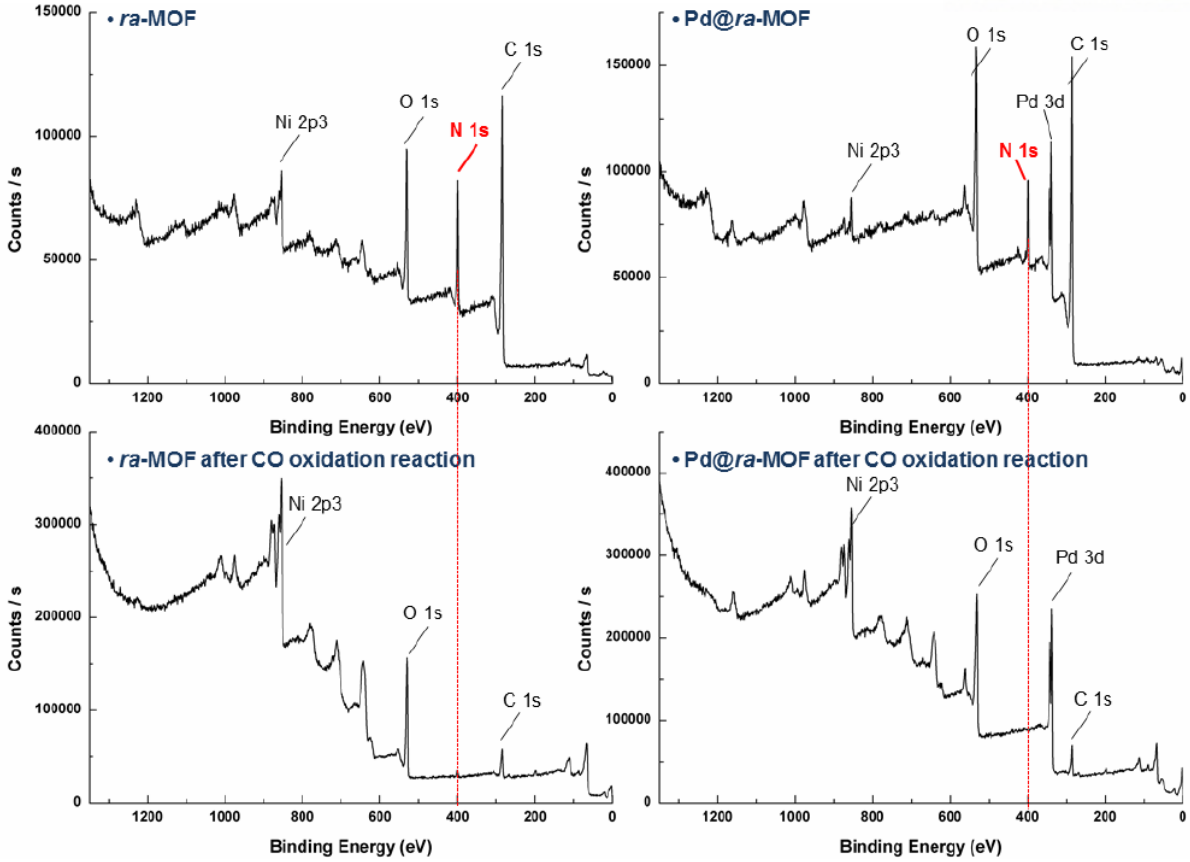

Figure 4.26 XPS wide scan spectra for *ra*-MOF and Pd@*ra*-MOF before and after CO oxidation reaction, respectively.

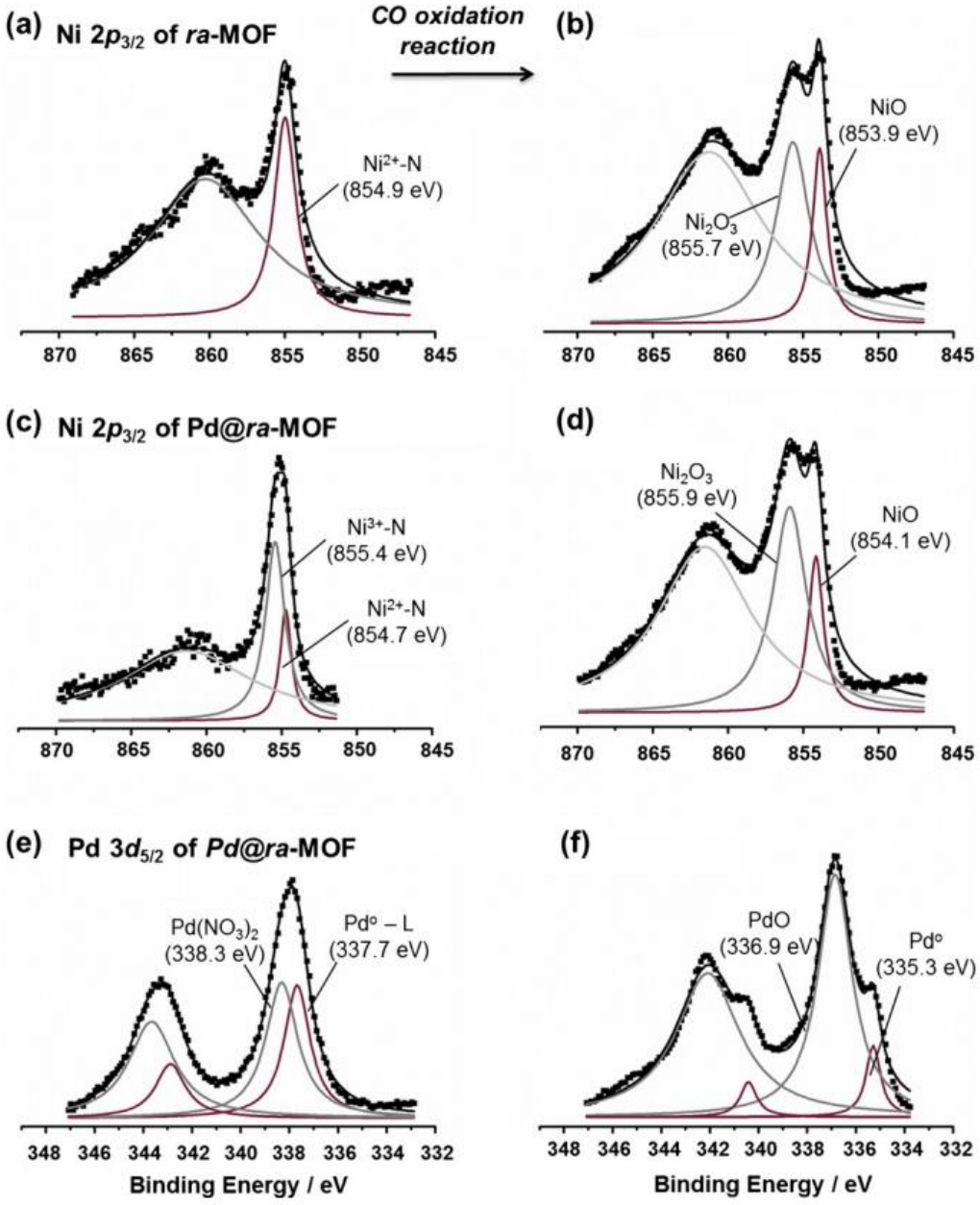

Figure 4.27 XPS spectra. (a) Ni $2p_{3/2}$ of *ra*-MOF, (c) Ni $2p_{3/2}$ of Pd@*ra*-MOF, and (e) Pd $3d_{5/2}$ of Pd@*ra*- MOF before and (b, d, f) after CO oxidation reaction (fifth run).

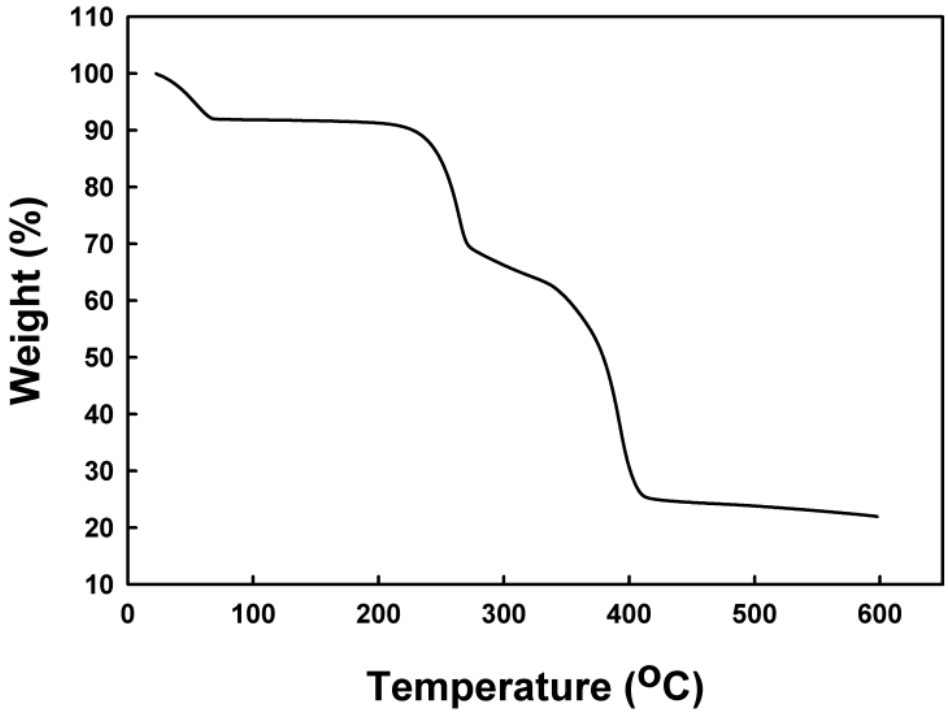

Figure 4.28 TGA trace of *ra*-MOF.

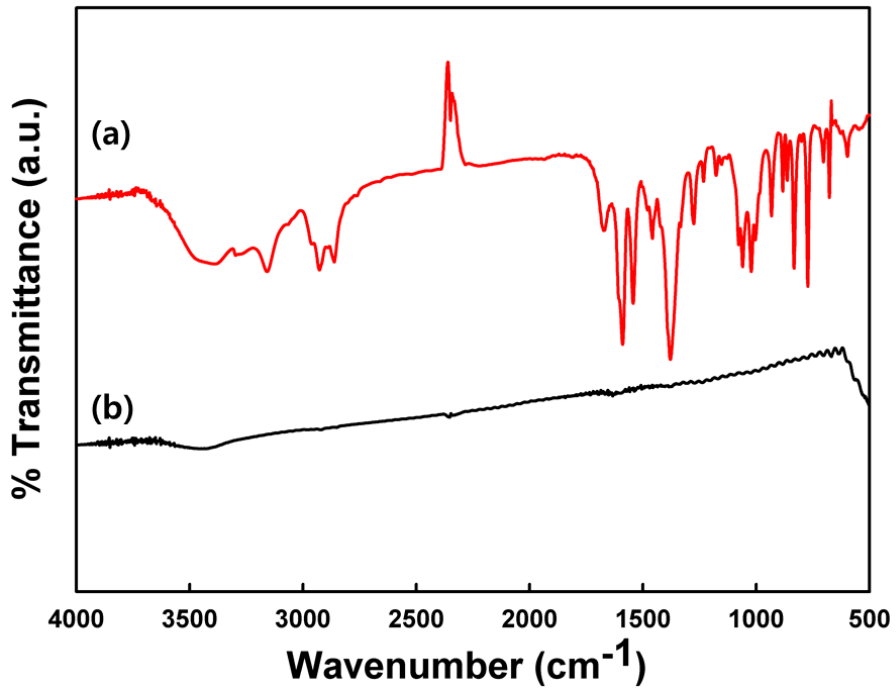

Figure 4.29 Comparison of IR spectra for *ra*-MOF (a) before and (b) after CO oxidation reaction upto 500 ºC.

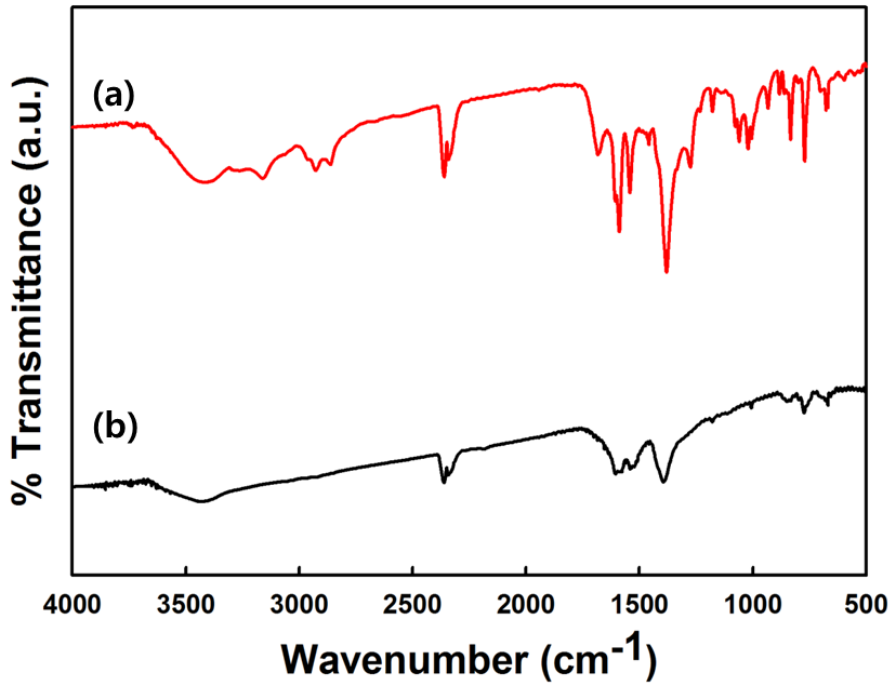

Figure 4.30 Comparison of IR spectra for Pd@*ra*-MOF (a) before and (b) after CO oxdiation reaction upto 300 ºC.

A similar transformation also occurred for the Pd@*ra*-MOF catalyst during CO oxidation. The XRD pattern of the catalyst after 5th run of CO oxidation reactions up to 300℃ (Figure 4.24b) exhibited the formation of NiO and PdO as well as the presence of existing metallic Pd species. The NiO was obtained by the thermal transformation of *ra*-MOF (as explained above), and the PdO NPs were generated by the oxidation of metallic Pd NPs during the reaction. The XRD peaks for converted NiO and PdO species were quite broad, and the crystalline sizes estimated by the Scherrer equation were 8.9, 9.9, and 10.3 nm for NiO, PdO, and Pd, respectively. The observation of TEM image for Pd@*ra*-MOF before and after the CO oxidation (Figure 4.25b) also revealed the formation of NiO and PdO NPs. Unlike the complete decomposition of *ra*-MOF at 500℃, the organic ligands ($bpdc^{2-}$) in Pd@*ra*-MOF, were partially decomposed and transformed into carbogenic supports and partially intact at a relatively low temperature, 300℃ as an IR spectrum showed characteristic peaks of a *ra*-MOF scaffold such as $\nu_{O\text{-}C=O}$ at 1,593(s) cm^{-1} and $\nu_{C=C(aromatic)}$ at 1,528(s) cm^{-1}, respectively (Figure 4.30). As shown in Figure 4.25c, EDS mapping of the PdO_x-NiO_y/C catalyst after CO oxidation shown that the PdO_x and NiO_y NPs were well dispersed throughout the carbogenic support. Additionally, the morphology and size of the PdO_x NPs were well-maintained after repeated CO oxidation runs, as shown in TEM images (Figure 4.25b, right).

This will be ascribed to the immobilizing the PdO_x and NiO_y NPs by the carbogenic support decomposed from organic ligands and the carbogenic species can effectively prevent migration and aggregation of NPs, even under the harsh and repeated CO oxidation reaction condition.

The compositional changes of Ni and Pd species in the Pd@*ra*-MOF after the catalytic reaction were examined by XPS. Before the CO oxidation reaction, Pd@*ra*-MOF properly contained N-coordinating Ni(III) species (855.4 eV) as well as Ni(II) (854.7 eV), which were produced by the redox reaction with Pd(II) (Figure 4.27c). After the CO oxidation reaction, however, Ni_2O_3 (855.9 eV) and NiO (854.1 eV) were generated by the thermal transformation of Ni(II/III) macrocycle molecules, similar to those of the as-prepared *ra*-MOF catalyst (Figure 4.27d). Before the Pd@*ra*-MOF experienced a catalytic reaction, the small-sized Pd^0 clusters (337.7 eV), which were strongly interacting with ligands of the *ra*-MOF scaffold,[24] co-existed with unreduced $Pd(NO_3)_2$ species (338.3 eV) (Figure 4.27e). After the reaction, most of the Pd species were oxidized to PdO (336.9 eV) under a harshly oxidative reaction condition, while the rest remained in the reduced metallic Pd^0 state (335.3 eV). Interestingly, it should be note that the binding energy of the latter was shifted to a lower energy level compared to that of Pd@*ra*-MOF before the catalytic reaction (Figure 4.27f) due to the bigger size of the Pd NPs from ca. 2 nm to ca. 10 nm, what were consistent with the XRD results (Figure 4.27b). Based on these analyses for XPS, XRD, and TEM results, during the CO catalytic reaction, the Pd@*ra*-MOF was converted into the PdO_x-NiO_y/C metal oxide-carbon nanocomposite ($0 \le x \le 1,\ 1 \le y \le 3/2$), where each species exhibited the synergetic catalytic effect for CO oxidation at a very low temperature. Furthermore, the

PdO_x-NiO_y/C catalyst after the fifth run showed a slightly higher BET surface area (35 m^2/g) than that of Pd@*ra*-MOF. Thus, the improved catalytic performance was attributed to providing active sites for catalyzing surface reaction (Figure 4.21). However, the surface area is still very low, indicating that the substantial portion of active sites of PdO and NiO NPs can be embedded and covered by carbon matrix. This may result in the loss of catalytic activity from the potentially expected.

The diverse metal oxides supporting metal nanoparticles catalysts have been studied for CO oxidation reaction. Machida *et al.* reported that the CO oxidation activity of metallic Pd NPs on CeO_2 supports was significantly enhanced by thermal aging of the catalyst.[25] It was revealed that the thermal treatment led to the strong metal-support interaction via Pd-O-Ce bonding, which effectively prevented the sintering of Pd-O species at high temperature and encouraged CO adsorption to react with oxygen. Haruta and other groups investigated on supported gold catalysts on metal oxides as a support including Fe_2O_3, TiO_2, CuO, La_2O_3, Al_2O_3, NiO, and Y_2O_3.[26-28] The activation of O_2 molecules has been shown to occur at the edges between Au NPs and the metal oxide support, highlighting the importance of metal-metal oxide interface in promoting CO oxidation.[29] In this study, the PdO_x-NiO_y/C nanocomposite which is catalytically active for CO oxidation reaction, was generated *in situ* in the reaction environment, and its stable, sustainable activity under cycling conditions could be attributed to the synergistic interaction among the PdO, NiO NPs, and carbogenic supports. Furthermore, compared to the conventional methods, this *in-situ* generation method of MO_x@C catalysts has a strength because of the simple synthetic procedure which can offer strong interactions between not only metal and metal oxide but also carbon and metal oxide nanoparticles during the reaction. Generally, MO_x@C catalysts are synthesized by loading metal precursors on carbon as a support and subsequent pyrolysis, which is almost carried out at high temperature for a long time.[30] In the present work, the *in-situ* spontaneously formed strong interactions provide the improvements of catalytic properties due to synergetic effect among metal, metal oxide and carbogenic supporter and prevent the agglomeration of nanoparticles because of reducing mobility of metal precursors on the supporter, which enhanced cycling performances with well-maintained morphology as revealed TEM images like small and monodispersed metal oxide nanocrystals.

4.4 Conclusion

We synthesized metal/metal oxide-carbon composites materials derived from transformation of MOFs. Based on the understanding of MOF conversion, we utilized their conversion behavior for synthesizing the target materials. Despite aware of the usefulness of the metallic Ge in a battery system, those NPs in pure phases are hardly synthesize by H_2 gas or carbothermic reduction. It is well-known that Zn is the proper reductant for metal oxides, as zincothermic reduction. Thus, we utilized Zn metal *in situ* evolved during the thermolysis of the Zn-MOF to reduce GeO_2 particles. The repeated occurrence of the zincothermic and carbothermic reduction reactions promotes a recyclable redox-metallothermic reaction. Along with MOF conversion, we found that during the CO oxidation reaction, the Pd@*ra*-MOF was transformed into a PdO_x-NiO_y/C nanocomposite that showed sustainable and enhanced catalytic activity through the synergistic stabilization of catalytically active PdO species. This study creates new opportunities for taking advantage of the MOF's vulnerable point to synthesize the diverse metal/metal oxide carbon composites by utilization of MOFs or metal NPs@MOF as precursors.

4.5 References

1. Jeong, G. H.; Baek, S.; Lee, S.; Kim, S.-W. Metal Oxide/Graphene Composites for Supercapacitive Electrode Materials. *Chemistry – An Asian Journal* **2012**, *11*, 949-964.
2. Chung, H. T.; Won, J. H.; Zelenay, P. Active and Stable Carbon Nanotube/Nanoparticle Composite Electrocatalyst for Oxygen Reduction. *Nature Communications* **2013**, *4*, 1922.
3. Wang, C.; Yin, L.; Zhang, L.; Xiang, D.; Gao, R. Metal Oxide Gas Snesors: Sensitivity and Influencing Factors *Sensors* **2010**, *10*, 2088-2106.
4. Tao, S.; Yue, W.; Zhong, M.; Chen, Z.; Ren, Y. Fabrication of Graphene-Encapsulated Porous Carbon-Metal Oxide Composites as Anode Materials for Lithium-Ion Batteries. *ACS Applied Materials and Interfaces* **2014**, *6*, 6332-6339.
5. Mondal, K.; Kumar, R.; Sharma, A. Metal-Oxide Decorated Multilayered Three-Dimensional (3D) Porous Carbon Thin Films for Supercapacitor Electrodes. *Industrial and Engineering Chemistry Research* **2016**, *55*, 12569-12581.
6. Liu, Y.; Jiang, H.; Zhu, Y.; Yang, X.; Li, C. Transition Metals (Fe, Co, and Ni) Encapsulated in Nitrogen-Doped Carbon Nanotubes as Bi-Functional Catalysts for Oxygen Electrode Reactions. *Journal of Materials Chemistry A* **2016**, *4*, 1694-1701.
7. Sampaio, M. J.; Bacsa, R. R.; Benyounes, A.; Axet, R.; Serp, P.; Silva, C. G.; Silva, A. M. T.; Faria, J. L. Synergistic Effect Between Carbon Nanomaterials and ZnO for Photocatalytic Water Decontamination. *Journal of Catalysis* **2015**, *331*, 172-180.
8. Song, J.; Li, G. R.; Xiong, F. Y.; Gao, X. P. Synergistic Effect of Molybdenum Nitride and Carbon Nanotubes on Electrocatalysis for Dye-Sensitized Solar Cells. *Journal of Materials Chemistry* **2012**, *22* (38), 20580-20585.
9. Liu, B.; Shioyama, H.; Akita, Y.; Xu, Q. Metal-Organic Framework as a Template for Porous Carbon Synthesis. *Journal of the American Chemical Society* **2008**, *130* (16), 5390-5391.
10. Yang, S. J.; Kim, T.; Im, J. H.; Kim, Y. S.; Lee, K.; Jung, H.; Park, C. R. MOF-Derived Hierarchically Porous Carbon with Exceptional Porosity and Hydrogen Storage Capacity. *Chemistry of Materials* **2012**, *24* (3), 464-470.
11. Zheng, Y.-Q.; Liu, W.-H.; Lin, J.-L.; Gu, L.-Y. Adipato-Bridged Mixed Ligand *catena* Complexes: $^{1}_{\infty}$ {[M(phen)(H_2O)]$L_{2/2}$} with M = Ni^{II}, Cu^{II}, Zn^{II}; H_2L = Adipic Acid. *Zeitschrift für anorganische und allgemeine Chemie* **2002**, *628* (4), 829-832.
12. Suh, M. P.; Kang, S. G. Synthesis and Properties of Nickel(II) and Copper(II) Complexes of 14-Membered Hexaaza Macrocycles, 1,8-Dimethyl- and 1,8-Diethyl-1,3,6,8,10,13-Hexaazacyclotetradecane. *Inorganic Chemistry* **1988**, *27* (14), 2544-2546.
13. Moon, H. R.; Kim, J. H.; Suh, M. P. Redox Active Porous Metal-Organic Framework Producing Silver Nanoparticles from AgI Ion at Room Temperature. *Angewandte Chemie International*

Edition **2005**, *44* (8), 1261-1265.

14. Laubengayer, A. W.; Morton, D. S. Germanium. XXXIX. The Polymorphism of Germanium Dioxide[1]. *Journal of the American Chemical Society* **1932**, *54* (6), 2303-2320.
15. Richet. P. GeO_2 vs SiO_2: Glass Transitions and Thermodynamic Properties of Polymorphs. *Physics and Chemistry of Minerals* **1990**, *17* (1), 79-88.
16. Seng, K. H.; Park, M.; Guo, Z. P.; Liu, H. K.; Cho, J. Catalytic Role of Ge in Highly Reversible GeO_2/Ge/C Nanocomposite Anode Material for Lithium Batteries. *Nano Letters* **2013**, *13* (3), 1230-1236.
17. Choi, S.; Kim, J.; Hwang, D. Y.; Park, H.; Ryu, J.; Kwak, S. K.; Park, S. Generalized Redox-Responsive Assembly of Carbon-Sheathed Metallic and Semiconducting Nanowire Heterostructures. *Nano Letters* **2016**, *16* (2), 1179-1185.
18. Suh, M. P.; Moon, H. R.; Lee, E. Y.; Jang, S. Y. A Redox-Active Two-Dimensional Coordination Polymer: Preparation of Silver and Gold Nanoparticles and Crystal Dynamics on Guest Removal. *Journal of the American Chemical Society* **2006**, *128* (14), 4710-4718.
19. Moon, H. R.; Suh, M. P. Flexible and Redox-Active Coordination Polymer: Control of the Network Structure by Pendant Arms of a Macrocyclic Complex. *European Journal of Inorganic Chemistry* **2010**, *2010* (24), 3795-3803.
20. Suh, M. P. Macrocyclic Chemistry of Nickel. *Advances in Inorganic Chemistry* **1996**, *44*, 93-146.
21. Engel, T.; Ertl, G. Elementary Steps in the Catalytic Oxidation of Carbon Monoxide on Platinum Metals. *Advances in Catalysis* **1979**, *28*, 1-78.
22. Somorjai, G. A. *Introduction to Surface Chemistry and Catalysis.* New York: Wiley; 1994.
23. Freund, H.-J.; Meijer, G.; Scheffler, M.; Schlögl, R.; Wolf, M. CO Oxidation as a Prototypical Reaction for Heterogeneous Processes. *Angewandte Chemie International Edition* **2011**, *50* (43), 10064-10094.
24. Bokman, F.; Gogoll, A.; Pettersson, L. G. M.; Bohman, O.; Siegbahn, H. O. G. Electronic Structure of Catalytically Important Palladium Complexes Studied by Photoelectron Spectroscopy. *Organometallics* **1992**, *11* (5), 1784-1788.
25. Hinokuma, S.; Fujii, H.; Okamoto, M.; Ikeue, K.; Machida, M. Metallic Pd Nanoparticles Formed by Pd–O–Ce Interaction: A Reason for Sintering-Induced Activation for CO Oxidation. *Chemistry of Materials* **2010**, *22* (22), 6183-6190.
26. Haruta, M.; Yamada, N.; Kobayashi, T.; Iijima, S. Gold Catalysts Prepared by Coprecipitation for Low-Temperature Oxidation of Hydrogen and of Carbon Monoxide. *Journal of Catalysis* **1989**, *115*, 301-309.
27. Haruta, M.; Tsubota, S.; Kobayashi, T.; Kageyama, H.; Genet, M. J.; Delmon, B. Low-Temperature Oxidation of CO over Gold Supported on TiO_2, α-Fe_2O_3, and Co_3O_4. *Journal of Catalysis* **1993**, *144* (1), 175-192.

28. Carabineiro, S. A. C.; Bogdanchikova, N.; Avalos-Borja, M.; Pestryakov, A.; Tavares, P. B.; Figueiredo, J. L. Gold Supported on Metal Oxides for Carbon Monoxide Oxidation. *Nano Research* **2011**, *4* (2), 180-193.
29. Guzman, J.; Carrettin, S.; Fierro-Gonzalez, J. C.; Hao, Y.; Gates, B.; Corma, A. CO Oxidation Catalyzed by Supported Gold: Cooperation between Gold and Nanocrystalline Rare-Earth Supports Forms Reactive Surface Superoxide and Peroxide Species. *Angewandte Chemie International Edition* **2005**, *44* (30), 4778-4781.
30. Liu, S. J.; Huang, C. H.; Huang, C. K.; Hwang, W. S. Chelating Agent-Assisted Heat Treatment of a Carbon-Supported Iron Oxide Nanoparticle Catalyst for PEMFC. *Chemical Communications* **2009**, 4809-4811.
31. Lee, K. J.; Kim, Y.; Lee, J. H.; Cho, S. J.; Kwak, J. H.; Moon, H. R. Facile Synthesis and Characterization of Nanostructured Transition Metal-Ceria Solid Solutions ($TM_xCe_{1-x}O_{2-\delta}$, TM = Mn, Ni, Co, or Fe) for CO Oxidation. *Chemistry of Materials* **2017**, *29*, 2874.
32. Kim, J. Y.; Jin, M.; Lee, K. J.; Cheon, J. Y.; Joo, S. H.; Kim, J. M.; Moon, H. R. *In-situ* Generated Metal Oxide Catalyst During CO Oxidation Reaction Transformed from Redox-Active Metal-Organic Framework-Supported Palladium Nanoparticles. *Nanoscale Research Letters* **2012**, *7*, 461.

Supporting information

Table S1. X-ray crystallographic data of *p*-MOF

Compound	***p*-MOF**
formula	$Co_3C_{36}H_{40}N_4O_{16}$
crystal system	*Monoclinic*
space group	*P2(1)/n*
fw	961.51
a, Å	16.182(3)
b, Å	9.4700(19)
c, Å	16.361(3)
α, deg	90.00
β, deg	111.28(3)
γ, deg	90.00
V, Å ^{3}	2336.3(8)
Z	2
ρ_{calcd}, g cm^{-3}	1.367
temp , K	100(2)
λ, Å	0.70002
μ, mm^{-1}	1.017
goodness-of-fit (F^2)	0.962
F(000)	986
reflections collected	17122
independent reflections	4776 [*R*(int) = 0.0841]
completeness to θ_{max}, %	99.4
data/parameters/restraints	4776/273/0
θ range for data collection, deg	2.59-26.00
diffraction limits (*h*, *k*, *l*)	$-20 \le h \le 20$, $-11 \le k \le 11$, $-20 \le l \le 20$
refinement method	Full-matrix least-squares on F^2
R_1, wR_2 [$I>2\sigma(I)$]	0.0801[a], 0.2160[b]
R_1, wR_2 (all data)	0.1174[a], 0.2357[b]
largest peak, hole, eÅ $^{-3}$	1.681, -0.647

[a] $R = \Sigma||Fo| - |Fc||/\Sigma|Fo|$. [b] $wR(F^2) = [\Sigma w(Fo^2 - Fc^2)^2/\Sigma w(Fo^2)^2]^{1/2}$ where $w = 1/[\sigma^2(Fo^2) + (0.1539P)^2 + (0.0000)P]$, $P = (Fo^2 + 2Fc^2)/3$.

Table S2. Selected bond distances (Å) and angles (°) of *p*-MOF

Co(1)-O(1)$^{\#1}$	2.059(4)	Co(1)-O(1)	2.059(4)
Co(1)-O(3)$^{\#2}$	2.063(4)	Co(1)-O(3)$^{\#3}$	2.063(4)
Co(1)-O(5)$^{\#1}$	2.117(4)	Co(1)-O(5)	2.117(4)
Co(2)-O(2)	2.040(4)	Co(2)-O(4)$^{\#2}$	2.043(4)
Co(2)-O(8)	2.067(5)	Co(2)-O(5)	2.134(4)
Co(2)-O(7)	2.189(5)	Co(2)-O(6)	2.247(5)
Co(2)-C(9)	2.517(7)	N(1)-C(13)	1.285(8)
N(1)-C(14)	1.443(10)	N(1)-C(15)	1.480(9)
N(2)-C(16)	1.337(8)	N(2)-C(18)	1.427(9)
N(2)-C(17)	1.447(9)	O(1)-C(1)	1.257(7)
O(2)-C(1)	1.238(8)	O(3)-C(8)	1.255(8)
O(3)-Co(1)$^{\#4}$	2.063(4)	O(4)-C(8)	1.262(7)
O(4)-Co(2)$^{\#5}$	2.043(4)	O(5)-C(9)	1.252(8)
O(6)-C(9)	1.243(8)	O(7)-C(13)	1.242(7)
O(8)-C(16)	1.227(8)	C(1)-C(2)	1.521(8)
C(2)-C(7)	1.361(9)	C(2)-C(3)	1.403(8)
C(3)-C(4)	1.387(9)	C(4)-C(5)	1.375(9)
C(5)-C(6)	1.379(9)	C(5)-C(8)	1.508(9)
C(6)-C(7)	1.398(9)	C(9)-C(10)	1.601(11)
C(10)-C(11)	1.374(10)	C(10)-C(12)$^{\#6}$	1.375(10)
C(11)-C(12)	1.381(11)	C(12)-C(10)$^{\#6}$	1.375(10)
O(1)$^{\#1}$-Co(1)-O(1)	179.999(1)	O(1)$^{\#1}$-Co(1)-O(3)$^{\#2}$	85.23(18)
O(1)-Co(1)-O(3)$^{\#2}$	94.77(18)	O(1)$^{\#1}$-Co(1)-O(3)$^{\#3}$	94.77(18)
O(1)-Co(1)-O(3)$^{\#3}$	85.23(18)	O(3)$^{\#2}$-Co(1)-O(3)$^{\#3}$	180
O(1)$^{\#1}$-Co(1)-O(5)$^{\#1}$	89.84(17)	O(1)-Co(1)-O(5)$^{\#1}$	90.16(17)
O(3)$^{\#2}$-Co(1)-O(5)$^{\#1}$	91.12(17)	O(3)$^{\#3}$-Co(1)-O(5)$^{\#1}$	88.88(17)
O(1)$^{\#1}$-Co(1)-O(5)	90.16(17)	O(1)-Co(1)-O(5)	89.84(17)
O(3)$^{\#2}$-Co(1)-O(5)	88.88(18)	O(3)$^{\#3}$-Co(1)-O(5)	91.13(17)

O(5)$^{\#1}$-Co(1)-O(5)	180	O(2)-Co(2)-O(4)$^{\#2}$	99.47(17)
O(2)-Co(2)-O(8)	88.01(18)	O(4)$^{\#2}$-Co(2)-O(8)	97.65(18)
O(2)-Co(2)-O(5)	97.97(18)	O(4)$^{\#2}$-Co(2)-O(5)	97.92(17)
O(8)-Co(2)-O(5)	162.15(18)	O(2)-Co(2)-O(7)	173.61(17)
O(4)$^{\#2}$-Co(2)-O(7)	86.44(17)	O(8)-Co(2)-O(7)	88.80(18)
O(5)-Co(2)-O(7)	83.52(17)	O(2)-Co(2)-O(6)	93.25(17)
O(4)$^{\#2}$-Co(2)-O(6)	155.42(17)	O(8)-Co(2)-O(6)	103.77(19)
O(5)-Co(2)-O(6)	59.29(17)	O(7)-Co(2)-O(6)	82.14(17)
O(2)-Co(2)-C(9)	97.9(2)	O(4)$^{\#2}$-Co(2)-C(9)	126.9(2)
O(8)-Co(2)-C(9)	132.9(2)	O(5)-Co(2)-C(9)	29.8(2)
O(7)-Co(2)-C(9)	80.3(2)	O(6)-Co(2)-C(9)	29.55(19)
C(13)-N(1)-C(14)	119.6(6)	C(13)-N(1)-C(15)	121.0(7)
C(14)-N(1)-C(15)	119.3(6)	C(16)-N(2)-C(18)	121.7(6)
C(16)-N(2)-C(17)	121.6(6)	C(18)-N(2)-C(17)	116.7(6)
C(1)-O(1)-Co(1)	138.4(4)	C(1)-O(2)-Co(2)	129.7(4)
C(8)-O(3)-Co(1)$^{\#4}$	140.5(4)	C(8)-O(4)-Co(2)$^{\#5}$	124.2(4)
C(9)-O(5)-Co(1)	133.2(4)	C(9)-O(5)-Co(2)	92.3(4)
Co(1)-O(5)-Co(2)	111.84(18)	C(9)-O(6)-Co(2)	87.4(4)
C(13)-O(7)-Co(2)	119.9(4)	C(16)-O(8)-Co(2)	126.1(4)
O(2)-C(1)-O(1)	127.7(6)	O(2)-C(1)-C(2)	117.5(5)
O(1)-C(1)-C(2)	114.7(6)	C(7)-C(2)-C(3)	120.2(6)
C(7)-C(2)-C(1)	119.2(6)	C(3)-C(2)-C(1)	120.6(6)
C(4)-C(3)-C(2)	119.0(6)	C(5)-C(4)-C(3)	121.6(6)
C(4)-C(5)-C(6)	118.3(6)	C(4)-C(5)-C(8)	121.1(6)
C(6)-C(5)-C(8)	120.5(6)	C(5)-C(6)-C(7)	121.4(7)
C(2)-C(7)-C(6)	119.5(6)	O(3)-C(8)-O(4)	126.3(6)
O(3)-C(8)-C(5)	116.9(5)	O(4)-C(8)-C(5)	116.8(6)
O(6)-C(9)-O(5)	120.8(6)	O(6)-C(9)-C(10)	122.9(6)
O(5)-C(9)-C(10)	115.9(6)	O(6)-C(9)-Co(2)	63.1(4)
O(5)-C(9)-Co(2)	57.9(3)	C(10)-C(9)-Co(2)	167.6(5)

C(11)-C(10)-C(12)$^{\#6}$	122.9(8)	C(11)-C(10)-C(9)	119.8(6)
C(12)$^{\#6}$-C(10)-C(9)	117.3(7)	C(10)-C(11)-C(12)	118.8(7)
C(10)$^{\#6}$-C(12)-C(11)	118.2(7)	O(7)-C(13)-N(1)	125.5(7)
O(8)-C(16)-N(2)	126.2(7)		

Symmetry transformation used to generate equivalent atoms:

$^{\#1}$, -x+1, -y+2, -z; $^{\#2}$, x-1/2, -y+5/2, z-1/2; $^{\#3}$, -x+3/2, y-1/2, -z+1/2; $^{\#4}$, -x+3/2, y+1/2, -z+1/2; $^{\#5}$, x+1/2, -y+5/2, z+1/2; $^{\#6}$, -x+1, -y+1, -z.

Table S3. X-ray crystallographic data of *r*-MOF

Compound	***r*-MOF**
formula	$Co_2C_{20}H_{20}S_2O_{10}$
crystal system	*Triclinic*
space group	*P-1*
fw	602.34
a, Å	7.3489(15)
b, Å	10.969(2)
c, Å	16.002(3)
α, deg	72.51(3)
β, deg	78.52(3)
γ, deg	73.12(3)
V, Å ^{3}	1168.5(4)
Z	2
ρ_{calcd}, g cm^{-3}	1.712
temp , K	173(2)
λ, Å	0.71073
μ, mm^{-1}	1.652
goodness-of-fit (F^2)	1.183
F(000)	612
reflections collected	11151
independent reflections	5300 [R(int) = 0.0983]
completeness to θ_{max}, %	99.8
data/parameters/restraints	5300/311/0
θ range for data collection, deg	3.02-27.48
diffraction limits (h, k, l)	$-9 \le h \le 9$, $-14 \le k \le 14$, $-20 \le l \le 20$
refinement method	Full-matrix least-squares on F^2
R_1, wR_2 [$I>2\sigma(I)$]	0.1242[a], 0.3121[b]
R_1, wR_2 (all data)	0.1750[a], 0.3591[b]
largest peak, hole, eÅ $^{-3}$	6.444, -1.655

[a] $R = \Sigma||Fo| - |Fc||/\Sigma|Fo|$. [b] $wR(F^2) = [\Sigma w(Fo^2 - Fc^2)^2/\Sigma w(Fo^2)^2]^{1/2}$ where $w = 1/[\sigma^2(Fo^2) + (0.2000P)^2 + (0.0000)P]$, $P = (Fo^2 + 2Fc^2)/3$.

Table S4. Selected bond distances (Å) and angles (°) of *r*-MOF

Co(1)-O(1)	2.041(7)	Co(1)-O(6)$^{\#1}$	2.047(7)
Co(1)-O(8)$^{\#2}$	2.051(7)	Co(1)-O(3)	2.051(6)
Co(1)-O(1D)	2.195(7)	Co(1)-O(2D)	2.213(6)
Co(2)-O(7)	2.041(7)	Co(2)-O(2)	2.055(7)
Co(2)-O(4)	2.055(7)	Co(2)-O(5)$^{\#3}$	2.058(7)
Co(2)-O(2D)	2.212(6)	Co(2)-O(1D)$^{\#4}$	2.218(7)
O(1)-C(1)	1.248(12)	O(2)-C(1)	1.262(12)
O(3)-C(5)	1.251(12)	O(4)-C(5)	1.230(12)
O(5)-C(12)	1.216(12)	O(5)-Co(2)$^{\#5}$	2.058(7)
O(6)-C(12)	1.261(12)	O(6)-Co(1)$^{\#6}$	2.047(7)
O(7)-C(13)	1.248(12)	O(8)-C(13)	1.266(12)
O(8)-Co(1)$^{\#4}$	2.051(7)	C(1)-C(2)	1.504(13)
C(2)-C(3)	1.383(15)	C(2)-C(4)	1.391(15)
C(3)-C(4)$^{\#7}$	1.365(15)	C(4)-C(3)$^{\#7}$	1.365(15)
C(5)-C(6)	1.517(12)	C(6)-C(7)	1.368(15)
C(6)-C(11)	1.392(14)	C(7)-C(8)	1.393(15)
C(8)-C(9)	1.405(15)	C(9)-C(10)	1.388(16)
C(9)-C(12)	1.507(13)	C(10)-C(11)	1.378(14)
C(13)-C(14)	1.518(14)	C(14)-C(15)	1.346(17)
C(14)-C(16)	1.398(16)	C(15)-C(16)$^{\#8}$	1.400(16)
C(16)-C(15)$^{\#8}$	1.400(16)	S(1)-O(1D)	1.536(6)
S(1)-C(17)	1.753(18)	S(1)-C(18)	1.777(16)
O(1D)-Co(2)$^{\#2}$	2.218(7)	S(2)-O(2D)	1.529(6)
S(2)-C(20)	1.712(17)	S(2)-C(19)	1.765(16)
O(1)-Co(1)-O(6)$^{\#1}$	85.0(3)	O(1)-Co(1)-O(8)$^{\#2}$	177.8(3)
O(6)$^{\#1}$-Co(1)-O(8)$^{\#2}$	95.6(3)	O(1)-Co(1)-O(3)	94.6(3)
O(6)$^{\#1}$-Co(1)-O(3)	177.6(3)	O(8)$^{\#2}$-Co(1)-O(3)	84.8(3)
O(1)-Co(1)-O(1D)	84.6(3)	O(6)$^{\#1}$-Co(1)-O(1D)	91.0(3)

O(8)$^{\#2}$-Co(1)-O(1D)	93.2(3)	O(3)-Co(1)-O(1D)	86.5(3)
O(1)-Co(1)-O(2D)	89.3(3)	O(6)$^{\#1}$-Co(1)-O(2D)	92.9(3)
O(8)$^{\#2}$-Co(1)-O(2D)	92.9(3)	O(3)-Co(1)-O(2D)	89.5(3)
O(1D)-Co(1)-O(2D)	172.4(2)	O(7)-Co(2)-O(2)	177.4(3)
O(7)-Co(2)-O(4)	85.4(3)	O(2)-Co(2)-O(4)	95.4(3)
O(7)-Co(2)-O(5)$^{\#3}$	94.4(3)	O(2)-Co(2)-O(5)$^{\#3}$	84.8(3)
O(4)-Co(2)-O(5)$^{\#3}$	179.4(3)	O(7)-Co(2)-O(2D)	85.2(3)
O(2)-Co(2)-O(2D)	92.4(3)	O(4)-Co(2)-O(2D)	91.9(3)
O(5)$^{\#3}$-Co(2)-O(2D)	87.5(3)	O(7)-Co(2)-O(1D)$^{\#4}$	88.4(3)
O(2)-Co(2)-O(1D)$^{\#4}$	94.1(3)	O(4)-Co(2)-O(1D)$^{\#4}$	91.3(3)
O(5)$^{\#3}$-Co(2)-O(1D)$^{\#4}$	89.3(3)	O(2D)-Co(2)-O(1D)$^{\#4}$	172.5(2)
C(1)-O(1)-Co(1)	134.5(7)	C(1)-O(2)-Co(2)	131.7(7)
C(5)-O(3)-Co(1)	137.0(6)	C(5)-O(4)-Co(2)	130.4(7)
C(12)-O(5)-Co(2)$^{\#5}$	132.2(7)	C(12)-O(6)-Co(1)$^{\#6}$	132.9(6)
C(13)-O(7)-Co(2)	139.2(7)	C(13)-O(8)-Co(1)$^{\#4}$	127.5(6)
O(1)-C(1)-O(2)	126.9(9)	O(1)-C(1)-C(2)	116.3(9)
O(2)-C(1)-C(2)	116.6(9)	C(3)-C(2)-C(4)	117.0(9)
C(3)-C(2)-C(1)	121.4(9)	C(4)-C(2)-C(1)	121.5(9)
C(4)$^{\#7}$-C(3)-C(2)	123.0(10)	C(3)$^{\#7}$-C(4)-C(2)	119.9(10)
O(4)-C(5)-O(3)	126.5(9)	O(4)-C(5)-C(6)	117.8(9)
O(3)-C(5)-C(6)	115.7(9)	C(7)-C(6)-C(11)	119.7(9)
C(7)-C(6)-C(5)	120.2(9)	C(11)-C(6)-C(5)	120.1(9)
C(6)-C(7)-C(8)	121.5(10)	C(7)-C(8)-C(9)	119.0(11)
C(10)-C(9)-C(8)	118.6(9)	C(10)-C(9)-C(12)	121.0(9)
C(8)-C(9)-C(12)	120.4(10)	C(11)-C(10)-C(9)	121.7(11)
C(10)-C(11)-C(6)	119.4(11)	O(5)-C(12)-O(6)	126.5(9)
O(5)-C(12)-C(9)	117.0(8)	O(6)-C(12)-C(9)	116.4(9)
O(7)-C(13)-O(8)	125.4(9)	O(7)-C(13)-C(14)	115.7(9)
O(8)-C(13)-C(14)	118.8(9)	C(15)-C(14)-C(16)	120.6(10)
C(15)-C(14)-C(13)	119.6(10)	C(16)-C(14)-C(13)	119.7(11)

C(14)-C(15)-C(16)#8	121.8(12)	C(14)-C(16)-C(15)#8	117.5(12)
O(1D)-S(1)-C(17)	106.8(6)	O(1D)-S(1)-C(18)	105.0(7)
C(17)-S(1)-C(18)	102.5(13)	S(1)-O(1D)-Co(1)	111.8(4)
S(1)-O(1D)-Co(2)#2	135.3(4)	Co(1)-O(1D)-Co(2)#2	112.9(3)
O(2D)-S(2)-C(20)	104.8(6)	O(2D)-S(2)-C(19)	105.8(6)
C(20)-S(2)-C(19)	100.5(12)	S(2)-O(2D)-Co(2)	111.5(4)
S(2)-O(2D)-Co(1)	135.6(4)	Co(2)-O(2D)-Co(1)	112.8(3)

Symmetry transformation used to generate equivalent atoms:

#1, x, y+1, z; #2, x+1, y, z; #3, x-1, y+1, z; #4, x-1, y, z; #5, x+1, y-1, z; #6, x, y-1, z;

#7, -x, -y+1, -z+1; #8, -x, -y, -z.

Table S5. X-ray crystallographic data of Mg-*aph*-MOF. [Squeezed data]

Compound	**Mg-*aph*-MOF**
formula	$Mg_8C_{56}H_{82}N_2O_{36}$
crystal system	*Monoclinic*
space group	*C2/c*
fw	1553.72
a, Å	35.558(5)
b, Å	13.495(5)
c, Å	29.699(5)
β, deg	122.628(5)
V, Å ^{3}	12002(5)
Z	4
ρ_{calcd}, g cm^{-3}	0.860
temp , K	173(2)
λ, Å	0.71069
μ, mm^{-1}	0.107
goodness-of-fit (F^2)	0.949
F(000)	3264
reflections collected	55468
independent reflections	13626 [R(int) = 0.1721]
completeness to θ_{max}, %	99.7
data/parameters/restraints	13626/455/0
θ range for data collection, deg	3.02-27.48
diffraction limits (h, k, l)	$-46 \le h \le 46$, $-17 \le k \le 17$, $-38 \le l \le 38$
refinement method	Full-matrix least squares on F^2
R_1, wR_2 [$I>2\sigma(I)$]	0.1025[a], 0.2772[b]
R_1, wR_2 (all data)	0.2133[a], 0.3232[b]
largest peak, hole, eÅ $^{-3}$	0.749, -0.459

[a] $R = \Sigma||F_o| - |F_c||/\Sigma|F_o|$. [b] $wR(F^2) = [\Sigma w(F_o^2 - F_c^2)^2/\Sigma w(F_o^2)^2]^{1/2}$ where $w = 1/[\sigma^2(F_o^2) + (0.1553P)^2 + (0.0000)P]$, $P = (F_o^2 + 2F_c^2)/3$.

Table S6. Selected bond distances (Å) and angles (deg) of Mg-*aph*-MOF. [Squeezed data]

Mg(1)-O(1)	2.051(4)	Mg(1)-O(3)$^{\#1}$	2.063(4)
Mg(1)-O(5)	2.115(4)	Mg(1)-O(7)	2.008(4)
Mg(1)-O(16)	2.148(4)	Mg(1)-Ow(2)	2.050(4)
Mg(2)-O(3)	2.160(4)	Mg(2)-O(4)	2.114(4)
Mg(2)-O(6)	2.048(4)	Mg(2)-O(8)	2.061(4)
Mg(2)-O(9)	2.040(4)	Mg(2)-O(13)	2.068(4)
Mg(3)-O(8)	2.091(4)	Mg(3)-O(10)	2.035(4)
Mg(3)-O(11)	2.038(4)	Mg(3)-O(13)	2.157(4)
Mg(3)-O(15)	2.047(4)	Mg(3)-Ow(1)	2.068(4)
Mg(4)-O(2)	2.018(4)	Mg(4)-O(5)	2.054(4)
Mg(4)-O(11)$^{\#2}$	2.098(4)	Mg(4)-O(12)	2.167(4)
Mg(4)-O(14)	2.042(4)	Mg(4)-O(16)	2.064(4)
Mg(2)-O(6)	2.048(4)	Mg(2)-O(8)	2.061(4)
Mg(2)-O(9)	2.040(4)	Mg(2)-O(13)	2.068(4)
Mg(3)-O(8)	2.091(4)	Mg(3)-O(10)	2.035(4)
Mg(3)-O(11)	2.038(4)	Mg(3)-O(13)	2.157(4)
Mg(3)-O(15)	2.047(4)	Mg(3)-Ow(1)	2.068(4)
Mg(4)-O(2)	2.018(4)	Mg(4)-O(5)	2.054(4)
Mg(4)-O(11)$^{\#2}$	2.098(4)	Mg(4)-O(12)	2.167(4)
Mg(4)-O(14)	2.042(4)	Mg(4)-O(16)	2.064(4)
O(1)-Mg(1)-O(3)$^{\#1}$	94.4(2)	O(1)-Mg(1)-O(5)	90.0(2)
O(1)-Mg(1)-O(7)	174.6(2)	O(1)-Mg(1)-O(16)	86.8(2)
O(1)-Mg(1)-Ow(2)	90.8(2)	O(3)$^{\#1}$-Mg(1)-O(5)	87.9(2)
O(3)$^{\#1}$-Mg(1)-O(7)	91.0(2)	O(3)$^{\#1}$-Mg(1)-O(16)	166.8(2)
O(3)$^{\#1}$-Mg(1)-Ow(2)	90.7(2)	O(5)-Mg(1)-O(7)	90.00(2)
O(5)-Mg(1)-O(16)	79.0(2)	O(5)-Mg(1)-Ow(2)	178.4(2)

O(7)-Mg(1)-O(16)	87.9 (2)	O(7)-Mg(1)-Ow(2)	89.4(2)
O(16)-Mg(1)-Ow(2)	102.4(2)	O(3)-Mg(2)-O(4)	61.1(2)
O(3)-Mg(2)-O(6)	85.7(2)	O(3)-Mg(2)-O(8)	106.4(2)
O(3)-Mg(2)-O(9)	91.0(2)	O(3)-Mg(2)-O(13)	171.8(2)
O(4)-Mg(2)-O(6)	86.0(2)	O(4)-Mg(2)-O(8)	167.0(2)
O(4)-Mg(2)-O(9)	87.2(2)	O(4)-Mg(2)-O(13)	111.8(2)
O(6)-Mg(2)-O(8)	96.9(2)	O(6)-Mg(2)-O(9)	173.2(2)
O(6)-Mg(2)-O(13)	89.8(2)	O(8)-Mg(2)-O(9)	89.8(2)
O(8)-Mg(2)-O(13)	80.9(2)	O(9)-Mg(2)-O(13)	92.7(2)
O(8)-Mg(3)-O(10)	88.1(2)	O(8)-Mg(3)-O(11)	168.8(2)
O(8)-Mg(3)-O(13)	78.2(2)	O(8)-Mg(3)-O(15)	88.3(2)
O(8)-Mg(3)-Ow(1)	100.0(2)	O(10)-Mg(3)-O(11)	95.8(2)
O(10)-Mg(3)-O(13)	86.3(2)	O(10)-Mg(3)-O(15)	176.1(2)
O(10)-Mg(3)-Ow(1)	86.5(2)	O(11)-Mg(3)-O(13)	91.5(2)
O(11)-Mg(3)-O(15)	87.5(2)	O(11)-Mg(3)-Ow(1)	90.7(2)
O(13)-Mg(3)-O(15)	91.6(2)	O(13)-Mg(3)-Ow(1)	172.5(2)
O(15)-Mg(3)-Ow(1)	95.6(2)	O(2)-Mg(4)-O(5)	88.8(2)
O(2)-Mg(4)-O(11)$^{\#3}$	93.9(2)	O(2)-Mg(4)-O(12)	85.9(2)
O(2)-Mg(4)-O(14)	173.4(2)	O(2)-Mg(4)-O(16)	89.4(2)
O(5)-Mg(4)-O(11)$^{\#3}$	174.8(2)	O(5)-Mg(4)-O(12)	162.4(2)
O(5)-Mg(4)-O(14)	89.6(2)	O(5)-Mg(4)-O(16)	82.3(2)
O(11)$^{\#3}$-Mg(4)-O(12)	64.5(2)	O(11)$^{\#3}$-Mg(4)-O(14)	87.2(2)
O(11)$^{\#3}$-Mg(4)-O(16)	102.1(2)	O(12)-Mg(4)-O(14)	88.8(2)
O(12)-Mg(4)-O(16)	162.4(2)	O(14)-Mg(4)-O(16)	96.8(2)

[a] Symmetry transformation used to generate equivalent atoms:

$^{\#1}$, -x+3/2, -y+3/2, -z+2; $^{\#2}$, x, -y+2, z+1/2; $^{\#3}$, x, -y+2, z-1/2

Acknowledgements

I gratefully acknowledge the support and guidance of FINE lab members at UNIST, most particularly my advisor, Prof. Dr. Hoi Ri Moon. Without her thoughtful encouragement and carful supervision, this work would not have been possible. Her unwavering enthusiasm for chemistry kept me constantly engaged with my research. I am truly grateful. I am privileged to have Tae Kyung Kim, Sung-min Hyun, Yun Kyeong Kim, Jin Yeong Kim, Jae Hwa Lee, Sungeun Jeoung, Byoungnam Moon, Jeong Min Hwang, In Tae Ju, and Songho Lee as my colleges who have shared their expertise and advice.

I would like to thank all the committee members, Prof. Dr. Myoung Soo Lah, Prof. Dr. Wonyoung Choe, Prof. Dr. Soojin Park, and Prof. Dr. Sang Hoon Joo for participating in my defense and advising me to pursue a sensible attitude as an independent scientist. I have received a great help directly or indirectly from many people for graduating the combined master's and doctoral program. I thank all those who have helped me both physically and spiritually.

Finally, I sincerely thank my family for all the help they have given me. I would like to dedicate this thesis to my family.

To everyone who has helped with my research, I express my thanks again. In conclusion, I want to quote the words of Winston Churchill: "This is not the end. It is not even the beginning of the end. But it is, perhaps, the end of the beginning."